2018

STRUCTURAL CHARACTERIZATION OF THE HUMAN C-MYC QUADRUPLEX AND MECHANISTIC EVALUATION OF ANTITUMOR AGENTS: ANTHRACENYL ISOXAZOLE AMIDES AND QUINOLINEDIONES

Sascha Christian LaMotte Stump

STRUCTURAL CHARACTERIZATION OF THE HUMAN C-MYC QUADRUPLEX AND MECHANISTIC EVALUATION OF ANTITUMOR AGENTS: ANTHRACENYL ISOXAZOLE AMIDES AND QUINOLINEDIONES

By
Sascha Christian LaMotte Stump

Bachelor of Science, Chemistry, University of Montana

Dissertation

Presented in partial fulfillment of the requirements for the degree of
Doctor of Philosophy in Toxicology

The University of Montana
Missoula, MT

December 2018

Approved by:

Scott Whittenburg, Dean of The Graduate School
Graduate School

Dr. Howard Beall, Chair
Department of Biomedical and Pharmaceutical Sciences

Dr. Andrij Holian
Department of Biomedical and Pharmaceutical Sciences

Dr. Nicholas Natale
Department of Biomedical and Pharmaceutical Sciences

Dr. Sarjubhai Patel
Department of Biomedical and Pharmaceutical Sciences

Dr. Jesse Hay
Division of Biological Sciences

Stump, Sascha, PhD, December 2018 Toxicology

STRUCTURAL CHARACTERIZATION OF THE HUMAN C-MYC QUADRUPLEX AND MECHANISTIC EVALUATION OF ANTITUMOR AGENTS: ANTHRACENYL ISOXAZOLE AMIDES AND QUINOLINEDIONES

Chairperson: Dr. Howard D. Beall

Cancer is a disease characterized by the abnormal proliferation of cells in the body. For many forms of cancer, there remain only limited and often ineffective treatment options available. Treatment of cancer is problematic for several reasons that include the difficulty in establishing molecular targets, finding interventions that cause selective toxicity to cancer cells, and the uniform capability of cancer cells to evade apoptosis. To address this, new strategies must be employed that take advantage of novel mechanisms of action to develop better therapies. The goal of this research is to aid in this effort through the study of emerging targets and antitumor agents. In these studies, we characterize the structure of an important target in the field of anticancer drug design, the quadruplex formed in the human c-MYC promoter region. The oncogene c-MYC is dysregulated or overexpressed in approximately 70% of human cancers and contributes to many survival pathways used by cancer cells to evade apoptosis. Stabilization of the c-MYC promoter quadruplex has been shown to reduce c-MYC expression and cause apoptosis in tumor cells. We also examine the mechanisms of action of two novel classes of antitumor agents, the anthracenyl isoxazole amides (AIMs) and a group of 5,8-quinolinedione analogs. We demonstrate interactions of the AIMs with quadruplex-forming sequences found in human telomeres, the c-MYC promoter, and mitochondrial DNA. Additionally, we provide evidence that the AIMs can inhibit the electron transport chain of mitochondria, specifically Complex II. Further, we show that treatment with the AIMs causes damage to mitochondrial DNA and loss of the mitochondrial membrane potential, leading to the intrinsic pathway of apoptosis in human glioblastoma cells. We also show a novel set of 5,8-quinolinedione analogs have potent antitumor activity in human breast cancer cells not related to their suitability as substrates for the NQO1-reductase that is often overexpressed in cancer. Together, this work has provided new insights to the field of anticancer drug discovery through characterization of an important target, the c-MYC promoter quadruplex, and through analysis of two novel classes of antitumor compounds, the AIMs and the 5,8-quinolinediones.

Table of Contents

List of Figures

List of Tables

Chapter 1 : Introduction

Sascha Stump[1] and Howard D. Beall[1*]

[1]Center for Environmental Health Sciences, Department of Biomedical and Pharmaceutical Sciences, University of Montana, Missoula, Montana 59812, United States of America

*Corresponding author

E-mail: howard.beall@umontana.edu

Human Cancers

Overview

Cancer is a disease defined by the abnormal proliferation of cells in the body which form tumors leading to adverse health outcomes and often death. Tumors are formed by cells containing genetic mutations and that have lost the normal mechanisms controlling cell growth, proliferation, and apoptosis. Additionally, tumors can undergo a process known as metastasis and invade and damage healthy tissues throughout the body. The National Cancer Institute estimates that approximately 1.7 million people will be diagnosed with cancer in the United States in 2018 alone (Siegel, Miller, and Jemal 2018). Significant progress has been made in the treatment options available to fight this deadly disease; the relative survival rate for cancer increased during the period of 2004 – 2010 to 68% from only 49% from 1975 – 1977 (Mitra et al. 2015). However, it remains the second leading cause of death in the United States, accounting for approximately 1 of every 4 deaths, and this highlights the need for development of improved anticancer therapies (Mitra et al. 2015; Siegel, Miller, and Jemal 2018).

Brain Cancer & Glioblastoma

It is estimated that brain and central nervous system tumors will cause approximately 17,000 deaths in 2018 and they are the leading form of childhood neoplasm, accounting for 26% of all pediatric cancers (Ostrom et al. 2014; Siegel, Miller, and Jemal 2018). Additionally, metastases in the brain can stem from many primary tumor types including lung, breast, melanoma and gastrointestinal tumors,

resulting in approximately 170,000 cases per year (Ulrich H. Weidle, Niewöhner, and Tiefenthaler 2015).

Glioblastoma is the most common form of brain cancer, accounting for approximately 15% of cases, and has an extremely poor prognosis with a median survival of only 12 – 15 months following initial diagnosis (American Cancer Society 2014). Glioblastoma tumors arise from astrocyte cells and represent the highest, Stage IV, classification of astrocytoma's on the WHO scale (Young et al. 2015). In contrast to more treatable forms of cancer, glioblastoma has very limited treatment options available. Complete surgical resection of glioblastoma tumors is often unsuccessful due to the difficulty in distinguishing diseased from healthy brain tissue. The extent of resection has been demonstrated to be linked to the rate of patient survival and survival is improved significantly when ≥ 98% of the tumor is excised; however, a greater extent of resection is also shown to increase the number of patients with permanent neural deficits due to damage to healthy neural tissue (Young et al. 2015). In addition, chemotherapeutic intervention is difficult for glioblastoma and other brain tumors due to the blood-brain barrier (BBB) which prevents many potential small-molecule treatments from reaching tumors in the brain (Ulrich H. Weidle, Niewöhner, and Tiefenthaler 2015). Regardless of these challenges, the current most common treatment of glioblastoma is a combination of resection of the tumor followed by a regiment of radiation and/or treatment with highly cytotoxic agents such as the first-line therapy temozolomide (Furnari et al. 2007; Young et al. 2015). Temozolomide is a non-specific alkylating agent that acts on guanine and adenine residues. It exerts its toxicity through methylation of the O6 atoms of guanine causing formation of O6-methyl-guanine bases

in DNA. These genetic lesions can be repaired by methylguanine-DNA-methyltransferase (MGMT), however it is a suicide repair enzyme and as a result the repair capacity is limited (J. Zhang, FG Stevens, and D Bradshaw 2012). Other primary treatments include the DNA alkylation agent carmustine and the DNA cross-linker cisplatin, both of which also exert their cytotoxic effect through damage to DNA (Reithmeier et al. 2010; Roux et al. 2017; Wang et al. 2017; Coluccia et al. 2018). In theory and in practice this non-specific DNA damage is more toxic to rapidly dividing tumor cells than to senescent healthy cells. However, the reality is that these treatments often lead to excess damage in healthy tissues.

Evasion of Apoptosis in Cancer

Evasion of apoptosis is an essential characteristic of cancer. This can be caused through upregulation of anti-apoptotic signaling or downregulation of pro-apoptotic proteins. The extrinsic pathway of apoptosis is often stunted through reduction in expression of death receptors on the cell surface. Prevention of caspase-8 activation through upregulation and direct binding of proteins such as cFLIP to the death receptor complex can also prevent activation of the extrinsic pathway (Fulda 2010). Similarly, the intrinsic apoptosis pathway can be inhibited through increases in expression of functional antiapoptotic (Bcl-2, Bcl-xL, Mcl-1) or decreases in expression of proapoptotic proteins (Bax, Bak, Bid, Apaf-1) (**Figure 1.1**) (Fulda 2009).

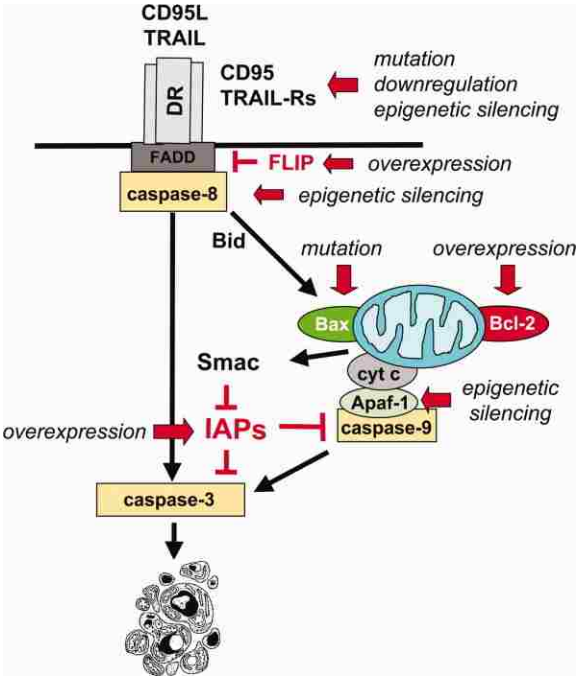

Figure 1.1 Evasion of Apoptosis in Cancer

(Fulda 2009)

Overexpression of antiapoptotic proteins such as inhibitor of apoptosis (IAP) proteins, Bcl-2, or genetic silencing/mutation of proapoptotic proteins such as Apaf-1 and Bax can contribute to evasion of apoptosis by cancer.

Apoptosis Overview

The two major apoptotic pathways are the intrinsic (mitochondrial-mediated) and extrinsic (death receptor-mediated) routes. Both of these pathways lead to eventual cell death through activation of a family of serine proteases known as caspases. Activation of a caspase cascade leads to proteolytic cleavage of target proteins in the cell causing cell death (Fulda 2010).

Extrinsic Apoptosis

Death receptor-mediated apoptosis, also known as the extrinsic pathway, is caused by activation of death receptors on the surface of the cell. Activation of death receptors leads to activation of initiator caspase-8 which can then act to cleave downstream effector caspase-3. Caspase-8 also is capable of cleaving the mitochondrial protein Bid to tBid, causing permeabilization of the outer mitochondrial membrane and subsequent cytochrome *c* release from the mitochondria (Fulda 2010).

Intrinsic Apoptosis

Mitochondrial mediated apoptosis is characterized by activation of caspase-9 following release of cytochrome *c* from the mitochondria. Release of caspase-9 also causes activation of caspase-3 through formation of a large protein complex termed the apoptosome (Fulda 2010). The apoptosome is formed by Apaf-1 and caspase-9 and requires the presence of cytochrome *c* and dATP. Procaspase-9 is recruited to CARD motifs on Apaf-1 and this activates caspase-9 (Yuan and Akey 2013).

Summary

The goal of anticancer therapeutics is to develop treatments which selectively target and induce apoptosis in tumor cells. Unfortunately, current therapies are often non-specific, especially in the case of brain tumors, and cause damage to healthy tissues. To address this issue, it is necessary to examine novel targets in the effort to develop more selective and effective medicines.

In this work, multiple potential targets for antitumor agents are explored, and the significant findings are reported. This work examines targeting quadruplex DNA structures, specifically the c-MYC quadruplex, for antitumor drug development. The mechanism underlying a class of novel antitumor compounds, the anthracenyl isoxazole amides (AIMs), is also addressed in detail as it pertains to quadruplex DNA and interactions in the mitochondrial electron transport chain. The work also contributes to studies of a novel set of synthetic analogs designed to utilize the NQO1-reductase to target tumor cells.

Targets for Development of Antitumor Compounds

Quadruplex DNA

History

Guanine-rich regions of DNA and RNA can form a secondary structure known as a quadruplex. The study of quadruplex structures can be traced back to a report in 1910 of solutions of guanylic acid forming gels at high concentrations, indicating the presence of a higher-order structure (Bang, I. 1910). Later, this higher order structure was identified as helical through X-ray fiber diffraction studies and the basic unit of the quadruplex, now known as a G-quartet, was theorized (**Figure 1.2**) (Gellert, Lipsett, and Davies 1962).

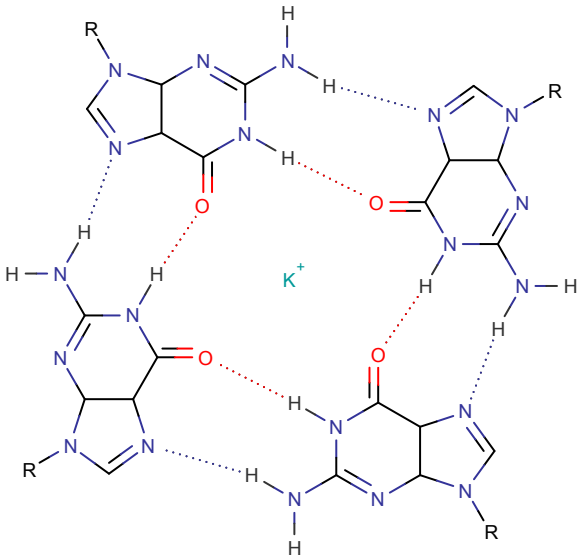

Figure 1.2 G-Quartet

Four guanines form the basic unit of the quadruplex structure, known as a G-quartet, through Hoogsteen bonding stabilized by surrounding a monovalent cation.

Although there were some structural studies completed, quadruplex structures were largely ignored for a long period of time following their discovery as it was unknown if they had any biological significance. However, it was later shown that these structures could form in guanine-rich DNA under physiological conditions and these guanine-rich regions were present in gene promoter and in human telomeres (Sen and Gilbert 1988; Sundquist and Klug 1989; Burge et al. 2006). Following this realization, quadruplex structures have become the subject of significant scientific study, with the number of quadruplex-related articles being published increasing almost every year since (**Figure 1.3**).

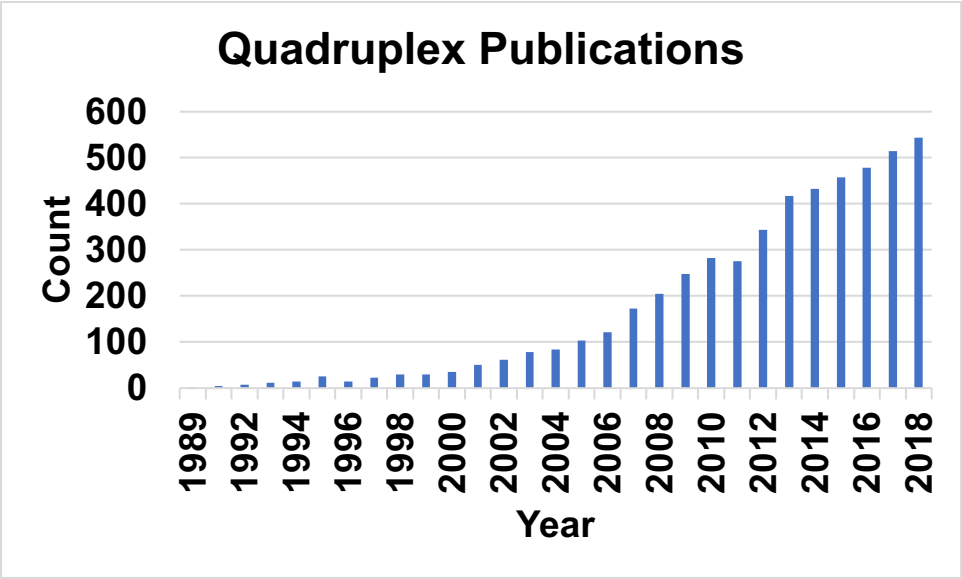

Figure 1.3 Quadruplex Publications

Articles published per year when searching “quadruplex” on PubMed.

Quadruplex Topology

As mentioned previously, quadruplex structures can form from DNA, RNA or a combination of both. The basic unit of the quadruplex is the G-quartet (**Figure 1.2**), which is comprised of four guanine nucleotides surrounding a monovalent cation such as sodium or potassium, held together through Hoogsteen bonding. The monovalent cation compensates for the electronegative charge of the O6 oxygen atoms of the guanine bases and is essential for this stable conformation (Burge et al. 2006; Bhattacharyya, Mirihana Arachchilage, and Basu 2016). Potassium is generally preferred to sodium and is observed in a square antiprismatic coordination with the O6 atoms between the interface of two G-quartets. Sodium is also commonly observed, however its smaller radius allows coordination by the O6 atoms of a single G-quartet in a square-planar conformation. Other, less physiologically relevant monovalent cations

can also be similarly involved in the quadruplex structure, however the small atomic radius of lithium does not allow it to stably occupy this space (Bhattacharyya, Mirihana Arachchilage, and Basu 2016).

Quadruplexes can form as intramolecular or intermolecular arrangements, arising from single or multiple nucleic acid strands, respectively. Unimolecular quadruplex structures arising from a single strand have been the subject of the majority of studies due to their physiological relevance, however bimolecular and tetramolecular quadruplex structures have also been characterized in solution and in crystal structures. The sequence motif that forms quadruplex structures is similar for both intramolecular and intermolecular quadruplexes with the general form of $G_{3-5}L_{<7}G_{3-5}L_{<7}G_{3-5}L_{<7}G_{3-5}$. The loop nucleotides are necessary for allowing the G-quartets to stack in a stable conformation, with smaller loop regions generally indicating a more stable quadruplex structure. Three types of loops have been shown to form (Burge et al. 2006; Balasubramanian, Hurley, and Neidle 2011).

Propeller, or strand-reversal loops, occur when the G-quartet at one side of the overall quadruplex is connected through a loop to the G-quartet on the opposing side. Diagonal loops refer to those which connect two corners of G-quartets on opposite sides relative to each other. Lateral loops are those which connect two corners of G-quartets on adjacent sides. The types of loops formed in the quadruplex determine the overall topology of the quadruplex, divided into three types (**Figure 1.4**) (Neidle 2017).

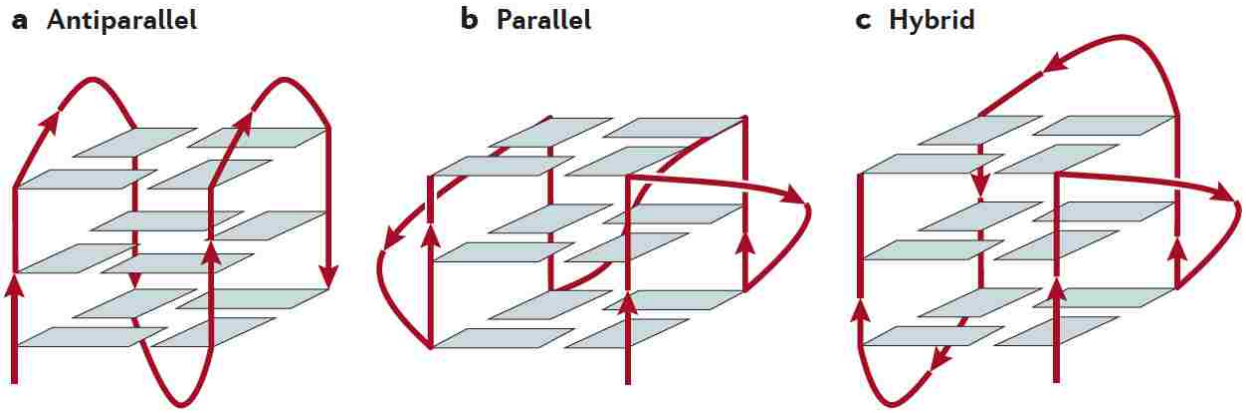

Figure 1.4 Quadruplex Topologies

(Neidle, 2017)

Three classes of quadruplex topology. Antiparallel, parallel and hybrid refer to the strand direction on each edge of the overall quadruplex (5' – 3').

Parallel quadruplexes are those in which the direction of the nucleic acid strands on each edge of the structure run parallel to one another in the 5' – 3' direction. Anti-parallel refers to quadruplexes in which the two edges oppose the direction of the other two edges. The third type is the hybrid, or mixed 3+1, type in which three of the nucleic acid strands on the edges proceed in the same direction and one in the opposite direction (Balasubramanian, Hurley, and Neidle 2011). All of these types have been demonstrated experimentally, and multiple forms have even been observed for the same sequence in an equilibrium such as is exemplified by the sequence found in human telomeres (Parkinson, Lee, and Neidle 2002; Luu et al. 2006; Phan, Kuryavyi, Luu, et al. 2007).

Quadruplexes in Telomeres

The terminal 3'-end of human telomeres have been shown to be single-stranded and comprised of a repeating sequence of the form TTAGGG (Burge et al. 2006). This allows for formation of repeating quadruplex structures and this has been described as "beads on a string" (Yu et al. 2012). However, the protein hPOT1 competes with quadruplex formation and allows telomerase to bind and maintain telomere length in cells as they divide. Excessive disruption of hPOT1 binding by inducing quadruplex formation causes a DNA damage response in cells and causes them to undergo apoptosis (Neidle 2010). This strategy is being actively explored as a possible mechanism to target for development of small-molecule anticancer therapies.

Expression of telomerase is upregulated in over 80% of cancers, allowing tumor cells to rapidly divide while maintaining telomere length and preventing the degradation of coding DNA. Telomerase activity is dependent on binding of hTERT, the catalytic subunit, to the single-stranded telomeric overhangs and hybridization of a telomeric RNA template to allow lengthening of the telomere. Formation of quadruplex structures in the telomeric overhangs prevents the catalytic activity of telomerase. It has been shown that small-molecules which bind telomeric quadruplex structures can shift the equilibrium to favor quadruplex formation and thereby prevent the lengthening of telomeres by telomerase. This results in induction of rapid senescence in tumor cells and activation of the DNA damage response leading to apoptosis (**Figure 1.5**) (Neidle 2010).

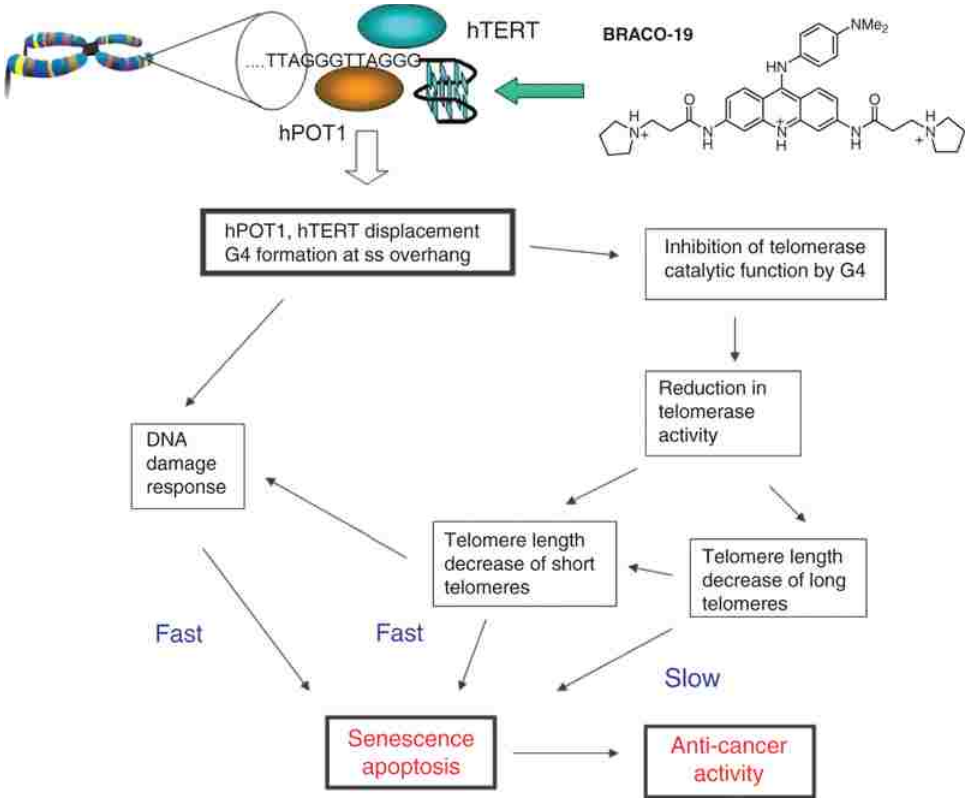

Figure 1.5 Telomeric Quadruplex Induced Apoptosis

(Neidle, 2010)

Mechanisms of inducing apoptosis in cancer cells using the telomeric quadruplex ligand BRACO-19 as an example. hPOT1 and hTERT are displaced by formation of a quadruplex in the telomeric overhang and stabilization with the BRACO-19 ligand.

Quadruplexes in Gene Promoters

Quadruplex-forming sequences are prevalent in gene promoter regions, and specifically in multiple genes important to the pathogenesis of cancer. These include the promoter regions of c-MYC, c-KIT, Bcl-2, VEGF, KRAS, and HIF-1α (Yang and Hurley 2006; Phan, Kuryavyi, Burge, et al. 2007; Dexheimer, Sun, and Hurley 2006, -2; Sun et al. 2005; Lavrado et al. 2015; De Armond et al. 2005). The most well-studied is

c-MYC due to its overexpression in approximately 70% of all human cancers and multiple roles essential to tumor cell survival. It has been demonstrated that quadruplex formation in the $NHEIII_1$ region of the c-MYC promoter prevents transcription of c-MYC, leading to apoptosis in multiple tumor cell types (**Figure 1.6**) (Ou et al. 2007). *A more complete description of the c-MYC promoter quadruplex and its functions in cancer will follow in* ***Chapter 2*** (Stump et al. 2018).

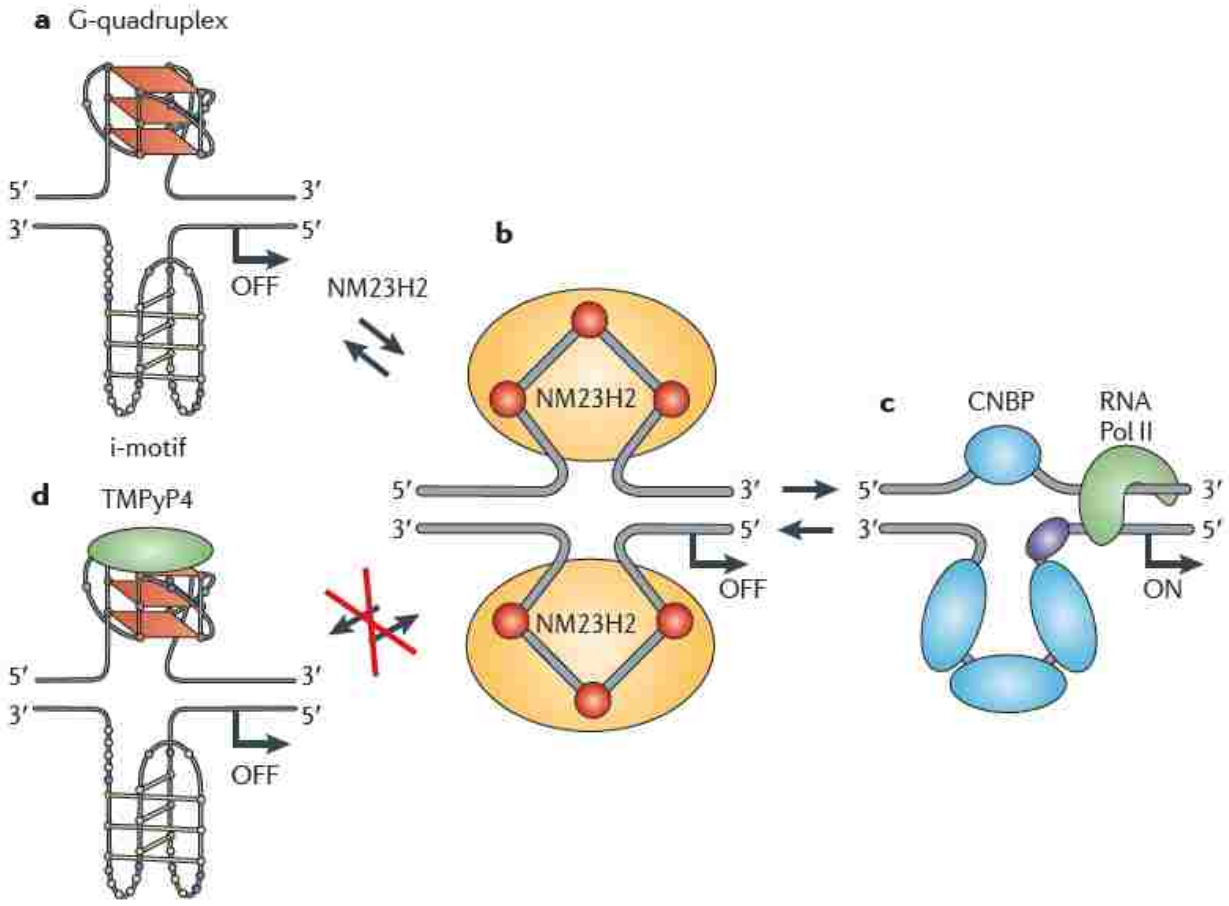

Figure 1.6 Reduction of c-MYC expression using a quadruplex stabilizing ligand (Balasubramanian, Hurley, and Neidle 2011)

Stabilization of the c-MYC promoter quadruplex with a ligand such as TMPyP4 interferes with binding of transcription factors and RNA polymerase II to prevent transcription and expression of c-MYC.

Another well-studied example is the quadruplexes formed in the c-KIT promoter region. The c-KIT promoter contains two quadruplex-forming sequences and encodes for a tyrosine kinase important in the development of gastrointestinal tumors and other human cancers (Fernando et al. 2006; Rankin et al. 2005; Phan, Kuryavyi, Burge, et al. 2007). Multiple studies have demonstrated reduction in c-KIT expression in tumor cells following treatment with quadruplex targeted ligands (Bejugam et al. 2007; McLuckie et al. 2011; Balasubramanian, Hurley, and Neidle 2011). Two quadruplex structures also form in the KRAS gene promoter. KRAS is a member of the RAS family of G-proteins which are involved in pathways affecting cell growth and apoptosis (Morgan et al. 2016). Overactivation of KRAS is commonly found in cancers and leads to enhanced cell proliferation and loss of tumor suppressor function. Previous studies have demonstrated that KRAS expression in cancer cells can be reduced using small-molecule quadruplex binding ligands (Lavrado et al. 2015; Morgan et al. 2016).

RNA Quadruplexes

Quadruplexes have also been shown to form in RNA and are generally more stable than their DNA counterparts (Agarwala, Pandey, and Maiti 2015; Bugaut and Balasubramanian 2012; Fay, Lyons, and Ivanov 2017). This is due to the fact that RNA is mostly single-stranded and the presence of a 2'-OH in the ribose sugar allowing for increased intramolecular interactions. Known biological RNA quadruplexes are also restricted to the parallel topology. For these reasons, the melting temperatures of RNA quadruplexes often exceed temperatures found in most biological systems. Interestingly, regardless of this remarkable stability, it has been suggested that RNA

quadruplexes do not form to any significant extent *in vivo*, and this is likely due to unwinding of these structures in the cell. There is evidence of several proteins that bind RNA quadruplexes, and even some that can unwind these structures *in vitro*, such as DHX36 (G4 resolvase) and DHX9 (RNA helicase A) (Fay, Lyons, and Ivanov 2017). Several biological roles of RNA and DNA:RNA hybrid quadruplexes have been suggested including in transcriptional regulation, 3'-end RNA processing, pre-mRNA splicing regulation and mRNA translation, however the field is still developing and many of the details remain to be discovered (Fay, Lyons, and Ivanov 2017).

Quadruplexes in Mitochondrial DNA

It has been demonstrated that quadruplexes are also able to form in mitochondrial DNA (mtDNA). Studies suggest that there are approximately 200 putative quadruplex-forming sequences present in the mitochondrial genome (Bharti et al. 2014; D. W. Dong et al. 2014). A recent study using fluorescent compounds has suggested that quadruplexes in mtDNA may be suitable targets for development of anticancer therapies (Huang et al., 2015). The researchers demonstrate that a set of carbazole ligands derivatized with pyridinium iodide, connected through varying lengths of alkyl chains, can bind quadruplex structures found in mtDNA. The researchers suggest the mechanism of action of these compounds is through prevention of mtDNA gene expression leading to apoptosis (Huang et al., 2015). This hypothesis is strengthened by previous studies demonstrating genes in mtDNA containing putative quadruplex-forming sequences are more susceptible to DNA damage (Bharti et al. 2014).

Another area of significant interest in the involvement of quadruplex structures in transcription and replication of mtDNA. A domain of mitochondrial DNA (mtDNA) known as conserved sequence block II (CSB II) has been demonstrated to form a parallel DNA:RNA hybrid quadruplex with nascent RNA during mtDNA transcription (Wanrooij et al. 2010; Zheng et al. 2013). Transcription of mtDNA can be prematurely terminated through formation of a structure known as the D-loop, which is responsible for generation of the RNA primers required for initiation of mtDNA replication. Multiple reports in the literature suggest the formation of the hybrid quadruplex as the mechanism responsible for the transition from transcription to synthesis of mtDNA (Wanrooij et al. 2010; Zheng et al. 2014).

Methods for Study of Quadruplexes

There are many common methods employed for the study of quadruplex structures. The major methods utilized and referenced in this work are outlined below, however this is by no means an exhaustive list.

Macromolecular X-ray Crystallography

One of the best methods used to reveal nuances in the overall topology of quadruplex structures is X-ray crystallography. Briefly, crystal growth conditions are evaluated using a high-throughput screening method, often in a 96-well format. Once preliminary crystals are attained, the conditions can be refined further to improve the quality and size of the crystals. Crystals suitable for structure determination are then placed in front of a detector and a focused beam of x-rays is directed at the crystal as it

is rotated in front of the detector. The detector collects the diffraction pattern from x-rays scattered as a result of the electrons present in the crystalline lattice. From this diffraction pattern, a map of the electron density of the macromolecule of interest can be calculated and the position of the atoms can be determined with high precision (N. H. Campbell and Parkinson 2007; N. Campbell, Collie, and Neidle 2012; Parkinson, Lee, and Neidle 2002; Wei et al. 2012; Stump et al. 2018).

At the time of writing, over 130 quadruplex structures have been determined using macromolecular crystallographic methods and deposited in the RCSB Protein Databank, a repository for macromolecular structures. Many of these structures also contain ligands bound to the quadruplex structures and this has allowed for further design and refinement of small molecules ligands.

NMR Spectroscopy

NMR spectroscopy is another common method employed for studying quadruplex structures and their interactions with ligands. The imino protons of the guanine bases in both DNA and RNA quadruplexes display characteristic peaks between 10 – 12 ppm in their ^{1}H spectra (Adrian, Heddi, and Phan 2012; Bao et al. 2017). This allows measurement of anisotropy changes resulting from perturbation of the quadruplex structure with ligands. Selectively N^{15} or F^{19} labeled nucleotide bases coupled with two-dimensional water-suppression NOSEY methods can also be employed in conjunction with molecular dynamics to accurately approximate the topology of specific quadruplex structures formed by different sequences of DNA and

RNA (Yang and Hurley 2006; Dai et al. 2011; Adrian, Heddi, and Phan 2012; Bao et al. 2017).

Circular Dichroism Spectroscopy

Circular dichroism spectroscopy (CD) measures the differential absorbance of polarized light by chiral molecules such as DNA and RNA. Quadruplex structures display characteristic peaks in their CD spectra and the method can be used to distinguish between parallel, anti-parallel and hybrid 3+1 type structures (Paramasivan, Rujan, and Bolton 2007). Temperature melts performed at the maximum of peaks in a quadruplex CD spectra can be used to make inferences about the stability of the secondary structure and the relative effect of bound small molecule ligands (Greenfield 2006; Paramasivan, Rujan, and Bolton 2007; Weaver et al. 2015).

Summary

Quadruplex structures represent a promising target for development of novel anticancer therapeutics. The involvement of quadruplexes in many processes regulating expression of many oncogenes both at the transcriptional and post-transcriptional level highlights the potential of these structures as targets. In addition, the roles of quadruplexes in mitochondria and specifically mtDNA are beginning to emerge and may provide another avenue for creating targeted therapies for cancer.

Mitochondria

History

Mitochondria are central to both energy metabolism and many processes governing homeostasis in human cells. One of the most important functions of mitochondria is the role they play in the initiation of the intrinsic pathway of apoptosis. Targeting this pathway has become a focus of many scientists as a possible mechanism to employ in finding new strategies for causing apoptosis in tumor cells and treatment of cancer. The suggestion that mitochondria may be important in the pathogenesis of cancer can be traced back to Nobel laureate Otto Warburg in 1924, when first proposed what is now known as the “Warburg effect” (Otto Warburg 1925; Liberti and Locasale 2016). The hypothesis was based on the observation that cancer cells have a metabolic shift relative to normal cells where they begin to produce energy in the form of ATP primarily by non-oxidative glycolysis rather than through oxidative phosphorylation by mitochondria. (Fulda, Galluzzi, and Kroemer 2010) (**Figure 1.7**).

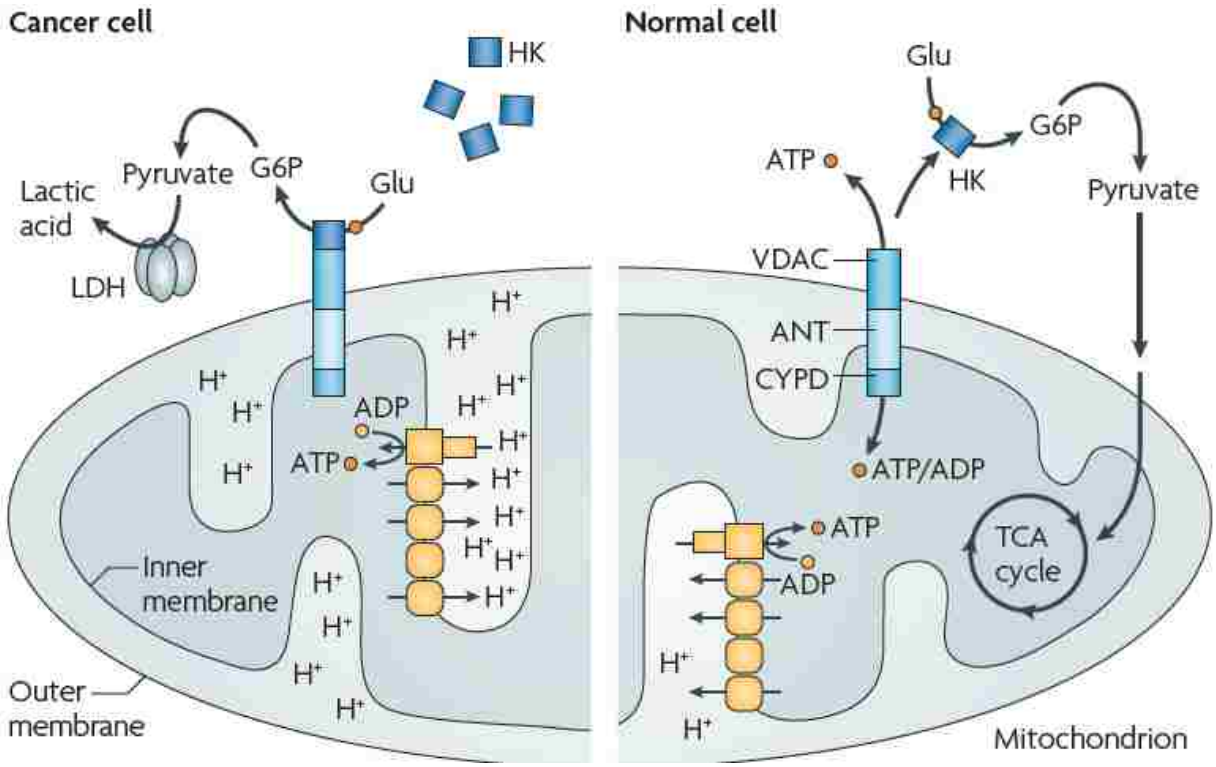

Figure 1.7 Mitochondria and metabolic reprogramming in cancer
(Fulda, Galluzzi, and Kroemer 2010)
Cancer cells shift metabolism to primarily generate ATP through conversion of pyruvate to lactic acid rather than by oxidative phosphorylation due to interaction of hexokinase directly with VDAC proteins.

Warburg hypothesized that this shift may be responsible for tumor initiation and growth, and if reversed may be a useful strategy to treat cancer. Although this strategy has not been singularly effective overall for treatment of cancer, it has led to discovery of other structural and functional abnormalities found in tumor cell mitochondria; and it has been demonstrated cancer cells become sensitized to mitochondrial disturbances (Fulda, Galluzzi, and Kroemer 2010). Many of these mechanisms are being utilized in currently used, and in developing cancer therapies (**Figure 1.8**) (Neuzil et al. 2013).

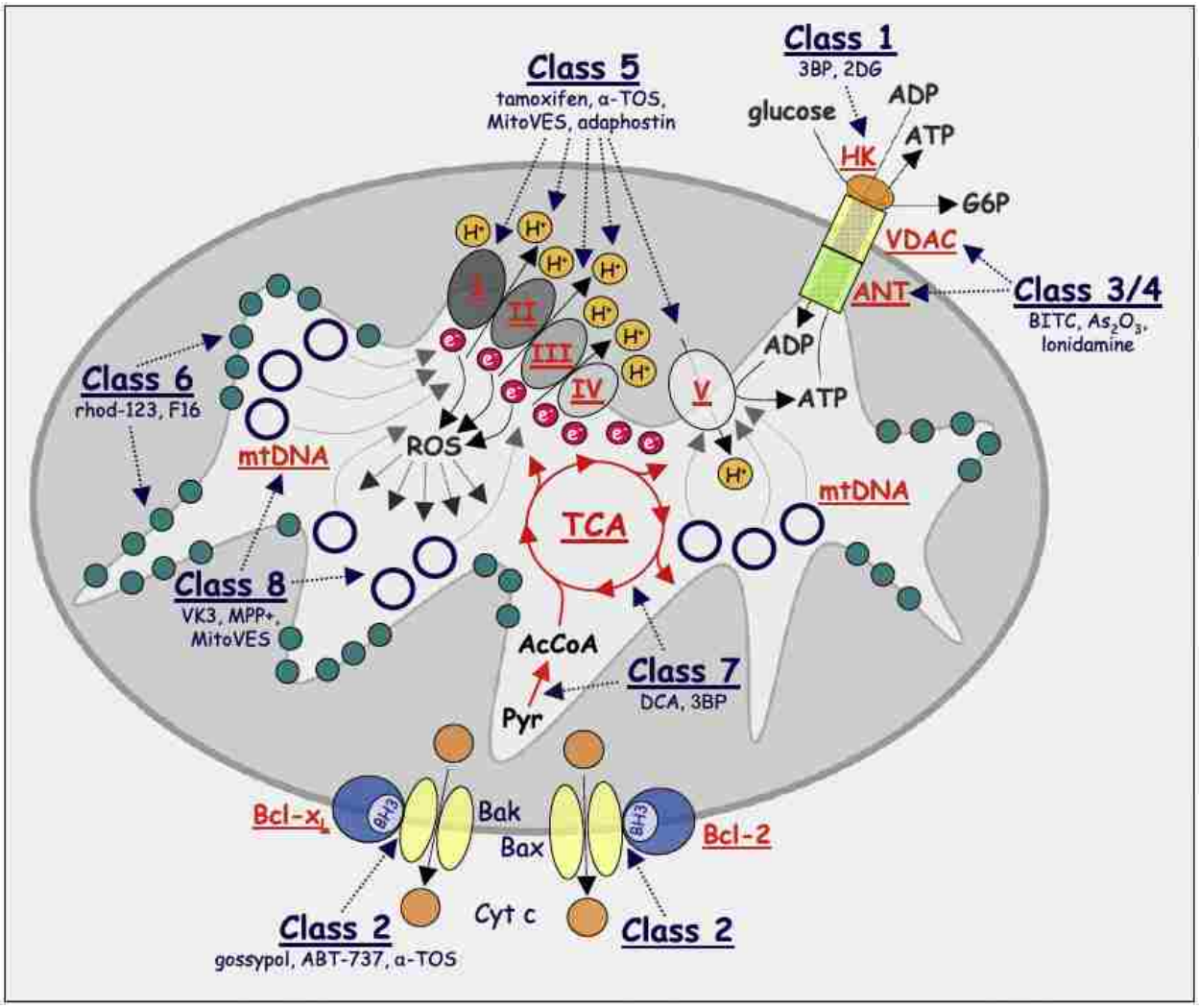

Figure 1.8 Mitochondrial targets of anti-tumor agents

(Neuzil et al. 2013)

Mitochondrially targeted anticancer drugs, “mitocans”, as classified by Neuzil et al. Notably, class 5 and class 8 compounds directed to target the electron transfer chain and mitochondrial DNA.

Mitochondrial Targets

Mitochondrial DNA (mtDNA)

Mitochondrial DNA (mtDNA) forms a ~17,000 base pair circular genome containing approximately 37 genes that code for 2 rRNAs, 22 tRNAs, and 13 polypeptides. All of the encoded polypeptides are involved in the electron transport chain machinery of the mitochondria (Taanman 1999). The sensitivity of tumor cells to mitochondrial disturbances may be in part due to the increased susceptibility of mtDNA to damage, as mitochondria lack efficient DNA repair machinery found in the nucleus (Yakes and Van Houten 1997; Berridge, Dong, and Neuzil 2015). Damage to mtDNA has been shown to induce senescence in tumor cells *in vivo* and, when combined with inhibition of mtDNA synthesis, lead to caspase-dependent apoptosis (Laberge et al. 2013). In human glioblastoma cells, intact mtDNA has also been shown to be important in the process of tumorigenesis and depletion of mtDNA reduces growth in transplanted human tumors *in vivo* in mice (Dickinson et al. 2013).

Electron Transport Chain (ETC)

The mitochondrial electron transport chain (ETC) is responsible for oxidative phosphorylation of pyruvate, using oxygen and cofactors generated in the TCA cycle, to phosphorylate ATP from ADP in the mitochondria of cells. This process relies on five enzymatic complexes (Complex I – V) that are located in the mitochondrial inner membrane. The reaction proceeds through reduction of ubiquinone by complex I and II using NADH or $FADH_2$ to pass electrons to Complex III. Complex III then reduces cytochrome *c* to pass electrons to Complex IV, which in turn reduces molecular oxygen

to water. The cascade of reactions in the ETC generates a proton gradient in the outward direction relative to the mitochondrial matrix. The flow of protons back into the matrix powers complex V, which uses energy from the proton gradient to produce ATP through phosphorylation of ADP using inorganic phosphate. The proton gradient and flow of electrons in the ETC also is responsible for maintaining the negative mitochondrial membrane potential ($\Delta\Psi m$) (Zorova et al. 2018). Loss of the $\Delta\Psi m$ causes cytochrome *c* release and caspase-9 activation in cells leading to apoptosis in tumor cells (Inayat-Hussain et al. 2003). The flow of electrons in the ETC has another consequence, production of reactive oxygen species (ROS) (**Figure 1.9**) (West, Shadel, and Ghosh 2011). Nominal levels of ROS are important for signaling in healthy cells, however excess ROS can damage the cell and also lead to apoptosis. Due to the ability of mitochondria to act as key regulators of the intrinsic apoptotic pathway, there has been great interest in the possibility of targeting the ETC to kill tumor cells.

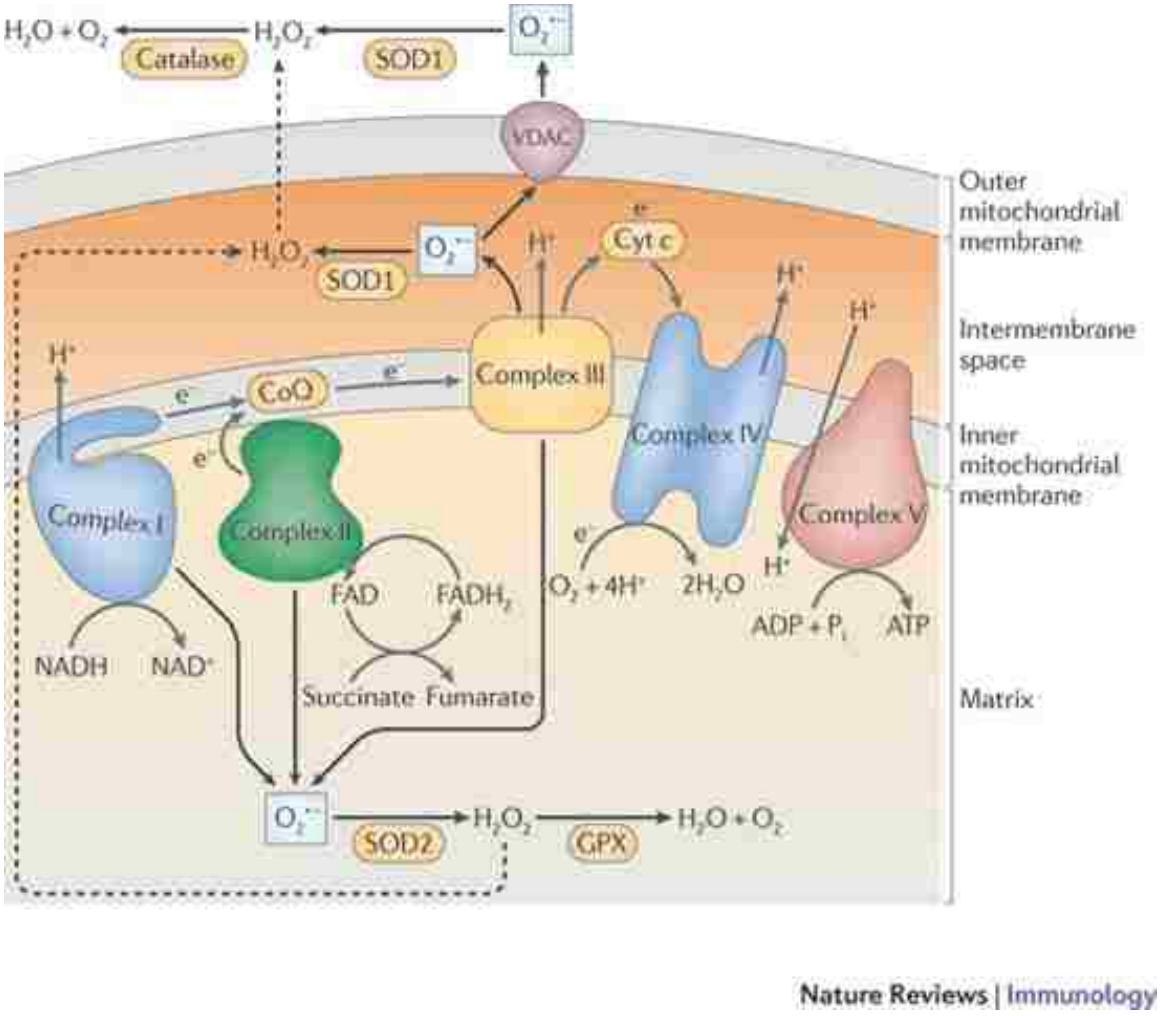

Figure 1.9 Sources of reactive oxygen species in the electron transport chain (West, Shadel, and Ghosh 2011)

Electron transport chain protein complexes I – III contribute to generation of reactive oxygen species (ROS) in the form of superoxide and hydrogen peroxide.

Complex I

ETC Complex I, also known as NADH ubiquinone oxidoreductase is responsible for transferring electrons from NADH to ubiquinone. Complex I is located in the inner mitochondrial membrane and exists as a large multimeric protein. The enzyme is a

major source of ROS inside the mitochondrial matrix through generation of superoxide. Complex I contributes approximately 4 protons per ubiquinone reduced to the outward proton gradient from the matrix to the intermembrane space (Lenaz et al. 2006). Inhibitors of Complex I such as the common inhibitor Rotenone can enhance its capability to produce ROS in the form of superoxide and hydrogen peroxide (Li et al. 2003). Rotenone-induced production of ROS has been demonstrated to lead to DNA damage and apoptosis in tumor cells through activation of caspase-3 (Liu, Fiskum, and Schubert 2002). The diabetes drug Metformin is also being explored for the potential to be repurposed as an anticancer therapeutic due to its inhibition of Complex I and the downstream effects leading to apoptosis in pancreatic cancer cells (Boukalova et al. 2016).

Complex II

Complex II (succinate dehydrogenase) is an approximately 100 kDa hetero-tetrameric protein located on the inner mitochondrial membrane (Kenney 1975; Miyadera et al. 2003; Ralph et al. 2011). Complex II couples the conversion of succinate to fumarate to reduce ubiquinone, which then acts as a carrier to transfer electrons to Complex III. The electrons for succinate oxidation are provided by the cofactor FAD, which is reduced to $FADH_2$ in the reaction. *A more complete introduction to the Complex II field of study is presented in* ***Chapter 3****.*

Complex III

The major function of Complex III (NADH:ubiquinone oxidoreductase) is to reduce cytochrome *c* through oxidation of ubiquinol passed from Complex I / II. This process is completed through a pathway termed the “Q-cycle”. The Q-Cycle is a two-step process; in the first step the electrons arising from oxidation of ubiquinol are transferred through an iron-sulfur cluster to reduce cytochrome *c* moving 2 H^+ to the intermembrane space and generating a semiquinone, in the second step a second ubiquinol is oxidized and an additional 2 H^+ are transferred to the matrix from the intermembrane space, reducing the semiquinone back to ubiquinol (Bleier and Dröse 2013). Complex III therefore contributes to the $\Delta\Psi m$, and also has been shown to be a major source of ROS in mitochondria (Chen et al. 2003). Antimycin A is a known inhibitor of Complex III, and generates superoxide through electron transfer to molecular oxygen (Bleier and Dröse 2013). Unlike Complex I / II, Complex III can generate ROS on either side of the inner mitochondrial membrane, in the matrix or the intermembrane space (West, Shadel, and Ghosh 2011).

Complex IV

Complex IV, known as cytochrome *c* oxidase, couples the oxidation of cytochrome *c* to the reduction of molecular oxygen to form water. This process utilizes 4 H^+ from the intermembrane space to reduce oxygen and translocates 4 H^+ across the inner mitochondrial membrane to the intermembrane space contributing to $\Delta\Psi m$. Altered expression of Complex IV subunits have been observed in colon and prostate cancer (Herrmann et al. 2003; K. Zhang et al. 2016). Complex IV inhibition does not

produce ROS directly, however it can indirectly affect the production by other ETC complexes through changes in ΔΨm (Lee, Bender, and Kadenbach 2002). Complex IV inhibition also has been shown to suppress mitochondrial respiration and induce degradation of HIF-1α in cancer cells. This was an important finding because HIF-1α is essential for adaptive response pathways used by cancer cells to promote angiogenesis (Krock, Skuli, and Simon 2011).

Complex V

Complex V is more well-known as the F_oF_1-ATPase, and is responsible for generating ATP from ADP in the mitochondria. ATP is synthesized through phosphorylation of ADP using inorganic phosphate; the reaction is driven by the ΔΨm and movement of H^+ back into the mitochondrial matrix. The movement of H^+ through the enzyme in the membrane causes a turbine-like rotation of the c-ring portion of the protein complex and this rotational energy is utilized to generate ATP from ADP and inorganic phosphate. Inhibition of Complex V does not contribute to significant production of ROS, but changes in its activity does have documented roles in cancer cells. Complex V can be inhibited by an oncometabolite 2-HG ((R)-2-hydroxyglutarate), which is highly expressed in some gliomas and leukemias. Complex V inhibition by 2-HG decreases mitochondrial respiration in U87 glioma cells transfected to express the common glioma mutation IDH1(R132H), which increases the amount of 2-HG produced in the cell (Fu et al. 2015).

Summary

Targeting mitochondria for treatment of cancer is a growing field due to the abundant roles of mitochondria and associated pathways in metabolism, proliferation, and apoptosis. Inhibition of the ETC complexes with drugs such as Metformin and α-TOS, and adapting their structures to target mitochondria is being explored as a way to selectively kill tumor cells (Lan-Feng Dong et al. 2007; L.-F. Dong et al. 2008; Neuzil et al. 2013; Boukalova et al. 2016). Additionally, it has now been observed that some currently used cancer drugs such as Cisplatin, previously thought to affect nuclear DNA, instead exert their cytotoxicity to tumor cells through interactions with mtDNA (Marrache, Pathak, and Dhar 2014; Kohno et al. 2015). Taken together, this shows the significance of continued research focused on targeting mitochondria for development of anticancer therapeutics.

NAD(P)H Quinone Oxidoreductase 1 (NQO1)

NAD(P)H Quinone Oxidoreductase 1 (NQO1)

A major mechanism proposed for the cytotoxic action of quinolinediones in tumor cells involves their reduction by the quinone reduction enzyme known as NAD(P)H:quinone oxidoreductase 1 (NQO1). NQO1 is overexpressed in multiple types of tumors; these include brain, breast, liver, lung and colon cancers (Hassani et al. 2005). NQO1 can catalyze the two-electron reduction of quinones to hydroquinones. The reaction requires cofactors FAD and NAD(P)H to be bound; the reaction proceeds through a hydride transfer from NAD(P)H to FAD followed by reduction of the quinone to a hydroquinone. Depending on the stability of the hydroquinone formed, it has been

suggested this conversion can cause redox cycling and subsequent generation of reactive oxygen species leading to apoptosis in tumor cells both in vitro and in mice (Keyari et al. 2013; Ross and Siegel 2017).

Hypotheses and Specific Aims

Specific Aim 1: Characterize the structure of the human c-MYC promoter quadruplex; demonstrate interaction of the AIMs with quadruplex DNA structures.

Hypothesis: AIMs will stabilize the human c-MYC promoter quadruplex and the characterization of the c-MYC quadruplex structure will inform development of more potent and selective AIM ligands.

Specific Aim 2: Measure the cytotoxicity of the AIMs in tumor cells and evaluate the mitochondrial mechanism contributing to the antitumor activity of the AIMs.

Hypothesis: Current generation AIMs will exhibit improved toxicity to tumor cells. Mitochondrial reductases and damage to mitochondria DNA are involved in the mechanisms underlying the AIMs antitumor efficacy.

Specific Aim 3: Examine the cytotoxicity of a novel set of quinolinedione analogs in parent breast cancer cells relative to NQO1 overexpressing cells and determine the compounds suitability as substrates for NQO1

Hypothesis: The set of quinolinediones will exhibit toxicity to the breast cancer cells and this will be enhanced in the NQO1 overexpressing cells. Differential substitutions on the quinolinedione analogs will relate to their toxicity in tumor cells and enhance their suitability as substrates for NQO1.

References

Adrian, Michael, Brahim Heddi, and Anh Tuân Phan. 2012. “NMR Spectroscopy of G-Quadruplexes.” *Methods*, Quadruplex DNA Methods, 57 (1): 11–24. https://doi.org/10.1016/j.ymeth.2012.05.003.

Agarwala, Prachi, Satyaprakash Pandey, and Souvik Maiti. 2015. “The Tale of RNA G-Quadruplex.” *Organic & Biomolecular Chemistry* 13 (20): 5570–85. https://doi.org/10.1039/C4OB02681K.

American Cancer Society. 2014. “Cancer Facts & Figures.” *Cancer Facts and Figures*.

Balasubramanian, Shankar, Laurence H. Hurley, and Stephen Neidle. 2011. “Targeting G-Quadruplexes in Gene Promoters: A Novel Anticancer Strategy?” *Nature Reviews Drug Discovery* 10 (4): 261–75. https://doi.org/10.1038/nrd3428.

Bang, I. 1910. “Untersuchungen über Die Guanylsäure.” *Biochemische Zeitschrift.* 26: 293–311.

Bao, Hong-Liang, Takumi Ishizuka, Takashi Sakamoto, Kenzo Fujimoto, Tamayo Uechi, Naoya Kenmochi, and Yan Xu. 2017. “Characterization of Human Telomere RNA G-Quadruplex Structures in Vitro and in Living Cells Using 19F NMR Spectroscopy.” *Nucleic Acids Research* 45 (9): 5501–11. https://doi.org/10.1093/nar/gkx109.

Bejugam, Mallesham, Sven Sewitz, Pravin S. Shirude, Raphaël Rodriguez, Ramla Shahid, and Shankar Balasubramanian. 2007. “Trisubstituted Isoalloxazines as a New Class of G-Quadruplex Binding Ligands: Small Molecule Regulation of c-Kit Oncogene Expression.” *Journal of the American Chemical Society* 129 (43): 12926–27. https://doi.org/10.1021/ja075881p.

Berridge, Michael V., Lanfeng Dong, and Jiri Neuzil. 2015. “Mitochondrial DNA in Tumor Initiation, Progression, and Metastasis: Role of Horizontal mtDNA Transfer.” *Cancer Research* 75 (16): 3203–8. https://doi.org/10.1158/0008-5472.CAN-15-0859.

Bharti, Sanjay Kumar, Joshua A. Sommers, Jun Zhou, Daniel L. Kaplan, Johannes N. Spelbrink, Jean-Louis Mergny, and Robert M. Brosh. 2014. “DNA Sequences Proximal to Human Mitochondrial DNA Deletion Breakpoints Prevalent in Human Disease Form G-Quadruplexes, a Class of DNA Structures Inefficiently Unwound by the Mitochondrial Replicative Twinkle Helicase.” *Journal of Biological Chemistry* 289 (43): 29975–93. https://doi.org/10.1074/jbc.M114.567073.

Bhattacharyya, Debmalya, Gayan Mirihana Arachchilage, and Soumitra Basu. 2016. “Metal Cations in G-Quadruplex Folding and Stability.” *Frontiers in Chemistry* 4 (September). https://doi.org/10.3389/fchem.2016.00038.

Bleier, Lea, and Stefan Dröse. 2013. “Superoxide Generation by Complex III: From

Mechanistic Rationales to Functional Consequences." *Biochimica et Biophysica Acta (BBA) - Bioenergetics*, Respiratory complex III and related bc complexes, 1827 (11): 1320–31. https://doi.org/10.1016/j.bbabio.2012.12.002.

Boukalova, Stepana, Jan Stursa, Lukas Werner, Zuzana Ezrova, Jiri Cerny, Ayenachew Bezawork-Geleta, Alena Pecinova, Lanfeng Dong, Zdenek Drahota, and Jiri Neuzil. 2016. "Mitochondrial Targeting of Metformin Enhances Its Activity against Pancreatic Cancer." *Molecular Cancer Therapeutics* 15 (12): 2875–86. https://doi.org/10.1158/1535-7163.MCT-15-1021.

Bugaut, Anthony, and Shankar Balasubramanian. 2012. "5′-UTR RNA G-Quadruplexes: Translation Regulation and Targeting." *Nucleic Acids Research* 40 (11): 4727–41. https://doi.org/10.1093/nar/gks068.

Burge, Sarah, Gary N. Parkinson, Pascale Hazel, Alan K. Todd, and Stephen Neidle. 2006. "Quadruplex DNA: Sequence, Topology and Structure." *Nucleic Acids Research* 34 (19): 5402–15. https://doi.org/10.1093/nar/gkl655.

Campbell, Nancy, Gavin W. Collie, and Stephen Neidle. 2012. "Crystallography of DNA and RNA G-Quadruplex Nucleic Acids and Their Ligand Complexes." In *Current Protocols in Nucleic Acid Chemistry*, edited by Serge L. Beaucage, Donald E. Bergstrom, Piet Herdewijn, and Akira Matsuda. Hoboken, NJ, USA: John Wiley & Sons, Inc. http://doi.wiley.com/10.1002/0471142700.nc1706s50.

Campbell, Nancy H., and Gary N. Parkinson. 2007. "Crystallographic Studies of Quadruplex Nucleic Acids." *Methods*, Quadruplex DNA, 43 (4): 252–63. https://doi.org/10.1016/j.ymeth.2007.08.005.

Chen, Qun, Edwin J. Vazquez, Shadi Moghaddas, Charles L. Hoppel, and Edward J. Lesnefsky. 2003. "Production of Reactive Oxygen Species by Mitochondria CENTRAL ROLE OF COMPLEX III." *Journal of Biological Chemistry* 278 (38): 36027–31. https://doi.org/10.1074/jbc.M304854200.

Coluccia, Daniel, Carlyn A. Figueiredo, Megan YiJun Wu, Alexandra N. Riemenschneider, Roberto Diaz, Amanda Luck, Christian Smith, et al. 2018. "Enhancing Glioblastoma Treatment Using Cisplatin-Gold-Nanoparticle Conjugates and Targeted Delivery with Magnetic Resonance-Guided Focused Ultrasound." *Nanomedicine: Nanotechnology, Biology and Medicine* 14 (4): 1137–48. https://doi.org/10.1016/j.nano.2018.01.021.

Dai, Jixun, Megan Carver, Laurence H. Hurley, and Danzhou Yang. 2011. "Solution Structure of a 2:1 Quindoline–c-MYC G-Quadruplex: Insights into G-Quadruplex-Interactive Small Molecule Drug Design." *Journal of the American Chemical Society* 133 (44): 17673–80. https://doi.org/10.1021/ja205646q.

De Armond, Richard, Stacey Wood, Daekyu Sun, Laurence H. Hurley, and Scot W.

Ebbinghaus. 2005. “Evidence for the Presence of a Guanine Quadruplex Forming Region within a Polypurine Tract of the Hypoxia Inducible Factor 1α Promoter.” *Biochemistry* 44 (49): 16341–50. https://doi.org/10.1021/bi051618u.

Dexheimer, Thomas S., Daekyu Sun, and Laurence H. Hurley. 2006. “Deconvoluting the Structural and Drug-Recognition Complexity of the G-Quadruplex-Forming Region Upstream of the Bcl-2 P1 Promoter.” *Journal of the American Chemical Society* 128 (16): 5404–15. https://doi.org/10.1021/ja0563861.

Dickinson, A, K Y Yeung, J Donoghue, M J Baker, R DW Kelly, M McKenzie, T G Johns, and J C St. John. 2013. “The Regulation of Mitochondrial DNA Copy Number in Glioblastoma Cells.” *Cell Death and Differentiation* 20 (12): 1644–53. https://doi.org/10.1038/cdd.2013.115.

Dong, Dawei W., Filipe Pereira, Steven P. Barrett, Jill E. Kolesar, Kajia Cao, Joana Damas, Liliya A. Yatsunyk, F. Brad Johnson, and Brett A. Kaufman. 2014. “Association of G-Quadruplex Forming Sequences with Human mtDNA Deletion Breakpoints.” *BMC Genomics* 15 (1): 677. https://doi.org/10.1186/1471-2164-15-677.

Dong, Lan-Feng, Emma Swettenham, Johanna Eliasson, Xiu-Fang Wang, Mikhal Gold, Yasmine Medunic, Marina Stantic, et al. 2007. “Vitamin E Analogues Inhibit Angiogenesis by Selective Induction of Apoptosis in Proliferating Endothelial Cells: The Role of Oxidative Stress.” *Cancer Research* 67 (24): 11906–13. https://doi.org/10.1158/0008-5472.CAN-07-3034.

Dong, L.-F., P. Low, J. C. Dyason, X.-F. Wang, L. Prochazka, P. K. Witting, R. Freeman, et al. 2008. “α-Tocopheryl Succinate Induces Apoptosis by Targeting Ubiquinone-Binding Sites in Mitochondrial Respiratory Complex II.” *Oncogene* 27 (31): 4324–35. https://doi.org/10.1038/onc.2008.69.

Fay, Marta M., Shawn M. Lyons, and Pavel Ivanov. 2017. “RNA G-Quadruplexes in Biology: Principles and Molecular Mechanisms.” *Journal of Molecular Biology* 429 (14): 2127–47. https://doi.org/10.1016/j.jmb.2017.05.017.

Fernando, Himesh, Anthony P. Reszka, Julian Huppert, Sylvain Ladame, Sarah Rankin, Ashok R. Venkitaraman, Stephen Neidle, and Shankar Balasubramanian. 2006. “A Conserved Quadruplex Motif Located in a Transcription Activation Site of the Human c-Kit Oncogene.” *Biochemistry* 45 (25): 7854–60. https://doi.org/10.1021/bi0601510.
Fulda, Simone. 2009. “Tumor Resistance to Apoptosis.” *International Journal of Cancer* 124 (3): 511–15. https://doi.org/10.1002/ijc.24064.

Fulda, Simone. 2010. “Evasion of Apoptosis as a Cellular Stress Response in Cancer.” *International Journal of Cell Biology* 2010 (January): 1–6. https://doi.org/10.1155/2010/370835.

Fulda, Simone, Lorenzo Galluzzi, and Guido Kroemer. 2010. “Targeting Mitochondria

for Cancer Therapy." *Nature Reviews Drug Discovery* 9 (6): 447–64. https://doi.org/10.1038/nrd3137.

Furnari, Frank B., Tim Fenton, Robert M. Bachoo, Akitake Mukasa, Jayne M. Stommel, Alexander Stegh, William C. Hahn, et al. 2007. "Malignant Astrocytic Glioma: Genetics, Biology, and Paths to Treatment." *Genes & Development* 21 (21): 2683–2710. https://doi.org/10.1101/gad.1596707.

Fu, Xudong, Randall M. Chin, Laurent Vergnes, Heejun Hwang, Gang Deng, Yanpeng Xing, Melody Y. Pai, et al. 2015. "2-Hydroxyglutarate Inhibits ATP Synthase and mTOR Signaling." *Cell Metabolism* 22 (3): 508–15. https://doi.org/10.1016/j.cmet.2015.06.009.
Gellert, Martin, Marie N. Lipsett, and David R. Davies. 1962. "Helix Formation by Guanylic Acid." *Proceedings of the National Academy of Sciences* 48 (12): 2013–18. https://doi.org/10.1073/pnas.48.12.2013.

Greenfield, Norma J. 2006. "Using Circular Dichroism Collected as a Function of Temperature to Determine the Thermodynamics of Protein Unfolding and Binding Interactions." *Nature Protocols* 1 (6): 2527–35. https://doi.org/10.1038/nprot.2006.204.

Hassani, Mary, Wen Cai, David C. Holley, Jayana P. Lineswala, Babu R. Maharjan, G. Reza Ebrahimian, Hassan Seradj, et al. 2005. "Novel Lavendamycin Analogues as Antitumor Agents: Synthesis, in Vitro Cytotoxicity, Structure−Metabolism, and Computational Molecular Modeling Studies with NAD(P)H:Quinone Oxidoreductase 1." *Journal of Medicinal Chemistry* 48 (24): 7733–49. https://doi.org/10.1021/jm050758z.

Herrmann, Paul C., John W. Gillespie, Lu Charboneau, Verena E. Bichsel, Cloud P. Paweletz, Valerie S. Calvert, Elise C. Kohn, Michael R. Emmert-Buck, Lance A. Liotta, and Emanuel F. Petricoin. 2003. "Mitochondrial Proteome: Altered Cytochrome c Oxidase Subunit Levels in Prostate Cancer." *PROTEOMICS* 3 (9): 1801–10. https://doi.org/10.1002/pmic.200300461.

Inayat-Hussain, S. H, B. O Annuar, L. B Din, A. M Ali, and D Ross. 2003. "Loss of Mitochondrial Transmembrane Potential and Caspase-9 Activation during Apoptosis Induced by the Novel Styryl-Lactone Goniothalamin in HL-60 Leukemia Cells." *Toxicology in Vitro* 17 (4): 433–39. https://doi.org/10.1016/S0887-2333(03)00051-1.

Kenney, W. C. 1975. "The Reaction of N-Ethylmaleimide at the Active Site of Succinate Dehydrogenase." *Journal of Biological Chemistry* 250 (8): 3089–94.

Keyari, Charles M., Alison K. Kearns, Nathan S. Duncan, Emily A. Eickholt, Geoffrey Abbott, Howard D. Beall, and Philippe Diaz. 2013. "Synthesis of New Quinolinequinone Derivatives and Preliminary Exploration of Their Cytotoxic Properties." *Journal of Medicinal Chemistry* 56 (10): 3806–19. https://doi.org/10.1021/jm301689x.

Kohno, Kimitoshi, Ke-Yong Wang, Mayu Takahashi, Tomoko Kurita, Yoichiro Yoshida, Masakazu Hirakawa, Yoshikazu Harada, Akihiro Kuma, Hiroto Izumi, and Shinji

Matsumoto. 2015. “Mitochondrial Transcription Factor A and Mitochondrial Genome as Molecular Targets for Cisplatin-Based Cancer Chemotherapy.” *International Journal of Molecular Sciences* 16 (8): 19836–50. https://doi.org/10.3390/ijms160819836.

Krock, Bryan L., Nicolas Skuli, and M. Celeste Simon. 2011. “Hypoxia-Induced Angiogenesis.” *Genes & Cancer* 2 (12): 1117–33. https://doi.org/10.1177/1947601911423654.

Laberge, R.-M., D. Adler, M. DeMaria, N. Mechtouf, R. Teachenor, G. B. Cardin, P.-Y. Desprez, J. Campisi, and F. Rodier. 2013. “Mitochondrial DNA Damage Induces Apoptosis in Senescent Cells.” *Cell Death & Disease* 4 (7): e727. https://doi.org/10.1038/cddis.2013.199.

Lavrado, João, Hugo Brito, Pedro M. Borralho, Stephan A. Ohnmacht, Nam-Soon Kim, Clara Leitão, Sílvia Pisco, et al. 2015. “*KRAS* Oncogene Repression in Colon Cancer Cell Lines by G-Quadruplex Binding indolo[3,2-*c*]quinolines.” *Scientific Reports* 5 (April): 9696. https://doi.org/10.1038/srep09696.

Lee, Icksoo, Elisabeth Bender, and Bernhard Kadenbach. 2002. “Control of Mitochondrial Membrane Potential and ROS Formation by Reversible Phosphorylation of Cytochrome c Oxidase.” *Molecular and Cellular Biochemistry* 234 (1): 63–70.

Lenaz, Giorgio, Romana Fato, Maria Luisa Genova, Christian Bergamini, Cristina Bianchi, and Annalisa Biondi. 2006. “Mitochondrial Complex I: Structural and Functional Aspects.” *Biochimica et Biophysica Acta (BBA) - Bioenergetics*, Mitochondria: from Molecular Insight to Physiology and Pathology, 1757 (9): 1406–20. https://doi.org/10.1016/j.bbabio.2006.05.007.

Liberti, Maria V., and Jason W. Locasale. 2016. “The Warburg Effect: How Does It Benefit Cancer Cells?” *Trends in Biochemical Sciences* 41 (3): 211–18. https://doi.org/10.1016/j.tibs.2015.12.001.

Li, Nianyu, Kathy Ragheb, Gretchen Lawler, Jennie Sturgis, Bartek Rajwa, J. Andres Melendez, and J. Paul Robinson. 2003. “Mitochondrial Complex I Inhibitor Rotenone Induces Apoptosis through Enhancing Mitochondrial Reactive Oxygen Species Production.” *Journal of Biological Chemistry* 278 (10): 8516–25. https://doi.org/10.1074/jbc.M210432200.

Liu, Yuanbin, Gary Fiskum, and David Schubert. 2002. “Generation of Reactive Oxygen Species by the Mitochondrial Electron Transport Chain.” *Journal of Neurochemistry* 80 (5): 780–87. https://doi.org/10.1046/j.0022-3042.2002.00744.x.

Luu, Kim Ngoc, Anh Tuân Phan, Vitaly Kuryavyi, Laurent Lacroix, and Dinshaw J. Patel. 2006. “Structure of the Human Telomere in K+ Solution: An Intramolecular (3 + 1) G-Quadruplex Scaffold.” *Journal of the American Chemical Society* 128 (30): 9963–70. https://doi.org/10.1021/ja062791w.

Marrache, Sean, Rakesh K. Pathak, and Shanta Dhar. 2014. “Detouring of Cisplatin to Access Mitochondrial Genome for Overcoming Resistance.” *Proceedings of the National Academy of Sciences* 111 (29): 10444–49. https://doi.org/10.1073/pnas.1405244111.

McLuckie, Keith I. E., Zoë A. E. Waller, Deborah A. Sanders, David Alves, Raphaël Rodriguez, Jyotirmayee Dash, Grahame J. McKenzie, Ashok R. Venkitaraman, and Shankar Balasubramanian. 2011. “G-Quadruplex-Binding Benzo[a]phenoxazines Down-Regulate c-KIT Expression in Human Gastric Carcinoma Cells.” *Journal of the American Chemical Society* 133 (8): 2658–63. https://doi.org/10.1021/ja109474c.

Mitra, Ashim K., Vibhuti Agrahari, Abhirup Mandal, Kishore Cholkar, Chandramouli Natarajan, Sujay Shah, Mary Joseph, et al. 2015. “NOVEL DELIVERY APPROACHES FOR CANCER THERAPEUTICS.” *Journal of Controlled Release : Official Journal of the Controlled Release Society* 219 (December): 248–68. https://doi.org/10.1016/j.jconrel.2015.09.067.

Miyadera, Hiroko, Kazuro Shiomi, Hideaki Ui, Yuichi Yamaguchi, Rokuro Masuma, Hiroshi Tomoda, Hideto Miyoshi, Arihiro Osanai, Kiyoshi Kita, and Satoshi Ōmura. 2003. “Atpenins, Potent and Specific Inhibitors of Mitochondrial Complex II (succinate-Ubiquinone Oxidoreductase).” *Proceedings of the National Academy of Sciences* 100 (2): 473–77. https://doi.org/10.1073/pnas.0237315100.

Morgan, Rhianna K., Harshul Batra, Vanessa C. Gaerig, Jennifer Hockings, and Tracy A. Brooks. 2016. “Identification and Characterization of a New G-Quadruplex Forming Region within the kRAS Promoter as a Transcriptional Regulator.” *Biochimica et Biophysica Acta (BBA) - Gene Regulatory Mechanisms* 1859 (2): 235–45. https://doi.org/10.1016/j.bbagrm.2015.11.004.

Neidle, Stephen. 2010. “Human Telomeric G-Quadruplex: The Current Status of Telomeric G-Quadruplexes as Therapeutic Targets in Human Cancer.” *The FEBS Journal* 277 (5): 1118–25. https://doi.org/10.1111/j.1742-4658.2009.07463.x.

Neidle, Stephen. 2017. “Quadruplex Nucleic Acids as Targets for Anticancer Therapeutics.” *Nature Reviews Chemistry* 1 (5): 0041.Neuzil, Jiri, Lan-Feng Dong, Jakub Rohlena, Jaroslav Truksa, and Stephen J. Ralph. 2013. “Classification of Mitocans, Anti-Cancer Drugs Acting on Mitochondria.” *Mitochondrion*, Mitochondria, Apoptosis and Cancer, 13 (3): 199–208. https://doi.org/10.1016/j.mito.2012.07.112.

Ostrom, Quinn T., Haley Gittleman, Peter Liao, Chaturia Rouse, Yanwen Chen, Jacqueline Dowling, Yingli Wolinsky, Carol Kruchko, and Jill Barnholtz-Sloan. 2014. “CBTRUS Statistical Report: Primary Brain and Central Nervous System Tumors Diagnosed in the United States in 2007–2011.” *Neuro-Oncology* 16 (Suppl 4): iv1–63. https://doi.org/10.1093/neuonc/nou223.

Otto Warburg. 1925. “The Metabolism of Carcinoma Cells.” *The Journal of Cancer Research* 9 (1): 148–63.
Ou, Tian-Miao, Yu-Jing Lu, Chi Zhang, Zhi-Shu Huang, Xiao-Dong Wang, Jia-Heng Tan, Yuan Chen, et al. 2007. “Stabilization of G-Quadruplex DNA and Down-Regulation of Oncogene c-Myc by Quindoline Derivatives.” *Journal of Medicinal Chemistry* 50 (7): 1465–74. https://doi.org/10.1021/jm0610088.

Paramasivan, Sattanathan, Iulian Rujan, and Philip H. Bolton. 2007. “Circular Dichroism of Quadruplex DNAs: Applications to Structure, Cation Effects and Ligand Binding.” *Methods* 43 (4): 324–31. https://doi.org/10.1016/j.ymeth.2007.02.009.
Parkinson, Gary N., Michael P. H. Lee, and Stephen Neidle. 2002. “Crystal Structure of Parallel Quadruplexes from Human Telomeric DNA.” *Nature* 417 (6891): 876–80. https://doi.org/10.1038/nature755.

Phan, Anh Tuân, Vitaly Kuryavyi, Sarah Burge, Stephen Neidle, and Dinshaw J. Patel. 2007. “Structure of an Unprecedented G-Quadruplex Scaffold in the Human c-Kit Promoter.” *Journal of the American Chemical Society* 129 (14): 4386–92. https://doi.org/10.1021/ja068739h.

Phan, Anh Tuân, Vitaly Kuryavyi, Kim Ngoc Luu, and Dinshaw J. Patel. 2007. “Structure of Two Intramolecular G-Quadruplexes Formed by Natural Human Telomere Sequences in K+ Solution.” *Nucleic Acids Research* 35 (19): 6517–25. https://doi.org/10.1093/nar/gkm706.

Ralph, Stephen J., Rafael Moreno-Sánchez, Jiri Neuzil, and Sara Rodríguez-Enríquez. 2011. “Inhibitors of Succinate: Quinone Reductase/Complex II Regulate Production of Mitochondrial Reactive Oxygen Species and Protect Normal Cells from Ischemic Damage but Induce Specific Cancer Cell Death.” *Pharmaceutical Research* 28 (11): 2695. https://doi.org/10.1007/s11095-011-0566-7.

Rankin, Sarah, Anthony P. Reszka, Julian Huppert, Mire Zloh, Gary N. Parkinson, Alan K. Todd, Sylvain Ladame, Shankar Balasubramanian, and Stephen Neidle. 2005. “Putative DNA Quadruplex Formation within the Human c-Kit Oncogene.” *Journal of the American Chemical Society* 127 (30): 10584–89. https://doi.org/10.1021/ja050823u.
Reithmeier, Thomas, Erika Graf, Tobias Piroth, Michael Trippel, Marcus O. Pinsker, and Guido Nikkhah. 2010. “BCNU for Recurrent Glioblastoma Multiforme: Efficacy, Toxicity and Prognostic Factors.” *BMC Cancer* 10 (1): 30. https://doi.org/10.1186/1471-2407-10-30.

Román, Marta, Iosune Baraibar, Inés López, Ernest Nadal, Christian Rolfo, Silvestre Vicent, and Ignacio Gil-Bazo. 2018. “KRAS Oncogene in Non-Small Cell Lung Cancer: Clinical Perspectives on the Treatment of an Old Target.” *Molecular Cancer* 17 (February). https://doi.org/10.1186/s12943-018-0789-x.

Ross, David, and David Siegel. 2017. “Functions of NQO1 in Cellular Protection and CoQ10 Metabolism and Its Potential Role as a Redox Sensitive Molecular Switch.”

Frontiers in Physiology 8 (August). https://doi.org/10.3389/fphys.2017.00595.
Roux, A., F. Caire, J. Guyotat, P. Menei, P. Metellus, and J. Pallud. 2017. “Carmustine Wafer Implantation for High-Grade Gliomas: Evidence-Based Safety Efficacy and Practical Recommendations from the Neuro-Oncology Club of the French Society of Neurosurgery.” *Neurochirurgie* 63 (6): 433–43. https://doi.org/10.1016/j.neuchi.2017.07.003.

Sen, Dipankar, and Walter Gilbert. 1988. “Formation of Parallel Four-Stranded Complexes by Guanine-Rich Motifs in DNA and Its Implications for Meiosis.” *Nature* 334 (6180): 364–66. https://doi.org/10.1038/334364a0.

Siegel, Rebecca L., Kimberly D. Miller, and Ahmedin Jemal. 2018. “Cancer Statistics, 2018.” *CA: A Cancer Journal for Clinicians* 68 (1): 7–30. https://doi.org/10.3322/caac.21442.

Stump, Sascha, Tung-Chung Mou, Stephen R. Sprang, Nicholas R. Natale, and Howard D. Beall. 2018. “Crystal Structure of the Major Quadruplex Formed in the Promoter Region of the Human c-MYC Oncogene.” *PLOS ONE* 13 (10): e0205584. https://doi.org/10.1371/journal.pone.0205584.

Sun, Daekyu, Kexiao Guo, Jadrian J. Rusche, and Laurence H. Hurley. 2005. “Facilitation of a Structural Transition in the Polypurine/polypyrimidine Tract within the Proximal Promoter Region of the Human VEGF Gene by the Presence of Potassium and G-Quadruplex-Interactive Agents.” *Nucleic Acids Research* 33 (18): 6070–80. https://doi.org/10.1093/nar/gki917.

Sundquist, W. I., and A. Klug. 1989. “Telomeric DNA Dimerizes by Formation of Guanine Tetrads between Hairpin Loops.” *Nature* 342 (6251): 825–29. https://doi.org/10.1038/342825a0.

Taanman, Jan-Willem. 1999. “The Mitochondrial Genome: Structure, Transcription, Translation and Replication.” *Biochimica et Biophysica Acta (BBA) - Bioenergetics* 1410 (2): 103–23. https://doi.org/10.1016/S0005-2728(98)00161-3.

Ulrich H. Weidle, Jens Niewöhner, and Georg Tiefenthaler. 2015. “The Blood–Brain Barrier Challenge for the Treatment of Brain Cancer, Secondary Brain Metastases, and Neurological Diseases.” *Cancer Genomics - Proteomics* 12 (4): 167–77.

Wang, Yu, Xiangyi Kong, Yi Guo, Renzhi Wang, and Wenbin Ma. 2017. “Continuous Dose-Intense Temozolomide and Cisplatin in Recurrent Glioblastoma Patients.” *Medicine* 96 (10). https://doi.org/10.1097/MD.0000000000006261.

Wanrooij, Paulina H., Jay P. Uhler, Tomas Simonsson, Maria Falkenberg, and Claes M. Gustafsson. 2010. “G-Quadruplex Structures in RNA Stimulate Mitochondrial Transcription Termination and Primer Formation.” *Proceedings of the National Academy of Sciences* 107 (37): 16072–77. https://doi.org/10.1073/pnas.1006026107.

Weaver, Matthew J., Alison K. Kearns, Sascha Stump, Chun Li, Mariusz P. Gajewski, Kevin C. Rider, Donald S. Backos, Philip R. Reigan, Howard D. Beall, and Nicholas R. Natale. 2015. “AIMing towards Improved Antitumor Efficacy.” *Bioorganic & Medicinal Chemistry Letters* 25 (8): 1765–70. https://doi.org/10.1016/j.bmcl.2015.02.063.

Wei, Dengguo, Gary N. Parkinson, Anthony P. Reszka, and Stephen Neidle. 2012. “Crystal Structure of a c-Kit Promoter Quadruplex Reveals the Structural Role of Metal Ions and Water Molecules in Maintaining Loop Conformation.” *Nucleic Acids Research* 40 (10): 4691–4700. https://doi.org/10.1093/nar/gks023.

West, A. Phillip, Gerald S. Shadel, and Sankar Ghosh. 2011. “Mitochondria in Innate Immune Responses.” *Nature Reviews. Immunology* 11 (6): 389–402. https://doi.org/10.1038/nri2975.

Yakes, F. Michael, and Bennett Van Houten. 1997. “Mitochondrial DNA Damage Is More Extensive and Persists Longer than Nuclear DNA Damage in Human Cells Following Oxidative Stress.” *Proceedings of the National Academy of Sciences* 94 (2): 514–19. https://doi.org/10.1073/pnas.94.2.514.

Yang, Danzhou, and Laurence H. Hurley. 2006. “Structure of the Biologically Relevant G-Quadruplex in The c-MYC Promoter.” *Nucleosides, Nucleotides and Nucleic Acids* 25 (8): 951–68. https://doi.org/10.1080/15257770600809913.

Young, Richard M., Aria Jamshidi, Gregory Davis, and Jonathan H. Sherman. 2015. “Current Trends in the Surgical Management and Treatment of Adult Glioblastoma.” *Annals of Translational Medicine* 3 (9). https://doi.org/10.21037/6698.
Yuan, Shujun, and Christopher W. Akey. 2013. “Apoptosome Structure, Assembly, and Procaspase Activation.” *Structure* 21 (4): 501–15. https://doi.org/10.1016/j.str.2013.02.024.

Yu, Haiqing, Xiaobo Gu, Shu-ichi Nakano, Daisuke Miyoshi, and Naoki Sugimoto. 2012. “Beads-on-a-String Structure of Long Telomeric DNAs under Molecular Crowding Conditions.” *Journal of the American Chemical Society* 134 (49): 20060–69. https://doi.org/10.1021/ja305384c.

Zhang, Jihong, Malcolm FG Stevens, and Tracey D Bradshaw. 2012. “Temozolomide: Mechanisms of Action, Repair and Resistance.” *Current Molecular Pharmacology* 5 (1): 102–14.

Zhang, Kun, Yibing Chen, Xiaojun Huang, Ping Qu, Qiuzhong Pan, Lin Lü, Shanshan Jiang, Tingitng Ren, and Haichuan Su. 2016. “Expression and Clinical Significance of Cytochrome c Oxidase Subunit IV in Colorectal Cancer Patients.” *Archives of Medical Science : AMS* 12 (1): 68–77. https://doi.org/10.5114/aoms.2016.57581.
Zheng, Ke-wei, Ren-yi Wu, Yi-de He, Shan Xiao, Jia-yu Zhang, Jia-quan Liu, Yu-hua Hao, and Zheng Tan. 2014. “A Competitive Formation of DNA:RNA Hybrid G-

Quadruplex Is Responsible to the Mitochondrial Transcription Termination at the DNA Replication Priming Site." *Nucleic Acids Research*, August, gku764. https://doi.org/10.1093/nar/gku764.

Zheng, Ke-wei, Shan Xiao, Jia-quan Liu, Jia-yu Zhang, Yu-hua Hao, and Zheng Tan. 2013. "Co-Transcriptional Formation of DNA:RNA Hybrid G-Quadruplex and Potential Function as Constitutional Cis Element for Transcription Control." *Nucleic Acids Research* 41 (10): 5533–41. https://doi.org/10.1093/nar/gkt264.
Zorova, Ljubava D., Vasily A. Popkov, Egor Y. Plotnikov, Denis N. Silachev, Irina B. Pevzner, Stanislovas S. Jankauskas, Valentina A. Babenko, et al. 2018. "Mitochondrial Membrane Potential." *Analytical Biochemistry* 552 (July): 50–59. https://doi.org/10.1016/j.ab.2017.07.009.

Chapter 2 : Structure of the Human c-MYC Quadruplex and Interaction of the Anthracenyl Isoxazole Amides with Quadruplex DNA

Section I: Crystal structure of the major quadruplex formed in the promoter region of the human c-MYC oncogene

Adapted from PLOS ONE

Sascha Stump[1], Tung-Chung Mou[2], Stephen R. Sprang[2], Nicholas R. Natale[1], and Howard D. Beall[1*]

[1]Center for Environmental Health Sciences, Department of Biomedical and Pharmaceutical Sciences, University of Montana, Missoula, Montana 59812, United States of America

[2]Center for Biomolecular Structure and Dynamics, Division of Biological Sciences, University of Montana, Missoula, Montana 59812, United States of America

*Corresponding author

E-mail: howard.beall@umontana.edu

PLOS ONE 13 (10): e0205584. https://doi.org/10.1371/journal.pone.0205584.

Abstract

The c-MYC oncogene mediates multiple tumor cell survival pathways and is dysregulated or overexpressed in the majority of human cancers. The NHE III_1 region of the c-MYC promoter forms a DNA quadruplex. Stabilization of this structure with small molecules has been shown to reduce expression of c-MYC, and targeting the c-MYC quadruplex has become an emerging strategy for development of antitumor compounds. Previous solution NMR studies of the c-MYC quadruplex have assigned the major conformer and topology of this important target, however, regions outside the G-quartet core were not as well-defined. Here, we report a high-resolution crystal structure (2.35 Å) of the major quadruplex formed in the NHE III_1 region of the c-MYC promoter. The crystal structure is in general agreement with the solution NMR structure, however, key differences are observed in the position of nucleotides outside the G-quartet core. The crystal structure provides an alternative model that, along with comparisons to other reported quadruplex crystal structures, will be important to the rational design of selective compounds. This work will aid in development of ligands to target the c-MYC promoter quadruplex with the goal of creating novel anticancer therapies.

Introduction

Guanine-rich sequences of DNA and RNA can form a secondary nucleic acid structure known as a quadruplex. Quadruplex motifs have become the subject of significant interest due to their presence in human telomeres, 5'-untranstranslated regions of mRNA, and in gene promoter regions (Burge et al. 2006). One such quadruplex-forming sequence is found in the promoter region of the human c-MYC oncogene. c-MYC is estimated to be dysregulated or overexpressed in approximately 70% of all

human cancers and is responsible for mediating multiple pathways important in tumor cell survival. Stabilization of the major quadruplex formed in the c-MYC promoter by various small molecules has been shown to inhibit transcription of c-MYC thereby reducing expression of the oncogene (Siddiqui-Jain et al. 2002; Ou et al. 2007). This reduction in c-MYC expression has been demonstrated to induce apoptosis in multiple types of tumor cells (Su et al. n.d.; Brown et al. 2011). Taken together, these findings suggest that the c-MYC promoter quadruplex is a promising antitumor target. Several research groups are designing small molecules to stabilize the c-MYC promoter quadruplex as a strategy to develop potential therapies for treatment of human cancers (Phan, Modi, and Patel 2004; Dai et al. 2011; Hu et al. 2018).

The general sequence motif that forms a quadruplex consists of several short guanine repeats (G), separated by short "loop" regions (L) comprised of other nucleotides with the overall general sequence of $G_{3\text{-}5}L_{<7}G_{3\text{-}5}L_{<7}G_{3\text{-}5}L_{<7}G_{3\text{-}5}$ (Burge et al. 2006). Quadruplexes can form as intramolecular or intermolecular arrangements, consisting of single or multiple nucleic acid strands, respectively. The basic unit of the quadruplex is the G-quartet, which is formed as a planar arrangement of four guanine residues held together through Hoogsteen bonding and stabilized by a central monovalent cation. Multiple G-quartets, usually three or more, stack upon each other to form the quadruplex secondary structure and are connected through external loop region nucleotides. The central channel cations are essential for quadruplex formation, with potassium generally preferred to sodium. Potassium cations are observed in a symmetric square antiprismatic coordination at the interface of two G-quartets, coordinated by the guanine O6 atoms, whereas the relatively smaller sodium atoms display square-planar coordination and are

central to a single G-quartet. The species and abundance of these and other cations in solution can also serve to influence and stabilize the overall quadruplex topology (Bhattacharyya, Mirihana Arachchilage, and Basu 2016). Quadruplexes can be further categorized as parallel, anti-parallel, or hybrid by the types of loops formed and direction of the backbone in relation to the G-quartets (**Figure 2.1**) (Burge et al. 2006).

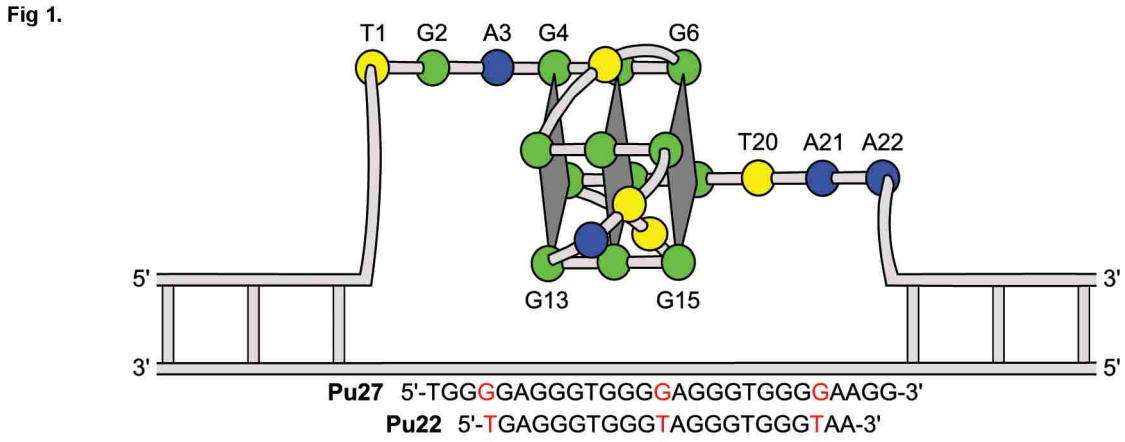

Figure 2.1 Topology of the c-MYC promoter quadruplex

Diagram showing fully parallel topology of the c-MYC promoter quadruplex crystal structure with all reversal loops continuing in the right to left direction (5' to 3'). Thymines are represented in yellow, adenines in blue, and guanines in green. Sequence modifications in Pu22 are shown highlighted in red.

Parallel-type quadruplexes are found in promoter regions of c-MYC and several other oncogenes that are potential therapeutic targets for cancer including c-KIT, Bcl-2, VEGF, and HIF-1α (Siddiqui-Jain et al. 2002; Fernando et al. 2006; Rankin et al. 2005; Dexheimer, Sun, and Hurley 2006; Agrawal et al. 2014; Sun et al. 2005; De Armond et al. 2005). The human c-MYC promoter quadruplex is formed under negative supercoiling conditions in the nuclease hypersensitivity element III_1 region (NHE III_1) (Sun and Hurley

2009). NHE III_1 is 27 residues in length and responsible for the regulation of 80 - 90% of c-MYC oncogene transcription (Pu27) (Ambrus et al. 2005). Duplex/quadruplex or single-stranded forms of the NHE III_1 region can be bound by transcription factors SP1 or CNBP/hnRNP, respectively, to increase c-MYC expression while formation of the quadruplex structure prevents transcription (Brooks and Hurley 2009; Raiber et al. 2012). NHE III_1 contains 20 guanines grouped into five segments of 3 to 4 guanine nucleotides separated by one or two adenine or thymine nucleotides. This guanine-rich character allows formation of four possible quadruplex topologies, with the major form being a parallel intramolecular quadruplex comprised of the four guanine segments at the 3'-end of the sequence (Ambrus et al. 2005).

In a previous NMR study, it was found that the major biologically relevant conformation adopted by the c-MYC promoter quadruplex could be selected from other conformers by mutating residues G4, G14 and G23 to thymines and truncating the sequence to 22 nucleotides in length (Pu22) (Ambrus et al. 2005). In a separate NMR study, the binding of a quindoline compound with Pu22 and the wild-type Pu27 sequence in solution was described (Dai et al. 2011). The latter study revealed the small molecule bound in an "induced fit" manner at two sites on the quadruplex, with the 5' and 3' flanking sequences recruited to form a binding pocket for both the Pu27 and Pu22 sequences. To select the desired biologically relevant conformation, the same Pu22 sequence was further utilized in this work to obtain the reported crystal structure.

Our interest in obtaining the crystal structure of the c-MYC quadruplex formed by Pu22 stemmed from differences previously observed between solution and solid-state structures of other quadruplexes in the literature. Additionally, crystal structures often

reveal other important structural information that may be absent in solution, such as the involvement of ions or water molecules important to the overall quadruplex topology, or potentially relevant quaternary interactions. On comparison of crystal and solution NMR structures of similar quadruplex sequences, differences are sometimes observed in the type of cation in the central channel and the overall topology of the quadruplexes. For example, multiple quadruplex topologies have been demonstrated in studies using the sequence repeat found in human telomeres, d(GGGTTA). Solution NMR studies have revealed that an anti-parallel quadruplex is formed in the presence of sodium ions, and alternatively, a 3+1 hybrid-type quadruplex is observed in solution containing potassium ions, with three parallel strand-edges and one anti-parallel (Wang and Patel 1993; Luu et al. 2006; Phan, Kuryavyi, Luu, et al. 2007). In contrast, the reported crystal structure of the same sequence adopts a fully parallel arrangement with potassium cations occupying the central channel (Parkinson, Lee, and Neidle 2002). This parallel topology was also shown to be favored in studies of solutions containing molecular crowding conditions (Xue et al. 2007; Heddi and Phan 2011). However, this is not always the case: for example, the c-KIT oncogene promoter quadruplex in both solution NMR and crystal structures adopts a strictly parallel form containing potassium in the central channel, with the position of the nucleotides highly-conserved (Phan, Kuryavyi, Burge, et al. 2007; Wei et al. 2012; Wei, Husby, and Neidle 2015). This led us to question whether the crystal structures of other oncogene promoter quadruplexes would be analogous to their NMR solution counterparts, or if they would differ significantly as is seen with the telomeric sequences. Knowledge of the distinct topology of these quadruplexes is crucial to the design of small molecules that stabilize their structures, and there is evidence that subtle

differences in structural features could allow for selectivity between specific quadruplex targets (Balasubramanian, Hurley, and Neidle 2011; Hu et al. 2018).

Here, we report a high-resolution crystal structure of the major Pu22 quadruplex formed in the human c-MYC promoter and describe several features observed that are potentially important for small molecule binding and quadruplex stabilization. We compare the crystal structure of Pu22 with previously reported solution NMR structures in an effort to inform future design of quadruplex-targeted compounds (Ambrus et al. 2005; Yang and Hurley 2006; Dai et al. 2011; Weaver et al. 2015). In addition, we have examined the features of the Pu22 crystal structure in conjunction with other quadruplex crystal structures to probe for similar features including positions of ions, water molecules and quaternary interactions. This research aims to aid future development of novel quadruplex-targeted compounds and provide information helpful in co-crystallization studies with molecules designed to bind the c-MYC promoter and other quadruplex structures.

Materials and Methods

Crystallization

The 22-residue DNA oligonucleotide (5'-TGAGGGTGGGTAGGGTGGGTAA-3') was synthesized and purified by Integrated DNA Technologies (standard desalting). The oligonucleotide was diluted into a stock concentration of 10 mM in DNAse/RNAse free water and the concentration was determined using a Thermo Scientific NanoDrop spectrometer. The oligonucleotide was then diluted to 2.0 mM in 20 mM sodium cacodylate buffer at pH 6.5 containing 30 mM KCl and annealed by heating for 10 minutes at 95° C and cooled overnight at 4° C prior to crystallization experiments. Initial crystal

screening was done in a 96-well plate format using an Art Robbins Instruments GRYPHON liquid-handling crystallization robot. Various precipitants (PEGs, 2-Methyl-2,4-pentanediol (MPD)) were screened along with varying concentrations of salts (NaCl, KCl, LiCl etc.) as previously outlined (Campbell and Parkinson 2007). Crystals used for diffraction data collection were grown in a 24-well plate format using the hanging-drop vapor diffusion technique with 300 mM KCl, 50 mM LiCl, and 22.5% MPD in 50 mM sodium cacodylate at pH 6.5 with a 1:1 ratio of oligonucleotide to reservoir solution. Crystals were harvested using the reservoir solution or additional MPD (30%) as a cryo-protectant and flash cooled in liquid nitrogen for storage prior to data collection.

Data collection and refinement

Initial diffraction screening was performed using a Rigaku MicroMax 007HF X-ray generator with VariMax HighFlux optic and R-AXIS IV image plate detector. Diffraction data for structure determination were taken at the Stanford Synchrotron Radiation Lightsource (SSRL) beam line 12-2. The native dataset was collected at a wavelength of 0.9793 Å over a 360° range with 0.2° rotation per image. Data were processed using XDS with autoxds script at SSRL (Kabsch 2010). These data were analyzed using Xtriage in Phenix prior to phasing (Adams et al. 2010). Initial phases were obtained by molecular replacement using Phaser in Phenix using the truncated guanine decks of a CKIT-1 promoter quadruplex as a search model (PDBID: 4WO2) (Wei et al. 2012). An improved, complete model was constructed through iterative cycles of refinement, phasing, and manual model building using Phenix and Coot, respectively (Emsley et al. 2010). Refinement was performed in Phenix refine, followed by submission to the PDB Redo webserver (Joosten et al. 2014). The structure obtained from the PDB Redo

webserver was then re-refined in Phenix refine with simulated annealing and randomized atomic displacement parameters to reduce any potential bias in R_{free}. The final structure was refined in Phenix using data from 34.91 – 2.35 Å with a final R_{work}, R_{free} of 0.220 and 0.245, respectively (**Table 2.1**). Atomic coordinates and structure factors are deposited in the RCSB Protein Databank with ID 6AU4 (Berman et al. 2000). Visualization and RMSD calculations were performed using Pymol (http://www.pymol.org) (Schrodinger 2015). Pearson correlation coefficient (CC) was calculated by randomly assigning the experimental reflection data to two half-datasets (x, y) as described by Karplus and Diederichs (**Table 2.1**) (Karplus and Diederichs 2012).

Circular dichroism spectroscopy

Circular dichroism spectra were measured using a Jasco J-810 spectropolarimeter or on a Chirascan CD spectrophotometer at room temperature in a quartz cuvette with a 10 mm or 4 mm pathlength for sample A or B, respectively. The oligonucleotide sample was made at 2 μM concentration with 300 mM KCl, 50 mM LiCl, and 22.5% MPD in a 50 mM sodium cacodylate buffer at pH 6.5 to mimic the crystallization conditions (A) or at 5 μM in 10 mM potassium phosphate buffer pH 6 to replicate the conditions used in previous studies (Paramasivan, Rujan, and Bolton 2007; Dai et al. 2011) (B). The solutions were annealed by heating to 95° C for 10 minutes and cooled overnight to 4° C prior to data collection.

Results

The 22 residue c-MYC promoter sequence Pu22 crystallized in the $P2_12_12$ space group in a stacked dimer formation with two parallel, single-stranded quadruplex structures per asymmetric unit (**Table 2.1** and **Figure 2.1**). The two independent

quaduplexes (A, B) are structurally similar with the majority of the core guanine-residue positions being maintained between the strands (G4-G6$_{A/B}$, G8-G10$_{A/B}$, G13-G15$_{A/B}$, and G17-G19$_{A/B}$ RMSD = 0.190 Å). Each individual quadruplex contains three loops and a 5'-head and 3'-tail region. The 5'-head region consists of residues T1-G2-A3 and is observed stretched away from the central G-quartets with the residues roughly orthogonal relative to the core guanines. The two related 5'-head regions appear in a quasi-mirror-related arrangement with the related atomic positions maintained (T1-G2-A3$_{A/B}$, RMSD = 0.568 Å). The 3'-tail regions of the two quadruplexes in the asymmetric unit are comprised of residues T20-A21-A22 and are positioned below and approximately planar to the central G-quartets. The quadruplex structure also contains three double-chain reversal propeller-type loops, with two consisting of single thymine residues (T7, T16) that flank a third, two-residue loop (T11-A12). These regions display less similarity between quadruplex A and B, owing predominately to the loop formed by residues T11 and A12 (T7$_{A/B}$, T16$_{A/B}$, and T11-A12$_{A/B}$ RMSD = 2.182 Å). All of the loops, the head, and the tail regions are involved in interactions important for the crystal packing. Electron density is also observed for a non-channel potassium ion and several water molecules.

Table 2.1 Data collection and refinement statistics

Sequence	5'-TGAGGGTGGGTAGGGTGGGTAA-3'
Data Collection	
Space group	P 2_1 2_1 2
Unit cell dimensions (*a*, *b*, *c*) (Å) *α*, *β*, *γ* (°)	65.7 69.8 33.0 90 90 90
Wavelength (Å)	0.9793
Resolution (Å)*	34.91 – 2.35 (2.43 – 2.35)
Total reflections*	85280 (8398)
Unique reflections*	6774 (652)
Multiplicity*	12.6 (12.9)
Completeness (%)*	99.4% (99.7%)
I/σ*	33.9 (4.4)

Wilson B-factor (Å^2)	58.8
R_{meas}†*	0.042 (0.605)
$CC_{1/2}$‡*	1.000 (0.966)
Refinement	
Resolution (Å)*	34.91 – 2.35 (2.53 – 2.35)
R_{work}§*	0.220 (0.319)
R_{free}§*	0.245 (0.322)
Macromolecules	2
DNA Residues	44
Total Atoms	956
Potassium ions	6
Waters	16
Average Overall B-factor (Å^2)	80.2
Average B-factor DNA Residues (Å^2)	80.7
Average B-factor Potassium Ions (Å^2)	53.1
Average B-factor Waters (Å^2)	59.7
RMS (bonds) (Å)	0.009
RMS (angles) (°)	1.08
TLS groups	2
PDB ID	6AU4

*Statistics in parentheticals are for the high-resolution shell

† $R_{meas} = \frac{\sum_{hkl}\sqrt{\frac{n}{n-1}}\sum_{i=1}^{n}|I_i(hkl)-\bar{I}(hkl)|}{\sum_{hkl}\sum_{i=1}^{n}I_i(hkl)}$, where $I_i(hkl)$ is the *i*th observation of the intensity of the reflection *hkl* and *n* is the multiplicity.

§ $R_{work} = \frac{\sum_{hkl}||F_{obs}|-|F_{calc}||}{\sum_{hkl}|F_{obs}|}$, where F_{obs} and F_{calc} are the observed and calculated structure-factor amplitudes for each reflection *hkl*. R_{free} was calculated with 10% of the diffraction data that were selected randomly and excluded from refinement.

‡$CC_{1/2}$ is the intra-dataset Pearson correlation coefficient (CC) calculated by randomly assigning the experimental reflection data to two half-datasets (x, y). $CC = \frac{\sum_{i=1}^{n}(x_i-\bar{x})-(y_i-\bar{y})}{\sqrt{\sum_{i=1}^{n}(x_i-\bar{x})^2}\sqrt{\sum_{i=1}^{n}(y_i-\bar{y})^2}}$

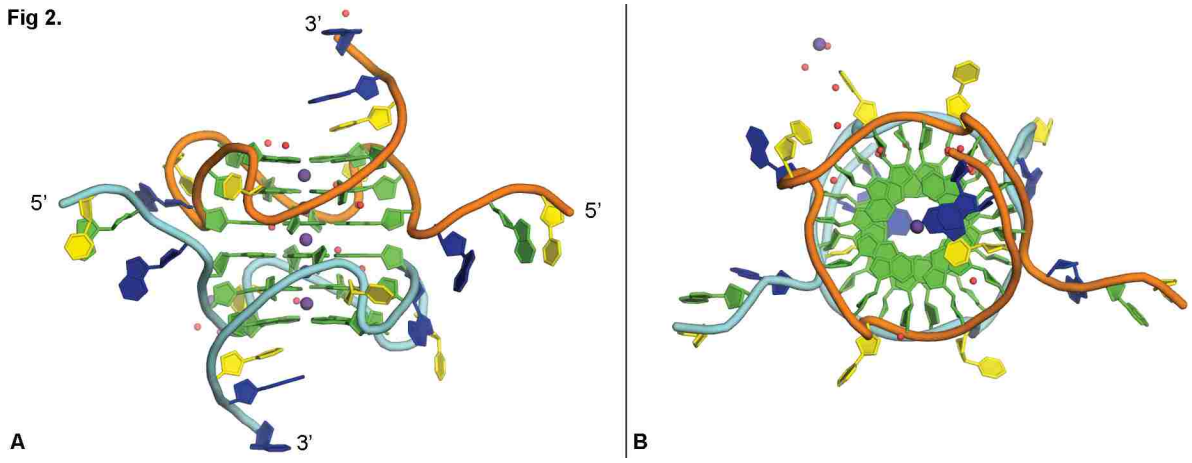

Figure 2.2 Crystal structure of c-MYC quadruplex

Side-view (A) and top-view (B) of the crystal structure of the c-MYC promoter quadruplex formed by Pu22, guanine bases in green, thymine in yellow, adenine in blue. Potassium ions in purple (two shown positioned behind strand backbones), waters in red. Orange/cyan backbone coloring represents strand A and B, respectively.

Potassium ions

Each individual quadruplex contains two potassium ions at the centers of two stacked G-quartets and an additional potassium ion similarly positioned at the interface that forms the dimer in the asymmetric unit, for a total of five potassium ions in the central cavity (**Figure 2.2**). The positions of these potassium ions relative to the G-quartets is consistent with that reported for other quadruplex crystal and NMR structures (Yang and Hurley 2006; Phan, Kuryavyi, Burge, et al. 2007). The ions central to the G-quartets are observed in symmetric square antiprismatic coordination with the O6 atoms of the guanine residues, as expected, with an average bond distance of 2.65 Å. An additional potassium ion is positioned between two adjacent symmetry-related strand B quadruplexes, interacting with O4 oxygen of T7 of one and backbone phosphate of G9 of

the other (**Figure 2.3B**). This ion is also observed in close proximity (< 3.7 Å) to three additional water molecules. This additional potassium ion was placed following careful consideration of each of the other components present in the crystallization conditions.

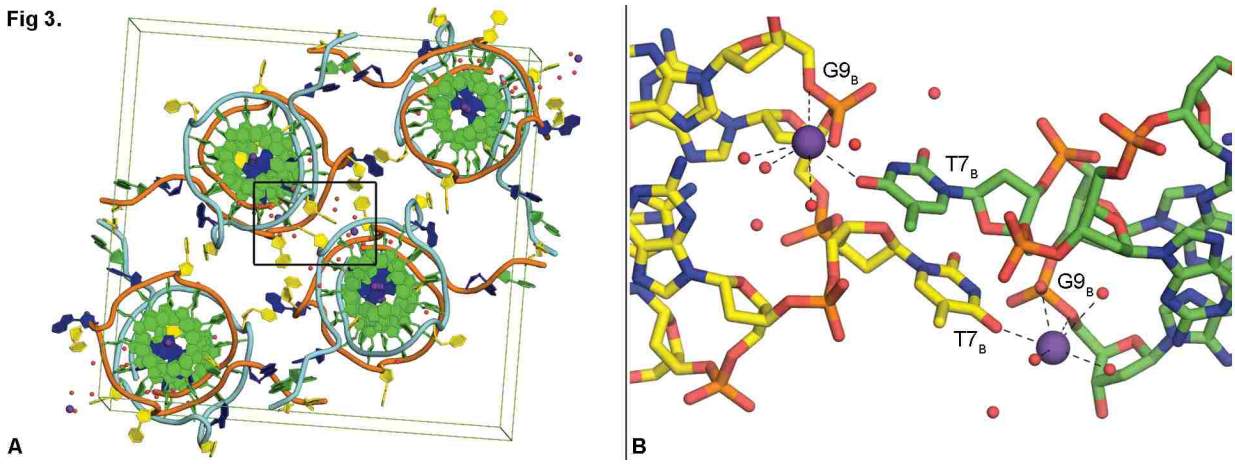

Figure 2.3 Crystal packing and non-channel potassium ions

Packing arrangement in the unit cell of c-MYC promoter quadruplex crystal structure formed by Pu22, coloring scheme same as Figure 2.2; black box indicates region shown in Figure 2.3B (A). Non-channel potassium ions interact with residues T7 and G9 (B).

Packing interactions

The Pu22 c-MYC promoter quadruplex structure displays several interesting packing interactions that induce a more elongated conformation than that observed for the same sequence by solution NMR. The two quadruplex strands, A and B, π–π stack together at the G-quartets near their 5'-ends with the G-quartets containing residues G4, G8, G13, and G17 of each quadruplex interacting to create the extended dimer structure (**Figure 2.2**). Residues T1-G2-A3 from the 5'-head of four quadruplexes in the lattice, two of A and two of B, form stacked structures stretched away from the central G-quartets, with base pairing between $T1_A/T1_B$, $G2_A/G2_B$ and $G3_A/G3_B$ (**Figure 2.4A**).

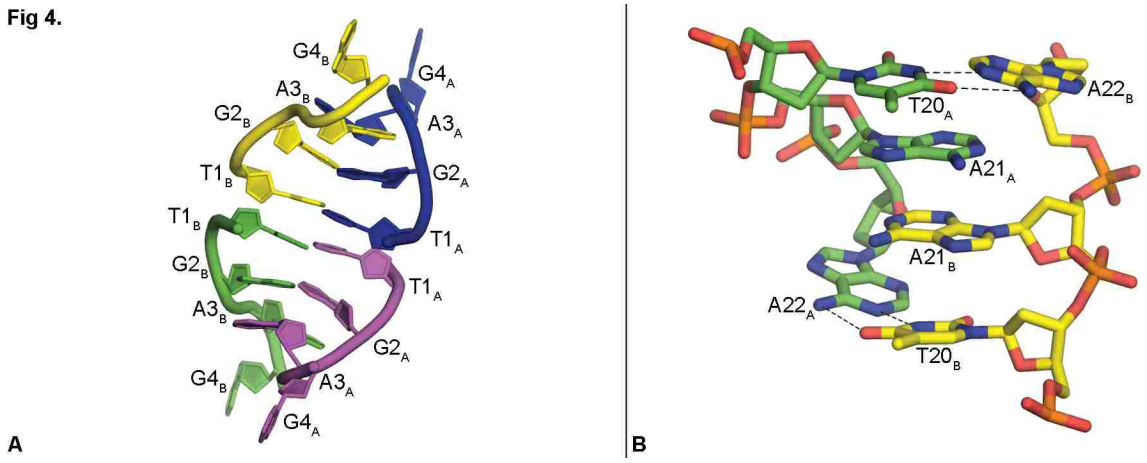

Figure 2.4 Packing interactions

Quaternary interaction of four 5'-head regions (T1-G2-A3); each color represents a separate symmetry-related strand (A). Stacked helical structure formed between 3'-tail regions of (T20-A21-A22) in the crystal lattice (B).

This exposes the G-quartet composed of residues G4, G7, G12, and G17, allowing the stacking of the two quadruplexes head-to-head in the asymmetric unit (**Figure 2.2**). Residues T20-A21-A22 from the 3'-tail of the two quadruplexes, A and B, interact forming a near-planar double helical structure (**Figure 2.4B**). Residue $T20_{A/B}$ and $A22_{A/B}$ form Watson-Crick base pairs with slightly elongated hydrogen bonds and $A21_A$ and $A21_B$ are involved in an apparent π-stacking interaction.

Conserved water molecules

Two water molecules were observed in nearly identical positions in each of the independent quadruplexes formed by strand A and B (**Figure 2.5**). The conserved positions of these waters suggests their presence may be important in stabilizing the quadruplex secondary structure. The first water is seen interacting with O4' of residue G6, OP1 of G8 and N2 of G5. The second water is seen in interaction with N2/N3 of

residue G8 and O4' of G9. These waters were placed based on the presence of positive density observed in the difference map. More bound waters of this type may be present, however, the high B-factor of the data did not allow for confident placement of additional atoms even at this near-atomic resolution.

Fig 5.

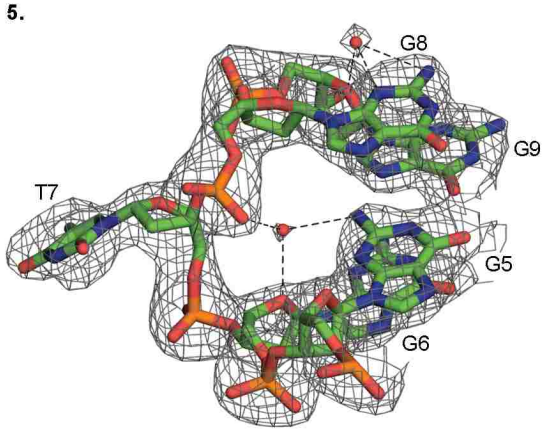

Figure 2.5 Conserved water molecules

Water molecules in conserved positions between strand A and B of the c-MYC promoter crystal structure (only strand A shown as an example), 2Fo-Fc map shown contoured at 1.0 σ.

Comparison of the crystal and solution structures of Pu22

The overall topology of the crystal structure is consistent to that reported for the same sequence by solution NMR with several notable differences (**Table 2.2**, PDB:1XAV). The most striking difference between the solution and crystal structure is observed in the T1-G2-A3 region at the 5'-head of the quadruplexes (**Figure 2.6**). In the NMR structure, these residues lay stacked on top of the G-quartet composed of residues G4, G7, G12, and G17. ((Ambrus et al. 2005, 20015), PDB: 1XAV). In contrast, in the crystal structure this 5'-head region is observed extended and the top, nearest, G-quartet

is the interface where the dimer is formed. The difference in this region in comparison to the NMR structure is also likely responsible for the high RMSD observed in the position of loop residue T7 and differences in the general shape of the phosphate backbone in this region. The 3'-tail region is also extended, albeit to a lesser degree, away from the G-quartet comprised of residues G6-G10-G15-G19 in the crystal structure in comparison to the NMR structure. The difference in the position of loop residue T16 can also likely be attributed to this extended conformation that is involved in crystal packing interactions.

Table 2.2 RMSD of strand A of Pu22 (PDB: 6AU4) to published DNA quadruplex structures

RMSD (Å)			
	c-MYC (NMR, PDB: 1XAV)	c-KIT (X-ray, PDB: 4WO2)	HTelo (X-ray, PDB: 4FXM)
G-quartets*	1.36	6.65	1.03
T1-G2-A3 (5'-head)	4.16	-	-
T20-A21-A22 (3'-tail)	3.45	-	-
T7, T11-A12, T17 (loop)	4.34	-	-
Overall	7.31	10.38	2.78

*G-quartets are comprised of G4-G5-G6, G8-G9-G10, G13-G14-G15, and G17-G18-G19. RMSD comparisons were not made between distinct quadruplex structures (c-KIT, telomeric) for the loop, head and tail regions due to significant sequence differences.

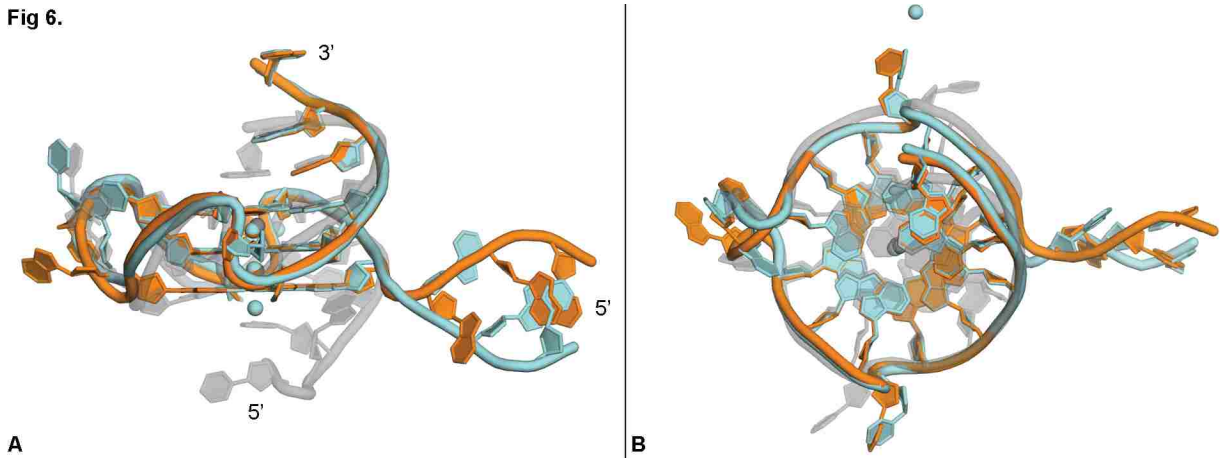

Figure 2.6 Comparison to NMR solution structure

Overlay of NMR solution structure (PDB:1XAV, grey) with strand A (orange) and strand B (cyan) of the c-MYC promoter crystal structure, side view (A), top view (B).

To examine the effect of the crystallization conditions on the conformation of Pu22, we performed circular dichroism spectroscopy at conditions analogous to those used in solution NMR studies (Dai et al. 2011). Parallel quadruplex structures display characteristic peaks at approximately positive 265 nm and negative 240 nm in their CD spectra (Burge et al. 2006). The parallel topology was confirmed for the Pu22 oligonucleotide under both the conditions used in the solution NMR studies as well as at the crystallization conditions to provide additional evidence the conformation observed in the crystal structure is not an artifact of the crystallization environment (**Figure 2.7**).

Fig 7.

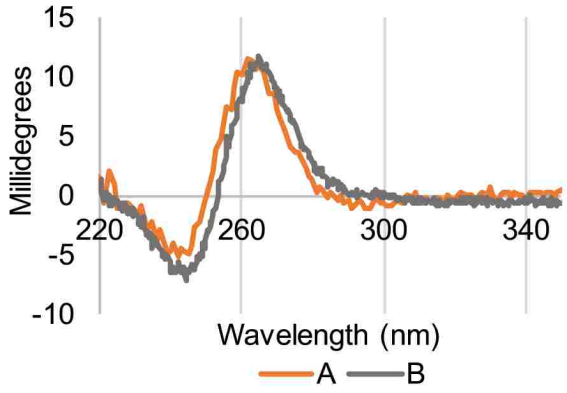

Figure 2.7 Circular dichroism spectroscopy

CD spectra of the Pu22 oligonucleotide under crystallization conditions (A) or conditions previously reported to form the parallel c-MYC promoter quadruplex (B).

Comparison to other crystal structures

The human c-KIT promoter region also contains a quadruplex sequence motif, and its crystal structure has some distinct similarities and differences to the c-MYC quadruplex formed by Pu22 (**Figure 2.8A** and **Table 2.2**, PDB: 4WO2). In both crystal structures, a quadruplex dimer forms the asymmetric unit, with the G-quartets closest to the 5'-region observed in a stacked formation. The c-KIT strands (A & B) forming the dimer are rotated one guanine relative to one another (approximately 90°), whereas the c-MYC strands (A & B) are rotated two guanines relative to one other (approximately 180°). This causes the c-KIT quadruplex loop region nucleotide $C9_A$ to occupy the same space as loop nucleotide $A12_A$ of the c-MYC quadruplex, and this is regardless of the additional $T11_A$ present in this loop region of the c-MYC structure. The loop nucleotide $C9_B$ of c-KIT superimposes with loop nucleotide $T7_B$ of the c-MYC quadruplex. The c-MYC quadruplex structure contains a non-channel potassium ion interacting with residues T7 and G9. A

non-channel potassium ion is also observed at an unrelated site in the c-KIT crystal structure interacting with residues A16 and G17.

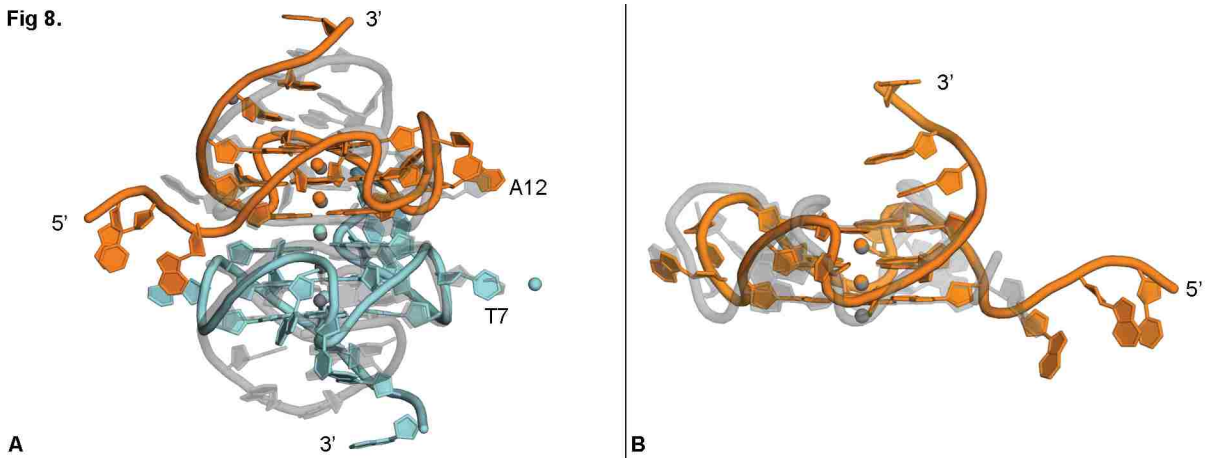

Figure 2.8 Comparison to other quadruplex crystal structures

Overlay of c-KIT crystal structure (PDB:4WO2, grey) with strand A (orange) and strand B (cyan) of the c-MYC promoter crystal structure; loop residue labels correspond to c-MYC crystal structure (A). Overlay of human telomeric crystal structure (PDB: 4FXM, grey, ligand not shown) with strand A (orange) of the c-MYC promoter crystal structure (B).

Several crystal structures of the fully parallel quadruplex formed by the human telomeric repeat sequence in complex with a small molecule ligand have been reported, including an example of the intramolecular arrangement at 1.65 Å (**Figure 2.8B**, PDB: 4FXM) (Nicoludis et al. 2012). The telomeric quadruplex forms a dimer with both strands reported as identical in the asymmetric unit. The telomeric structure is remarkably similar to the Pu22 c-MYC quadruplex with the exception of the loop regions. In the c-MYC structure, these loops are formed by one or two nucleotides, whereas the telomeric structure contains loops made of three nucleotides each. However, even with this difference in loop region length, the c-MYC quadruplex can be superimposed on the

telomeric quadruplex with an RMSD of only 2.78 Å (**Table 2.2,** PDB: 4FXM). Interestingly, the Watson-Crick packing interaction seen with the T20-A21-A22 tail of two c-MYC quadruplexes is also observed in the crystal structure of the telomeric quadruplex, but between two loop regions containing residues T11-A13 and A1, suggesting that a 3'-terminal TAA sequence may be useful for crystallization of other quadruplexes (Nicoludis et al. 2012).

During preparation of this manuscript, a 3.8 Å structure was reported of a sequence modified c-MYC promoter quadruplex in complex with the DEAH/RNA helicase DHX36 (Chen et al. 2018). In the reported complex structure, it is suggested quadruplex destabilization by the helicase results in a one-residue shift of the nucleotides involved in formation of the three G-quartets, causing the quartet nearest to the 5'-head region to be reformed by G4, G8, A12, and T16. This finding is noteworthy, however, due to the low-resolution of the structure and rearrangement observed in the presence of the helicase, it did not appear relevant for comparison with our crystal structure.

Discussion

In this manuscript we report a high-resolution crystal structure of the major quadruplex formed in the promoter region of the human c-MYC oncogene. The overall topology is in general agreement with the previously published solution NMR structures, with the major differences occurring predominately in the head and tail regions of the sequence and not in the central G-quartet structure (Ambrus et al. 2005; Dai et al. 2011). This is important as it strengthens the validity of previous and ongoing computational and synthetic studies that have used the NMR solution structures as a guide.

The more exposed G-quartets observed in the crystal structure, in comparison to those reported using solution NMR, confirm both the flexibility of the head and tail regions of the promoter sequence and the rigid nature of the G-quartets in this quadruplex. This could be biologically relevant as the flanking regions would not be terminal residues in genomic DNA and are likely able to project away from the G-quartets as is observed in the crystal structure (**Figure 2.2**). This will be important in future studies with the goal of developing small molecule ligands to bind the c-MYC quadruplex. For example, in the solution NMR study of a small molecule interaction with the c-MYC promoter quadruplex, it was observed that part of the ligand binding pocket involved nucleotides in the 5'-head (A3) and 3'-tail regions (T20, A21) (PDB: 2L7V, (Dai et al. 2011)). It is possible, as suggested by the c-MYC quadruplex crystal structure, that these residues are not in close proximity to provide such interactions in the biological setting as illustrated schematically in **Figure 2.1**. In this scenario, the reported "induced fit" mode of ligand binding would require major structural rearrangement and be less energetically favorable. Therefore, an alternative strategy would be to design ligands with a binding mode that takes advantage of the more linearized conformation of the head and tail regions, potentially affording tighter binding and selectivity for the c-MYC quadruplex. This alternative binding hypothesis will be a crucial consideration in the future design of c-MYC quadruplex-targeted small molecule ligands.

The packing interactions observed in the crystal highlight the importance of the loop, head and tail regions of the sequence to allow for crystal formation and will be generally helpful in optimizing quadruplex sequences for crystallization. The Watson-Crick bonding observed at the 3'-tail of the Pu22 sequence also suggests a preference

for nucleotides not involved in the G-quartet core region to follow the normal B-DNA base pairing paradigm even in very close proximity to the G-quartets. However, there is previous evidence that these flanking regions may remain single-stranded under conditions of negative supercoiling (Sun and Hurley 2009).

Comparison of the c-MYC quadruplex crystal structure to the c-KIT quadruplex and the human telomeric quadruplex show the majority of differences occur in the head, tail and loop regions. Differences in the length of loop regions and position of the loop nucleotides will provide useful tools for designing ligands that would be selective for specific quadruplex structures as has been suggested previously (Neidle 2017; Hu et al. 2018). Overall, this work has provided the basis for ongoing co-crystallization studies with the Pu22 c-MYC promoter quadruplex and our set of novel quadruplex ligands, the anthracenyl isoxazole amides (AIMs) (Han et al. 2009; Weaver et al. 2015). These findings will also be of benefit to other researchers in their efforts to target the c-MYC promoter and other therapeutically relevant quadruplex targets.

Accession number

Atomic coordinates and structure factors for the reported crystal structures have been deposited with the Protein Data bank under accession number 6AU4.

Acknowledgements

We would like to acknowledge Dr. Bruce Bowler and Dr. Levi McClelland for their assistance with CD spectroscopy. We would also like to acknowledge Dr. Clyde Smith and Dr. Enrique Rudiño Piñera for their assistance with the data collection at SSRL.

Use of the Stanford Synchrotron Radiation Lightsource, SLAC National Accelerator Laboratory, is supported by the U.S. Department of Energy, Office of Science,

Office of Basic Energy Sciences under Contract No. DE-AC02-76SF00515. The SSRL Structural Molecular Biology Program is supported by the DOE Office of Biological and Environmental Research, and by the National Institutes of Health, National Institute of General Medical Sciences (including P41GM103393). The contents of this publication are solely the responsibility of the authors and do not necessarily represent the official views of NIGMS or NIH.

Supporting information

S1 Fig.

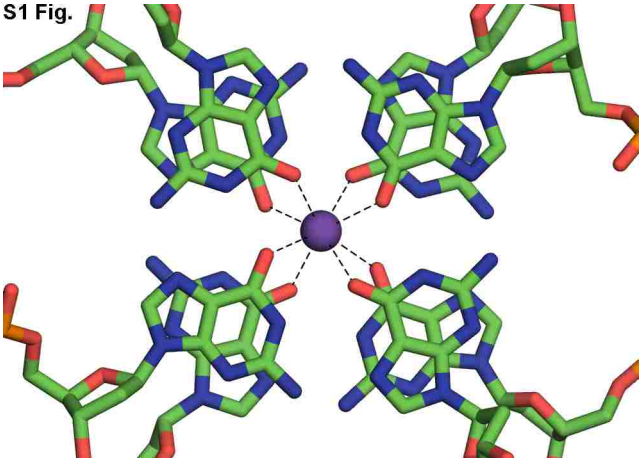

Figure S.2.1 G-quartet potassium ions

Example of square antiprismatic coordinated potassium ions central to two stacked G-quartets in the crystal structure

Section II: Interactions of AIMs with Quadruplex DNA

Sascha Stump[1], **Matthew J. Weaver**[1], **Nicholas R. Natale**[1], **and Howard D. Beall**[1*]

[1]Center for Environmental Health Sciences, Department of Biomedical and Pharmaceutical Sciences, University of Montana, Missoula, Montana 59812, United States of America

*Corresponding author

E-mail: howard.beall@umontana.edu

Abstract

The anthracenyl isoxazole amides (AIMs) are a novel class of compounds previously demonstrated to have significant antitumor activity. The AIMs interact with quadruplex DNA structures and are being investigated as quadruplex-ligands designed to treat human cancers. Previous studies have examined the interaction of the AIMs with quadruplex DNA using methods including fluorescence spectroscopy, mass spectrometry, and computational modeling. In this work we provide evidence of the interaction of the AIMs with quadruplex-forming DNA sequences found in the human c-MYC promoter region and in human telomeres. The interaction of the AIMs with quadruplex DNA and the consequent increase in the stability of these structures is examined through circular dichroism thermal melting studies and by ^{1}H NMR.

Introduction

Anthracenyl Isoxazole Amides (AIMs)

The class of compounds known as the anthracenyl isoxazole amides (AIMs) are synthesized in the Natale laboratory at the University of Montana. The AIMs have previously been submitted to the National Cancer Institute 60 cell line panel (NCI60) and demonstrated significant activity in multiple cancer cell lines. A subsequent COMPARE analysis of the NCI60 revealed that the AIMs mechanism of action did not correlate significantly with any known agents in the database (Han et al. 2009). Additional studies showed the compounds had a preference toward quadruplex DNA structures relative to the B-form found in duplex DNA. Computational modeling has also been previously performed to develop a potential structure activity relationship for

the AIMs with quadruplex sequences found in human telomeres and in oncogene promoters. This led to design of the current generation of AIM compounds by the Natale laboratory. The general structure of the AIMs consists of a hydrophobic anthracene region connected through an isoxazole-pyrrole scaffold to two alkyl amine tails, with a variable substitution at the 10-position of the anthracene (**Figure 2.9**). This includes a variety of double-tail AIM analogs, including the 10-Chloro and 10-Phenyl AIMs, which have been reported to have low- and sub-micromolar antitumor activity in SNB-19 glioblastoma cells (Han et al. 2009; Weaver et al. 2015).

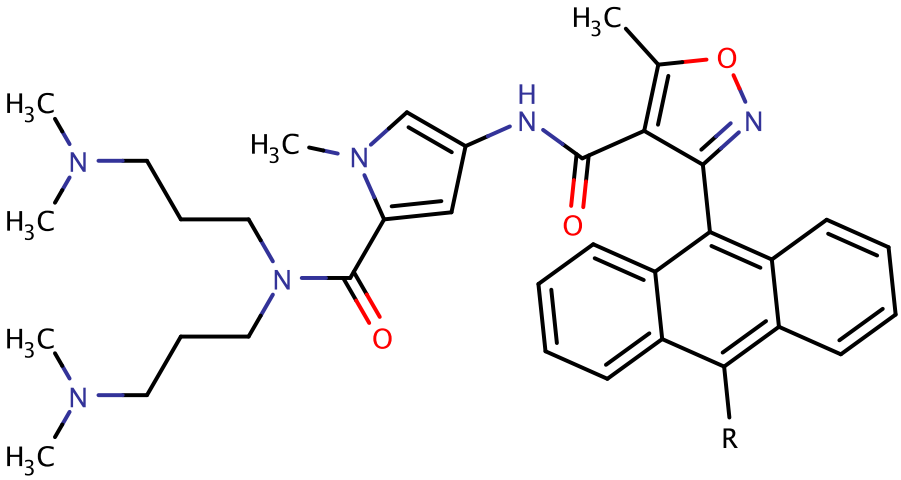

Figure 2.9 Structure of the anthracenyl isoxazole amides (AIMs)

Structure of the anthracenyl isoxazole amides (AIMs) demonstrating the double-tail tertiary alkyl amines, isoxazole pyrrole scaffold, and the hydrophobic anthracene region with variable substitutions at the 10-position.

In this work, we demonstrate the interactions of the 10-Chloro and 10-Phenyl AIMs with quadruplex DNA structures using circular dichroism (CD) and NMR spectroscopy. Thermal melting curves were measured in the presence of the AIMs to determine their effect on the stability of various quadruplex sequences and topologies.

In addition, ^{1}H NMR spectra were acquired to examine interactions of quadruplexes with the AIMs through chemical shift measurements of readily identifiable peaks in the imino region of the spectra that are observed for quadruplex structures.

Methods

Circular Dichroism

Oligonucleotide Sequences

Pu22: 5'-TGAGGGTGGGTAGGGTGGGTAA-3'

HTelo: 5'-TTAGGGTTAGGGTTAGGGTTAGGG-3'

mt9438: 5'-GGCGTAGGTTTGGTCTAGGG-3'

CSB II: 5'-AAGGGGGAGGGGGGGTTTrGrGrGrArA-3' (r prefix means RNA base)

c-MYC Promoter Sequence & Human Telomeric Sequence (Pu22 & HTelo)

Oligonucleotides were added to pH 6 10 mM potassium phosphate buffer to make a 1 mM DNA stock solutions. Samples were made using previously made 5 mM stock solutions of AIM compounds in DMSO. Three independent samples were made at 5 μM strand concentration in pH 6 10 mM potassium phosphate buffer for the oligonucleotide strands alone and oligonucleotides plus 2 equiv. compounds. Samples were annealed by heating to 90 °C for 10 minutes and then gradually cooling to 4 °C overnight prior to data collection.

CD spectra and thermal melting curves were acquired using an Applied Photophysics Chirascan CD Spectrophotometer. CD spectra were gathered from 200 nm – 400 nm with a 1 nm bandwidth and 0.2 nm step-size at 5 °C and 0.5 seconds time-per-point. CD thermal melting curves were gathered at 295 nm (HTelo) or 265 nm (Pu22)

from 10 °C – 90 °C at a rate of 1 °C/min in 0.5 °C steps. The CD thermal melting curves were acquired at 24 seconds time-per-point with 1 nm bandwidth.

Mitochondrial COX I Sequence (mt9438)

Samples were made using previously made 5 mM stock solutions of AIM compounds in DMSO. Three independent samples were made at 4 μM strand concentration in 20 mM potassium phosphate buffer for the oligonucleotide alone or with 4 equiv. of the AIM compounds. Samples were annealed by heating to 90 °C for 10 minutes and then gradually cooling to 4 °C overnight prior to data collection.

CD spectra and thermal melting curves were acquired using a Jasco J-810 spectropolarimeter. CD spectra were gathered from 220 nm – 350 nm. CD thermal melting curves were gathered at 290 nm 10 °C – 60 °C at a rate of 1 °C/min in 0.1 °C steps.

Mitochondrial CSB II Sequence (CSB II)

Samples were made at 2 μM strand concentration in 10 mM potassium phosphate buffer at the desired pH for the oligonucleotide alone or with 1 equiv. of the AIM compound. Samples were annealed by heating to 90 °C for 10 minutes and then gradually cooling to 4 °C overnight prior to data collection.

CD spectra and thermal melting curves were acquired using a Jasco J-810 spectropolarimeter. CD spectra were gathered from 200 nm – 400 nm. CD thermal melting curves at pH 6 were gathered at 265 nm 60 °C – 90 °C at a rate of 1 °C/min in 0.5 °C steps. CD thermal melts of pH 4, 8, 9 were gathered at varying temperature ranges

due to intermittent issues with the temperature controller, however all covered the range of interest, determined to be 50 °C – 80 °C.

Data Analysis

Following data collection, thermal melting curves were fit to a six-parameter logistic curve using the qpcR package for the R statistical computing software environment (R Core Team, 2014; Spiess, 2014). The six-parameter logistic fit was chosen to minimize the number fitting parameters while maximizing goodness-of-fit using criteria such as AIC, BIC and R^2. Thermal melting values (T_m) for each condition were assigned by computing the minimum value of the first derivative of the fitted curve for each sample. A statistical analysis between the sample groups was then conducted where appropriate using the ANOVA method in R and additionally a post-hoc Tukey's range test.

NMR Spectroscopy

The Pu22 sample was made at a concentration of 1 mM oligonucleotide in 10 mM potassium phosphate buffer at pH 6 in H_2O containing 10% D_2O. The HTelo sample was made at a concentration of 2.5 mM oligonucleotide in 100 mM potassium phosphate buffer at pH 6 in H_2O containing 10% D2O. Spectra were taken using water suppression techniques on a 500 MHz Varian NMR as described previously (Weaver et al. 2015).

Results

Circular Dichroism Spectroscopy

In these studies, we examined the interaction of the AIMs with multiple quadruplex-forming DNA sequences using circular dichroism spectroscopy (CD). First, we collected a CD spectra of the quadruplex formed in the c-MYC promoter using the Pu22 oligonucleotide sequence with and without two equivalents of the 10-Chloro or 10-Phenyl substituted AIMs in solution. The CD spectra of the Pu22 oligonucleotide confirmed the presence of a fully parallel quadruplex topology, demonstrated by the characteristic peaks at approximately +265 nm and -240 nm. The obtained spectra also display a hypsochromic shift in the presence of the AIMs (**Figure 2.10**). To determine if interaction of the AIMs would affect the stability of the quadruplex structure, we performed thermal melting studies near the CD signal maxima (265 nm). The presence of both the 10-Chloro and 10-Phenyl AIMs created a noticeable right shift of the thermal melting curves (**Figure 2.11**). Next, we calculated the melting temperature (T_m) of the curves as defined by maximum slope of the curve. This revealed that the presence of the 10-Chloro and the 10-Phenyl AIMs in solution caused a statistically significant increase in the T_m for the quadruplex structure formed by Pu22 of 3.2° C and 2.1 C°, respectively (**Figure 2.12**).

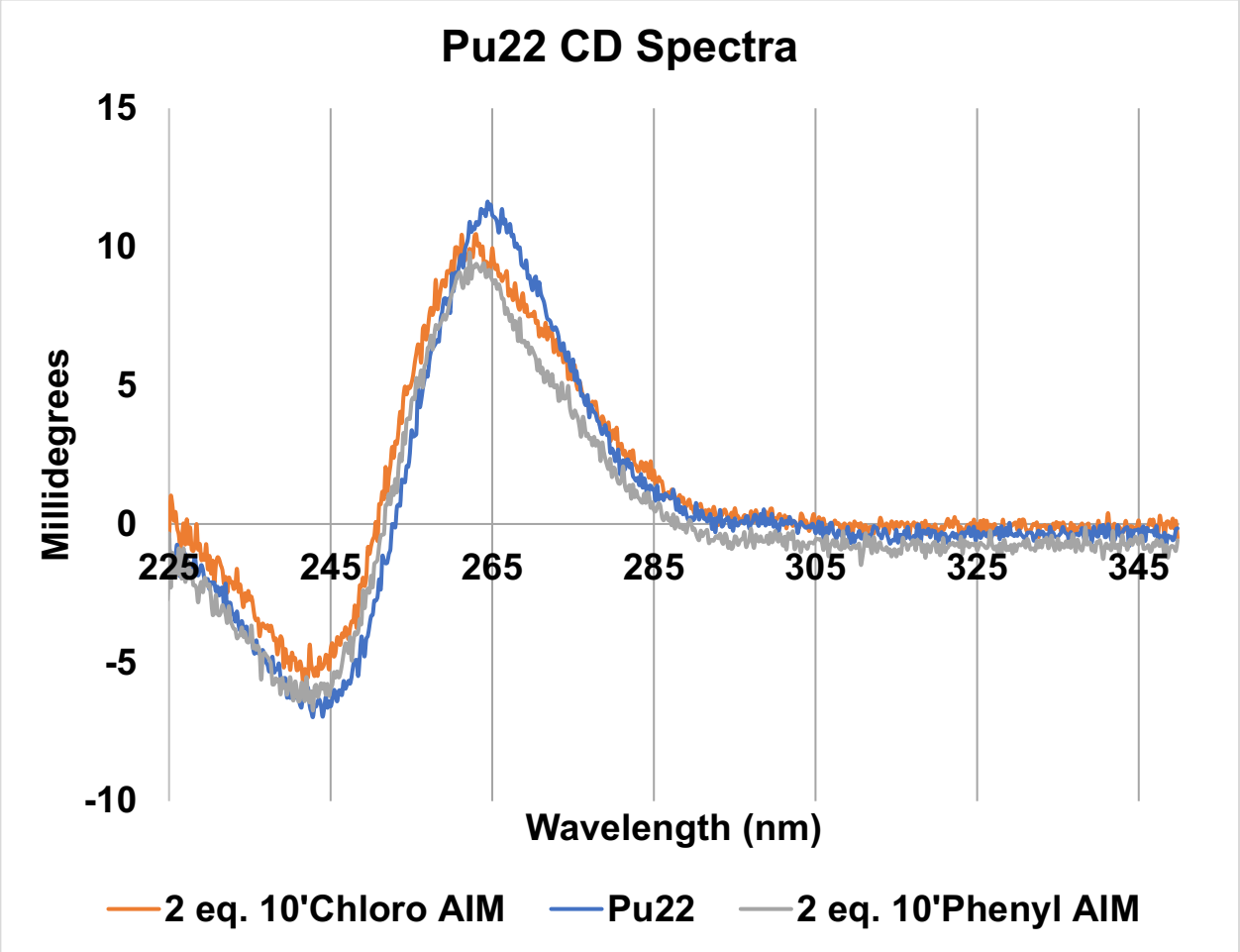

Figure 2.10 Circular dichroism spectra of Pu22 oligonucleotide

Circular dichroism spectra of Pu22 oligonucleotide with and without two equivalents of AIM compounds in solution. Pu22 only (blue), 10-Chloro (orange), and 10-Phenyl (grey).

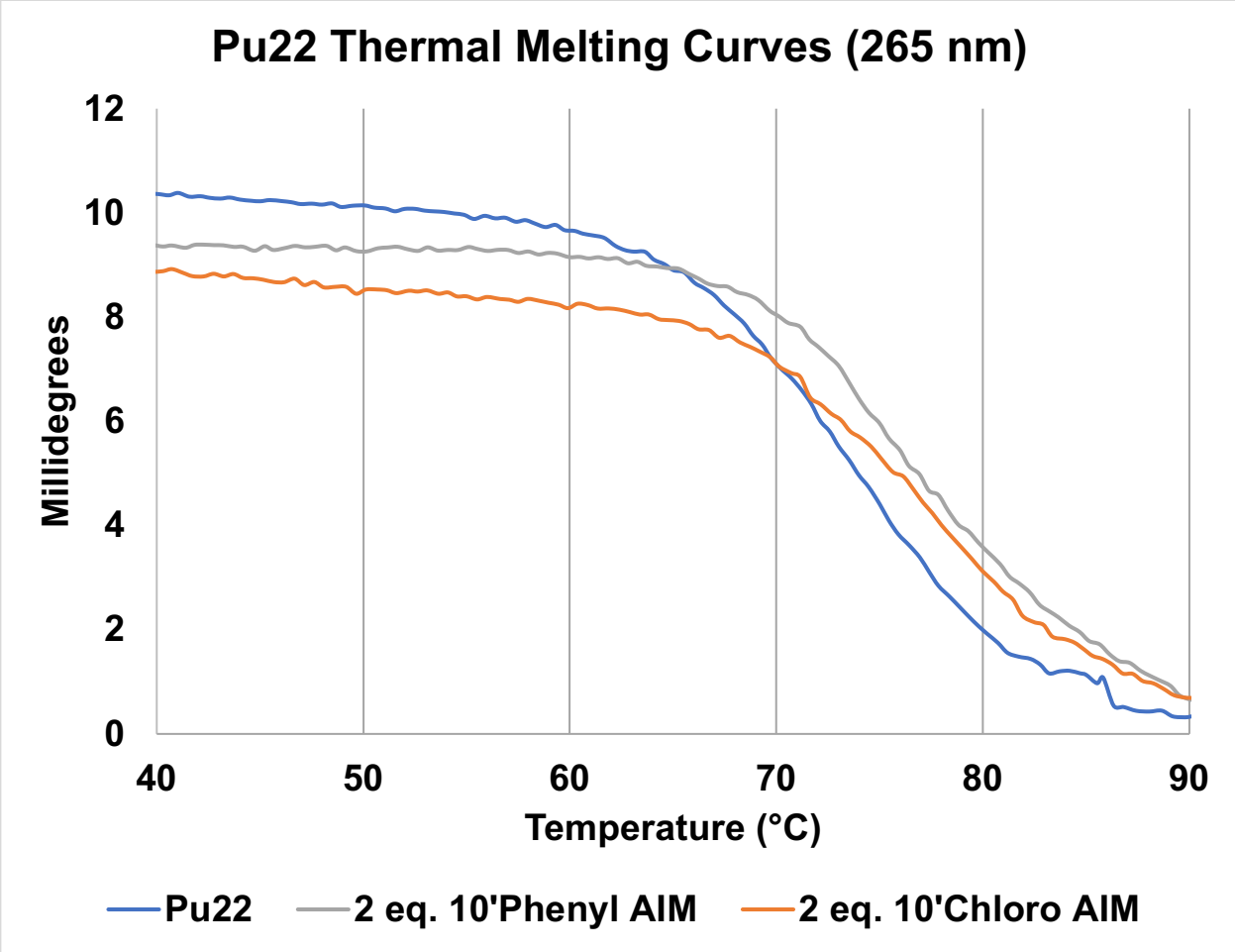

Figure 2.11 Thermal melting curves of the Pu22 oligonucleotide

Circular dichroism thermal melting curves of the Pu22 oligonucleotide taken at 265 nm with and without two equivalents of AIM compounds in solution. Pu22 only (blue), 10-Chloro (orange), and 10-Phenyl (grey).

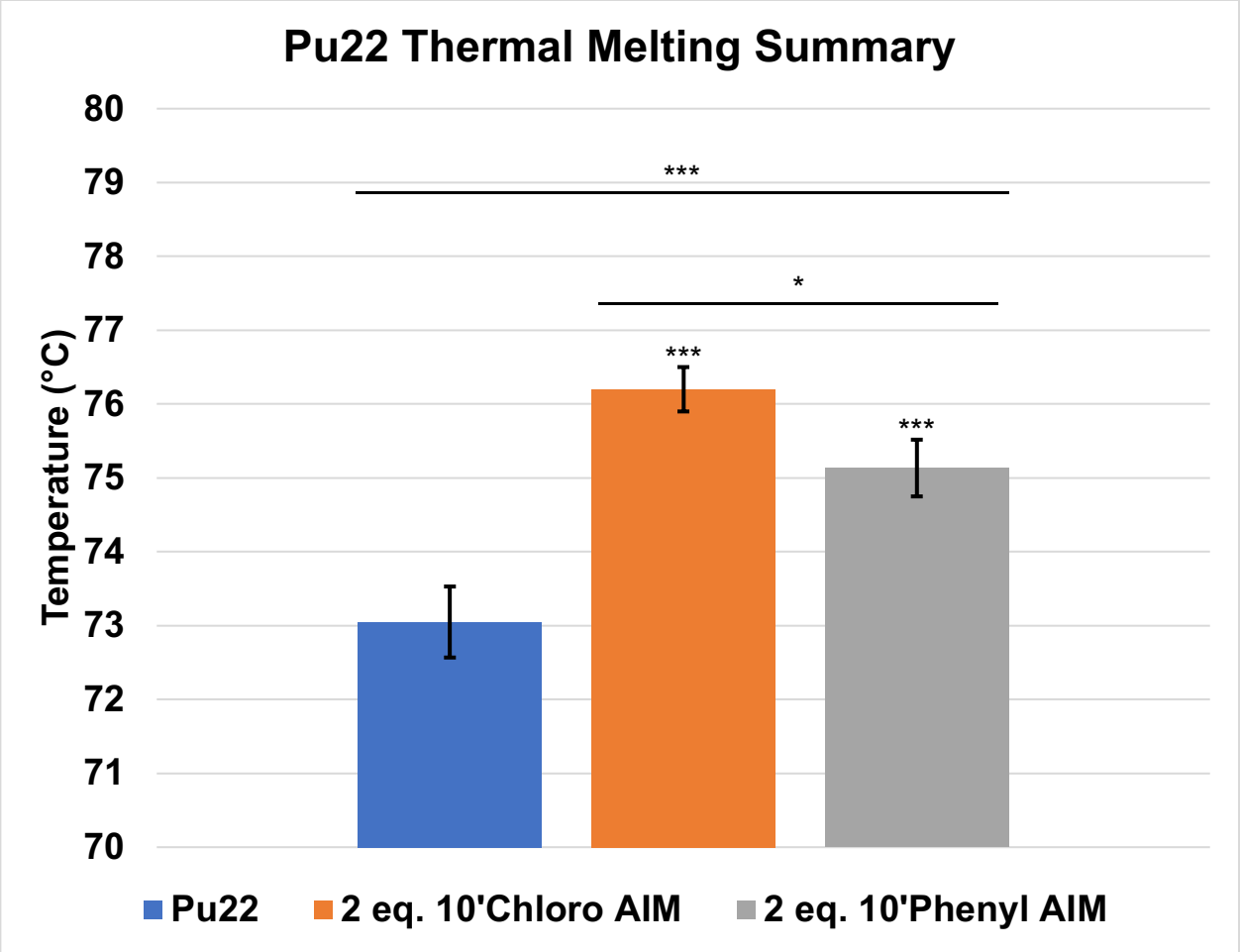

Figure 2.12 Statistical analysis of Pu22 thermal melting

T_m change induced by two equivalents of both the 10-Chloro AIM (P = 0.00008) and 10-Phenyl AIM (P = 0.0008) compared to Pu22 alone (ANOVA P = 9.5E-05). Post-hoc testing also reveals a difference between T_m 10-Chloro AIM and 10-Phenyl AIM at two equivalents (P = 0.02). Error bars represent 95% confidence intervals for three independent samples (n=3). Tukey's post-hoc test used for comparisons between groups. Symbols represent significance levels (P < 0.05 *, P < 0.01 **, P < 0.001 ***).

Next, we repeated the above series of studies using the same conditions with the sequence known to form quadruplex structures in human telomeres (HTelo). The HTelo oligonucleotide displayed peaks at +295 nm and -240 nm with a shoulder at approximately +270 nm, consistent with the expected mixed 3+1 quadruplex topology. The 10-Chloro and 10-Phenyl AIMs both cause a similar hypsochromic shift as previously observed for the Pu22 sequence (**Figure 2.13**) (Weaver et al. 2015). Additionally, the shoulder region observed in the spectra of HTelo alone at approximately 270 nm appeared to shift left in the presence of the 10-Phenyl AIM. Thermal melting experiments with the HTelo sequence also demonstrated a right-ward shift in the presence of both AIMs (**Figure 2.14**). Analysis of the melting curves indicated the presence of the 10-Chloro and 10-Phenyl AIMs increased the T_m of the quadruplex formed by the HTelo sequence by 3.3° C for both compounds (**Figure 2.15**) (Weaver et al. 2015).

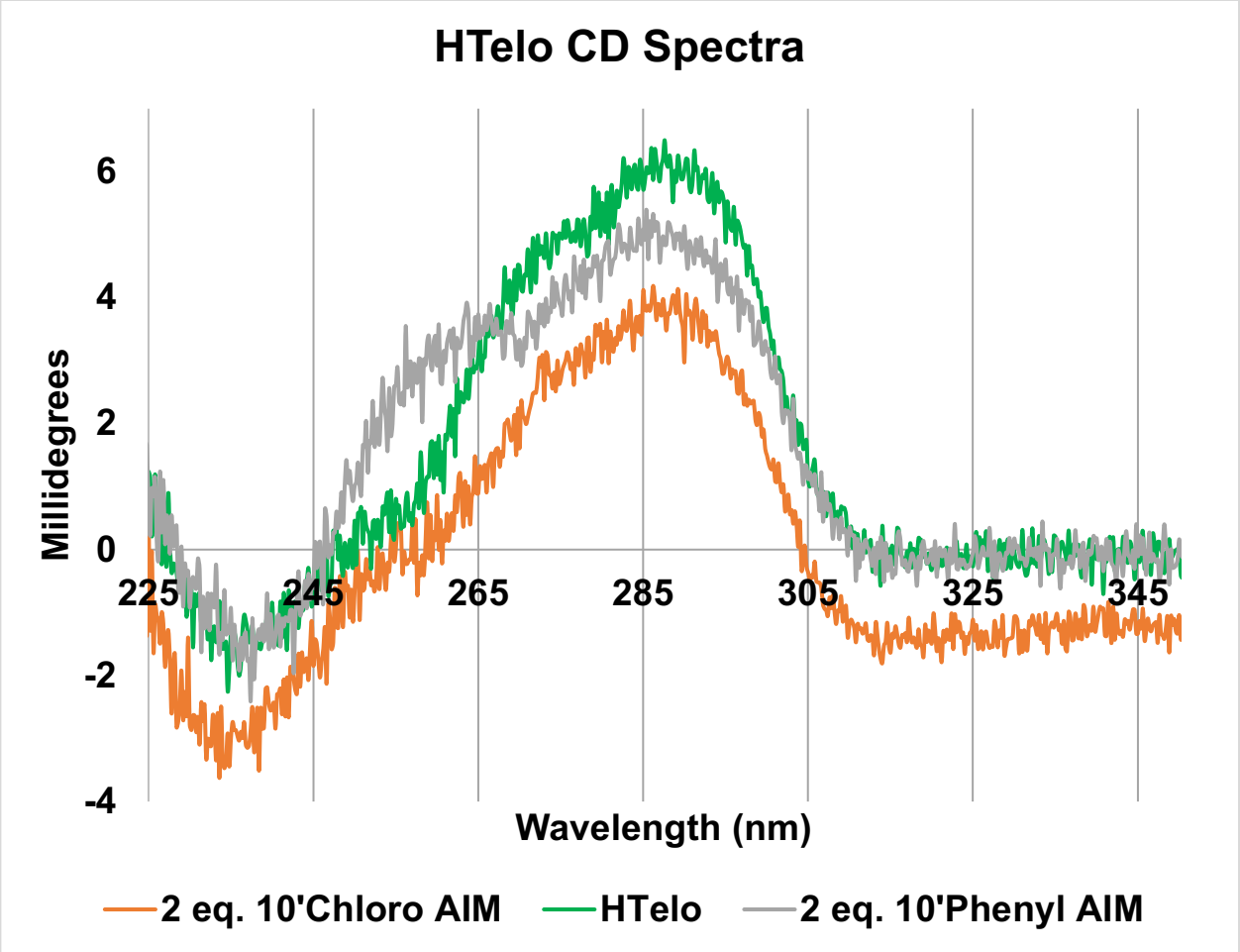

Figure 2.13 Circular dichroism spectra of HTelo oligonucleotide

Circular dichroism spectra of HTelo oligonucleotide with and without two equivalents of AIM compounds in solution. HTelo only (green), 10-Chloro (orange), and 10-Phenyl (grey). (Weaver et al. 2015)

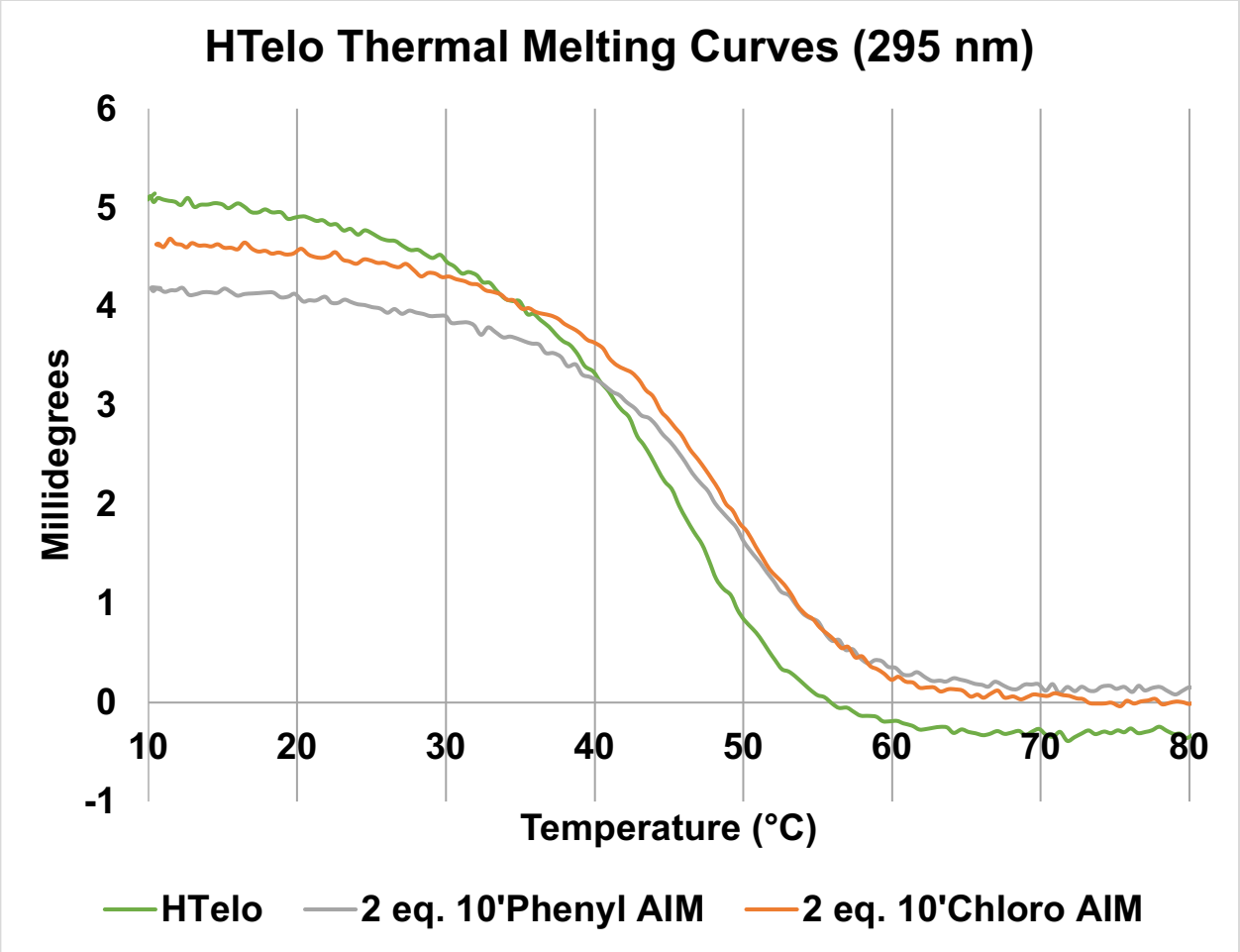

Figure 2.14 Thermal melting curves of the HTelo oligonucleotide

Circular dichroism thermal melting curves of the HTelo oligonucleotide taken at 295 nm with and without two equivalents of AIM compounds in solution. HTelo only (green), 10-Chloro (orange), and 10-Phenyl (grey). (Weaver et al. 2015)

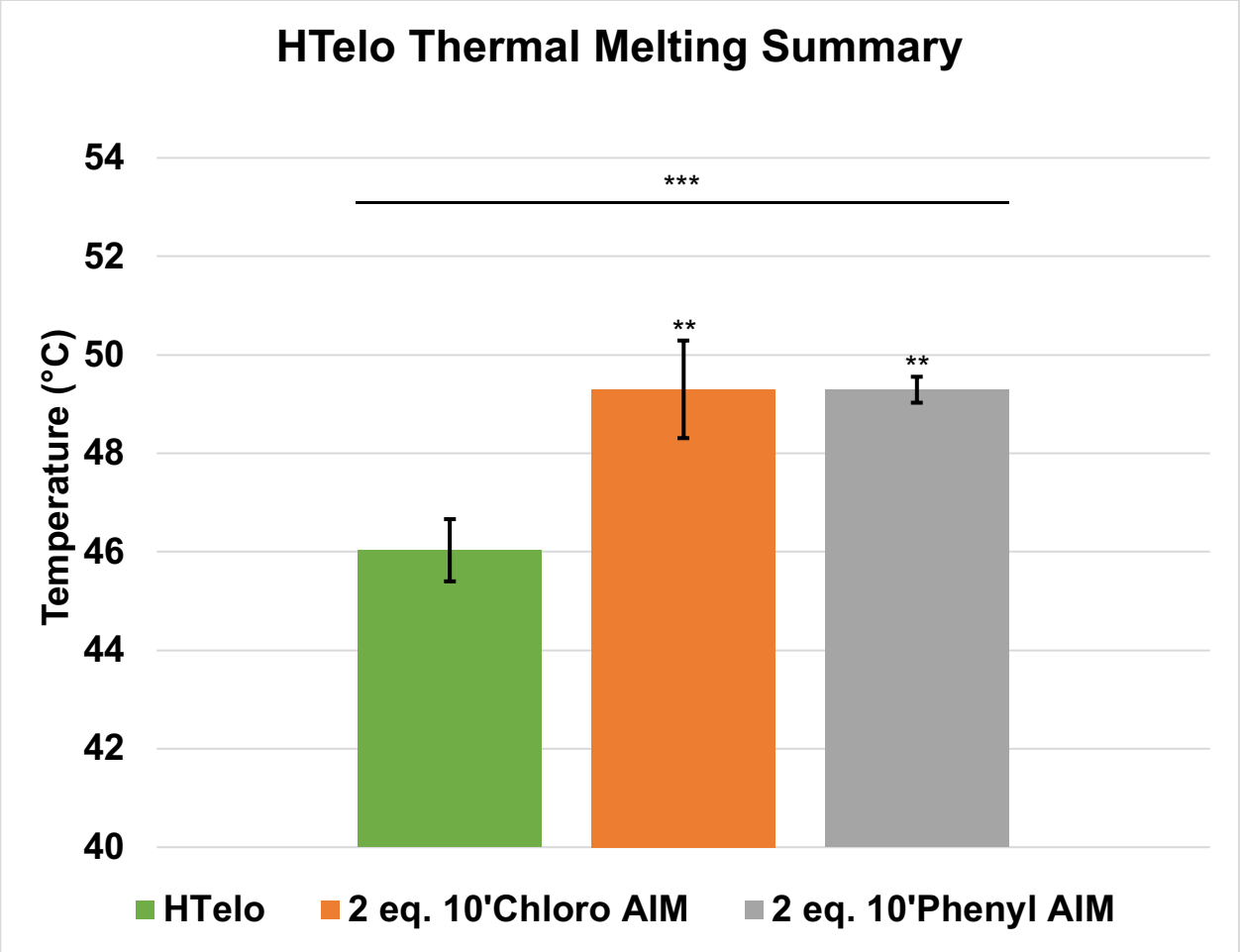

Figure 2.15 Statistical analysis of HTelo thermal melting

T_m change induced by two equivalents of both the 10-Chloro AIM (P = 0.002) and 10-Phenyl AIM (P = 0.002) compared to HTelo alone (ANOVA P = 0.0009). Error bars represent 95% confidence intervals for three independent samples (n=3). Tukey's post-hoc test used for comparisons between groups. Symbols represent significance levels (P < 0.05 *, P < 0.01 **, P < 0.001 ***). (Weaver et al. 2015)

We then similarly measured the effect of the AIMs on two sequences that form quadruplex structures in mitochondrial DNA (mt9438 & CSB II). The mt9438 oligonucleotide displays peaks characteristic of a fully anti-parallel quadruplex (+290 nm, -260 nm). The 10-Phenyl AIM did not create a significant shift in the spectra even at four equivalents of compound in solution (**Figure 2.16**). No right-ward shift was observed in the thermal melting curves measured in the presence of either of the 10-Chloro or 10-Phenyl AIM (**Figure 2.17**). This was verified by comparison of the T_m calculated for each curve, which demonstrated there was no statistically significant change observed in the presence of the AIMs (**Figure 2.18**).

The CSB II oligonucleotide displayed peaks at +265 nm and -240 nm, indicating a fully parallel quadruplex topology. A hypsochromic shift was observed for the CSB II spectra in the presence of one equivalent of the 10-Phenyl AIM (**Figure 2.19**). However, we were unable to calculate a T_m for this sequence to determine the effect of the AIMs, as the CSB II sequence is remarkably stable and could not be unfolded even at 90° C (**Figure 2.20**). Due to this finding, we also performed pH titrations and found the CSB II quadruplex is able to form in solutions with a wide-range of pH's from 4 – 9 (**Figure 2.21**). Additional melting studies with the CSB II quadruplex in pH 4 – 9 solutions confirmed its resistance to temperature melting even under these variable conditions (**Figure 2.22**).

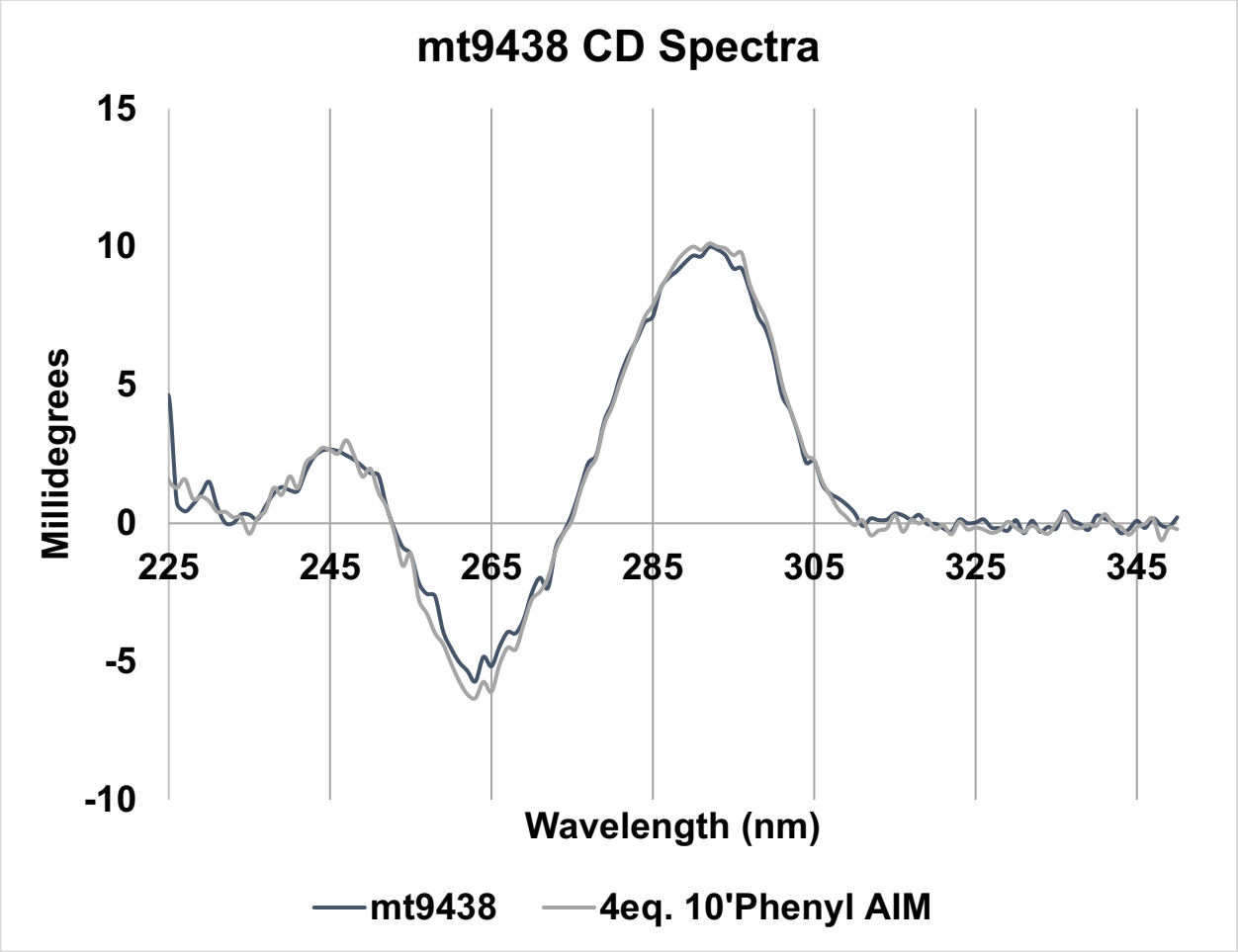

Figure 2.16 Circular dichroism spectra of mt9438 oligonucleotide

Circular Dichroism spectra of mt9438 oligonucleotide with and without four equivalents of AIM compounds in solution. mt9438 only (dark blue) and 10-Phenyl (grey).

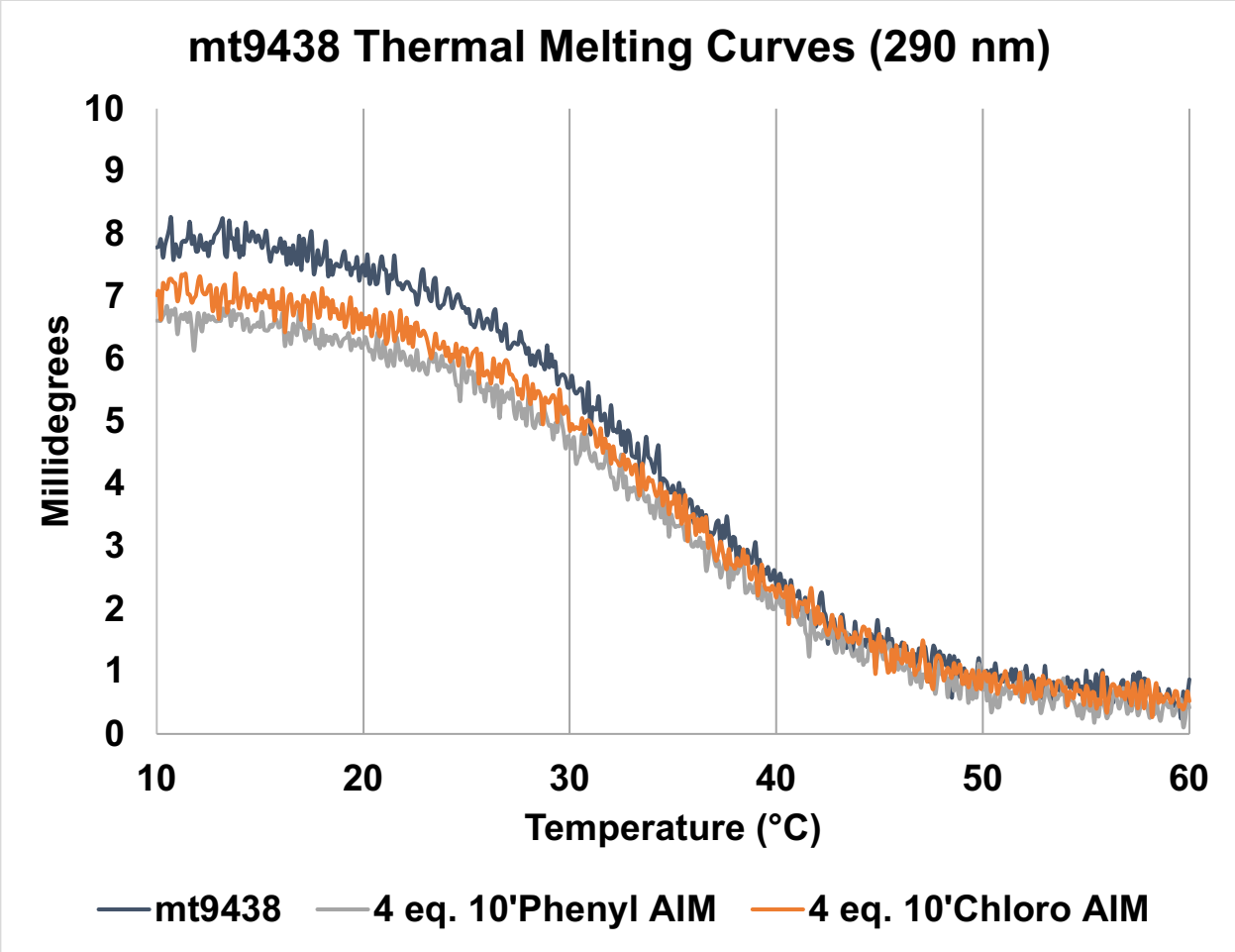

Figure 2.17 Thermal melting curves of the mt9438 oligonucleotide

Circular dichroism thermal melting curves of the mt9438 oligonucleotide taken at 290 nm with and without four equivalents of AIM compounds in solution. mt9438 only (blue), 10-Chloro (orange), and 10-Phenyl (grey).

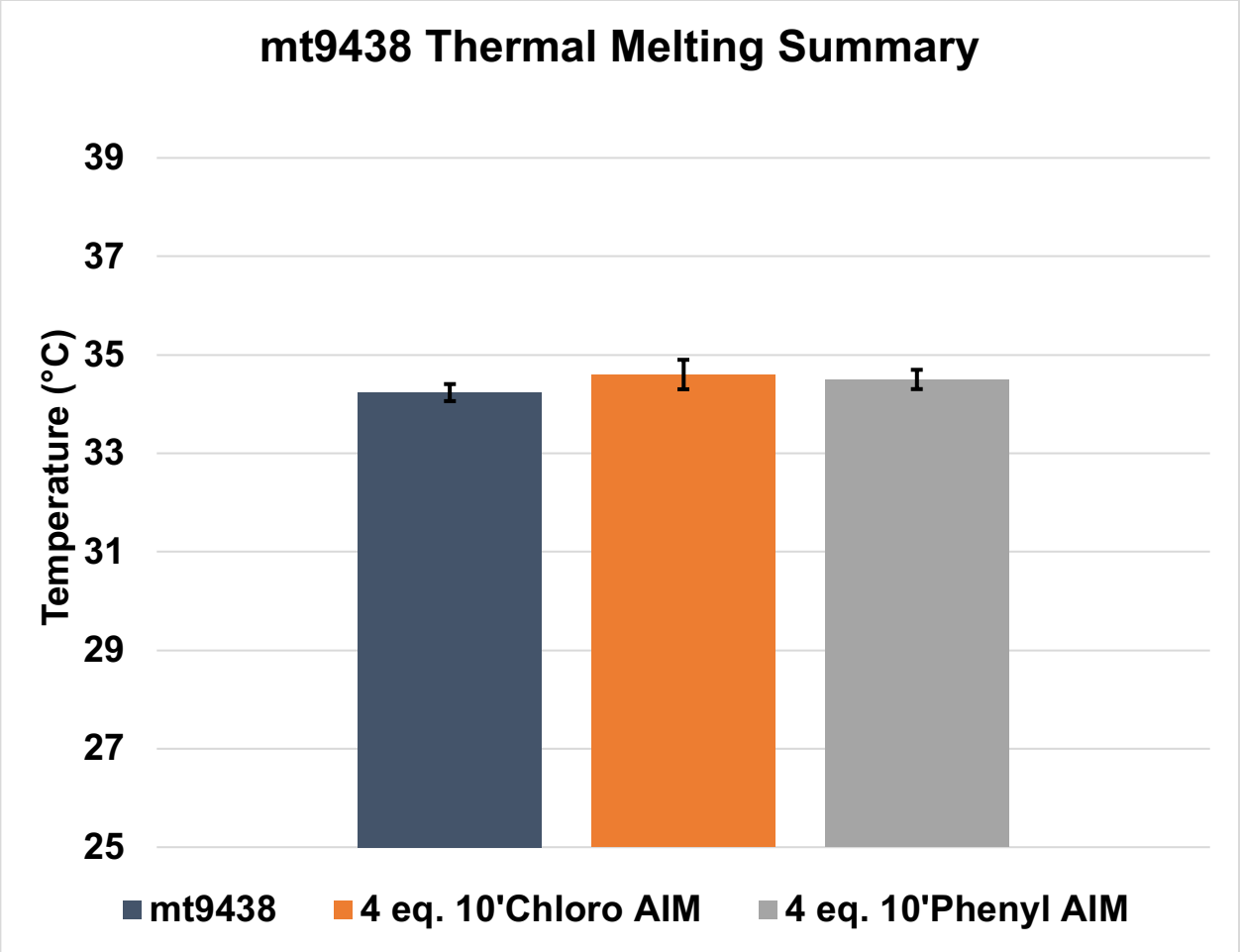

Figure 2.18 Statistical analysis of mt9438 thermal melting

No significant change in T_m was observed with four equivalents the 10-Chloro AIM and 10-Phenyl AIM compared to mt9438 alone. Error bars represent 95% confidence intervals for three independent samples (n=3).

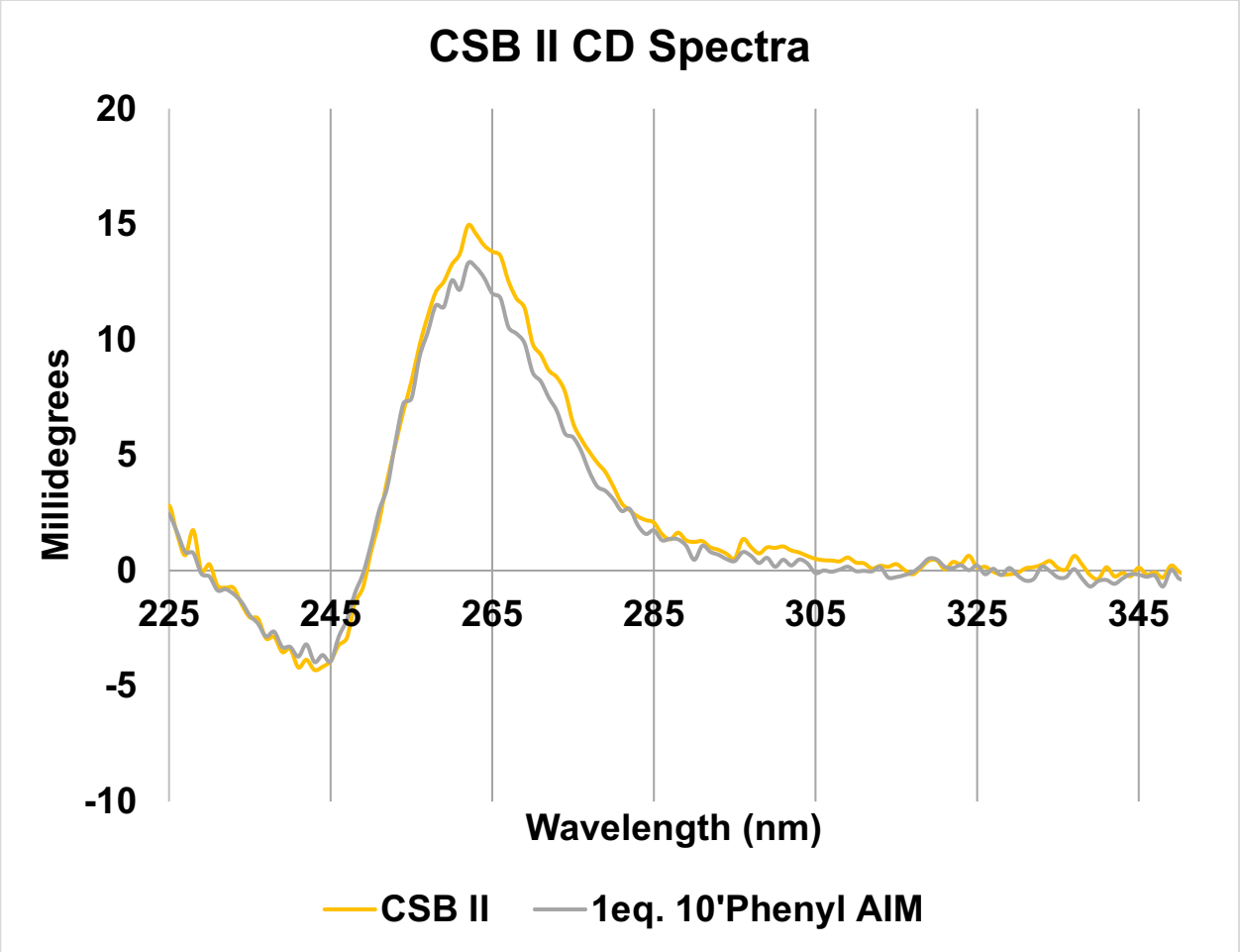

Figure 2.19 Circular dichroism spectra of CSB II oligonucleotide

Circular Dichroism spectra of CSB II oligonucleotide with and without one equivalent of 10-Phenyl AIM in solution. CSB II only (yellow) and 10-Phenyl (grey).

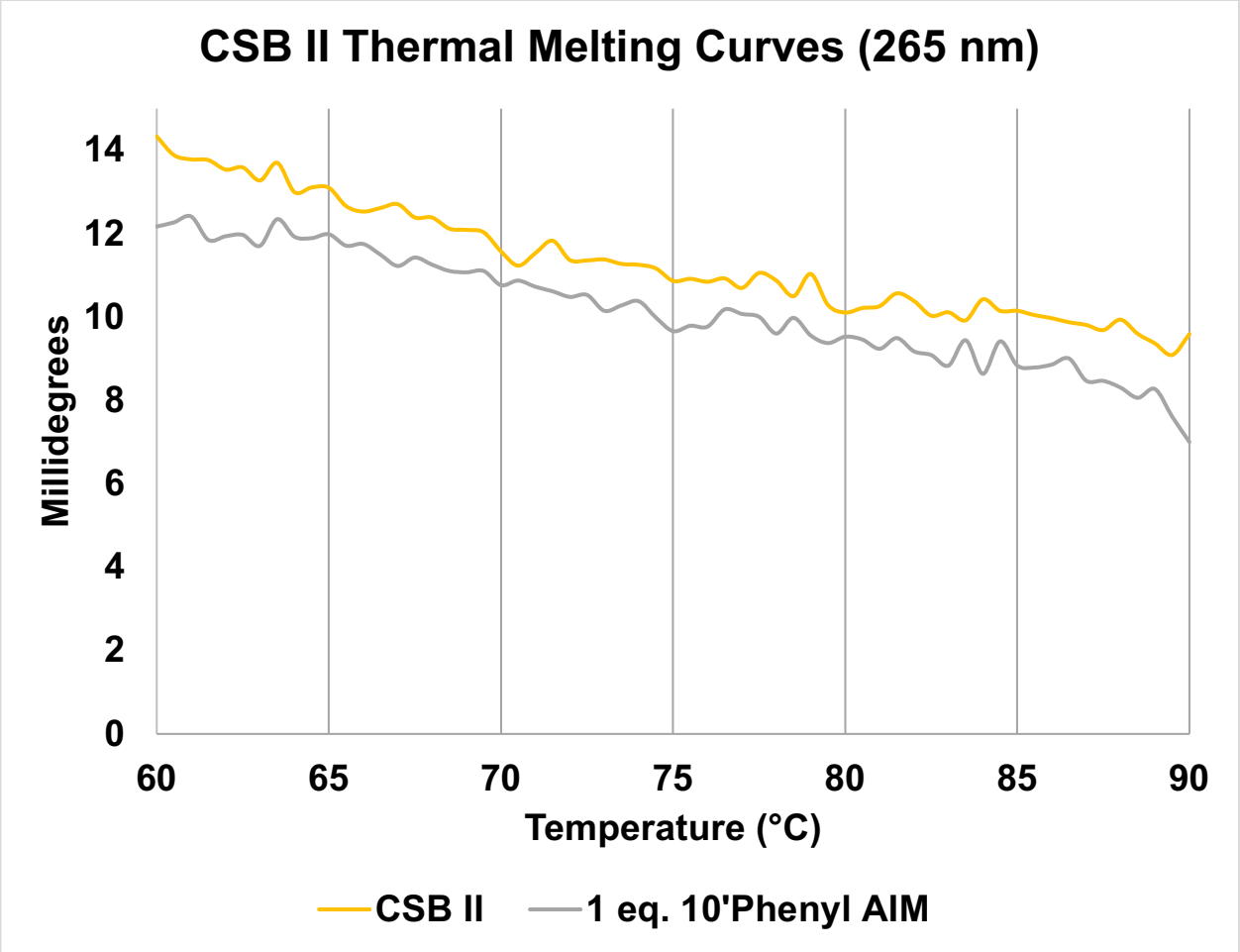

Figure 2.20 Thermal melting curves of the CSB II oligonucleotide

Thermal melting curves of the CSB II oligonucleotide at 265 nm with and without one equivalent of 10-Phenyl AIM. CSB II only (yellow) and 10-Phenyl (grey).

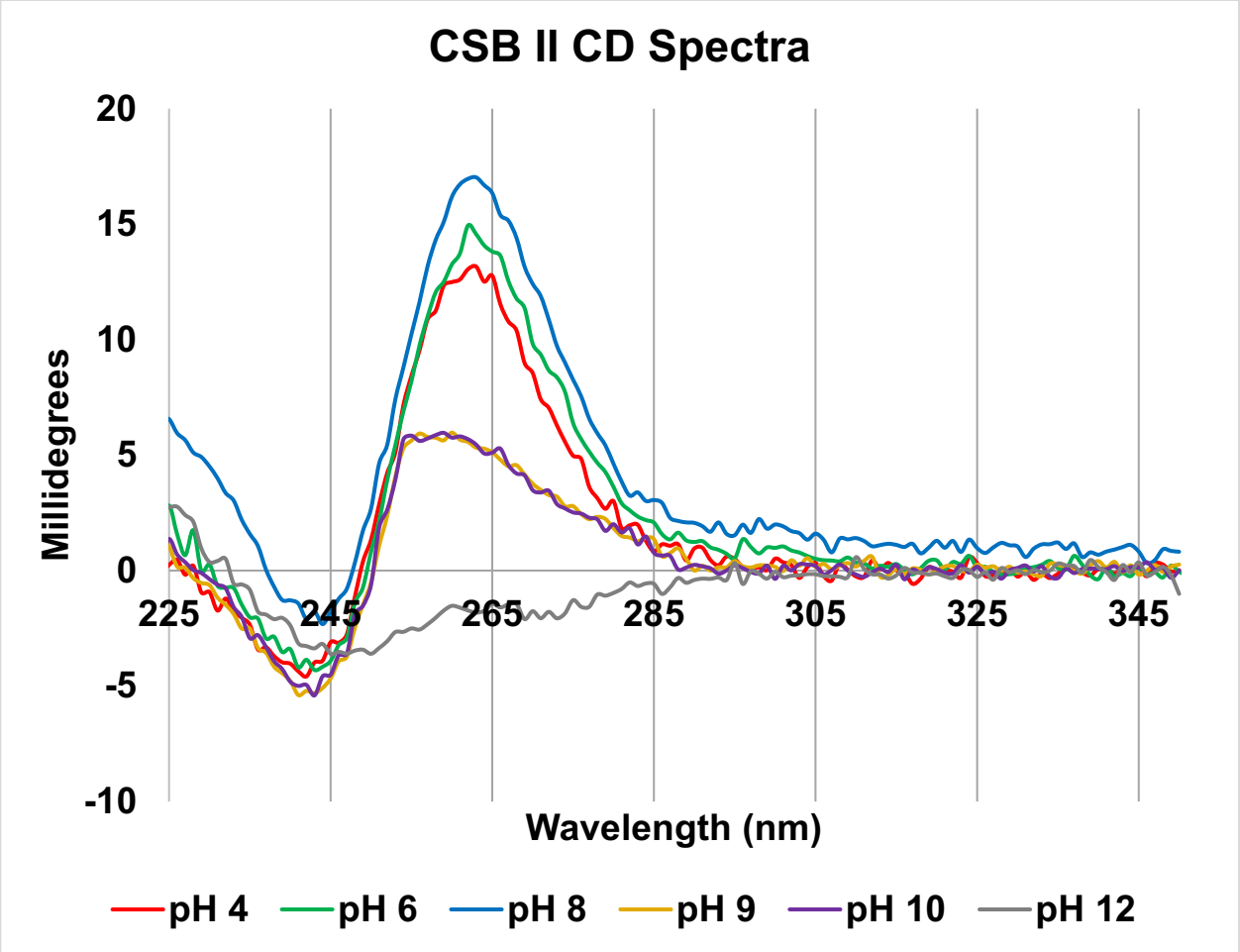

Figure 2.21 Circular dichroism spectra of CSB II oligonucleotide in varying pH solutions

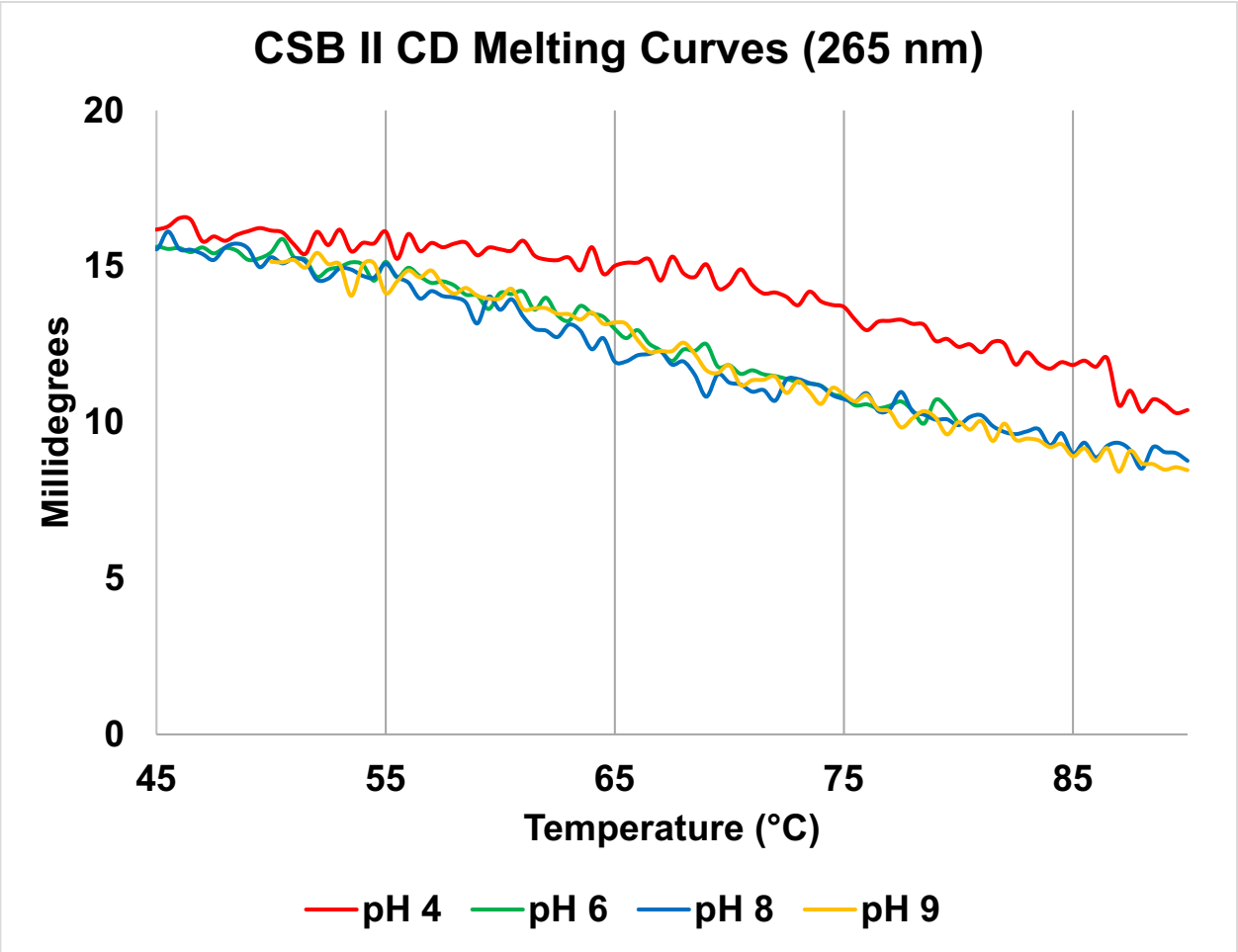

Figure 2.22 Thermal melting curves of the CSB II oligonucleotide in varying pH solutions

NMR Spectroscopy

The authors would like to acknowledge Matthew J. Weaver of the Natale laboratory, and Dr. Earle Adams at the University of Montana for their contributions to these experiments.

We examined interactions of the AIMs with quadruplex DNA using nuclear magnetic resonance spectroscopy (NMR). The ^{1}H NMR spectra for the Pu22 oligonucleotide displayed shifts in the anisotropy observed for protons in the key imino region in the presence of two equivalents of the 10-Phenyl AIM (**Figure 2.23**). The peaks for the Pu22 sequence have been previously assigned, and this will allow for insight into the precise interactions between the AIMs and the c-MYC promoter quadruplex. This analysis is currently being performed by the Natale laboratory and will be reported on in a subsequent publication.

Shifts in the imino region were also observed for the HTelo oligonucleotide at two equivalents of the 10-Chloro AIM in solution (**Figure 2.24**) (Weaver et al. 2015). The peaks for this sequence are less well-defined, owing to the existence of an equilibrium of folded and unfolded states as reported previously (Luu et al. 2006).

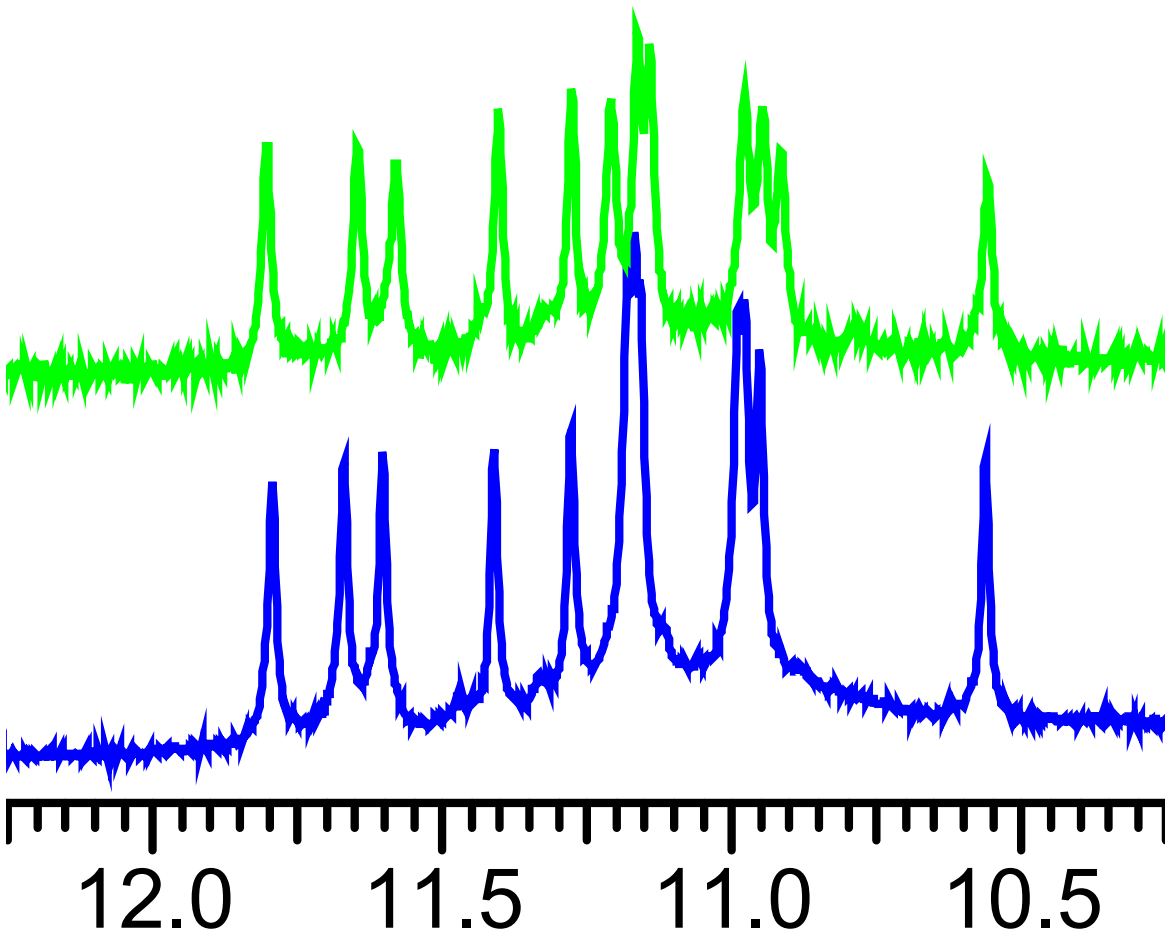

Figure 2.23 NMR spectra of the Pu22 oligonucleotide

Comparison of the imino proton region of the ^{1}H NMR spectra for the quadruplex formed by the human c-MYC promoter sequence (Pu22) in the presence and absence of two equivalents of the 10-Phenyl AIM. Chemical shifts in ppm. Pu22 alone (blue), 10-Phenyl AIM (green).

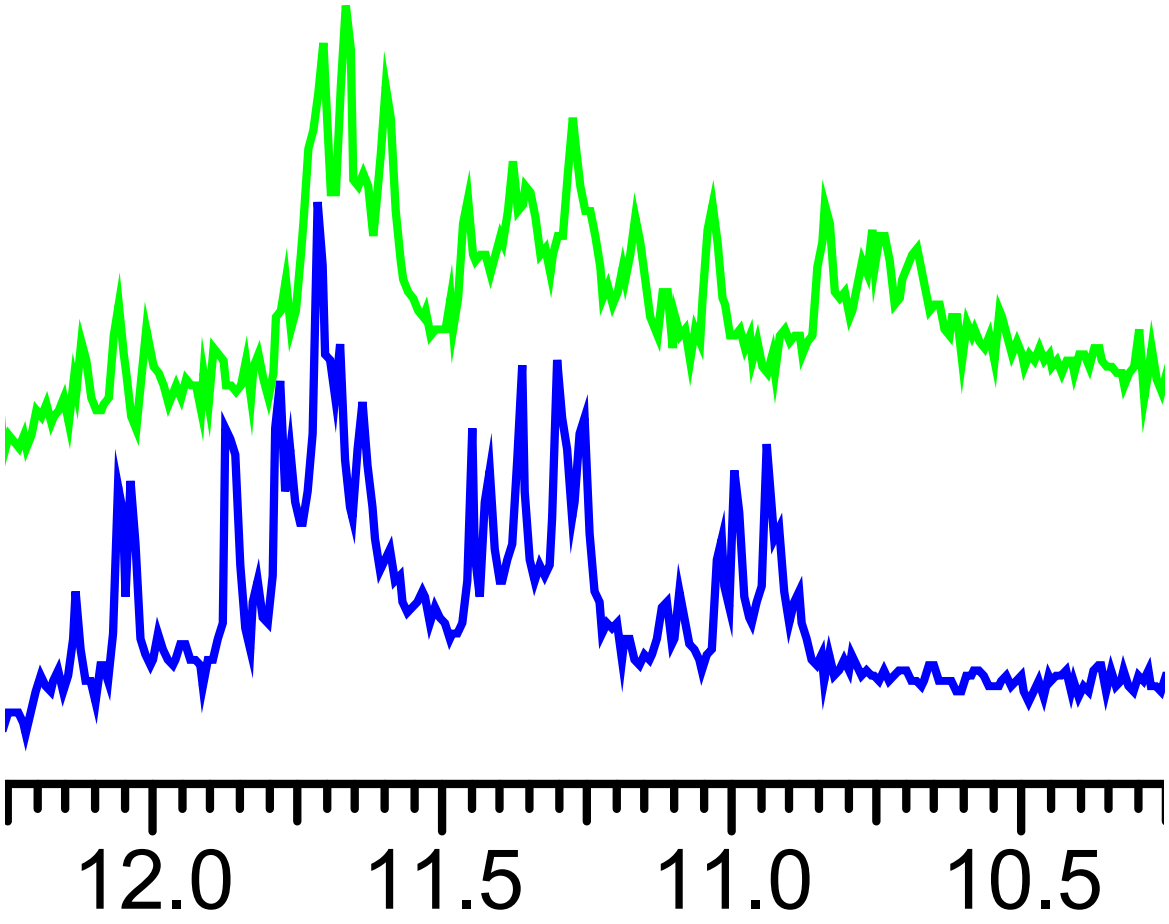

Figure 2.24 NMR spectra of the HTelo oligonucleotide

Comparison of the imino proton region of the ^{1}H NMR spectra for the quadruplex formed by the human telomeric (HTelo) sequence in the presence and absence two equivalents of the 10-Chloro AIM. Chemical shifts in ppm. HTelo alone (blue), 10-Chloro AIM (green). (Weaver et al. 2015)

Discussion

In this study we demonstrated that the AIMs stabilize multiple quadruplex DNA structures in solution using both NMR and CD. The hypsochromic shifts observed in spectra the Pu22, HTelo, and CSB II sequences in the presence of the AIMs is similar to that observed for other quadruplex binding ligands (Zhou et al. 2005; Freyer et al. 2007; Paramasivan, Rujan, and Bolton 2007) (**Figures 2.10**, **2.13**, and **2.19**). In addition, the 10-Chloro and 10-Phenyl AIMs were shown to stabilize the quadruplex structure formed by both the Pu22 and HTelo sequences as demonstrated by increases in the T_m of the structures measured by CD spectroscopy (**Figures 2.12** and **2.15**). The Pu22 and HTelo quadruplexes are examples of mixed 3+1 and parallel topologies, respectively. In contrast, no significant change in melting temperature was observed for the anti-parallel quadruplex formed by the mt9438 sequence found in mitochondrial DNA (**Figure 2.18**). This suggests the AIMs could have selectivity between distinct quadruplex topologies and their binding could be affected by the type of loops present in the specific quadruplex structure. This is an important finding as the field has expressed both curiosity and skepticism regarding the possibility of selectively targeting specific quadruplex sequences or topologies (Burge et al. 2006; Neidle 2017). The high melting point of the CSB II DNA:RNA hybrid quadruplex structure did not allow for characterizing the effect of the AIMs on its stability. However, it was shown that the hybrid quadruplex is remarkably resistant to changes in temperature and pH, and it was confirmed that the chimeric sequence did form a parallel quadruplex as expected. The stability of the CSB II quadruplex is likely due to the incorporation of the RNA nucleotides, as recent reports indicate RNA quadruplexes are generally more stable than their DNA counterparts (Fay,

Lyons, and Ivanov 2017). This is consistent with previous studies that suggest a helicase is involved in resolution of the CSB II hybrid quadruplex in cells, as the structure is unlikely to spontaneously resolve under physiological conditions (Wanrooij et al. 2012). Our studies using solution ^{1}H NMR also demonstrated the interaction of the AIMs for both the Pu22 and HTelo oligonucleotides as indicated by shifts in the peaks observed for the imino region of the spectra.

Overall, this work will significantly contribute to the continued development of the AIMs as quadruplex-targeted ligands. The CD experiments provide the basis for efficiently screening future generations of AIM compounds with various quadruplex-forming sequences. Additional analysis of the NMR experiments is underway by the Natale laboratory and should reveal insights about the precise interactions between the AIMs and quadruplex DNA.

Additional Acknowledgements

We would also like to acknowledge Dr. Bruce Bowler and Dr. Levi McClelland for their assistance with CD spectroscopy and acknowledge Nichol Smith for her contributions to the CD experiments with the mt9438 oligonucleotide.

References

Adams, P. D., P. V. Afonine, G. Bunkóczi, V. B. Chen, I. W. Davis, N. Echols, J. J. Headd, et al. 2010. “PHENIX: A Comprehensive Python-Based System for Macromolecular Structure Solution.” *Acta Crystallographica Section D: Biological Crystallography* 66 (2): 213–21. https://doi.org/10.1107/S0907444909052925.

Agrawal, Prashansa, Clement Lin, Raveendra I. Mathad, Megan Carver, and Danzhou Yang. 2014. “The Major G-Quadruplex Formed in the Human BCL-2 Proximal Promoter Adopts a Parallel Structure with a 13-Nt Loop in K+ Solution.” *Journal of the American Chemical Society* 136 (5): 1750–53. https://doi.org/10.1021/ja4118945.

Ambrus, Attila, Ding Chen, Jixun Dai, Roger A. Jones, and Danzhou Yang. 2005. “Solution Structure of the Biologically Relevant G-Quadruplex Element in the Human c-MYC Promoter. Implications for G-Quadruplex Stabilization.” *Biochemistry* 44 (6): 2048–58. https://doi.org/10.1021/bi048242p.

Balasubramanian, Shankar, Laurence H. Hurley, and Stephen Neidle. 2011. “Targeting G-Quadruplexes in Gene Promoters: A Novel Anticancer Strategy?” *Nature Reviews. Drug Discovery* 10 (4): 261–75. https://doi.org/10.1038/nrd3428.

Berman, Helen M., John Westbrook, Zukang Feng, Gary Gilliland, T. N. Bhat, Helge Weissig, Ilya N. Shindyalov, and Philip E. Bourne. 2000. “The Protein Data Bank.” *Nucleic Acids Research* 28 (1): 235–42. https://doi.org/10.1093/nar/28.1.235.

Bhattacharyya, Debmalya, Gayan Mirihana Arachchilage, and Soumitra Basu. 2016. “Metal Cations in G-Quadruplex Folding and Stability.” *Frontiers in Chemistry* 4 (September). https://doi.org/10.3389/fchem.2016.00038.

Brooks, Tracy A., and Laurence H. Hurley. 2009. “The Role of Supercoiling in Transcriptional Control of MYC and Its Importance in Molecular Therapeutics.” *Nature Reviews Cancer* 9 (12): 849–61. https://doi.org/10.1038/nrc2733.

Brown, Robert V., Forest L. Danford, Vijay Gokhale, Laurence H. Hurley, and Tracy A. Brooks. 2011. “Demonstration That Drug-Targeted Down-Regulation of MYC in Non-Hodgkins Lymphoma Is Directly Mediated through the Promoter G-Quadruplex.” *Journal of Biological Chemistry* 286 (47): 41018–27. https://doi.org/10.1074/jbc.M111.274720.

Burge, Sarah, Gary N. Parkinson, Pascale Hazel, Alan K. Todd, and Stephen Neidle. 2006. “Quadruplex DNA: Sequence, Topology and Structure.” *Nucleic Acids Research* 34 (19): 5402–15. https://doi.org/10.1093/nar/gkl655.

Campbell, Nancy H., and Gary N. Parkinson. 2007. “Crystallographic Studies of Quadruplex Nucleic Acids.” *Methods*, Quadruplex DNA, 43 (4): 252–63. https://doi.org/10.1016/j.ymeth.2007.08.005.

Chen, Michael C., Ramreddy Tippana, Natalia A. Demeshkina, Pierre Murat, Shankar Balasubramanian, Sua Myong, and Adrian R. Ferré-D'Amaré. 2018. "Structural Basis of G-Quadruplex Unfolding by the DEAH/RHA Helicase DHX36." *Nature* 558 (7710): 465–69. https://doi.org/10.1038/s41586-018-0209-9.

Dai, Jixun, Megan Carver, Laurence H. Hurley, and Danzhou Yang. 2011. "Solution Structure of a 2:1 Quindoline–c-MYC G-Quadruplex: Insights into G-Quadruplex-Interactive Small Molecule Drug Design." *Journal of the American Chemical Society* 133 (44): 17673–80. https://doi.org/10.1021/ja205646q.

De Armond, Richard, Stacey Wood, Daekyu Sun, Laurence H. Hurley, and Scot W. Ebbinghaus. 2005. "Evidence for the Presence of a Guanine Quadruplex Forming Region within a Polypurine Tract of the Hypoxia Inducible Factor 1α Promoter." *Biochemistry* 44 (49): 16341–50. https://doi.org/10.1021/bi051618u.

Dexheimer, Thomas S., Daekyu Sun, and Laurence H. Hurley. 2006. "Deconvoluting the Structural and Drug-Recognition Complexity of the G-Quadruplex-Forming Region Upstream of the Bcl-2 P1 Promoter." *Journal of the American Chemical Society* 128 (16): 5404–15. https://doi.org/10.1021/ja0563861.

Emsley, P., B. Lohkamp, W. G. Scott, and K. Cowtan. 2010. "Features and Development of *Coot*." *Acta Crystallographica Section D Biological Crystallography* 66 (4): 486–501. https://doi.org/10.1107/S0907444910007493.

Fay, Marta M., Shawn M. Lyons, and Pavel Ivanov. 2017. "RNA G-Quadruplexes in Biology: Principles and Molecular Mechanisms." *Journal of Molecular Biology* 429 (14): 2127–47. https://doi.org/10.1016/j.jmb.2017.05.017.

Fernando, Himesh, Anthony P. Reszka, Julian Huppert, Sylvain Ladame, Sarah Rankin, Ashok R. Venkitaraman, Stephen Neidle, and Shankar Balasubramanian. 2006. "A Conserved Quadruplex Motif Located in a Transcription Activation Site of the Human c-Kit Oncogene." *Biochemistry* 45 (25): 7854–60. https://doi.org/10.1021/bi0601510.

Freyer, Matthew W., Robert Buscaglia, Kimberly Kaplan, Derek Cashman, Laurence H. Hurley, and Edwin A. Lewis. 2007. "Biophysical Studies of the c-MYC NHE III1 Promoter: Model Quadruplex Interactions with a Cationic Porphyrin." *Biophysical Journal* 92 (6): 2007–15. https://doi.org/10.1529/biophysj.106.097246.

Han, Xiaochun, Chun Li, Michael D. Mosher, Kevin C. Rider, Peiwen Zhou, Ronald L. Crawford, William Fusco, Andrzej Paszczynski, and Nicholas R. Natale. 2009. "Design, Synthesis and Biological Evaluation of a Novel Class of Anticancer Agents: Anthracenylisoxazole Lexitropsin Conjugates." *Bioorganic & Medicinal Chemistry* 17 (4): 1671–80. https://doi.org/10.1016/j.bmc.2008.12.056.

Heddi, Brahim, and Anh Tuân Phan. 2011. "Structure of Human Telomeric DNA in Crowded Solution." *Journal of the American Chemical Society* 133 (25): 9824–33.

https://doi.org/10.1021/ja200786q.

Hu, Ming-Hao, Yu-Qing Wang, Ze-Yi Yu, Lu-Ni Hu, Tian-Miao Ou, Shuo-Bin Chen, Zhi-Shu Huang, and Jia-Heng Tan. 2018. “Discovery of a New Four-Leaf Clover-Like Ligand as a Potent *c-MYC* Transcription Inhibitor Specifically Targeting the Promoter G-Quadruplex.” *Journal of Medicinal Chemistry*, March. https://doi.org/10.1021/acs.jmedchem.7b01697.

Joosten, Robbie P., Fei Long, Garib N. Murshudov, and Anastassis Perrakis. 2014. “The *PDB_REDO* Server for Macromolecular Structure Model Optimization.” *IUCrJ* 1 (4): 213–20. https://doi.org/10.1107/S2052252514009324.

Kabsch, Wolfgang. 2010. “XDS.” *Acta Crystallographica Section D: Biological Crystallography* 66 (Pt 2): 125–32. https://doi.org/10.1107/S0907444909047337.

Karplus, P. Andrew, and Kay Diederichs. 2012. “Linking Crystallographic Model and Data Quality.” *Science (New York, N.Y.)* 336 (6084): 1030–33. https://doi.org/10.1126/science.1218231.

Luu, Kim Ngoc, Anh Tuân Phan, Vitaly Kuryavyi, Laurent Lacroix, and Dinshaw J. Patel. 2006. “Structure of the Human Telomere in K+ Solution: An Intramolecular (3 + 1) G-Quadruplex Scaffold.” *Journal of the American Chemical Society* 128 (30): 9963–70. https://doi.org/10.1021/ja062791w.

Neidle, Stephen. 2017. “Quadruplex Nucleic Acids as Targets for Anticancer Therapeutics.” *Nature Reviews Chemistry* 1 (5): 0041.

Nicoludis, John M., Stephen T. Miller, Philip D. Jeffrey, Steven P. Barrett, Paul R. Rablen, Thomas J. Lawton, and Liliya A. Yatsunyk. 2012. “Optimized End-Stacking Provides Specificity of N-Methyl Mesoporphyrin IX for Human Telomeric G-Quadruplex DNA.” *Journal of the American Chemical Society* 134 (50): 20446–56. https://doi.org/10.1021/ja3088746.

Ou, Tian-Miao, Yu-Jing Lu, Chi Zhang, Zhi-Shu Huang, Xiao-Dong Wang, Jia-Heng Tan, Yuan Chen, et al. 2007. “Stabilization of G-Quadruplex DNA and Down-Regulation of Oncogene c-Myc by Quindoline Derivatives.” *Journal of Medicinal Chemistry* 50 (7): 1465–74. https://doi.org/10.1021/jm0610088.

Paramasivan, Sattanathan, Iulian Rujan, and Philip H. Bolton. 2007. “Circular Dichroism of Quadruplex DNAs: Applications to Structure, Cation Effects and Ligand Binding.” *Methods* 43 (4): 324–31. https://doi.org/10.1016/j.ymeth.2007.02.009.

Parkinson, Gary N., Michael P. H. Lee, and Stephen Neidle. 2002. “Crystal Structure of Parallel Quadruplexes from Human Telomeric DNA.” *Nature* 417 (6891): 876–80. https://doi.org/10.1038/nature755.

Phan, Anh Tuân, Vitaly Kuryavyi, Sarah Burge, Stephen Neidle, and Dinshaw J. Patel. 2007. “Structure of an Unprecedented G-Quadruplex Scaffold in the Human c-Kit Promoter.” *Journal of the American Chemical Society* 129 (14): 4386–92. https://doi.org/10.1021/ja068739h.

Phan, Anh Tuân, Vitaly Kuryavyi, Kim Ngoc Luu, and Dinshaw J. Patel. 2007. “Structure of Two Intramolecular G-Quadruplexes Formed by Natural Human Telomere Sequences in K+ Solution.” *Nucleic Acids Research* 35 (19): 6517–25. https://doi.org/10.1093/nar/gkm706.
Phan, Anh Tuân, Yasha S Modi, and Dinshaw J Patel. 2004. “Propeller-Type Parallel-Stranded G-Quadruplexes in the Human c-Myc Promoter.” *Journal of the American Chemical Society* 126 (28): 8710–16. https://doi.org/10.1021/ja048805k.

Raiber, Eun-Ang, Ramon Kranaster, Enid Lam, Mehran Nikan, and Shankar Balasubramanian. 2012. “A Non-Canonical DNA Structure Is a Binding Motif for the Transcription Factor SP1 in Vitro.” *Nucleic Acids Research* 40 (4): 1499–1508. https://doi.org/10.1093/nar/gkr882.

Rankin, Sarah, Anthony P. Reszka, Julian Huppert, Mire Zloh, Gary N. Parkinson, Alan K. Todd, Sylvain Ladame, Shankar Balasubramanian, and Stephen Neidle. 2005. “Putative DNA Quadruplex Formation within the Human c-Kit Oncogene.” *Journal of the American Chemical Society* 127 (30): 10584–89. https://doi.org/10.1021/ja050823u.

Schrodinger. 2015. “The PyMOL Molecular Graphics System, Version 1.8.”
Siddiqui-Jain, Adam, Cory L. Grand, David J. Bearss, and Laurence H. Hurley. 2002. “Direct Evidence for a G-Quadruplex in a Promoter Region and Its Targeting with a Small Molecule to Repress c-MYC Transcription.” *Proceedings of the National Academy of Sciences* 99 (18): 11593–98. https://doi.org/10.1073/pnas.182256799.

Spiess, Andrej-Nikolai, 2014. qpcR: Modeling and analysis of real-time PCR data. R package version 1.3-8. http://CRAN.R-project.org/package=qpcR

Su, Lijuan, Huaqin Zheng, Zeng Li, Jun Qiu, Siqi Chen, Jinggong Liu, Tian-Miao Ou, et al. n.d. “Mechanistic Studies on the Anticancer Activity of 2,4-Disubstituted Quinazoline Derivative.” *Biochimica et Biophysica Acta (BBA) - General Subjects*. Accessed July 17, 2014. https://doi.org/10.1016/j.bbagen.2014.07.004.

Sun, Daekyu, Kexiao Guo, Jadrian J. Rusche, and Laurence H. Hurley. 2005. “Facilitation of a Structural Transition in the Polypurine/polypyrimidine Tract within the Proximal Promoter Region of the Human VEGF Gene by the Presence of Potassium and G-Quadruplex-Interactive Agents.” *Nucleic Acids Research* 33 (18): 6070–80. https://doi.org/10.1093/nar/gki917.

Sun, Daekyu, and Laurence H. Hurley. 2009. “The Importance of Negative Superhelicity in Inducing the Formation of G-Quadruplex and I-Motif Structures in the c-Myc Promoter: Implications for Drug Targeting and Control of Gene Expression.” *Journal of*

Medicinal Chemistry 52 (9): 2863–74. https://doi.org/10.1021/jm900055s.

Wang, Yong, and Dinshaw J Patel. 1993. “Solution Structure of the Human Telomeric Repeat d[AG3(T2AG3)3] G-Tetraplex.” *Structure* 1 (4): 263–82. https://doi.org/10.1016/0969-2126(93)90015-9.

Wanrooij, Paulina H., Jay P. Uhler, Yonghong Shi, Fredrik Westerlund, Maria Falkenberg, and Claes M. Gustafsson. 2012. “A Hybrid G-Quadruplex Structure Formed between RNA and DNA Explains the Extraordinary Stability of the Mitochondrial R-Loop.” *Nucleic Acids Research* 40 (20): 10334–44. https://doi.org/10.1093/nar/gks802.

Weaver, Matthew J., Alison K. Kearns, Sascha Stump, Chun Li, Mariusz P. Gajewski, Kevin C. Rider, Donald S. Backos, Philip R. Reigan, Howard D. Beall, and Nicholas R. Natale. 2015. “AIMing towards Improved Antitumor Efficacy.” *Bioorganic & Medicinal Chemistry Letters* 25 (8): 1765–70. https://doi.org/10.1016/j.bmcl.2015.02.063.

Wei, Dengguo, Jarmila Husby, and Stephen Neidle. 2015. “Flexibility and Structural Conservation in a c-KIT G-Quadruplex.” *Nucleic Acids Research* 43 (1): 629–44. https://doi.org/10.1093/nar/gku1282.

Wei, Dengguo, Gary N. Parkinson, Anthony P. Reszka, and Stephen Neidle. 2012. “Crystal Structure of a c-Kit Promoter Quadruplex Reveals the Structural Role of Metal Ions and Water Molecules in Maintaining Loop Conformation.” *Nucleic Acids Research* 40 (10): 4691–4700. https://doi.org/10.1093/nar/gks023.

Xue, Yong, Zhong-yuan Kan, Quan Wang, Yuan Yao, Jiang Liu, Yu-hua Hao, and Zheng Tan. 2007. “Human Telomeric DNA Forms Parallel-Stranded Intramolecular G-Quadruplex in K+ Solution under Molecular Crowding Condition.” *Journal of the American Chemical Society* 129 (36): 11185–91. https://doi.org/10.1021/ja0730462.

Yang, Danzhou, and Laurence H. Hurley. 2006. “Structure of the Biologically Relevant G-Quadruplex in The c-MYC Promoter.” *Nucleosides, Nucleotides and Nucleic Acids* 25 (8): 951–68. https://doi.org/10.1080/15257770600809913.

Zhou, Jin-Lin, Yu-Jing Lu, Tian-Miao Ou, Jun-Min Zhou, Zhi-Shu Huang, Xiao-Feng Zhu, Cui-Juan Du, et al. 2005. “Synthesis and Evaluation of Quindoline Derivatives as G-Quadruplex Inducing and Stabilizing Ligands and Potential Inhibitors of Telomerase.” *Journal of Medicinal Chemistry* 48 (23): 7315–21. https://doi.org/10.1021/jm050041b.

Chapter 3 : Evaluation of the Mitochondrial Mechanism of Apoptosis Induction in Tumor Cells by Anthracenyl Isoxazole Amides

Sascha Stump[1], Alison K. Kearns[1], Michael J. Campbell[1], Matthew J. Weaver[1], Nathan S. Duncan[1], Nicholas R. Natale[1], and Howard D. Beall[1*]

[1]Center for Environmental Health Sciences, Department of Biomedical and Pharmaceutical Sciences, University of Montana, Missoula, Montana 59812, United States of America

*Corresponding author

E-mail: howard.beall@umontana.edu

Abstract

Mitochondria are regulators of many important processes in cells including metabolism and apoptosis. Targeting mitochondria to induce the intrinsic pathway of apoptosis is being examined in the field of anticancer drug design as a way to kill tumor cells for treatment of cancer. One strategy involves inhibition of the electron transfer chain (ETC) of mitochondria causing loss of the mitochondrial membrane potential ($\Delta\Psi m$) and leading to apoptosis in tumor cells. In this study we provide evidence for a mitochondrial mechanism of action for a novel set of antitumor compounds, the anthracenyl isoxazole amides (AIMs), mediated by their inhibition of the ETC. We first demonstrate that the AIMs can inhibit ETC protein complexes, specifically Complex II, using spectrophotometric assays and provide an initial binding hypothesis for the interaction of the AIMs with Complex II using computational molecular docking. We also show that treatment with the AIMs leads to rapid damage in mitochondrial DNA (mtDNA) and an associated reduction in mtDNA copy number. Further, we confirm a dose-dependent loss of the $\Delta\Psi m$ and induction of the intrinsic pathway of apoptosis in glioblastoma cells following treatment with the AIMs.

Introduction

Mitochondria are crucial regulators of many homeostatic processes in cells and are responsible for both energy metabolism and as gatekeepers to the intrinsic pathway of apoptosis. Targeting mitochondria to induce apoptosis in tumor cells has been the focus of many researchers with the goal of developing new anticancer therapeutics (Fulda, Galluzzi, and Kroemer 2010). Multiple agents that act on the mitochondria have been demonstrated to have selective toxicity to tumor cells (Neuzil et al. 2013).

Targeting mitochondria could be especially advantageous when developing therapeutics as they are present throughout all types of human cancers; therefore a mitochondrial-targeted agent could be more universally applicable in contrast to targeting a mutation or gene expression pattern specific to only a smaller subset of cancers (Neuzil et al. 2013).

One strategy employed to target mitochondria is perturbation of the electron transport chain (ETC). The ETC refers to five protein complexes (Complex I – V) that are located in the inner mitochondrial membrane and responsible for the generation of cellular ATP through oxidative phosphorylation. Complex I (NADH ubiquinone oxidoreductase) converts ubiquinone to ubiquinol using NADH to pass electrons to Complex III. Similarly, Complex II passes electrons to Complex III through reduction of ubiquinone to ubiquinol coupled with oxidation of succinate to fumarate. Due to the high electron flow through Complexes I, II, and III, all of these represent sites of significant reactive oxygen species (ROS) production as superoxide and hydrogen peroxide (Liu, Fiskum, and Schubert 2002; St-Pierre et al. 2002; Indo et al. 2007; West, Shadel, and Ghosh 2011). Complex IV and V are not major contributors to the production of ROS, however they have also been explored as potential mitochondrial targets of antitumor agents (Lee, Bender, and Kadenbach 2002; Fu et al. 2015).

Complex II has several known inhibitors, and they fit into two groups, those that bind at one of two ubiquinone sites (U_p and U_d) or those that bind at the succinate site. Some examples of known ubiquinone site inhibitors include thenoyltrifluoroacetone (TTFA), Atpenin 5 (AA5), and carboxin (Miyadera et al. 2003). Ubiquinone is held in the binding pocket through a hydrogen bonding interaction with residue Tyr-D83. As the

reaction proceeds, hydrogen bonds are formed between His-B207 and Ser-C27, ubiquinone is then reduced to ubiquinol and leaves the binding pocket (Sun et al. 2005). It is thought that the His-207B allows flow of electrons from the 3Fe-4S iron-sulfur cluster in Complex II (Horsefield et al. 2006). Inhibitors of Complex II at the ubiquinone site can take the place of ubiquinone in the binding pocket, preventing reduction of ubiquinone (Sun et al. 2005). The result of this is an increase in ROS, partially due to leak of electrons in the mitochondrial matrix and loss of succinate to fumarate conversion. It has also been suggested that Complex II inhibition can cause an increase in ROS generation by Complex I through a reverse electron flow mechanism. The evidence for this is a reduction in the amount of ROS produced by Complex II inhibition in the presence of rotenone, a potent inhibitor of Complex I (Ralph et al. 2011). The increase in ROS has been demonstrated to induce apoptosis in multiple types of tumor cells (L.-F. Dong et al. 2008; Byun et al. 2008; Ralph et al. 2011; Wang et al. 2016). Inhibition of Complex II specifically, using the known ubiquinone site inhibitor TTFA, has been shown to delay cell cycle progression by prolonging G1, S and G2/M phases, as well as causing oxidation of glutathione (Byun et al. 2008). Another set of studies with TTFA demonstrated an increase in autophagy in cancer and transformed cells following treatment, and this was mediated through ROS (Chen et al. 2007). The vitamin E analog α-Tocopheryl succinate (α-TOS) is yet another example of a Complex II inhibitor that disrupts ubiquinone binding, generating superoxide and ultimately causing apoptosis in tumor cells (Sun et al. 2005; L.-F. Dong et al. 2008). In the case of α-TOS and a targeted derivative “MitoVES”, this toxicity has been shown to be selective for tumor cells relative to normal endothelial cells and to inhibit tumor

angiogenesis *in vivo* in mice (L.-F. Dong et al. 2008). The ROS generated by Complex II inhibition is exacerbated by damage to mtDNA, and increased mitochondrial ROS can cause damage to mtDNA and ETC proteins (Indo et al. 2007; Byun et al. 2008; Alexeyev et al. 2013). Additionally, mtDNA depleted transformed endothelial cells were shown to be resistant to apoptosis induced by α-TOS, suggesting mtDNA damage may mediate induction of apoptosis following inhibition of Complex II (Lan-Feng Dong et al. 2007). Together, these studies highlight the importance of exploring Complex II as a potential target for development of selective antitumor agents.

The anthracenyl isoxazole amides (AIMs) are a class of compounds synthesized in the laboratory of Nicholas Natale at the University of Montana. The AIMs structure consists of three major regions, the alkyl amine tails, the isoxazole pyrrole scaffold and the anthracene ring system. The compounds explored in this work also contain a variable substitution at the 10-position of the anthracene (**Figure 3.1**). Substitutions of electron-rich moieties at the 10-position have been demonstrated to improve the antitumor cell efficacy of these compounds (Weaver et al. 2015).

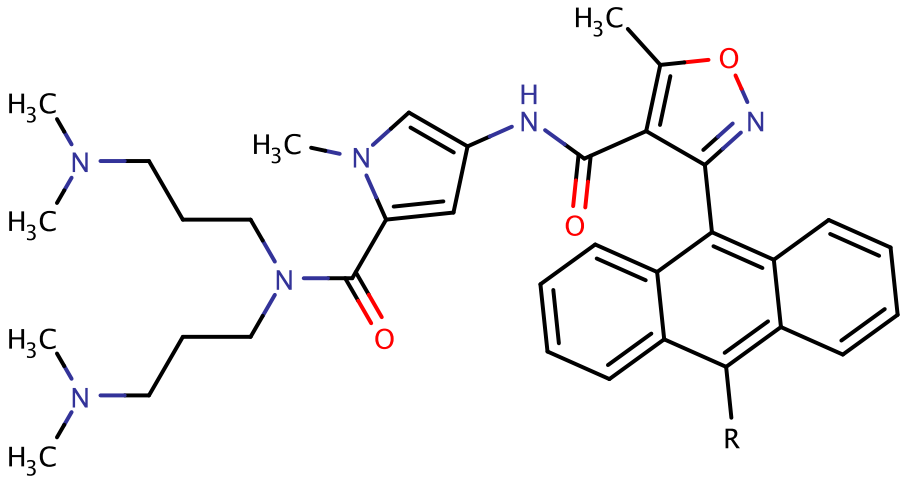

Figure 3.1 Structure of the anthracenyl isoxazole amides (AIMs)

Structure of the anthracenyl isoxazole amides (AIMs) demonstrating the double-tail tertiary alkyl amines, isoxazole pyrrole scaffold, and the hydrophobic anthracene region with variable substitutions at the 10-position.

The generation of compounds that are the focus of this work are referred to as the “double-tails”, referencing the addition of the two alkyl amine chains which has improved the pharmacokinetic properties and toxicity of these molecules over previous generations (Han et al. 2009; Weaver et al. 2015). The AIMs have previously demonstrated significant antitumor activity in a National Cancer Institute 60 human cancer cell line panel (NCI60) and sub-micromolar efficacy in human glioblastoma cells, specifically (Gajewski et al. 2009; Han et al. 2009; Weaver et al. 2015). The mechanism underlying the activity of the AIMs against these cancer lines could not be determined by an NCI60 COMPARE analysis as they did not correlate significantly with any agents of known mechanism of action. The AIMs have also previously been studied as ligands for quadruplex DNA, as our laboratory has demonstrated the interaction with these secondary structures (Han et al. 2009; Weaver et al. 2015). The

focus of this work is to characterize a mitochondrial mechanism of action for the AIMs that contributes to their antitumor activity in glioblastoma cells.

Dr. Alison K. Kearns of the Beall laboratory first demonstrated the possibility of a mitochondrial modulated mechanism of apoptosis induced by the AIMs in glioblastoma cells (Kearns 2013). This included the observation that AIMs appeared to localize to mitochondria of cells and that treatment with AIMs caused a subsequent increase in mitochondrial ROS (Kearns 2013). Initially, our cell viability studies with the AIMs relied on using MTT reduction as an indicator of AIM cytotoxicity, however MTT results can depend partially on involvement of mitochondrial reductases (Mosmann 1983; Berridge, Herst, and Tan 2005; Fedotcheva et al. 2017; Rai et al. 2018). Careful examination of our previous data and the methods used led us to the hypothesis that the AIMs may be acting through interactions with the electron transport chain or mitochondrial DNA.

To explore this further, this work evaluated the two most potent AIM compounds, the 10-Biphenoxy and 10-Phenyl analogs, in an effort to determine the mechanism underlying their effect on mitochondria in cells. We also performed confocal imaging experiments with glioblastoma cells treated with AIMs and a mitochondrial-specific fluorescent dye to confirm localization of the AIMs to mitochondria. Next, we employed a lactate dehydrogenase (LDH) activity assay as a measure of cell viability that is not dependent on mitochondrial reductases.

Comparison of the LDH results with our MTT data led us to consider the AIMs could be inhibiting activity of mitochondrial reductases and as a result display lower measured toxicity in the LDH assay. To test this hypothesis, we employ activity assays of several ETC protein complexes to measure the inhibitory activity of the AIMs. For

this purpose, we utilize several commercially available kits to measure the inhibitory effect of the AIMs on ETC complexes isolated using specific antibodies (complexes I, II and IV) and in intact mitochondria (complexes II + III) as described previously (Lai et al. 2013). Additionally, we perform molecular docking calculations to explore the potential of the AIMs as ubiquinone site inhibitors at Complex II. We also examine whether treatment with the AIMs increased mtDNA damage and reduced copy number as would be expected to occur alongside an increase in mitochondrial ROS due to inhibition of ETC complexes (Yakes and Van Houten 1997; Indo et al. 2007; Phillips, Sprouse, and Roby 2014). For this purpose, we use a previously reported method to accurately measure changes in mtDNA damage and copy number (Chan and Chen 2009; Chan et al. 2012). Analysis of glioblastoma cells treated with AIMs by flow cytometry allows for measurement of the expected downstream effects of inhibition of ETC activity. With this method we measured changes in $\Delta\Psi m$ using the mitochondrial redox sensor JC-1. Our analysis using JC-1 includes both the classic approach and an alternative approach that utilizes an alternative excitation at 405 nm to better distinguish JC-1 aggregates from monomers (Perelman et al. 2012). With this method, we were able to define populations of “hyperpolarized” mitochondria, which we defined as cells with greater mitochondrial update of the JC-1 dye due to increased $\Delta\Psi m$ (Giovannini et al. 2002; Perelman et al. 2012). We also measured activation of caspase-9 and caspase- 3/7 as indicators of activation of the intrinsic apoptotic pathway. Finally, we demonstrate induction of apoptosis in the glioblastoma cells using Annexin-V and propidium iodide.

Methods

Cell Culture

SNB-19 Human Glioblastoma

SNB-19 (American Type Cell Culture Cat No. CRL-2266) were grown in RPMI-1640 medium with 10% FBS, 2 mM L-Glutamine, and Penicillin Streptomycin added. Cells were grown under optimal growth conditions (37° C, 5% CO_2, humidified atmosphere) to approximately 90% confluence before use in experiments.

C6 Rat Glioma

C6 rat glioma cells were obtained as a gift from the Patel laboratory at the University of Montana. The cells were grown in RPMI-1640 medium with 10% FBS, 2 mM L-Glutamine, and Penicillin Streptomycin added. Cells were grown under optimal growth conditions (37° C, 5% CO_2, humidified atmosphere) to approximately 90% confluence before use in experiments.

E-18 Primary Rat Astrocytes

Primary E-18 astrocytes taken from the hippocampus and cortex of Sprague-Dawley rats were given to us by the Jackson Laboratory at the University of Montana. The cells were grown in BrainBits® NbASTRO® medium under optimal growth conditions (37° C, 5% CO_2, humidified atmosphere) prior to use.

MTT Cell Viability Assay

Cells were washed with PBS (2 mL) and then treated with Trypsin EDTA (2 mL) to detach cells from culture flask prior to counting with a Coulter counter. Cells were diluted to 10,000 cells / mL and plated on a 96-well plate with 100 µL per well (1000 cells / well). Cells were grown in optimal growth conditions and allowed to adhere overnight. Treatment solutions were prepared in growth medium at varying concentrations using a 5 mM compound stock solution prepared previously in sterile DMSO. Medium was removed from the 96-well plate via aspiration and treatment solutions were added as outlined (**Table 3.1**). Cells were grown in treatment medium for 24 hours and then treatment medium was removed via aspiration and 100 µL of untreated growth medium was added to each well. Cells were then allowed to grow for a four-day growth period. Following the growth period, 50 µL of MTT solution (1 mg/mL in growth medium) was added to each well and the 96-well plate was placed on a plate shaker for 5 minutes to mix. The plate was then incubated at growth conditions for 4 hours before removing medium/MTT solution from the wells carefully via aspiration to avoid disturbing the formazan crystals. One hundred µL of DMSO was then added to each well and the plate was placed on a plate shaker for 5 minutes to dissolve the crystals. A SpectraMax 190 plate reader was used to measure the absorbance of the wells at 562 nm.

Table 3.1 Example 96-well plate layout for MTT assay

Column:	**#1**	**#2**	**#3**	**#4**	**#5**	**#6**	**#7**	**#8**	**#9**	**#10**	**#11**	**#12**
Treatment:	**No Cells**	**DMSO Control**	**5 nM**	**10 nM**	**25 nM**	**50 nM**	**100 nM**	**250 nM**	**500 nM**	**1 µM**	**2.5 µM**	**5 µM**

Data Analysis

IC_{50} values were calculated using the 'R' statistical computing software and the 'ic50' package (R Core Team, 2014; Frommolt, 2010). This package fits a logistic model to the dose-response data collected using the MTT assay and approximates the concentration of the compound required to inhibit the growth of the cells by 50% versus the DMSO control (IC_{50}).

LDH Cell Viability Assay

LDH cytotoxicity assays were performed using a commercially available kit (Pierce™ LDH Cytotoxicity Kit #88953). The assays were carried out according to the manufacturer protocol. Cells were plated in sterile 96-well plates at approximately 7,500 cells / well in 100 µL medium (RPMI-1640 with 10% FBS, L-Glutamine, and Penicillin-Streptomycin added for SNB-19 & C6 cells; BrainBits® NbASTRO® for primary rat astrocytes). Cells were incubated overnight at optimal growth conditions to allow them to adhere to the bottom of the wells. Cells were treated by removing medium and adding treatment medium containing DMSO vehicle or AIMs at the desired concentration and incubated 24 hours at growth conditions (**Table 3.2**). Forty-five minutes prior to the end of the 24-hour incubation, 10 µL of lysis buffer (10x) was added to each of the maximum LDH release wells and the plates were placed back in the incubator to finish the 24-hour treatment period. Following treatment, 50 µL of medium from each well was transferred to a second 96-well plate and 50 µL of the LDH reaction solution was added to each well. These plates were then incubated again at growth conditions for 30 minutes in the dark. Fifty µL of stop solution was added to each well to

halt the LDH reaction and plates were measured at 490 nm and 680 nm using a SpectraMax 190 plate reader to measure LDH activity as formazan formation and background absorbance, respectively.

Data Analysis

IC_{50} values were calculated using the 'R' statistical computing software and the 'ic50' package (R Core Team, 2014; Frommolt, 2010). This package fits a logistic model to the dose-response data collected using the LDH assay and approximates the concentration of the compound required to inhibit the growth of the cells by 50% versus the DMSO control (IC_{50}).

Table 3.2 96-well plate layout for LDH assay

Column:	#1	#2	#3	#4	#5	#6	#7	#8	#9	#10	#11	#12
Treatment:	No Cells	Medium Only	DMSO Control	0.1 µM	0.25 µM	0.5 µM	1 µM	2.5 µM	5 µM	10 µM	25 µM	Maximum LDH Release

Confocal Microscopy

Cells were washed with PBS (2 mL) and then treated with Trypsin EDTA (2 mL) to detach cells from culture flask prior to counting with a Coulter counter. Cells were diluted to 100,000 cells / mL and plated on an 8-well Lab-Tek II chambered coverglass slide at a density of 20,000 cells / well in 0.2 mL growth medium. Cells were grown in optimal growth conditions and allowed to adhere overnight. The following day, treatment medium was made by dilution of 5 mM DMSO stock solutions of AIM compounds in growth medium. Culture medium was removed by aspiration and

treatment medium containing the desired compound was added. The cells were then incubated at growth conditions 10 minutes prior to removing treatment medium by aspiration. Each well was washed with 0.2 mL of PBS twice prior to addition of staining solution. For mitochondrial staining, 0.2 mL of 100 nM MitoTracker™ DeepRed FM (Invitrogen™) in culture medium was added prior to a second incubation under the previous conditions for 45 minutes. Following staining, the solutions were removed by aspiration and each well was washed twice with 0.2 mL of PBS. Cells were then fixed in 4% PFA, prepared fresh the previous day, for 10 minutes on ice prior to imaging. Imaging was completed on an Olympus FV-1000 confocal laser scanning microscope immediately following fixation. Images were captured using a 60x oil-immersion objective lens (NA 1.42). Compound fluorescence was captured using selective excitation at 405 nm and emission collected at 422 nm. MitoTracker™ fluorescence was measured at an excitation of 635 nm and emission at 688 nm.

Image Processing

Confocal images were processed using Fiji and ImageJ (Schindelin et al. 2012, 2015). Contrast was adjusted using image LUT to match intensity of the compound fluorescence to the MitoTracker™, avoiding oversaturation of regions of interest. The StackReg plugin was used to perform a translation, scaling, and rotation alignment of images to correct for chromatic aberration observed in the images due to the large difference in emission wavelengths of the compound versus the Mitotracker (422 nm vs. 668 nm, respectively) (Thevenaz, Ruttimann, and Unser 1998). Images were filtered

using the “Unsharp Mask” function of ImageJ. The unprocessed images are available upon request.

ETC Inhibition Assays

Complex I

Complex I inhibition was measured using a commercially available kit (Abcam MitoTox™ Complex I OXPHOS Activity Assay #ab109903) according to the manufacturer protocol. Bovine heart mitochondria (BHM) were solubilized through addition of 40 µL of the supplied detergent to 360 µL of BHM and mixture by vortex. The solubilized BHM were incubated on ice for 30 minutes and then centrifuged at 25,000 x g for 20 minutes at 4° C. The supernatant was collected, and the pellet discarded prior to adding 5 mL of Mito Buffer. Fifty µL of the above solution was then added to each well of a provided 96-well plate pre-coated with Complex I specific antibodies and incubated for two hours at room temperature. Following incubation, the solution was removed from the wells by inversion and blotting of the plate on a Kimwipe. Each well was washed with 300 µL of Wash Solution and subsequently inverted and blotted a second time. Forty µL of provided phospholipids were then added to each well and the plate was covered and incubated for 45 minutes at room temperature.

AIM compound solutions were made by diluting 32.4 µL of a 5 mM DMSO stock solution into a total volume of 1.8 mL of the provided Complex I activity solution to 90 µM and then performing serial dilutions to achieve 900 µL of each desired concentration. Rotenone solutions were made similarly using a 10 µM DMSO stock diluted in 1.8 mL of Complex I activity solution to 0.125 µM and then performing serial dilutions to achieve 900 µL of each desired concentration. DMSO controls were made

using 16.2 µL of DMSO in Complex I activity solution to a final volume of 900 µL to match the maximum DMSO concentration of the above AIMs solutions.

Following the 45-minute incubation, 200 µL of compound diluted in Complex I activity solution was added to each well of the plate as outlined (**Table 3.3**). Output was immediately measured as absorbance at 340 nm on a SpectraMax M4 microplate reader in kinetic mode, taking a reading once per minute for 2 hours at 30° C.

Table 3.3 Layout of Complex I 96-well plate

Rows ↓	**1**	**2**	**3**	**4**	**5**	**6**	**7**	**8**	**9**	**10**	**11**	**12**
A – D (µM Conc.)	90	45	22.5	11.25	5.625	2.813	1.406	0.703	0.352	0.176	0.088	DMSO
E – H (µM Conc.)	90	45	22.5	11.25	5.625	2.813	0.125	0.063	0.031	0.016	0.008	DMSO

10-Biphenoxy in blue, 10-Phenyl in yellow, Rotenone in green.

Data Analysis

The reaction rate was calculated as the change in absorbance per minute (mOD/min). This rate was calculated in the linear phase of the assay (0 – 4000 seconds) as determined by the fitted linear curves with the goal of achieving approximately R^2 of 0.99 for each well as per the manufacturer protocol. Row A + H do not contain the Complex I specific antibodies and therefore were used as "background" rates which were averaged and subtracted from the calculated rates prior to fitting the IC_{50} curves. The IC_{50} for each compound was calculated using the R statistical computing software with the package "drc" (R Core Team, 2014; Ritz et al., 2015). The data was fit to a three-parameter logistic curve and the IC_{50} was defined as the

concentration required to reach 50% inhibition of the activity of the DMSO control samples. Data was visualized in R using the package “ggplot2”.

Complex II

Complex II inhibition was measured using a commercially available kit (Abcam MitoTox™ Complex II OXPHOS Activity Assay #ab109904) according to the manufacturer protocol. Bovine heart mitochondria (BHM) were solubilized through addition of 36 µL of the supplied detergent to two 360 µL samples of BHM and mixture by vortex. The solubilized BHM were incubated on ice for 30 minutes and then centrifuged at 25,000 x g for 20 minutes at 4° C. The supernatant was collected, and the pellet discarded prior to adding 20 mL of Buffer Solution. 200 µL of the above solution was then added to each well of a provided 96-well plate pre-coated with Complex II specific antibodies and incubated for two hours at room temperature. Following incubation, the solution was removed from the wells by inversion and blotting of the plate on a Kimwipe. Each well was washed with 300 µL of Wash Solution and subsequently inverted and blotted a second time.

AIM compound solutions were made by diluting 32.4 µL of a 5 mM DMSO stock solution into a total volume of 1.8 mL of the provided Complex II activity solution to 90 µM and then performing serial dilutions to achieve 900 µL of each desired concentration. DMSO controls were made using 16.2 µL of DMSO in Complex II activity solution to a final volume of 900 µL to match the maximum DMSO concentration of the above AIMs solutions.

200 µL of compound diluted in Complex II activity solution was added to each well of the plate as outlined (**Table 3.4**). Output was immediately measured as

absorbance at 600 nm on a SpectraMax M4 microplate reader in kinetic mode, taking a reading once per minute for 1 hour at room temperature.

Table 3.4 Layout of Complex II 96-well plate

Rows ↓	**1**	**2**	**3**	**4**	**5**	**6**	**7**	**8**	**9**	**10**	**11**	**12**
A – D (μM Conc.)	90	45	22.5	11.25	5.625	2.813	1.406	0.703	0.352	0.176	0.088	DMSO
E – H (μM Conc.)	90	45	22.5	11.25	5.625	2.813	1.406	0.703	0.352	0.176	0.088	DMSO

10-Biphenoxy in blue, 10-Phenyl in yellow.

Data Analysis

The reaction rate was calculated as the change in absorbance per minute (mOD/min). This rate was calculated in the linear phase of the assay (720 – 3000 seconds) as determined by the fitted linear curves with the goal of achieving approximately R^2 of 0.99 for each well as per the manufacturer protocol. Row A + H do not contain the Complex II specific antibodies and therefore were used as "background" rates which were averaged and subtracted from the calculated rates prior to fitting the IC_{50} curves. Column 6 was excluded from the analysis for both compounds as the activity in this entire column contained outliers in the dose-response curve fits as determined by the residual standard error and residual plots of the fits. The IC_{50} for each compound was calculated using the R statistical computing software with the package "drc" (R Core Team, 2014; Ritz et al., 2015). The data was fit to a three-parameter logistic curve and the IC_{50} was defined as the concentration required to reach 50% inhibition of the activity of the DMSO control samples. Data was visualized in R using the package "ggplot2".

Complex II + III

Complex II + III inhibition was measured using a commercially available kit (Abcam MitoTox™ Complex II + III OXPHOS Activity Assay #ab109905) according to the manufacturer protocol. The Complex II + III activity solution was made using 12 mL of the succinate solution, 500 µL of the oxidized cytochrome C solution, 120 µL of 0.2 M KCN and 15.2 µL of 10 mM rotenone as per the manufacturer protocol.

AIM compound solutions were made by diluting 16.6 µL of a 5 mM DMSO stock solution into a total volume of 920 µL of the Complex II + III activity solution to 90 µM and then performing serial dilutions to achieve 460 µL of each desired concentration. DMSO controls were made using 8.3 µL of DMSO in Complex II + III activity solution to a final volume of 460 µL to match the maximum DMSO concentration of the above AIMs solutions. Antimycin A solutions were made by diluting 11.5 µL of a 10 µM antimycin A DMSO stock solution to 0.125 µM and then performing serial dilutions to achieve 460 µL of each desired concentration.

One hundred-twenty µL of BHM was diluted into 880 µL of Complex II + III Mito Buffer and 20 µL of this solution was rapidly added to the solutions containing the Complex II + III activity solutions and compounds. The solutions were mixed rapidly and 100 µL was transferred to the 96-well plate as outlined below for rows B, C, D and E, F, G (**Table 3.5**). The output was measured immediately as absorbance at 550 nm on a SpectraMax M4 microplate reader in kinetic mode, with a measurement every 20 seconds for 10 minutes at room temperature.

Table 3.5 Layout of Complex II + III 96-well plate

Rows ↓	**1**	**2**	**3**	**4**	**5**	**6**	**7**	**8**	**9**	**10**	**11**	**12**
A – D (µM Conc.)	90	45	22.5	11.25	5.625	2.813	1.406	0.703	0.352	0.176	0.088	DMSO
E – H (µM Conc.)	90	45	22.5	11.25	5.625	2.813	0.125	0.063	0.031	0.016	0.008	DMSO

10-Biphenoxy in blue, 10-Phenyl in yellow, Antimycin A in green.

Data Analysis

The reaction rate was calculated as the change in absorbance per minute (mOD/min). This rate was calculated in the linear phase of the assay (0 – 400 seconds) as determined by the fitted linear curves with the goal of achieving approximately R^2 of 0.99 for each well as per the manufacturer protocol. Row A + H do not contain the BHM and therefore were used as "background" rates which were averaged and subtracted from the calculated rates prior to fitting the IC_{50} curves. Column 6 was excluded from the analysis for the 10-Phenyl AIM and column 11 was excluded from the analysis for the 10-Biphenoxy AIM and antimycin A as the volume in these wells was double the volume of the other reaction wells due to the serial dilutions performed. The IC_{50} for each compound was calculated using the R statistical computing software with the package "drc" (R Core Team, 2014; Ritz et al., 2015). The data was fit to a three-parameter logistic curve and the IC_{50} was defined as the concentration required to reach 50% inhibition of the activity of the DMSO control samples. Data were visualized in R using the package "ggplot2".

Complex IV

Complex IV inhibition was measured using a commercially available kit (Abcam MitoTox™ Complex IV OXPHOS Activity Assay #ab109907) according to the manufacturer protocol. 300 µL of Blocking Solution was added to each well of the provided 96-well plate pre-coated with Complex IV specific antibodies and incubated at room temperature for 1 hour. Bovine heart mitochondria (BHM) were solubilized through addition of 10 µL of the supplied detergent to 90 µL of BHM and mixture by vortex. The solubilized BHM were incubated on ice for 30 minutes and then centrifuged at 25,000 x g for 20 minutes at 4° C. The supernatant was collected and kept on ice until use. The 96-well plate was emptied by inversion and blotted with a Kimwipe prior to a second addition of 300 µL blocking solution to each well. The plate was emptied and blotted a second time. Twenty µL of solubilized BHM solution was diluted into 22 mL of Mito Buffer. Twenty µL of the above solution was then added to each well of a provided 96-well plate pre-coated with Complex IV specific antibodies and incubated for 3 hours at room temperature. Following incubation, 300 µL of Mito Buffer was added to each well to wash and then the solution was removed from the wells by inversion and blotting of the plate on a Kimwipe. Each well was washed with 300 µL of Wash Solution and subsequently inverted and blotted a second time.

AIM compound solutions were made by diluting 32.4 µL of a 5 mM DMSO stock solution into a total volume of 1.8 mL of the provided Complex IV activity solution to 90 µM and then performing serial dilutions to achieve 900 µL of each desired concentration. DMSO controls were made using 16.2 µL of DMSO in Complex II activity

solution to a final volume of 900 µL to match the maximum DMSO concentration of the above AIMs solutions.

Two hundred µL of compound diluted in Complex IV activity solution was added to each well of the plate as outlined (**Table 3.6**). Output was immediately measured as absorbance at 550 nm on a SpectraMax M4 microplate reader in kinetic mode, taking a reading once per minute for 1 hour at room temperature.

Table 3.6 Layout of Complex IV 96-well plate

Rows ↓	**1**	**2**	**3**	**4**	**5**	**6**	**7**	**8**	**9**	**10**	**11**	**12**
A – D (µM Conc.)	90	45	22.5	11.25	5.625	2.813	1.406	0.703	0.352	0.176	0.088	DMSO
E – H (µM Conc.)	90	45	22.5	11.25	5.625	2.813	1.406	0.703	0.352	0.176	0.088	DMSO

10-Biphenoxy in blue, 10-Phenyl in yellow.

Data Analysis

The reaction rate was calculated as the change in absorbance per minute (mOD/min). This rate was calculated in the linear phase of the assay (600 – 2400 seconds) as determined by the fitted linear curves with the goal of achieving approximately R^2 of 0.99 for each well as per the manufacturer protocol. Row A + H were not used as "background" rates for this assay due to inconsistency of the readings. The IC_{50} for each compound was calculated using the R statistical computing software with the package "drc" (R Core Team, 2014; Ritz et al., 2015). The data was fit to a three-parameter logistic curve and the IC_{50} was defined as the concentration required to reach 50% inhibition of the activity of the DMSO control samples. Data was visualized in R using the package "ggplot2".

Computational Modeling

GOLD docking software (v5.2.2) was utilized to perform molecular docking calculations for the AIMs using a crystal structure of Complex II from porcine heart with waters removed (PDB:1ZOY) (Jones et al. 1997; Sun et al. 2005). The positions of the ubiquinone sites were determined using the related crystal structure of Complex II bound by the known inhibitors TTFA and 3-NP (PDB: 1ZP0). The AIM compounds were docked in a 20 Å sphere centered on the hydroxy of residues Tyr-D91 & Tyr-D61 of the two ubiquinone sites (Qp and Qd, respectively). The known inhibitor TTFA was also docked using the same method to validate the method. Docked poses were scored with the CHEMPLP scoring function and high-ranking poses were considered based on polar surface interaction distances and visualization by Pymol (Schrodinger 2015). Interaction diagrams were made using Discovery Studio (Dassault Systèmes, 2018).

Determination of mtDNA Copy Number and Measurement of mtDNA Damage

Cell Treatment & Sample Collection

Treatment solutions were prepared in growth medium at various concentrations using a 5 mM compound stock solution prepared previously in sterile DMSO. Medium was removed via aspiration and cells were rinsed with 2 mL of PBS. The PBS was removed and medium containing the desired treatment was added to the culture dish. Cells were then incubated at growth conditions for the desired treatment period. After treatment and incubation, medium was transferred to a 15 mL conical tube. The cells were washed with 2 mL PBS and the wash was added to the 15 mL tube. 1.5 mL of trypsin-EDTA was added to the cells and they were incubated at 37° C for

approximately 3 minutes to allow cells to detach. Two mL of fresh growth medium was added to inactivate the trypsin-EDTA and the cells plus medium were transferred to the corresponding 15 mL tube. Samples were centrifuged at 1,500 RPM for 5 minutes at 4° C, the supernatant was discarded, and pellets were resuspended in 1 mL PBS and transferred to 1.5 mL tubes. The samples were then centrifuged at 5,000 RPM for 10 minutes at 4 C. The supernatants were discarded, and the pellets were frozen at -80° C until use.

DNA Isolation

Nuclear and mtDNA were isolated using a QIAGEN Blood & Cell Culture DNA Mini Kit as described in the protocol outlined by Chand and Chen (Chan and Chen 2009). Briefly, cells were thawed on ice and resuspended in 50 µL of nuclease-free water. One mL of G2 digestion buffer was added to each tube and samples were vortexed immediately for 25 seconds. Three µL of RNase A was added to each sample, mixed, and briefly centrifuged. Twenty-five µL of reconstituted protease was added to each sample, and samples were inverted to mix. Samples were then incubated in a water bath at 50° C for 1 hour. Genomic tips were equilibrated for 15 minutes with QBT buffer and samples were vortexed 10 seconds and each transferred to a genomic tip following incubation. Genomic tips were washed three times with 1 mL of QC buffer. Each DNA sample was eluted into a 15 mL tube by adding 910 µL of buffer QF, pre-warmed to 50° C, twice to the corresponding genomic tip. DNA was mixed by inversion and briefly centrifuged before dividing each sample into two 1.5 mL tubes. DNA was precipitated from each sample by addition of 700 µL of isopropanol, mixture by

inversion, and incubating at room temperature for 10 minutes. Samples were centrifuged a 18,000 x g for 20 minutes at 4° C to pellet the nuclear and mitochondrial DNA. The sample DNA pellets were washed twice with 500 µL ethanol pre-chilled to -20° C, centrifuging at 18,000 x g for 10 minutes after each wash. The supernatant was removed, and the residual ethanol was allowed to evaporate approximately 10 minutes in air. Eighty µL TE buffer was added to each sample and the pellets were allowed to slowly dissolve overnight in the fridge at 4° C.

DNA Quantification

Sample DNA concentrations were measured using a NanoDrop instrument. Following initial measurements, dilutions were made at 10 ng/µL and measured again in triplicate. Five ng/µL dilutions were made, measured in triplicate, and then diluted to 1 ng/µL samples. Five ng/µL samples were used for the nuclear marker in qPCR reactions. One ng/µL samples were split equally, and one set was heated to 95° C for 6 minutes in a PCR instrument to relax supercoiled mtDNA. The 1 ng/µL samples, with and without heat treatment (native and relaxed), were then used for the mtDNA markers in qPCR reactions.

Standards Preparation

Standards were prepared using DNA isolated from untreated SNB-19 cells. For both mtDNA markers (D-loop & CO-2), standards were prepared by PCR using DNA isolated from untreated SNB-19 cells. Fifty µL PCR reactions were performed to amplify a 3285 b.p. fragment (CO-2) and a 2467 b.p. fragment (D-loop). Each reaction

contained 5 µL of 10x Thermophilus DNA polymerase buffer (Fisher Scientific), 4 µL of 25 mM MgCl2, 1 µL of 10 mM dNTP mixed bases, 0.5 µL of Tth DNA polymerase (Fisher Scientific), 0.4 µL of both the respective upstream and downstream primers, 17 µL of DNA stock at 0.031 µg / µL, and 21.9 µL of ddH_2O. Reactions were carried out in a thermocycler using the following settings: 94° C for 2 minutes, followed by 30 cycles of 94° C for 15 seconds, 60° C for 30 seconds, and 72° C for 3 minutes 30 seconds. Samples were then left at 72° C for 5 minutes prior to holding at 10° C at the end of the reaction. Reaction products were purified using the Qiagen "Qiaquick (50)" kit as per manufacturer instructions. The mtDNA (D-loop & CO-2) standards were then serially diluted to form standards from 3,000,000 to 30 copies. Primers used for the reactions are outlined in the protocol from Chan et al., 2012. For Calicin nuclear DNA standards, DNA isolated from SNB-19 control cells was serially 5-fold diluted from 40 ng / µL to 0.064 ng / µL to create the 5 nuclear standards used.

qPCR for Measurement of mtDNA Copy Number and Damage

Changes in mtDNA damage and copy number were measured using a protocol previously published method (Chan et al. 2012). Samples and standards were gently mixed by flicking and centrifuged briefly. PCR mastermixes were prepared for each marker (Calicin, CO-2, and d-loop) using stock solutions of the appropriate forward and reverse primers along with nuclease free water and SYBR Mix. Each reaction volume was set at 20 µL and contained 0.7 µL of the forward and reverse primers, 7.6 µL of nuclease-free water and 10 µL of SYBR mix along with 1 µL of template DNA. The primers used for these reactions are outlined in the protocol from Chan, 2012. The

qPCR reactions were carried out on a Stratagene qPCR instrument using the following settings: 95° C for 30 seconds, followed by 40 cycles of 95° C for 3 seconds and 60° C for 30 seconds. Following completion of the 40 cycles, a dissociation melting curve was created for each sample by heating to 95° C 30 seconds, cooling 55° C for 30 seconds, and finally heating to 95° C for 30 seconds.

Data Analysis

Six-point standard curves from 3e6 copies to 3e1 copies were created for the mtDNA markers (CO-2 & D-loop) using the qPCR standards reactions. This was used to quantify the precise copy number of the mtDNA markers in each of the control and treatment samples. For the nuclear marker (Calicin), a standard curve was constructed using the 5 standard samples ranging from 40 ng / µL to 0.064 ng / µL. Calicin is a single copy nuclear gene, and with this in mind the following equation was used to calculate the approximate number of cells in each standard sample:

$$(Approx.\ Number\ of\ Cells) = \frac{[SampleConcentration] \times (6.022 \times 10^{23})}{(3088286401) \times (660) \times (1 \times 10^{9})} \times \frac{1}{2}$$

Where 6.022 x 10^{23} is Avogadro's constant used to convert to moles, 3,088,286,401 are the number of base pairs in the human genome, 660 g/mol/bp is the average molecular weight of a DNA base pair, 1 x 10^{9} is a conversion factor (g to ng) and 1/2 to account for a diploid genome. The approximate number of cells in each qPCR control or treated sample was then calculated using the Calicin standard curve and normalized to 5 ng/µL using the concentration measured previously by NanoDrop. The percent of damage in each sample for both mtDNA markers (CO-2 & D-loop) was determined as outlined by Chen and Chan (Number of Copies in Unheated Sample / Number of Copies in related

Pre-heated sample) (Chan and Chen 2009). Statistical analysis was performed by ANOVA with Dunnett's post-hoc tests using the R statistical computing software and the library "DescTools" (R Core Team, 2014; Signorell, 2019).

Annexin-V / Propidium Iodide Flow Cytometry

Apoptosis was assessed using a commercially available Annexin-V / Propidium Iodide kit according to the manufacturer protocol (BD Biosciences FITC Annexin V Apoptosis Detection Kit I #556547). SNB-19 human glioblastoma cells were cultured at optimal growth conditions. Cells were seeded at a density of 250,000 cells / mL in sterile 6-well polystyrene plates (35mm / well) and let adhere overnight at growth conditions. Medium was removed by aspiration and cells were treated with medium containing either DMSO vehicle or AIMs at the desired concentration and incubated at optimal growth conditions for 24 hours. Following incubation, culture medium from each sample was collected in 15 mL tubes and cells were rinsed with 2 mL PBS prior to adding 2 mL Trypsin-EDTA to each well. Cells were again incubated at growth conditions for 5 minutes to detach adherent cells prior to adding 2 mL of fresh medium. The PBS rinse and medium containing unadhered cells, was combined with the medium contained in the corresponding 15 mL tube. Samples were centrifuged at 3,000 RPM for 5 minutes at 4 C° to pellet the cells. The supernatant from each sample was discarded and pellets were each resuspended in 1 mL PBS prior to transfer to 1.5 mL tubes. Cells were counted using a Beckman Coulter® automated cell counter prior to a second centrifugation at 3,000 RPM for 5 minutes. Sample supernatants were then discarded and cells were resuspended in Binding Buffer at approximately 1 million cells

/ mL. Approximately 200 µL of each sample was transferred to a new 1.5 mL tube and 5 µL of FITC Annexin-V dye was added to each sample prior to incubation for 15 minutes at room temperature. Following incubation, 300 uL of binding buffer was added to each sample before transfer to a 12x75mm culture tube through a 35 µm cell strainer cap. Samples were kept on ice and 1 µL of propidium iodide was added immediately prior to analysis on a Attune NxT flow cytometer. Data analysis was performed using the FlowJo v10.5.2 software. Statistical analysis was performed by ANOVA with Dunnett's post-hoc tests using the R statistical computing software and the library "DescTools" (R Core Team, 2014; Signorell, 2019).

JC-1 Flow Cytometry

Mitochondrial membrane potential (ΔΨm) was analyzed using a commercially available JC-1 assay kit according to the manufacturer protocol (Thermo Fisher MitoProbe™ JC-1 Assay Kit for Flow Cytometry #M34152). SNB-19 human glioblastoma cells were cultured at optimal growth conditions. Cells were seeded at a density of 250,000 cells / mL in sterile 6-well polystyrene plates (35mm / well) and let adhere overnight at growth conditions. Medium was removed by aspiration and cells were treated with medium containing either DMSO vehicle or AIMs at the desired concentration and incubated at 37 C° in 5% CO_2 for 24 hours. Following incubation, culture medium from each sample was collected in 15 mL tubes and cells were rinsed with 2 mL PBS prior to adding 2 mL Trypsin-EDTA to each well. Cells were again incubated at 37 C° in 5% CO_2 for 5 minutes to detach adherent cells prior to adding 2 mL of fresh medium. The PBS rinse and medium containing unadhered cells, was

combined with the medium contained in the corresponding 15 mL tube. Samples were centrifuged at 3,000 RPM for 5 minutes at 4 C° to pellet the cells. The supernatant from each sample was discarded and pellets were each resuspended in 1 mL PBS prior to transfer to 1.5 mL tubes. Cells were counted using a Beckman Coulter® automated cell counter prior to a second centrifugation at 3,000 RPM for 5 minutes. Sample supernatants were then discarded and cells were resuspended in 1 mL PBS at approximately 1 million cells / mL and allowed to equilibrate to room temperature. To each sample, 10 µL of JC-1 dye was added prior to incubation for 30 minutes at 37 C° in 5% CO_2. Following incubation, cells were pelleted by centrifugation at 3,000 RPM for 5 minutes at 4 C°. Sample pellets were resuspended in 500 µL of PBS before transfer to a 12x75mm culture tube through a 35 µm cell strainer cap. Samples were kept on ice until analysis on a Attune NxT flow cytometer. Data analysis was performed using the FlowJo v10.5.2 software. Statistical analysis was performed by ANOVA with Dunnett's post-hoc tests using the R statistical computing software and the library "DescTools" (R Core Team, 2014; Signorell, 2019).

Caspase-9 Flow Cytometry

Caspase-9 activity was determined using a commercially available kit according to the manufacturer protocol (SR-FLICA® Caspase-9 Assay Kit (#961)). SNB-19 human glioblastoma cells were cultured at optimal growth conditions. Cells were seeded at a density of 250,000 cells / mL in sterile 6-well polystyrene plates (35mm / well) and let adhere overnight at growth conditions. Medium was removed by aspiration and cells were treated with medium containing either DMSO vehicle or AIMs at the

desired concentration and incubated at 37 C° in 5% CO_2 for 24 hours. Following incubation, culture medium from each sample was collected in 15 mL tubes and cells were rinsed with 2 mL PBS prior to adding 2 mL Trypsin-EDTA to each well. Cells were again incubated at 37 C° in 5% CO_2 for 5 minutes to detach adherent cells prior to adding 2 mL of fresh medium. The PBS rinse and medium containing unadhered cells, was combined with the medium contained in the corresponding 15 mL tube. Samples were centrifuged at 3,000 RPM for 5 minutes at 4 C° to pellet the cells. The supernatant from each sample was discarded and pellets were each resuspended in 1 mL PBS prior to transfer to 1.5 mL tubes. Cells were counted using a Beckman Coulter® automated cell counter prior to a second centrifugation at 3,000 RPM for 5 minutes. Samples were resuspended in 500 µL of medium and 16.7 µL of the SR-FLICA reagent was added (1:30) prior to incubation for 1 hour at 37 C° in 5% CO_2 with brief mixing every 10 minutes. Samples were then centrifuged at 3,000 RPM for 5 minutes and, after removal of the supernatant, pellets were resuspended in 500 µL apoptosis wash buffer and incubated at 37 C° in 5% CO_2 for 10 minutes to allow unbound SR-FLICA reagent to diffuse out of the cells. The wash step was repeated two additional times prior to resuspension in 500 µL of fresh apoptosis wash buffer and transfer to a 12x75mm culture tube through a 35 µm cell strainer cap. Samples were kept on ice and immediately analyzed on a Attune NxT flow cytometer. Data analysis was performed using the FlowJo v10.5.2 software. Statistical analysis was performed by ANOVA with Dunnett's post-hoc tests using the R statistical computing software and the library "DescTools" (R Core Team, 2014; Signorell, 2019).

Caspase-3/7 Flow Cytometry

Caspase-3/7 activity was determined using a commercially available kit according to the manufacturer protocol (SR-FLICA® Caspase-3/7 Assay Kit (#931)). SNB-19 human glioblastoma cells were cultured at optimal growth conditions. Cells were seeded at a density of 250,000 cells / mL in sterile 6-well polystyrene plates (35mm / well) and let adhere overnight at growth conditions. Medium was removed by aspiration and cells were treated with medium containing either DMSO vehicle or AIMs at the desired concentration and incubated at 37 C° in 5% CO_2 for 24 hours. Following incubation, culture medium from each sample was collected in 15 mL tubes and cells were rinsed with 2 mL PBS prior to adding 2 mL Trypsin-EDTA to each well. Cells were again incubated at 37 C° in 5% CO_2 for 5 minutes to detach adherent cells prior to adding 2 mL of fresh medium. The PBS rinse and medium containing unadhered cells, was combined with the medium contained in the corresponding 15 mL tube. Samples were centrifuged at 3,000 RPM for 5 minutes at 4 C° to pellet the cells. The supernatant from each sample was discarded and pellets were each resuspended in 1 mL PBS prior to transfer to 1.5 mL tubes. Cells were counted using a Beckman Coulter® automated cell counter prior to a second centrifugation at 3,000 RPM for 5 minutes. Samples were resuspended in 500 µL of medium and 16.7 µL of the SR-FLICA reagent was added (1:30) prior to incubation for 1 hour at 37 C° in 5% CO_2 with brief mixing every 10 minutes. Samples were then centrifuged at 3,000 RPM for 5 minutes and, after removal of the supernatant, pellets were resuspended in 500 µL apoptosis wash buffer and incubated at 37 C° in 5% CO_2 for 10 minutes to allow unbound SR-FLICA reagent to diffuse out of the cells. The wash step was repeated two

additional times prior to resuspension in 500 µL of fresh apoptosis wash buffer and transfer to a 12x75mm culture tube through a 35 µm cell strainer cap. Samples were kept on ice and immediately analyzed on a Attune NxT flow cytometer. Data analysis was performed using the FlowJo v10.5.2 software. Statistical analysis was performed by ANOVA with Dunnett's post-hoc tests using the R statistical computing software and the library "DescTools" (R Core Team, 2014; Signorell, 2019).

Results

AIMs Reduce Cell Viability in Tumor Cells

MTT Cell Viability Assay

We utilized an MTT assay to determine the effect of the 10-Phenyl and 10-Biphenoxy AIMs on cell viability. The 10-Phenyl and the 10-Biphenoxy AIMs both demonstrated sub-micromolar toxicity in the SNB-19 human glioblastoma cells (**Table 3.7**). The 10-Biphenoxy AIM was the most effective at inhibiting the growth of SNB-19 cells, with a calculated IC_{50} of 0.68 ± 0.04 μM (**Figure 3.2**). The 10-Phenyl AIM showed similar toxicity of 0.89 ± 0.02 μM in the cells.

Table 3.7 Cell viability results from MTT assay

SNB-19 **(Human Glioblastoma)**		
Compound	IC_{50} (μM)	95% CI (±)
10-Phenyl AIM	0.89*	0.02*
10-Biphenoxy AIM	0.68	0.04

*Previously published in BMCL, error for these values is ±Standard Deviation (Weaver et al. 2015)

AIMs cause loss of cell viability in SNB-19 human glioblastoma cells at sub-micromolar concentrations following 24-hour treatment. Results shown are the average of three MTT experiments each. IC_{50} is defined as the concentration required to inhibit the growth of 50% of the cells.

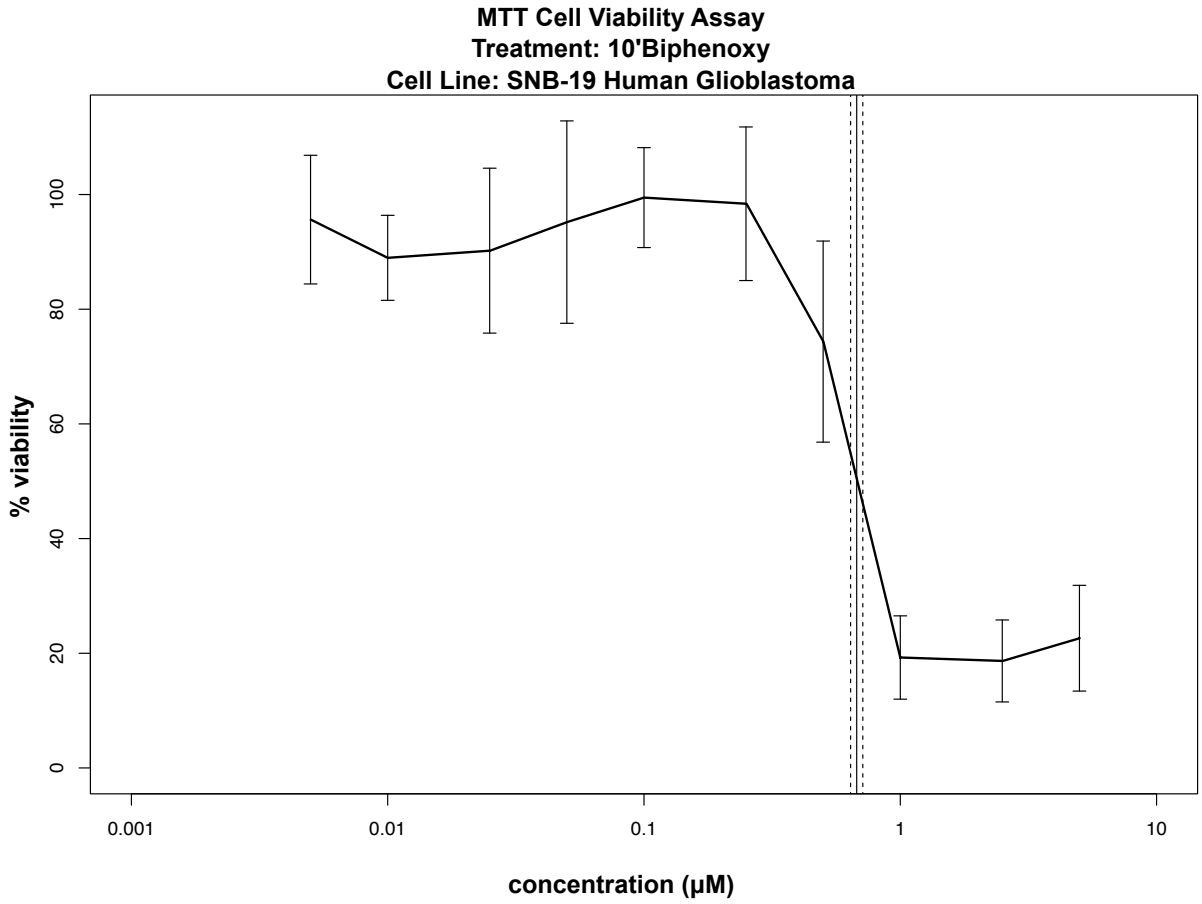

Figure 3.2 Example dose-response curve for MTT assay in SNB-19 cells

Example of SNB-19 dose-response curve generated using the MTT cell viability assay as described. Error bars represent standard deviations, IC_{50} shown as a vertical black line with dotted lines representing the respective 95% confidence interval.

LDH Cell Viability Assay

As a separate measure of cell viability not dependent on mitochondrial reductase function, we employed an LDH assay to measure the effect of the AIMs in multiple cell types (SNB-19, C6, and E-18). The AIMs demonstrated low-micromolar toxicity in all of the cells tested (**Table 3.8**). The 10-Biphenoxy remained the most potent compound tested in the SNB-19 human glioblastoma cells with an IC_{50} of 4.44±0.16 μM (**Figure 3.3**). The 10-Biphenoxy and 10-Phenyl had comparable activity in the C6 rat glioma cells (C6 IC_{50} = 3.83±0.10 μM and 3.76±0.12 μM, respectively) (**Figure 3.4**). Surprisingly, the 10-Biphenoxy and 10-Phenyl AIMs showed more toxicity toward the primary E-18 healthy rat astrocytes than the C6 rat glioma cells (E-18 IC_{50} = 2.09±0.20 μM and 2.20±0.16 μM, respectively) (**Figure 3.5**).

Table 3.8 Cell viability results from LDH assay

SNB-19 (Human Glioblastoma)			**C6 (Rat Glioma)**		**E-18 (Primary Rat Astrocytes)**	
Compound	IC_{50} (μM)	95% CI (±)	IC_{50} (μM)	95% CI (±)	IC_{50} (μM)	95% CI (±)
10-Phenyl AIM	5.92	0.68	3.76	0.12	2.20	0.16
10-Biphenoxy AIM	4.44	0.16	3.83	0.10	2.09	0.20

AIMs reduce cell viability in SNB-19 human glioblastoma cells at low-micromolar concentrations following 24-hour treatment. Results shown are the average of three LDH experiments each. IC_{50} is defined as the concentration required to inhibit the growth of 50% of the cells.

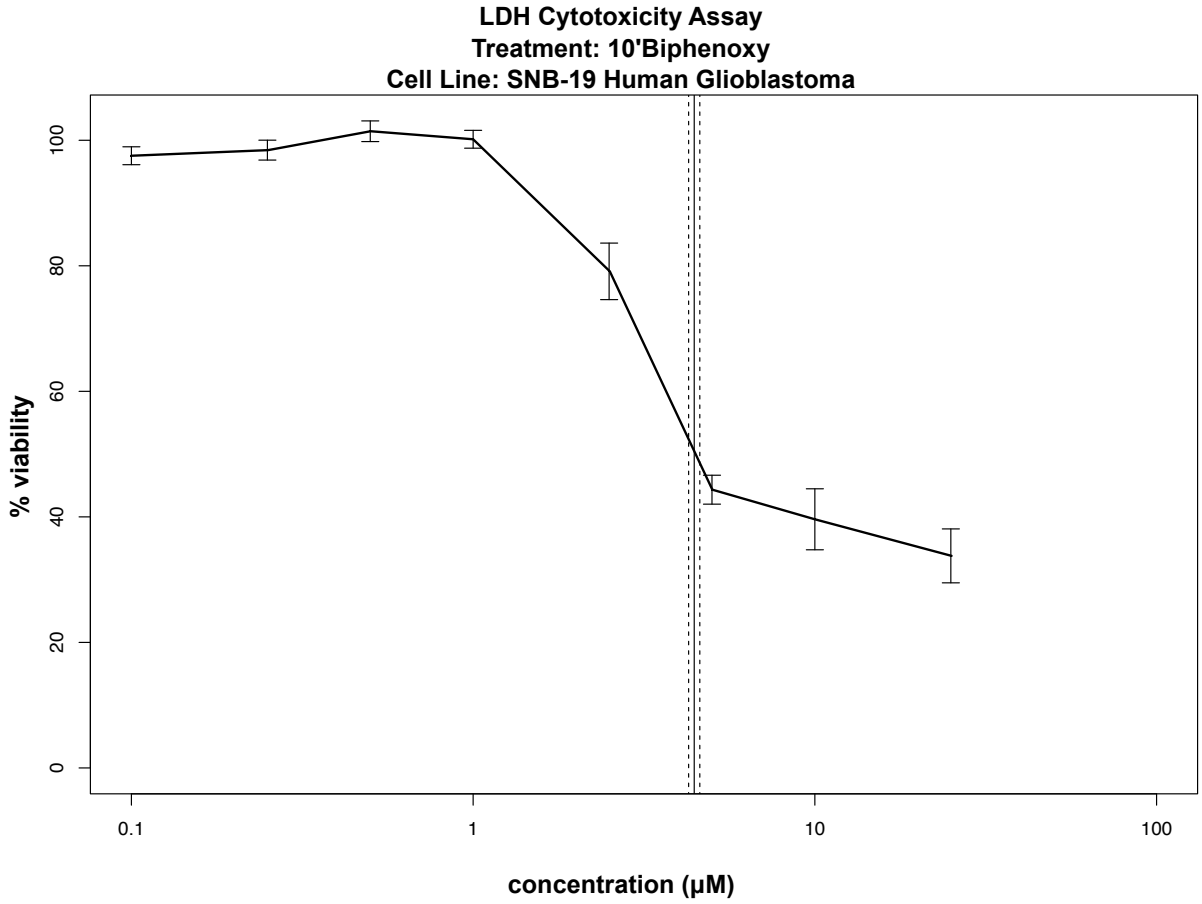

Figure 3.3 Example dose-response curve for LDH assay in SNB-19 cells

Example of SNB-19 dose-response curve generated using the LDH cytotoxicity assay as described. Error bars represent standard deviations, IC_{50} shown as a vertical black line with dotted lines representing the respective 95% confidence interval.

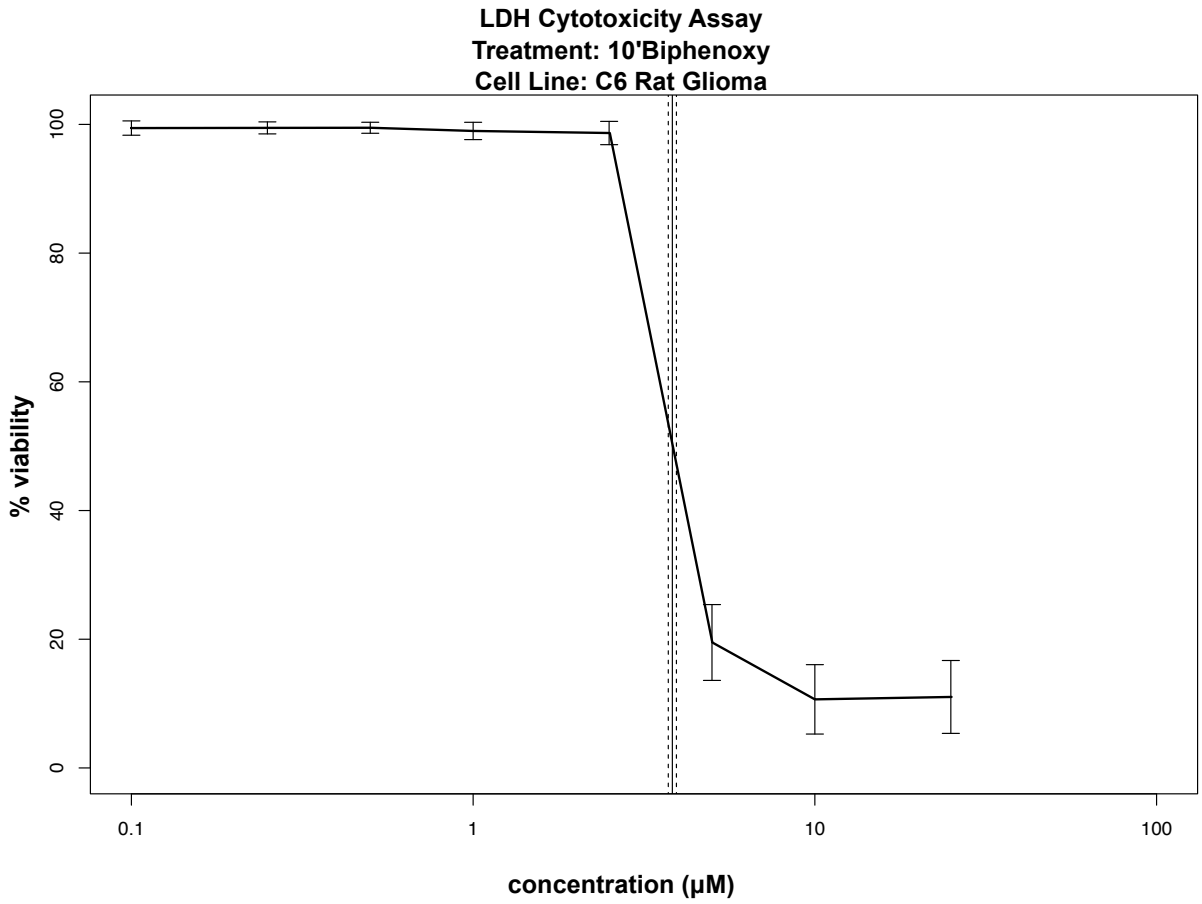

Figure 3.4 Example dose-response curve for LDH assay in C6 cells

Example of C6 dose-response curve generated using the LDH cytotoxicity assay as described. Error bars represent standard deviations, IC_{50} shown as a vertical black line with dotted lines representing the respective 95% confidence interval.

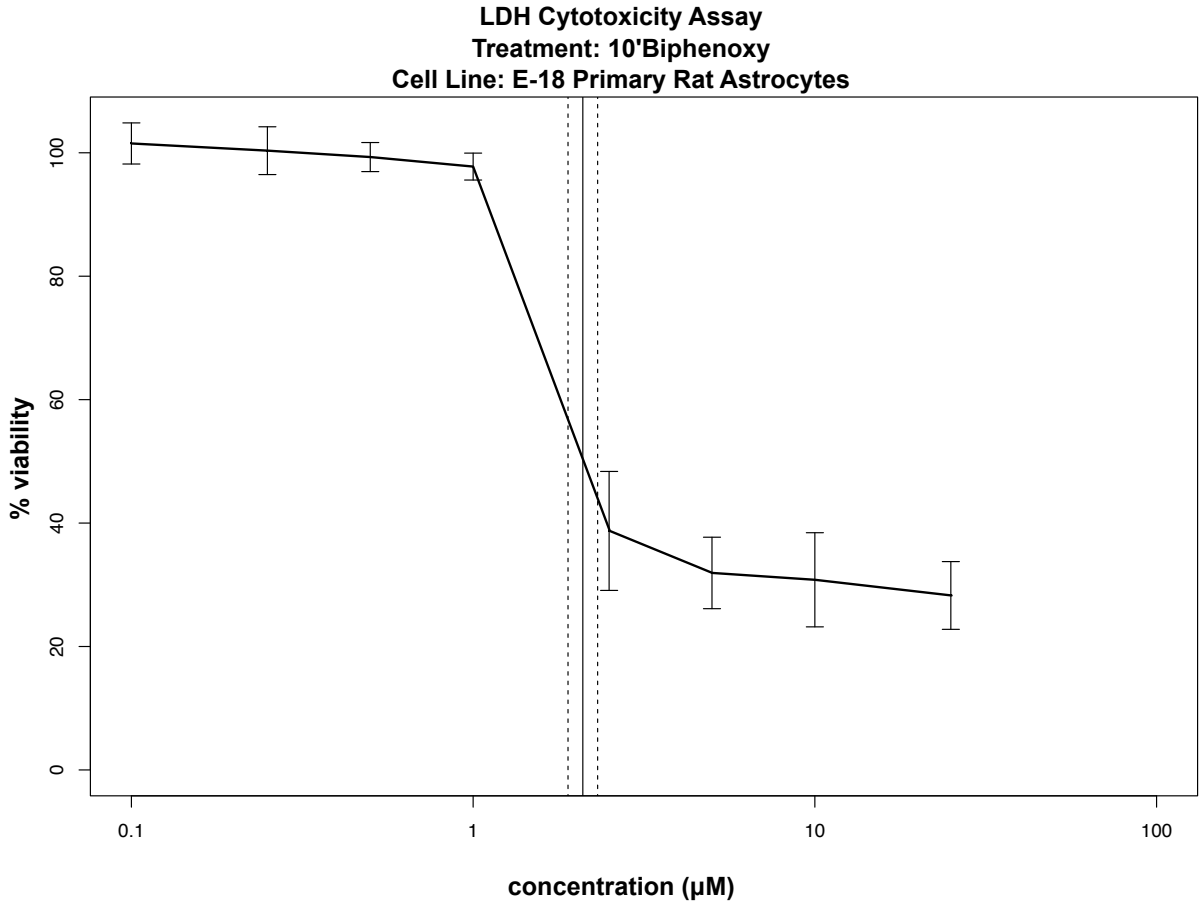

Figure 3.5 Example dose-response curve for LDH assay in E-18 cells

Example of E-18 dose-response curve generated using the LDH cytotoxicity assay as described. Error bars represent standard deviations, IC_{50} shown as a vertical black line with dotted lines representing the respective 95% confidence interval.

AIMs Localize to the Mitochondria of Glioblastoma Cells

Confocal Imaging

We performed confocal imaging of SNB-19 glioblastoma cells to examine the intracellular localization of the AIMs. The AIMs are conveniently auto-fluorescent and can be visualized in cells using laser excitation. The MitoTracker™ dye selectively stains the mitochondria of living cells. Treatment with 1 μM of the 10-Phenyl AIM and 100 nM MitoTracker™ demonstrates localization of the AIMs to the mitochondria of glioblastoma cells (**Figure 3.6**). This was also shown for the 10-Biphenoxy AIM under the same conditions (**Figure 3.7**). Confocal Z-stacks further verified the mitochondrial localization of the AIMs in the glioblastoma cells (**Figure 3.8** and **Figure 3.9**). However, it is noted that it appears the AIMs may also be present in other organelles or vesicles as well. Taken together, these results confirm both the 10-Phenyl and 10-Biphenoxy AIMs can localize to the mitochondria of glioblastoma cells.

10-Phenyl AIM Mitotracker Overlay

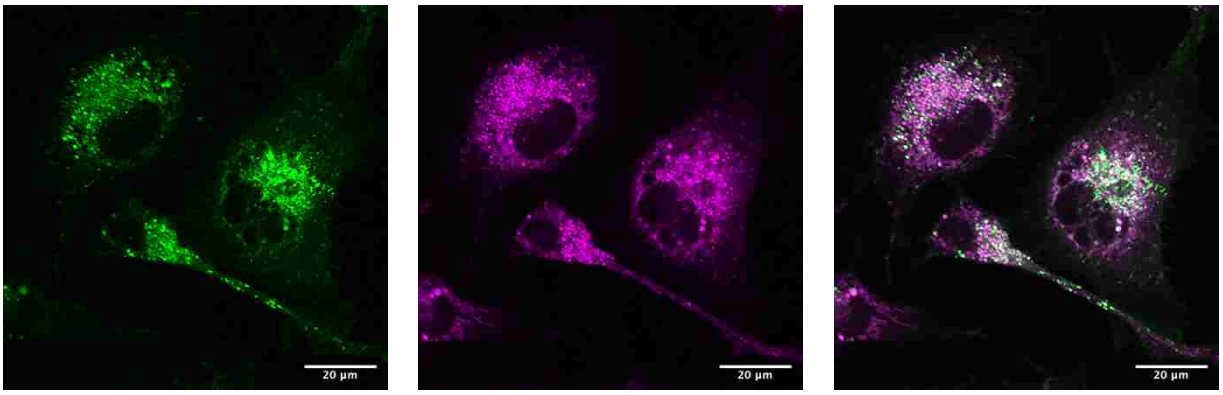

Figure 3.6 Confocal images of SNB-19 cells with 10-Phenyl AIM

Confocal images of SNB-19 human glioblastoma cells treated with 1 µM of the 10-Phenyl AIM (green, left), 100 nM Mitotracker (magenta, middle), and overlay (white, right). Scale bar shown is 20 µM.

10-Biphenoxy AIM Mitotracker Overlay

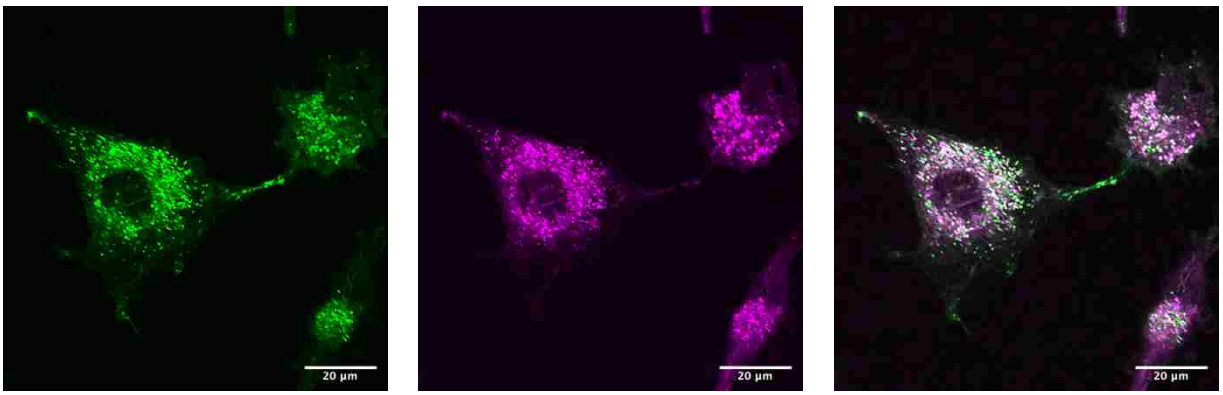

Figure 3.7 Confocal images of SNB-19 cells with 10-Biphenoxy AIM

Confocal images of SNB-19 human glioblastoma cells treated with 1 µM of the 10-Biphenoxy AIM (green, left), 100 nM Mitotracker (magenta, middle), and overlay (white, right). Scale bar shown is 20 µM.

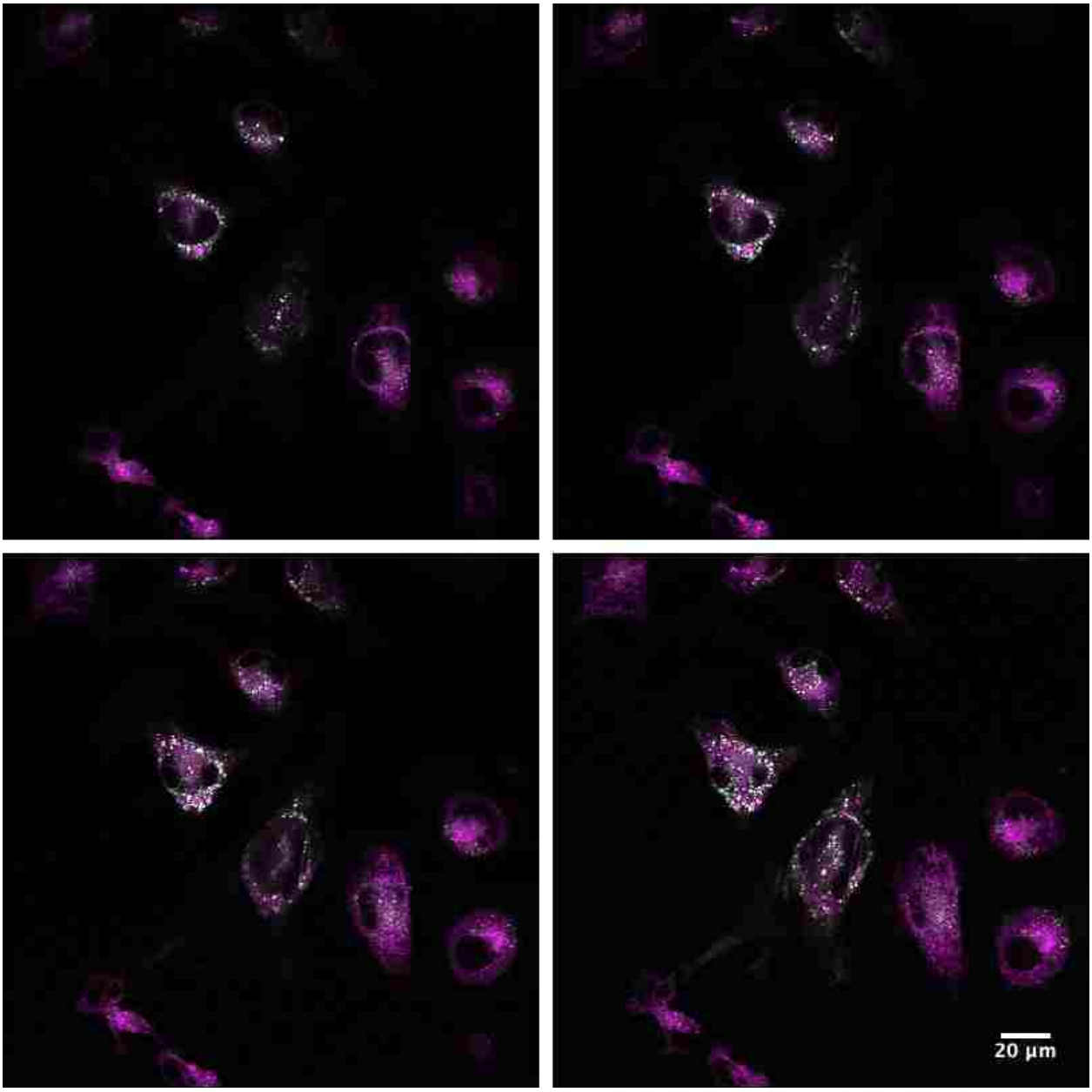

Figure 3.8 Confocal Z-stack images of SNB-19 cells with 10-Phenyl AIM

Confocal Z-stack images of SNB-19 human glioblastoma cells treated with 500 nM of the 10-Phenyl AIM and 100 nM Mitotracker with co-localization observed as white. Scale bar shown is 20 µM. Images shown represent 4 µm of total depth and each individual image is separated by 1 µm depth.

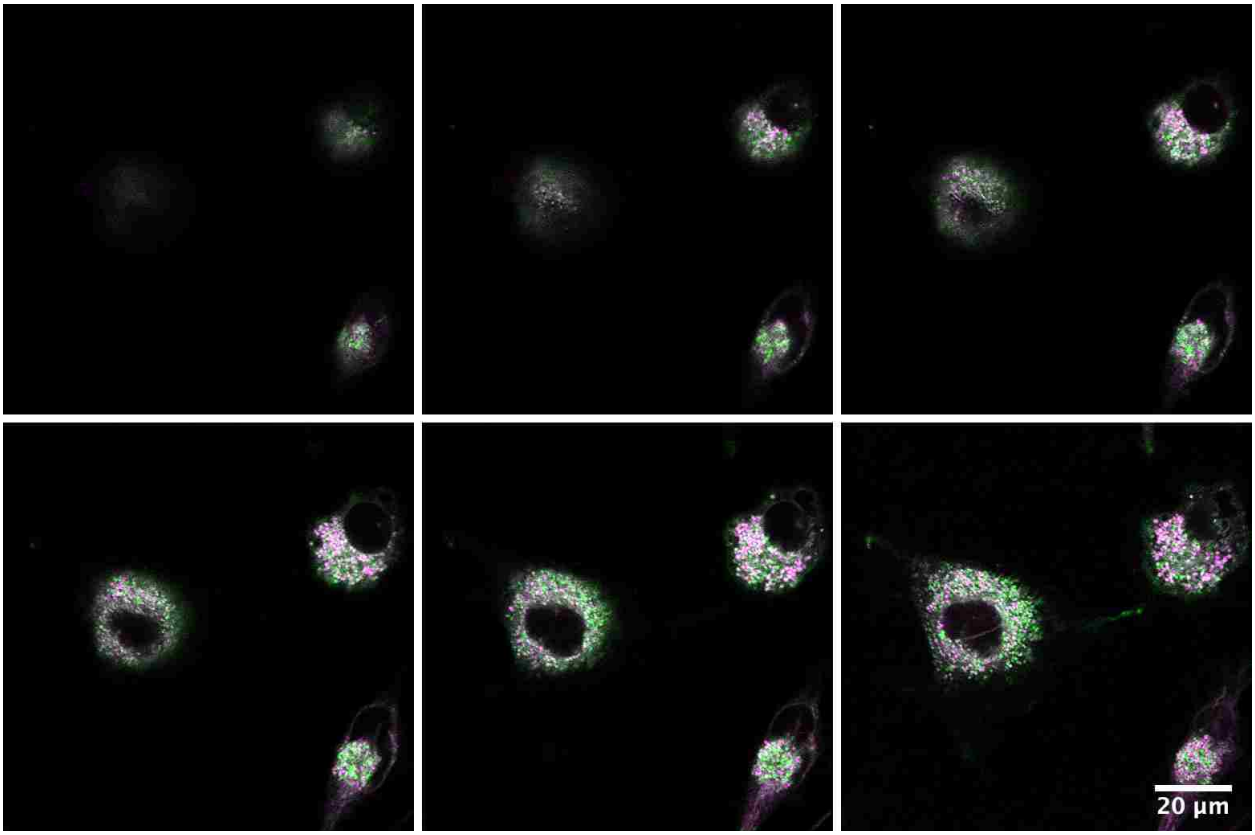

Figure 3.9 Confocal Z-stack images of SNB-19 cells with 10-Biphenoxy AIM

Confocal Z-stack images of SNB-19 human glioblastoma cells treated with 500 nM of the 10-Biphenoxy AIM and 100 nM Mitotracker with co-localization observed as white. Scale bar shown is 20 µM. Images shown represent 9 µm of total depth and each individual image is separated by 1.5 µm depth.

AIMs Inhibit Mitochondria ETC Complexes

We measured the inhibitory effect of the AIMs on Complex I – IV of the ETC using commercially available kits (**Table 3.9**). The AIMs were measured using the antibody isolated ETC complexes for Complex I, II, and IV. For Complex II + III, the assay utilized intact mitochondria, but cannot distinguish between the two ETC protein complexes.

The AIM compounds tested do not appear to be significant inhibitors of Complex I. However, both the 10-Phenyl and 10-Biphenoxy showed significant inhibition in the Complex II assay (IC_{50} = 18.3 ± 10.7 μM and 2.9 ± 1.2 μM, respectively) (**Figure 3.10** and **Figure 3.11**). The Complex II + III assay in intact mitochondria showed inhibition of 25.63 ± 3.78 μM for the 10-Phenyl AIM and 8.67 ± 0.68 for the 10-Biphenoxy AIM (**Figure 3.12** and **Figure 3.13**).

There was also some inhibition observed for Complex IV for the 10-Biphenoxy AIM with a calculated IC_{50} of 26.89 ± 2.87 μM, however even at 90 μM the 10-Phenyl did not reach 50% inhibition (**Appendix Figure A.3.10** and **Figure A.3.11**).

Table 3.9 Summary of ETC protein complex assay results

IC_{50} (μM ± 95%CI)	**10-Phenyl AIM**	**10-Biphenoxy AIM**	**Rotenone**	**Antimycin A**
Complex I	> 90	> 90	0.121 ± 0.031	
Complex II	18.27 ± 10.72	2.91 ± 1.21		
Complex II + III*	25.63 ± 3.78	8.67 ± 0.68		0.059 ± 0.008
Complex IV	> 90	26.89 ± 2.87		
*Intact Bovine Heart Mitochondria				

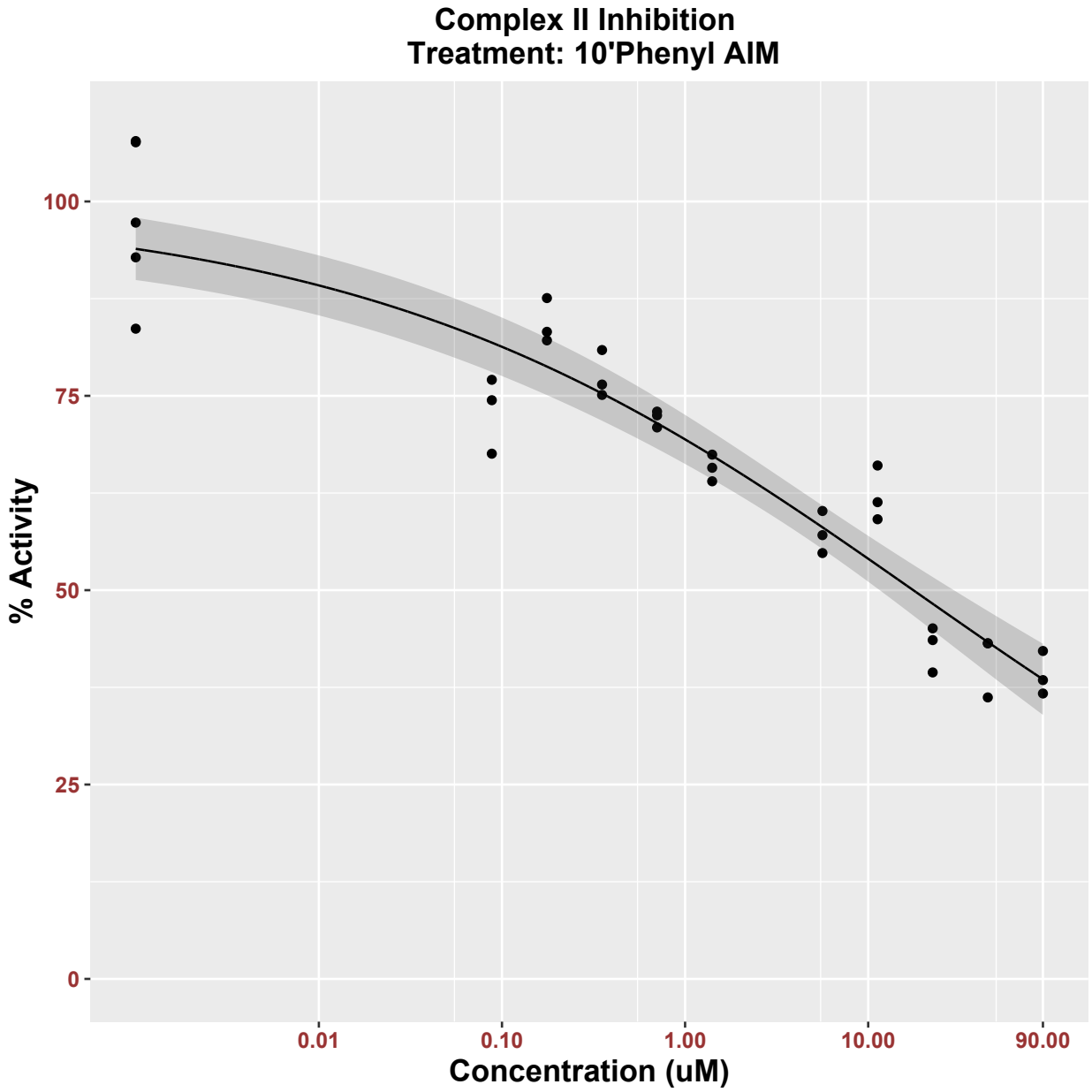

Figure 3.10 Complex II inhibition curve for the 10-Phenyl AIM

Complex II inhibition curve for the 10-Phenyl AIM. Points represent individual measurements, curve represents three-parameter logistic fit with shaded area indicating the 95% confidence interval of the fit. (n=3)

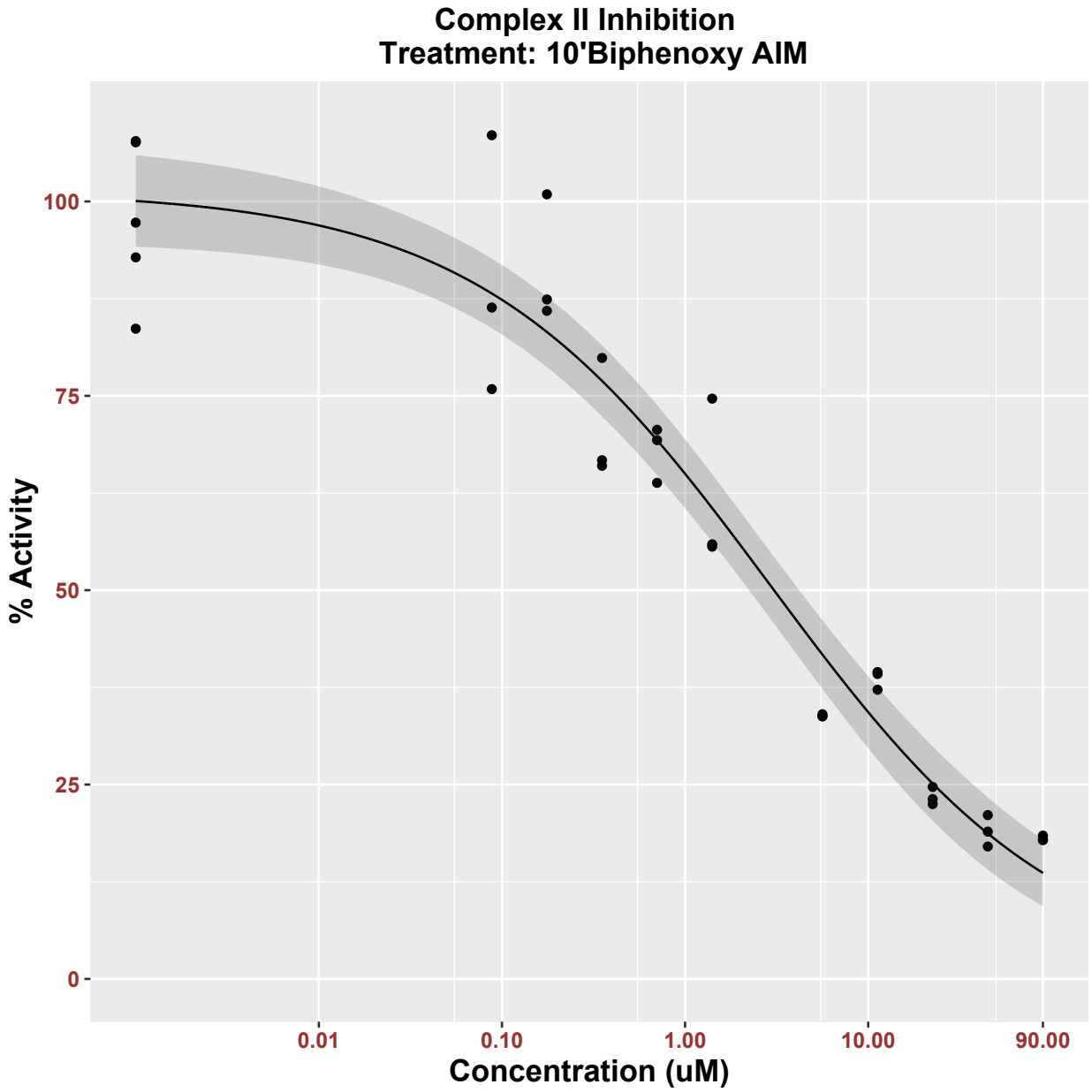

Figure 3.11 Complex II inhibition curve for the 10-Biphenoxy AIM

Complex II inhibition curve for the 10-Biphenoxy AIM. Points represent individual measurements, curve represents three-parameter logistic fit with shaded area indicating the 95% confidence interval of the fit. (n=3)

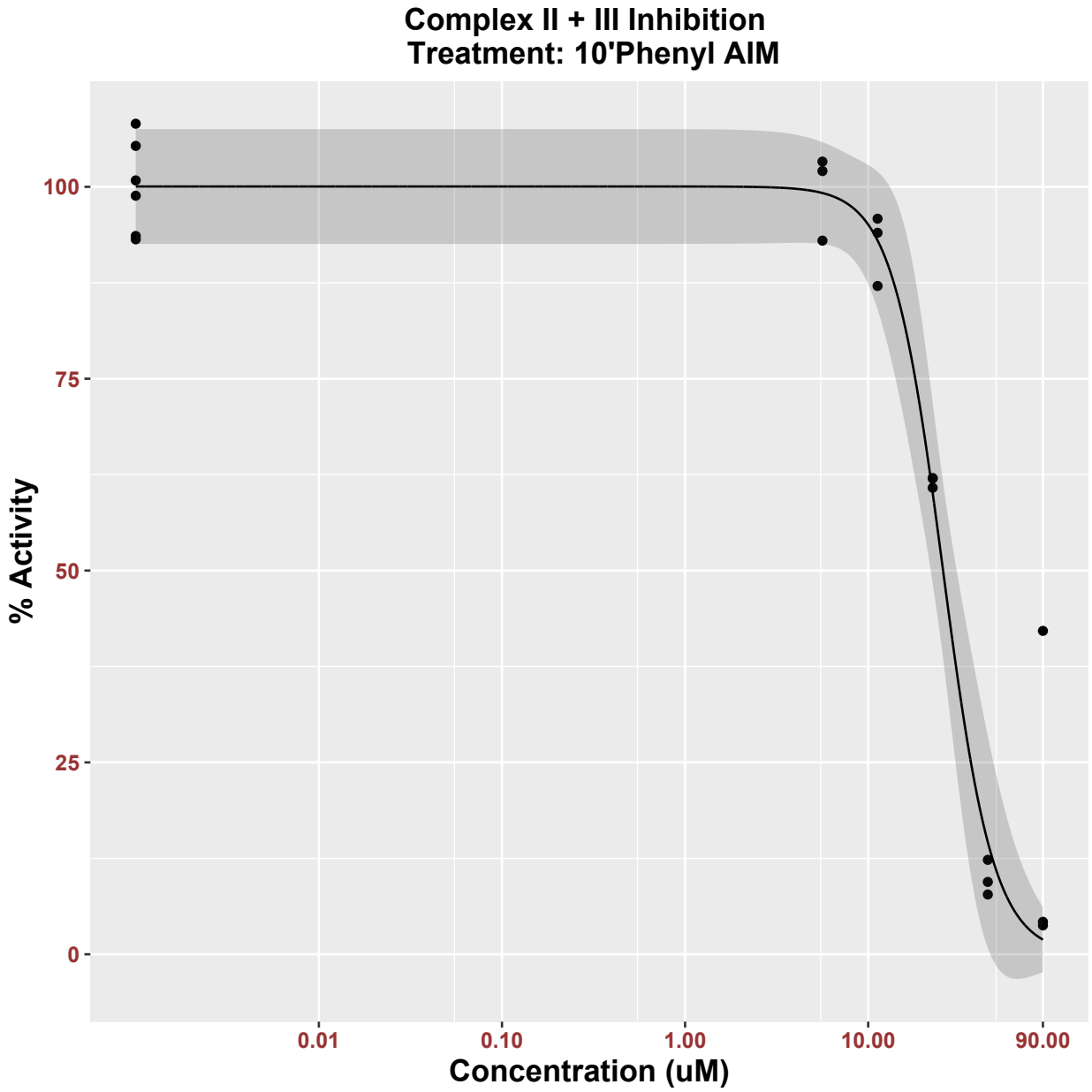

Figure 3.12 Complex II + III inhibition curve for the 10-Phenyl AIM

Complex II + III inhibition curve for the 10-Phenyl AIM in intact mitochondria. Points represent individual measurements, curve represents three-parameter logistic fit with shaded area indicating the 95% confidence interval of the fit. (n=3)

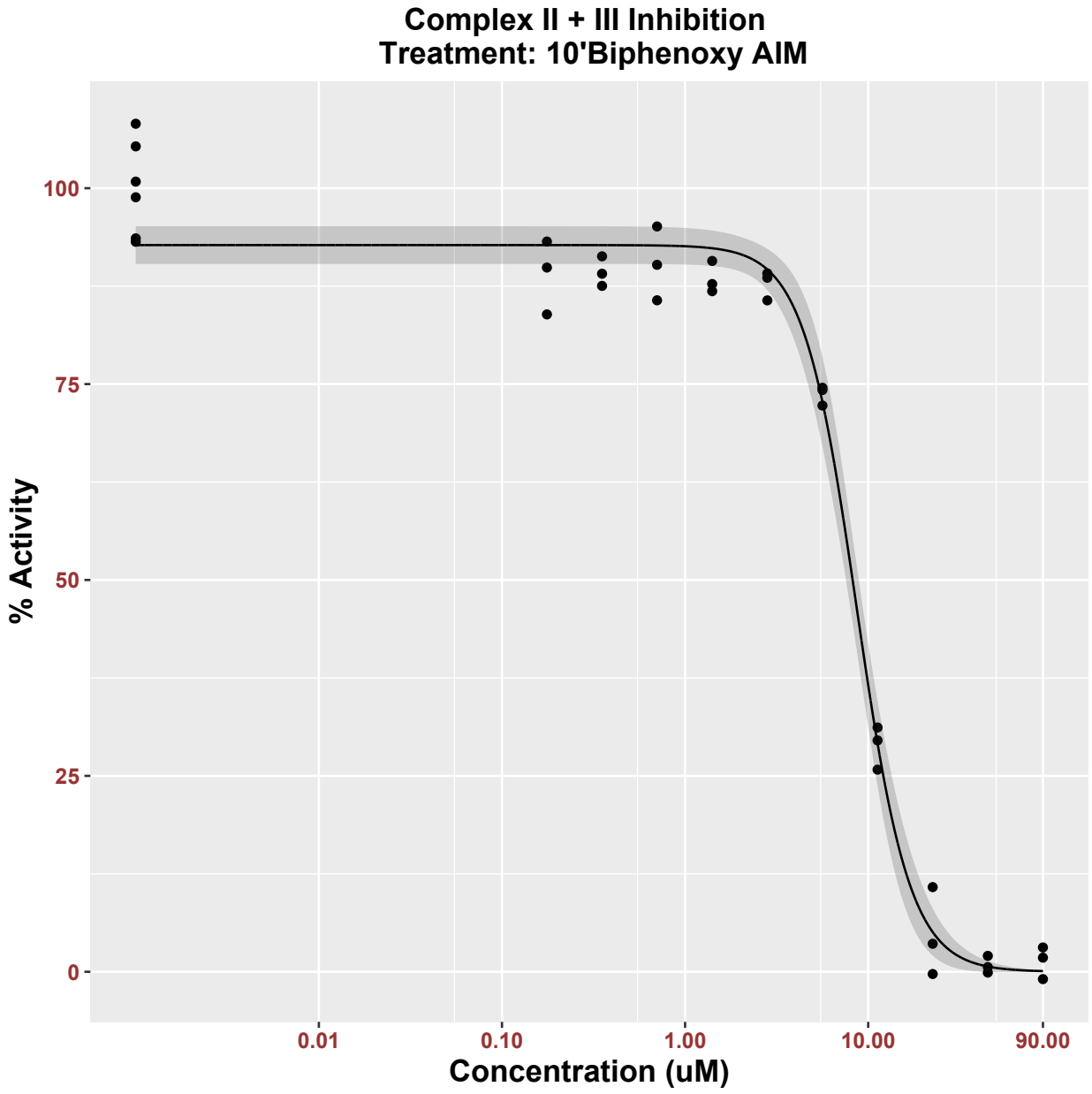

Figure 3.13 Complex II + III inhibition curve for the 10-Biphenoxy AIM

Complex II + III inhibition curve for the 10-Biphenoxy AIM in intact mitochondria. Points represent individual measurements, curve represents three-parameter logistic fit with shaded area indicating the 95% confidence interval of the fit. (n=3)

Computational Modeling

The authors would like to acknowledge Michael J. Campbell of the Natale Laboratory, and the Molecular Computational Core Facility (MCCF) at the University of Montana for their contributions to these experiments.

To further examine the interaction of the AIMs with Complex II, we performed molecular docking studies at the ubiquinone sites of a crystal structure of the protein complex (PDB: 1ZOY) (Sun et al. 2005). We chose the ubiquinone sites as the succinate site was determined to be too inaccessible for binding by AIMs. First, we verified the known Complex II inhibitor TTFA was docked correctly by GOLD in both ubiquinone sites (Q_p and Q_d) in comparison to a crystal structure of a Complex II / TTFA complex (PDB: 1ZP0) (**Figure 3.14**). Next, we performed molecular docking calculations for both the 10-Phenyl and 10-Biphenoxy AIMs and evaluated the top 10 docking poses determined by their CHEMPLP fitness scores (**Table 3.10** and **Table 3.11**). The top pose for the 10-Biphenoxy AIM show the biphenyl moiety in the ubiquinone binding pocket of the Q_p site, with the anthracene in proximity to allow for π-π interactions with the Trp-B173 and His-C29 (**Figure 3.15** and **Figure 3.16**). There are also carbon hydrogen bond interactions suggested at Tyr-91 and Val-81 by the alkyl amine tails. Finally, the biphenyl moiety interacts with Trp-B173, Met-C39, Pro-B169 and Ile-C43. The top pose for the 10-Phenyl AIM suggests the smaller phenyl moiety allows for deeper access in the binding pocket for the anthracene portion of the molecule and displays π-π interactions with Pro-B169 and Ile-C43. The phenyl moiety shows π-π interactions with Ile-B218 and Arg-C46, and other parts of the AIM molecule suggest various other potential interactions (**Figure 3.17** and **Figure 3.18**).

Table 3.10 Docking scores for Complex II Q_p site

Complex II Q_p Site GOLD Docking Results			
Solution #	*CHEMPLP Fitness Score*		
	10-Phenyl	*10-Biphenoxy*	*TTFA*
1	82.78	75.21	48.51
2	101.67	51.74	50.37
3	80.76	66.21	49.56
4	88.81	61.43	
5	78.59	78.05	
6	79.22	75.02	
7	92.00	82.75	
8	81.84	80.25	
9	78.14	66.68	
10	83.73	88.45	

Docking scores calculated for TTFA and the 10-Phenyl and 10-Biphenoxy AIMs at the Q_p ubiquinone site of a crystal structure of Complex II (PDB: 1ZOY).

Table 3.11 Docking scores for Complex II Q_d site

Complex II Q_d Site GOLD Docking Results			
Solution #	*CHEMPLP Fitness Score*		
	10-Phenyl	*10-Biphenoxy*	*TTFA*
1	86.54	78.32	44.38
2	79.88	74.56	43.35
3	88.98	80.46	43.91
4	85.29	69.66	44.45
5	84.56	85.98	44.10
6	90.12	71.36	
7	86.37	70.63	
8	86.97	70.82	
9	90.20	78.60	
10	84.65	71.38	

Docking scores calculated for TTFA and the 10-Phenyl and 10-Biphenoxy AIMs at the Q_d ubiquinone site of a crystal structure of Complex II (PDB: 1ZOY).

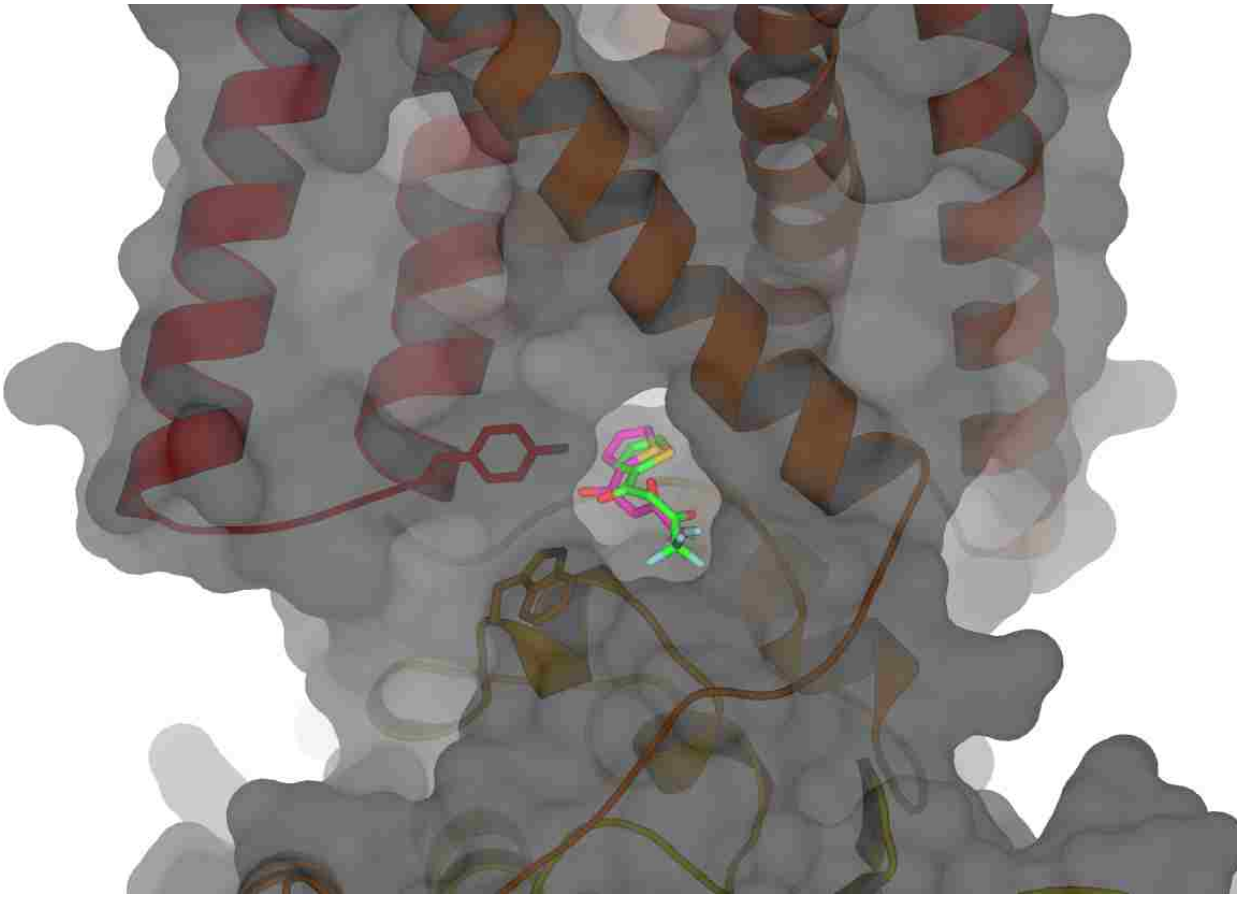

Figure 3.14 Complex II computational docking with TTFA

Overlay of TTFA from a published crystal structure (PDB: 1ZP0, magenta) with the highest scoring TTFA pose from GOLD (green) in the Q_p ubiquinone site of the crystal structure of Complex II (PDB: 1ZOY).

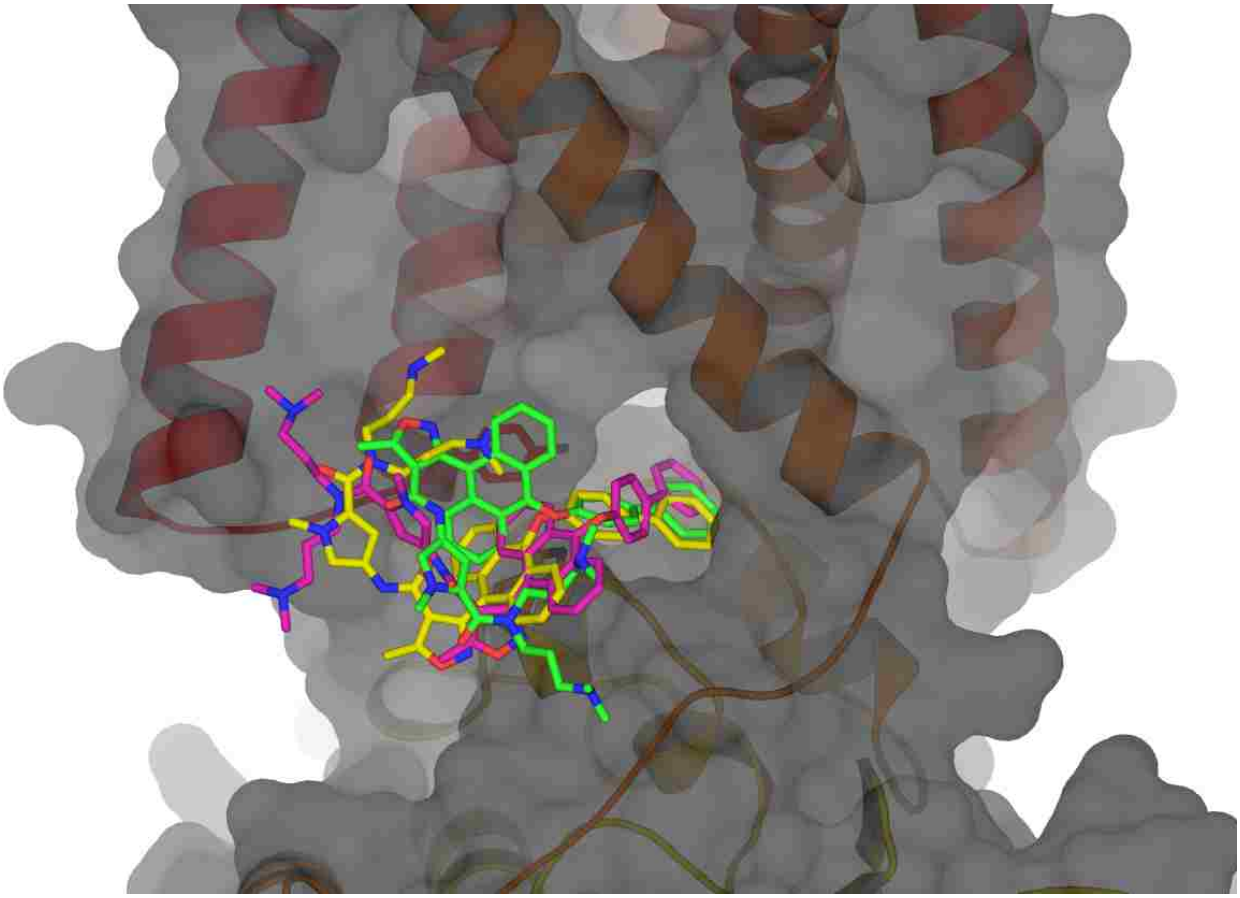

Figure 3.15 Complex II computational docking with 10-Biphenoxy AIM

Overlay of the three top scoring poses for the 10-Biphenoxy AIM from GOLD in the Q_p ubiquinone site. Solutions 5, 7 and 10 shown as green, magenta and yellow, respectively. View is the same orientation as **Figure 3.14**.

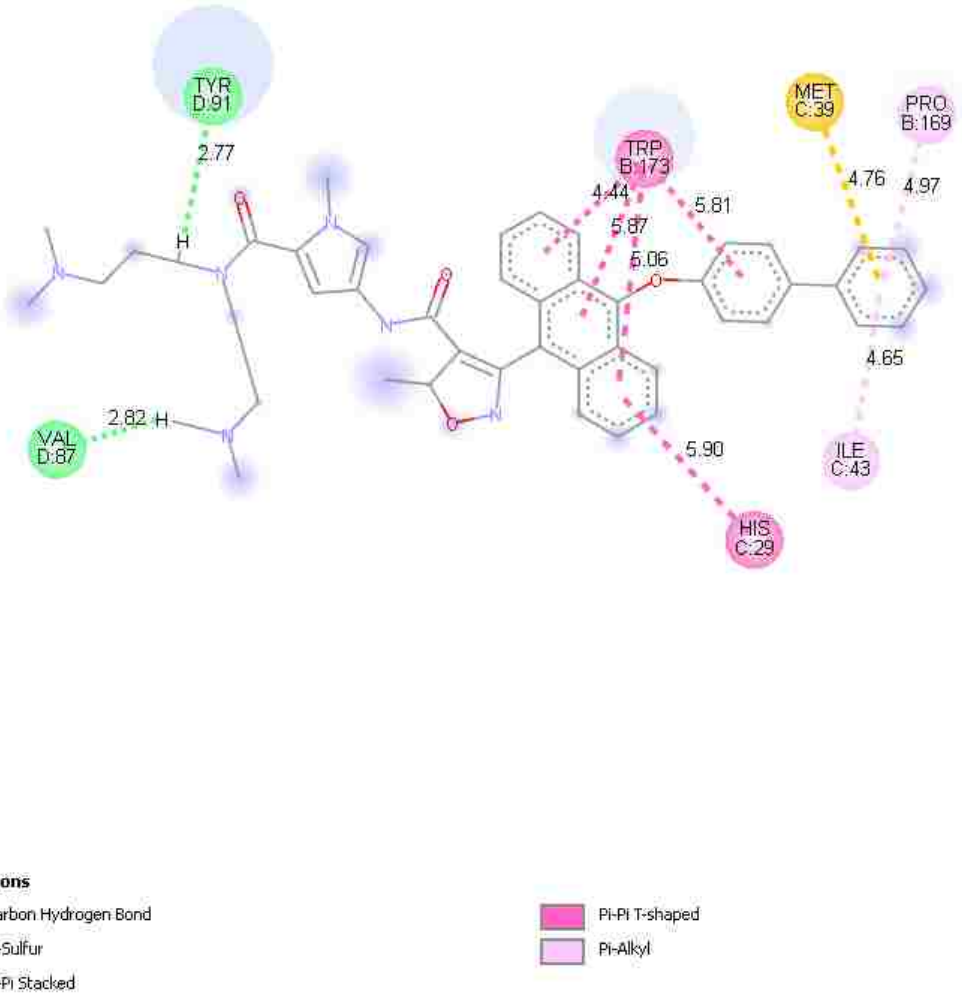

Figure 3.16 Diagram of ligand interactions for 10-Biphenoxy AIM

2D diagram showing ligand interactions for the top scoring pose for the 10-Biphenoxy AIM from GOLD in the Q_p ubiquinone site (Solution #10). Interaction distances are labeled in angstrom units.

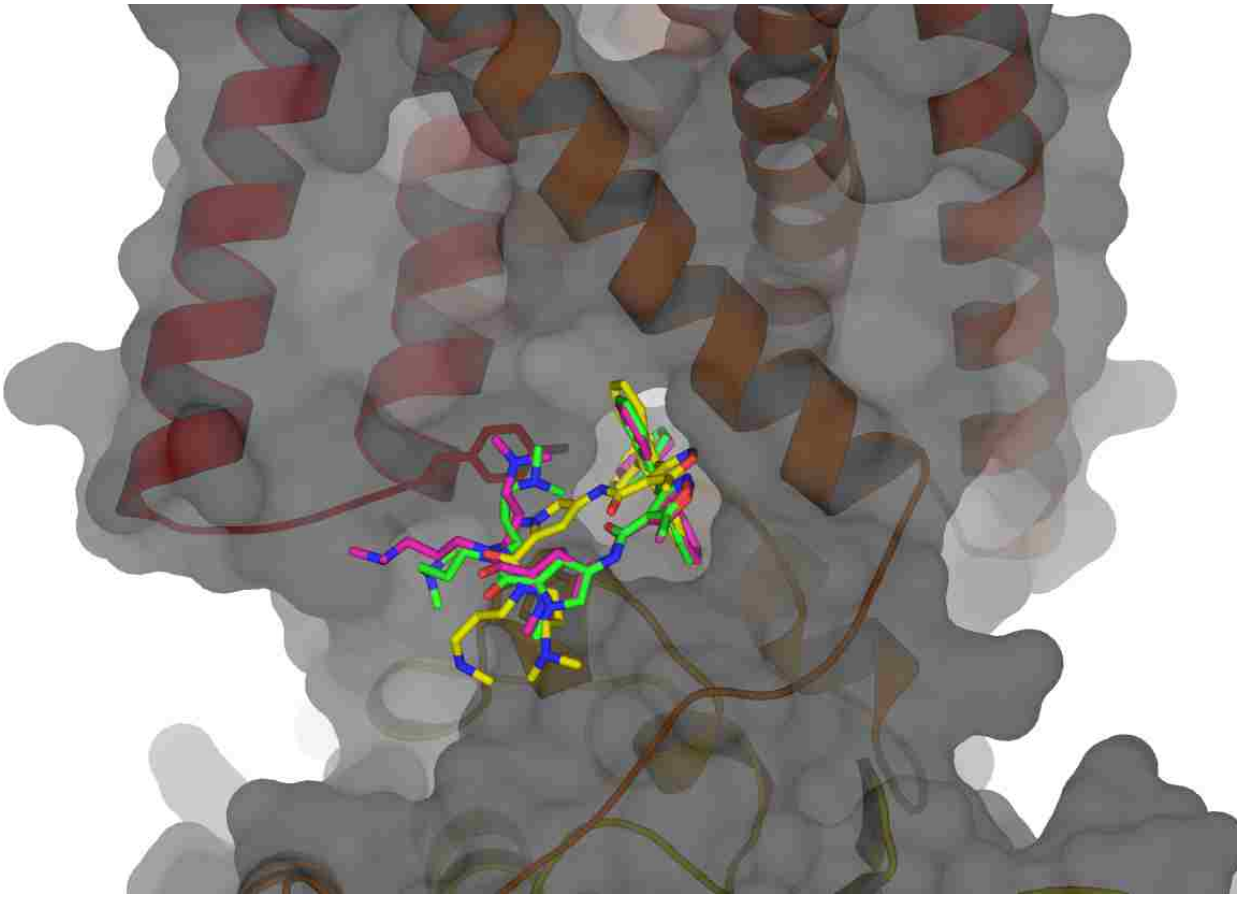

Figure 3.17 Complex II computational docking with 10-Phenyl AIM

Overlay of the three top scoring poses for the 10-Phenyl AIM from GOLD in the Q_p ubiquinone site. Solutions 2, 7 and 10 shown as green, magenta and yellow, respectively. View is the same orientation as **Figure 3.14**.

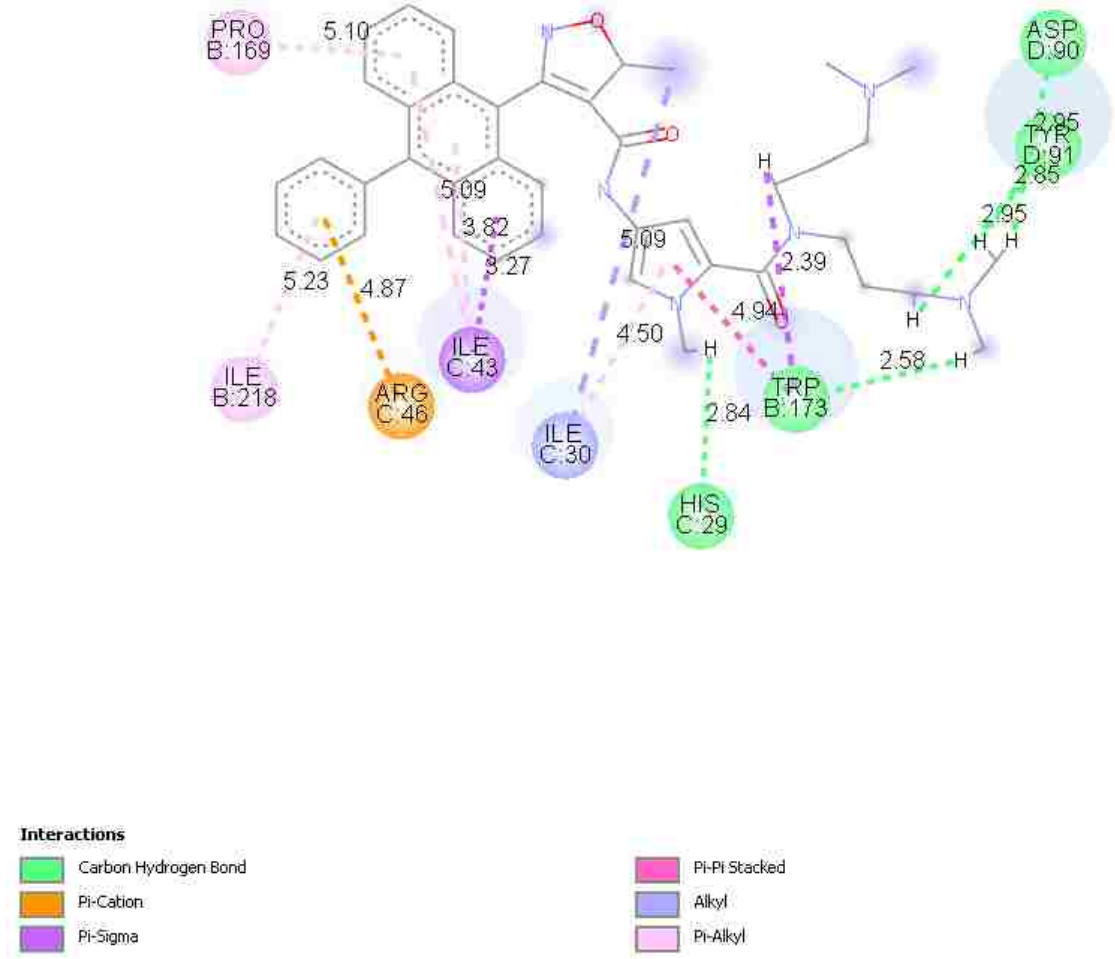

Figure 3.18 Diagram of ligand interactions for 10-Phenyl AIM

2D diagram showing ligand interactions for the top scoring pose for the 10-Phenyl AIM from GOLD in the Q_p ubiquinone site (Solution #2). Interaction distances are labeled in angstrom units.

Treatment with AIMs leads to rapid mtDNA damage and reduced mtDNA copy number in glioblastoma cells

To measure the effect of treatment with the 10-Biphenoxy AIM on mtDNA, we employed a previously reported method to examine changes in mtDNA damage and copy number (Chan and Chen 2009; Chan et al. 2012). A time-course was performed to determine the effect of 10-Biphenoxy AIM treatment at multiple exposure time points (3, 6, 12, and 24 hours). Treatment with 1 μM of the 10-Biphenoxy AIM caused a significant increase in percentage damaged mtDNA the CO-2 gene (**Figure 3.19**). A reduction in the number of intact copies, normalized to a single-copy nuclear gene Calicin, was significant at the 6-hour time-point for both the CO-2 and D-loop mtDNA markers (**Figure 3.20**). Further examination of the intact copy number per cell led us to determine the variance in the 24-hour group was a significant outlier in both markers as calculated by a Cochran's C test in R using the "outliers" package (P = 0.03 and P = 0.002 for D-loop and CO-2 genes, respectively) (R Core Team, 2014, Komsta, 2011). As a result, we excluded the 24-hour group and reanalyzed the time-course experiment data. This allowed us to demonstrate a significant change in the number of intact copies per cell for the CO-2 gene at the 3-, 6-, and 12-hour time-points, and for the D-loop gene at 6- and 12-hours following treatment with the 10-Biphenoxy AIM (**Figure 3.21**).

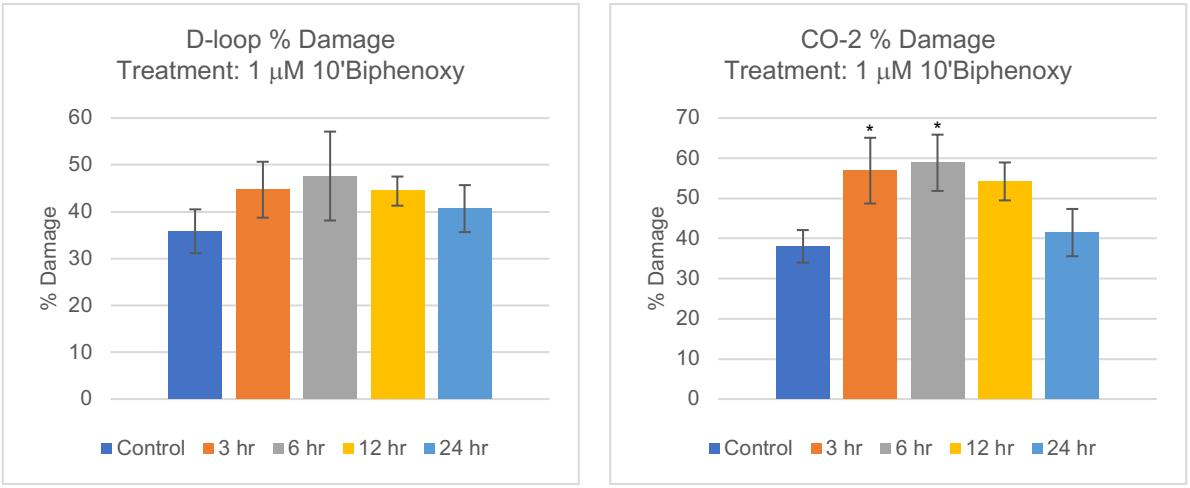

Figure 3.19 mtDNA damage following treatment with 10-Biphenoxy AIM

Treatment with 1 μM 10-Biphenoxy AIM causes a significant increase in the percent damage in CO-2 gene of mtDNA at 3 hours and 6 hours. Error bars represent standard deviation. Dunnett post-hoc test used for comparisons between treatment and control groups. Symbols represent significance levels ($P < 0.05$ *, $P < 0.01$ **, $P < 0.001$ ***) (n=3).

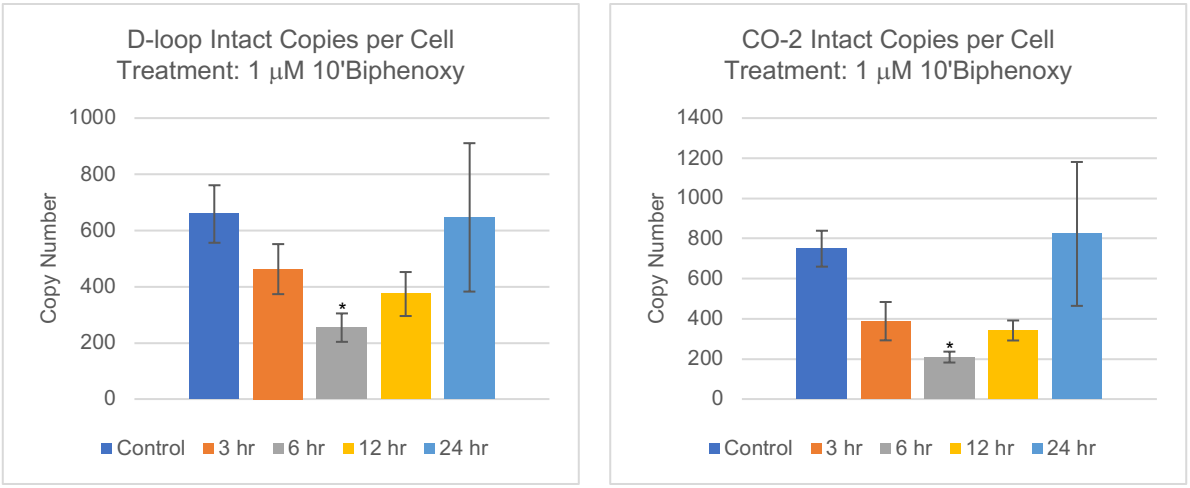

Figure 3.20 Intact copy number of mtDNA following treatment with 10-Biphenoxy AIM Treatment with 1 μM 10-Biphenoxy AIM causes a decrease in the intact copies per cell of two mtDNA markers (CO-2 & D-loop) after 6 hours. Error bars represent standard deviation. Dunnett post-hoc test used for comparisons between treatment and control groups. Symbols represent significance levels ($P < 0.05$ *, $P < 0.01$ **, $P < 0.001$ ***) (n=3).

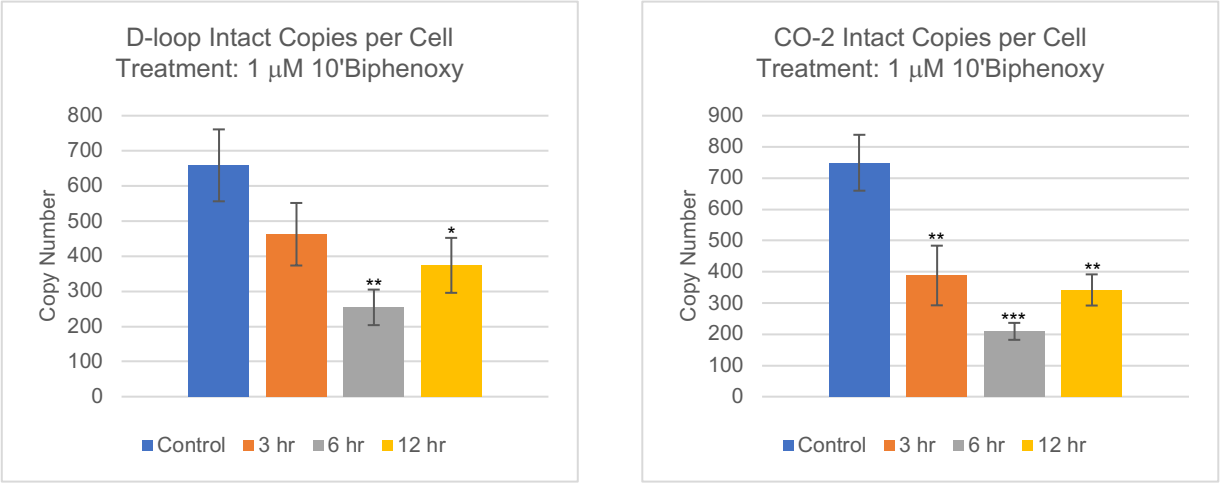

Figure 3.21 Intact copy number of mtDNA following treatment with 10-Biphenoxy AIM Treatment with 1 μM 10-Biphenoxy AIM causes a decrease in the intact copies per cell of two mtDNA markers (CO-2 & D-loop) at multiple time points. Same as previous figure except with 24-hour group excluded from analysis due to significantly higher variance in the group as determined by Cochran's C test ($P = 0.03$ and $P = 0.002$ for D-loop and CO-2 genes, respectively). Error bars represent standard deviation. Dunnett post-hoc test used for comparisons between treatment and control groups. Symbols represent significance levels ($P < 0.05$ *, $P < 0.01$ **, $P < 0.001$ ***) (n=3).

AIMs Induce Apoptosis in Glioblastoma Cells

Apoptosis was measured in SNB-19 human glioblastoma cells following treatment with the AIMs using flow cytometry in conjunction with Annexin-V and propidium iodide staining. The Annexin-V / PI results confirmed induction of apoptosis in SNB-19 glioblastoma cells by the 10-Biphenoxy AIM (**Figure 3.22**). Statistical analysis performed for the 10-Biphenoxy AIM showed a significant decrease in the healthy cell population for the 2.5 μM and 5 μM treatments (**Figure 3.23**). The 5 μM 10-Biphenoxy AIM treated samples showed a significant increase in apoptosis with a mean of 92.8% of the total cell population versus only 3.9% observed in the control samples. There was also a significant decrease observed in the amount of necrosis in the 5 μM treatment versus control samples. These results suggest the AIMs are potent activators of apoptosis in glioblastoma cells without causing an increase in necrosis.

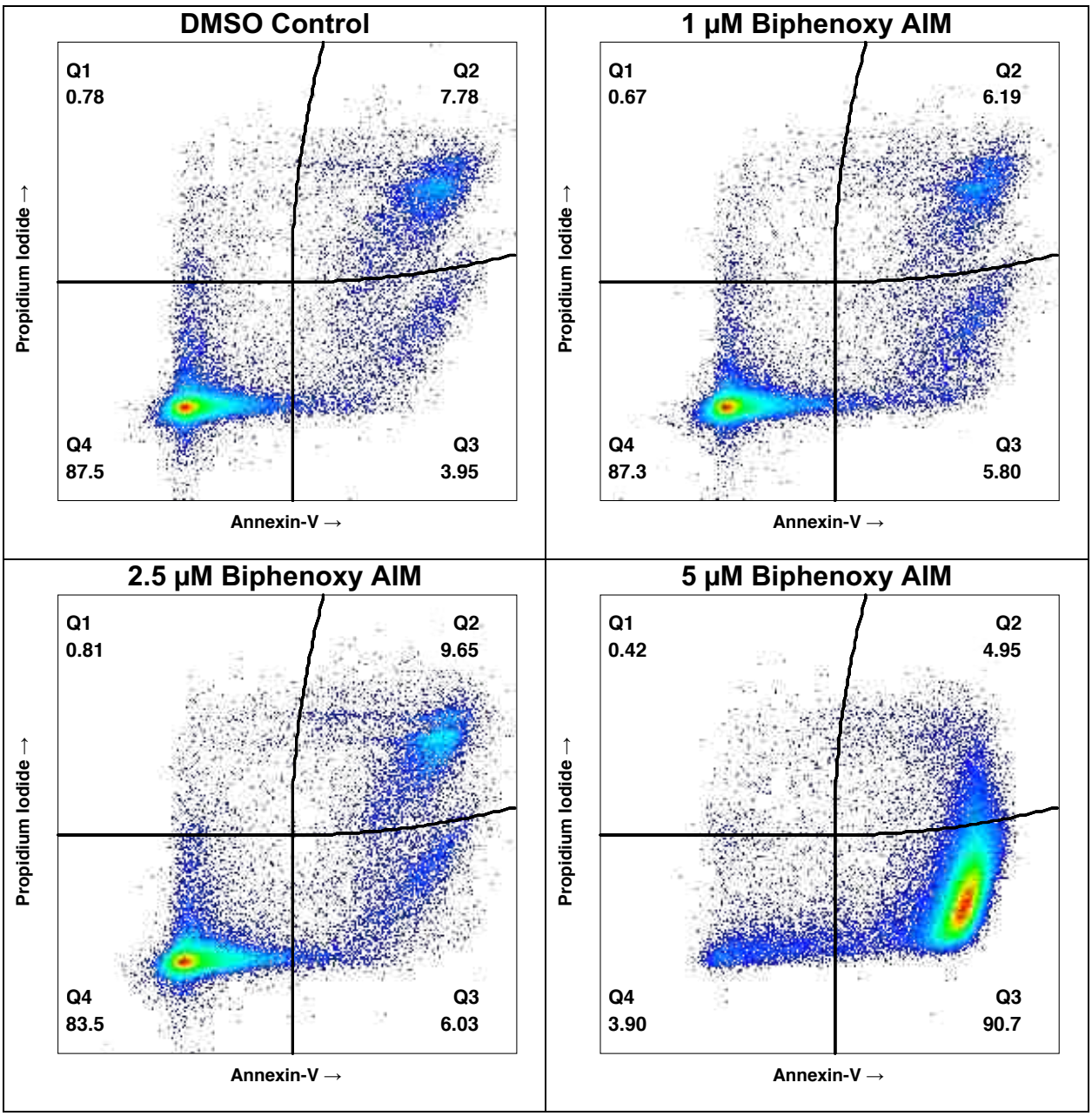

Figure 3.22 Dot-plots of the flow cytometry experiments with Annexin-V/PI

Representative dot-plots of the flow cytometry experiments with Annexin-V and propidium iodide staining. Quadrants are defined as follows: Q1 is necrosis, Q2 is late apoptosis, Q3 is early apoptosis, and Q4 is healthy non-apoptotic cells.

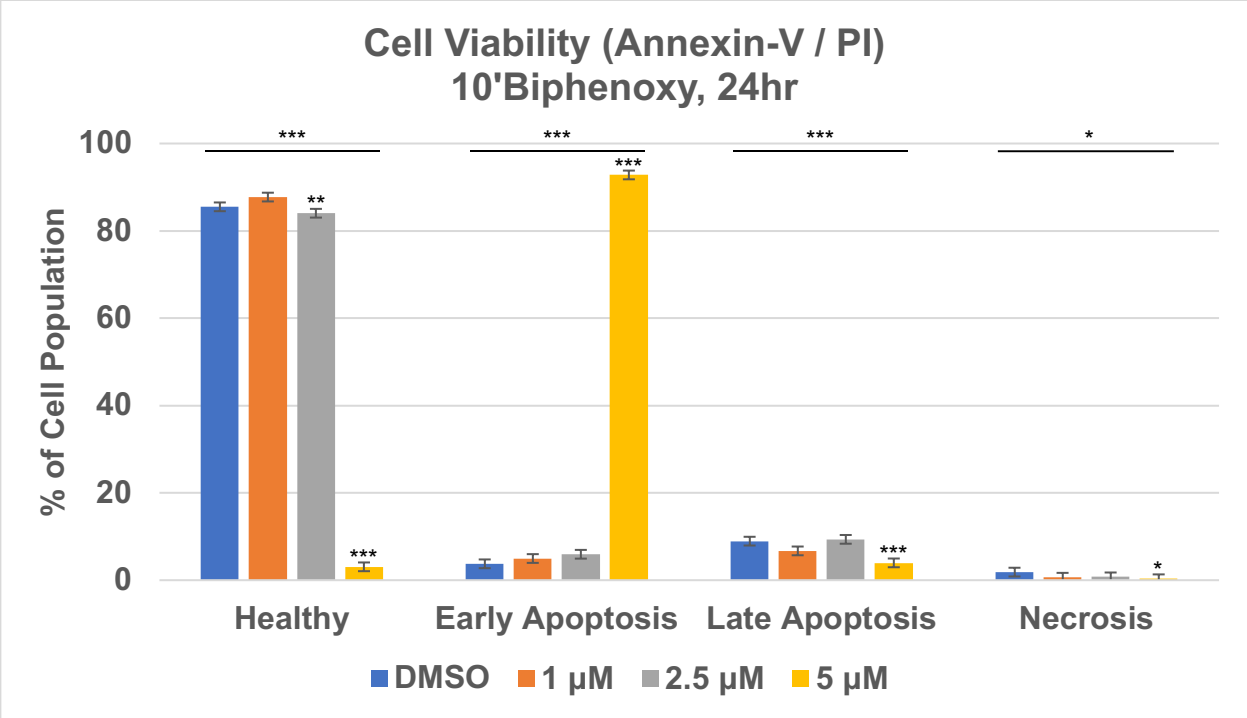

Figure 3.23 Statistical analysis of the flow cytometry experiments with Annexin-V/PI Treatment with 5 µM of 10-Biphenoxy AIM for 24-hours causes a significant increase in early apoptosis (P = 0.0001). A significant decrease in the population of healthy cells relative to control is observed for both the 2.5 µM and 5 µM 10-Biphenoxy AIM treated groups (P = 0.009 and P = 2E-16, respectively). No increase in necrosis is observed for any 10-Biphenoxy treatment group. Healthy ANOVA P = 1.58E-14. Early Apoptosis ANOVA P = 1.21E-13. Late Apoptosis ANOVA P = 1.11E-4. Necrosis ANOVA P = 0.04. Symbols represent significance levels (P < 0.05 *, P < 0.01 **, P < 0.001 ***) (n=3).

Treatment with AIMs Induces Loss of Mitochondrial Membrane Potential

To determine the effect of the 10-Biphenoxy AIM on the mitochondrial membrane potential, the mitochondrial dye JC-1 was utilized. JC-1 accumulates in mitochondria with a normal mitochondrial membrane potential ($\Delta\Psi m$) and the aggregates formed fluoresces red, however when there is a loss of the $\Delta\Psi m$, the dye leaks into the cytosol where it becomes monomers which fluoresce green.

In analysis of the JC-1 data utilizing only the 488 nm excitation wavelength, the 5 μM 10-Biphenoxy AIM treated cells revealed a dramatic shift to 88.0% of cells demonstrating mitochondrial depolarization, as indicated by the green fluorescence of JC-1 monomers (**Figure 3.24** and **Figure 3.25**). This is in stark contrast to only 6.4% of cells showing mitochondrial depolarization in the control samples. The positive control behaved as expected and the 50 μM CCCP treated group showed approximately 75.1% of the cells with depolarized mitochondria.

Consideration of the data collected using the alternative excitation wavelength of 405 nm to better distinguish JC-1 aggregates, we show that the increase in mitochondrial hyperpolarization, as defined by an increase in red fluorescence, was statistically significant for the 1 μM and 2.5 μM 10-Biphenoxy AIM treatment groups (**Figure 3.26** and **Figure 3.27**). The 5 μM 10-Biphenoxy AIM treatment group did not show a significant increase in hyperpolarization, however did show significant increases in partial and full depolarization populations as they were defined by our gating strategy, and this is similar to that observed for the 50 μM CCCP positive control group. As a result, the percentage of cells displaying normal mitochondrial polarization showed a

dose-dependent decrease with increasing concentrations of 10-Biphenoxy AIM treatment.

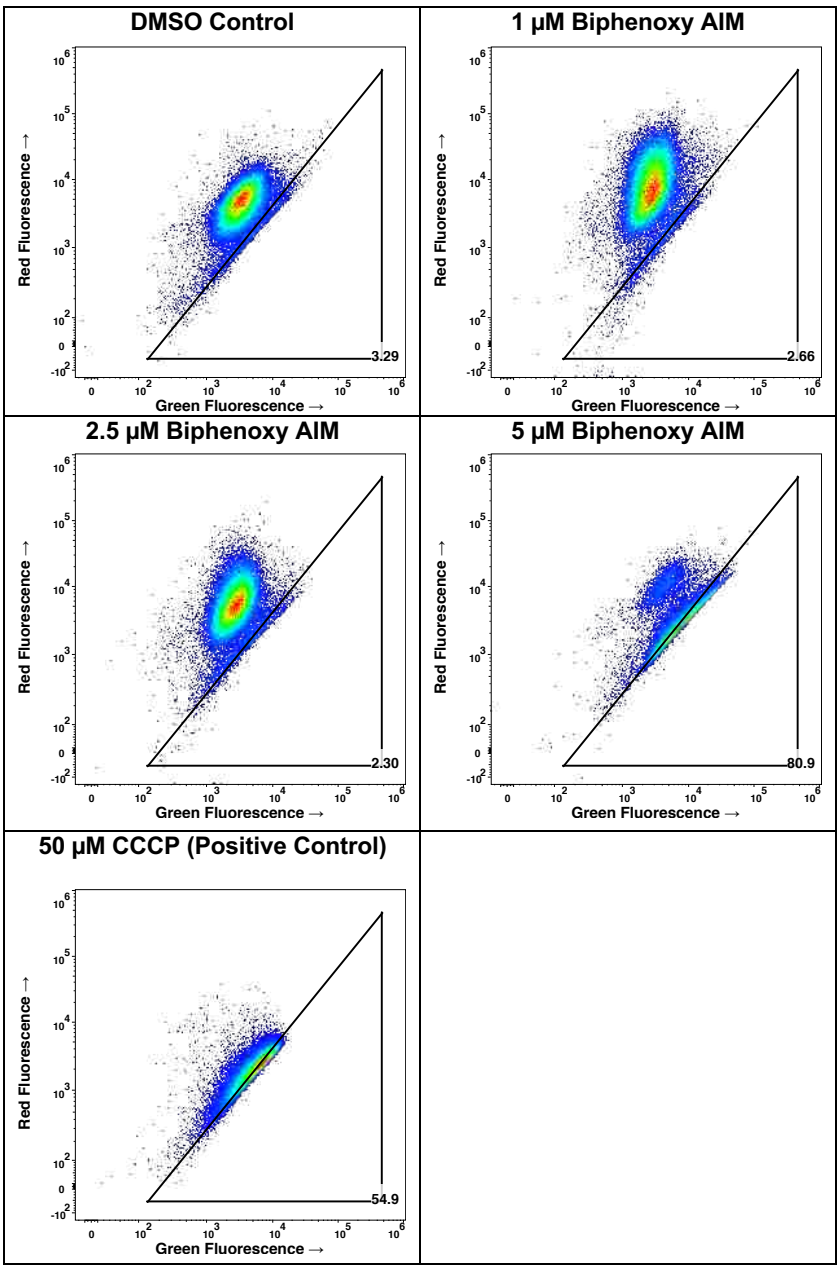

Figure 3.24 Dot-plots of the flow cytometry experiments with JC-1 at 488 nm Representative dot-plots of the flow cytometry experiments with JC-1 staining and 488 nm excitation. Gated area is defined as JC-1 monomers indicated by a decrease in red fluorescence (529 nm) and increase in green fluorescence (590 nm).

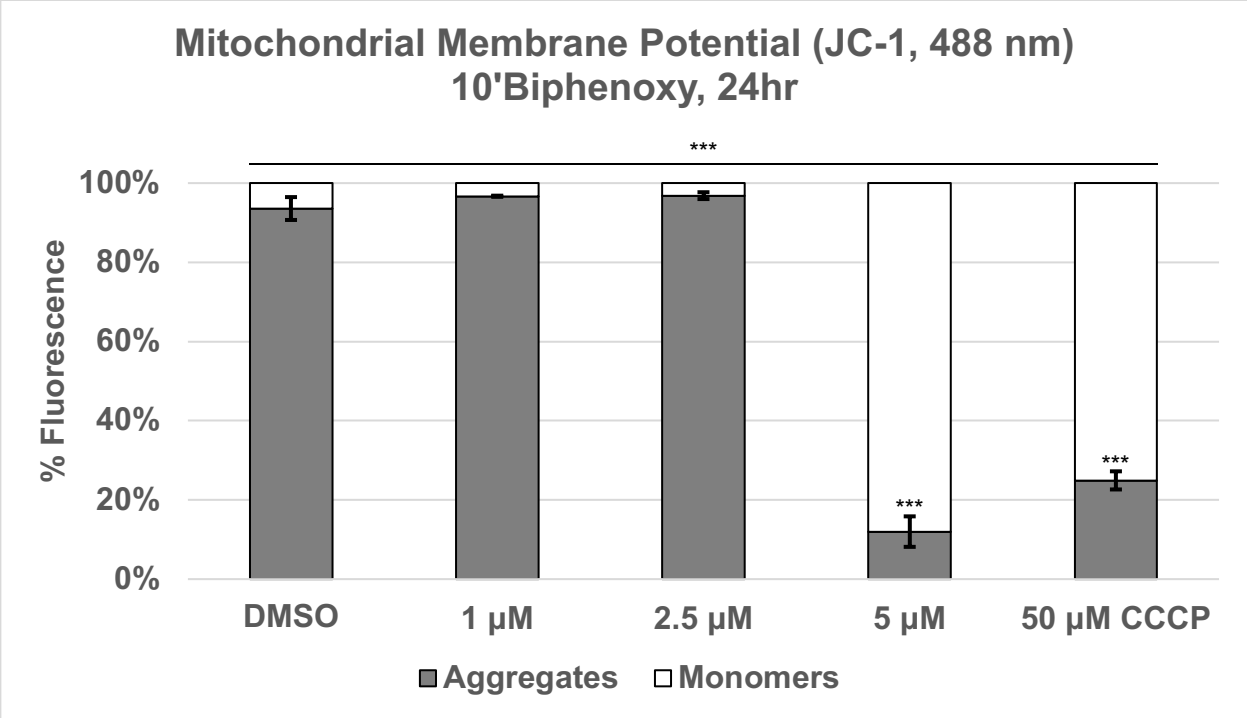

Figure 3.25 Analysis of mitochondrial membrane potential using JC-1 at 488 nm 24-hour treatment with 5 µM 10-Biphenoxy AIM causes a decrease in mitochondrial membrane potential observed as a significant increase of JC-1 monomers in SNB-19 human glioblastoma cells (P = <2E-16). 50 µM CCCP used as a positive control (P = < 2E-16). ANOVA P = 6.18E-12. Error bars represent standard deviation. Dunnett post-hoc test used for comparisons between treatment and control groups. Symbols represent significance levels (P < 0.05 *, P < 0.01 **, P < 0.001 ***) (n=3).

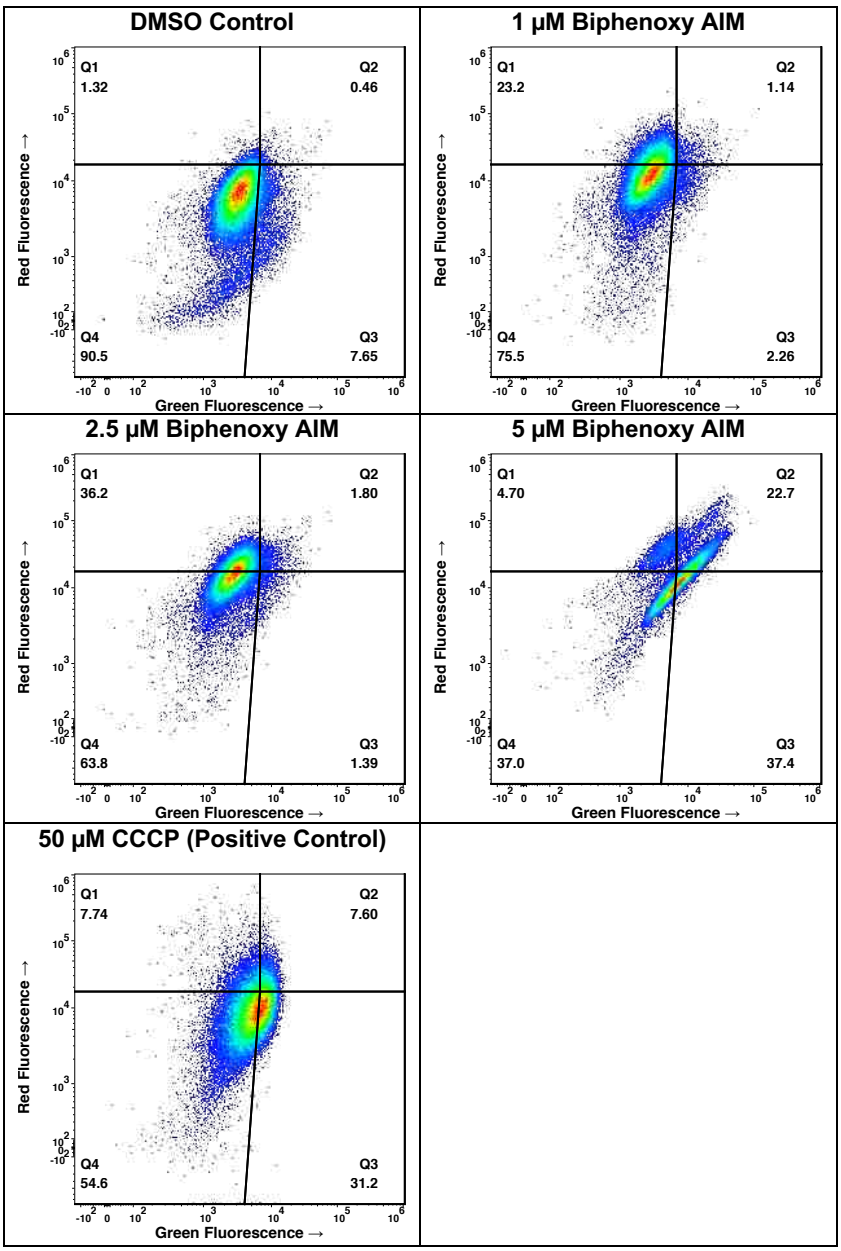

Figure 3.26 Analysis of mitochondrial membrane potential using JC-1 at 405/488 nm Representative dot-plots of the flow cytometry experiments with JC-1 staining and excitation at 405 nm and 488 nm. Quadrants are defined as follows: Q1 is hyperpolarized (↑ red fluorescence), Q2 is partially depolarized (↑ green & ↑ red fluorescence), Q3 depolarized (↑ green fluorescence), and Q4 is normal (control level red and green fluorescence).

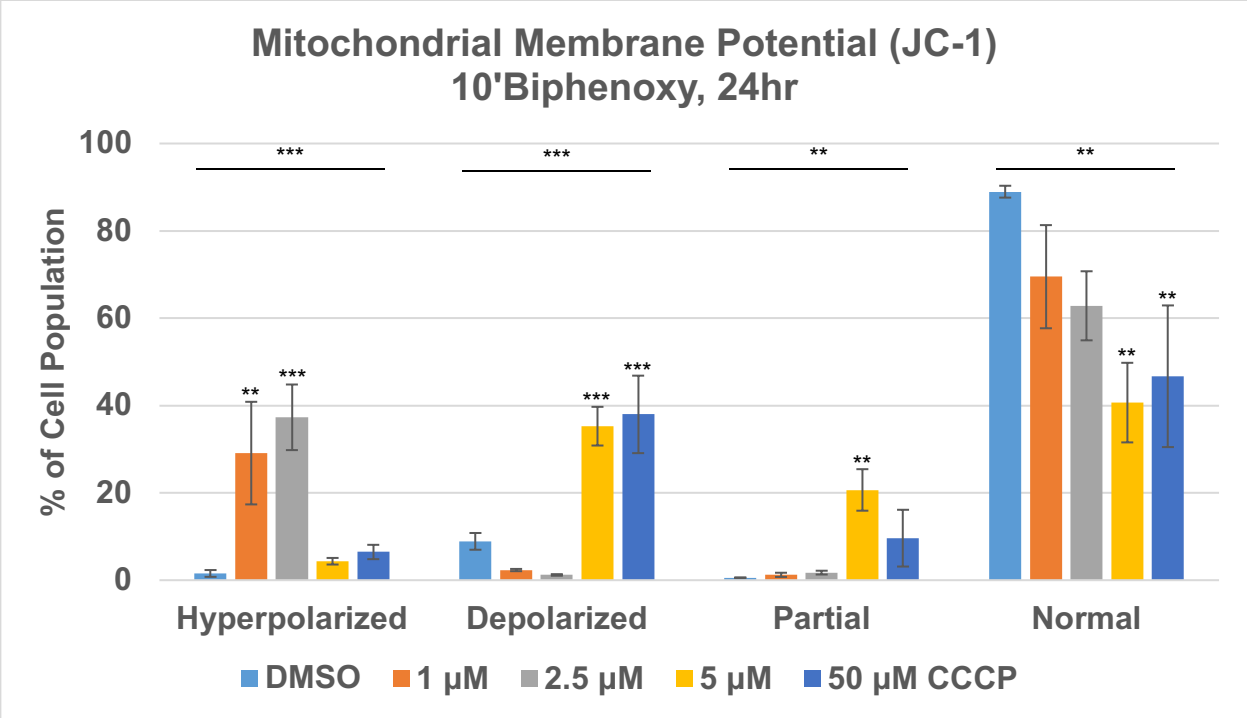

Figure 3.27 Analysis of mitochondrial membrane potential using JC-1 at 405/488 nm 24-hour treatment with 10-Biphenoxy AIM at increasing concentrations effects the mitochondrial membrane potential in SNB-19 human glioblastoma cells. 50 µM CCCP used as a positive control. Hyperpolarized (ΔΨm) ANOVA P = 0.0005. Depolarized (ΔΨm) ANOVA P = 1.14E-05. Partial Depolarization (ΔΨm) ANOVA P = 0.001. Normal (ΔΨm) ANOVA P = 0.007. Error bars represent standard deviation. Dunnett post-hoc test used for comparisons between treatment and control groups. Symbols represent significance levels (P < 0.05 *, P < 0.01 **, P < 0.001 ***).

AIMs Induce the Mitochondrial-mediated Intrinsic Pathway of Apoptosis

To measure activation of the intrinsic pathway of apoptosis, we performed flow cytometry experiments with SR-LEHD-FMK and SR-DEVD-FMK staining to detect activity of caspases 9 and 3/7, respectively. Caspase-9 is an initiator caspase and is involved in formation of the apoptosome that is responsible for cleavage of executioner pro-caspases-3 and 7 to their active forms. These data showed a significant 1.7-fold increase in caspase-9 staining in the 5 μM 10-Biphenoxy AIM treatment group in SNB-19 glioblastoma cells (**Figure 3.28** and **Figure 3.29**). Importantly, the increase in caspase-9 staining corresponded to a significant increase in caspase-3/7 staining (**Figure 3.30** and **Figure 3.31**). The increase in caspase-3/7 was approximately 1.9-fold in the 5 μM 10-Biphenoxy AIM treatment group, similar to that observed for caspase-9. The amount of caspase-3/7 staining appeared higher in the cells than caspase-9, however this is likely a result of the SR-DEVD-FMK staining both active caspases 3 and 7.

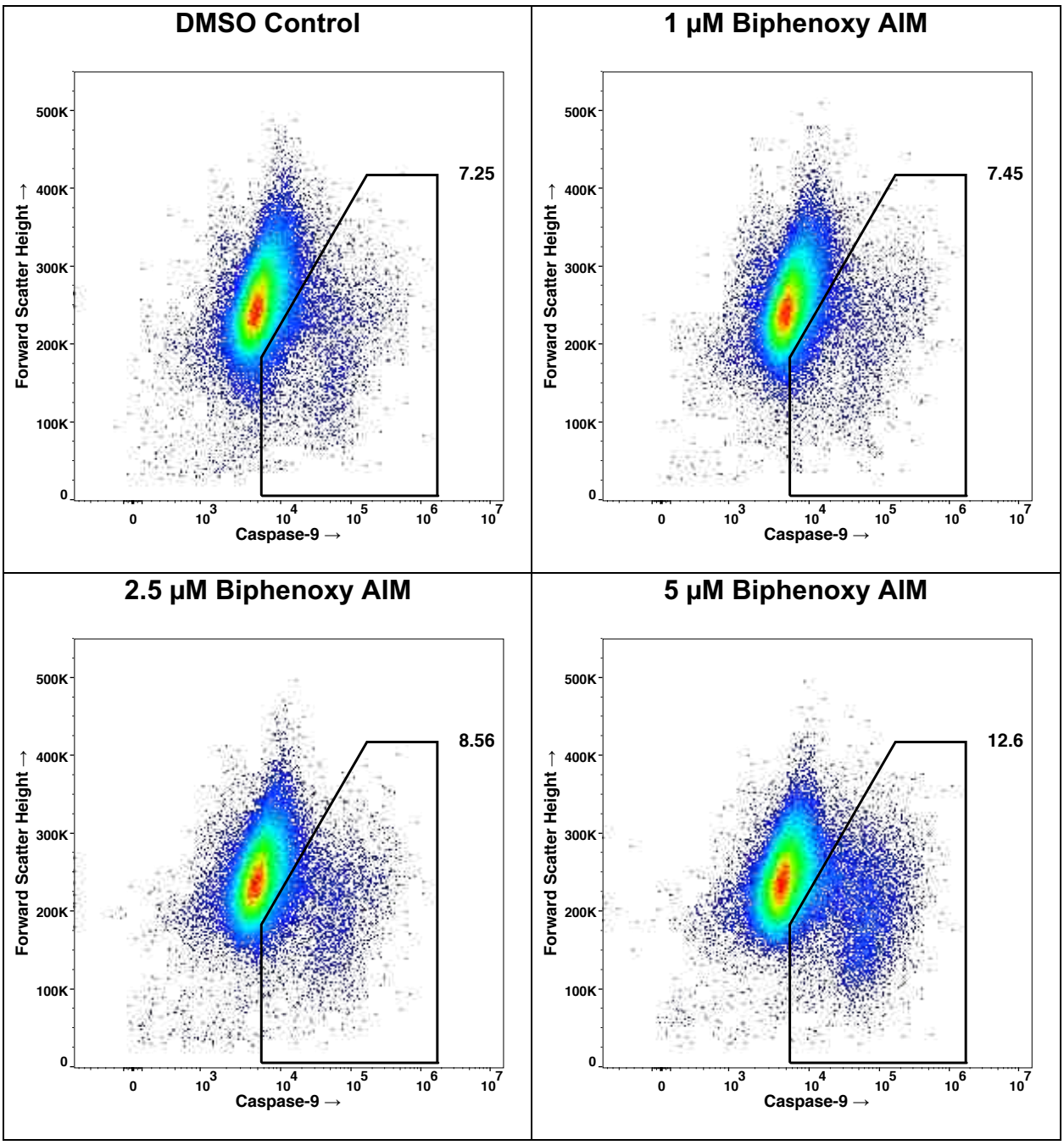

Figure 3.28 Dot-plots of the caspase-9 flow cytometry experiments

Representative dot-plots of the flow cytometry experiments with SR-LEHD-FMK to stain for caspase-9 activity. Gated region is defined as positive for caspase-9 activity.

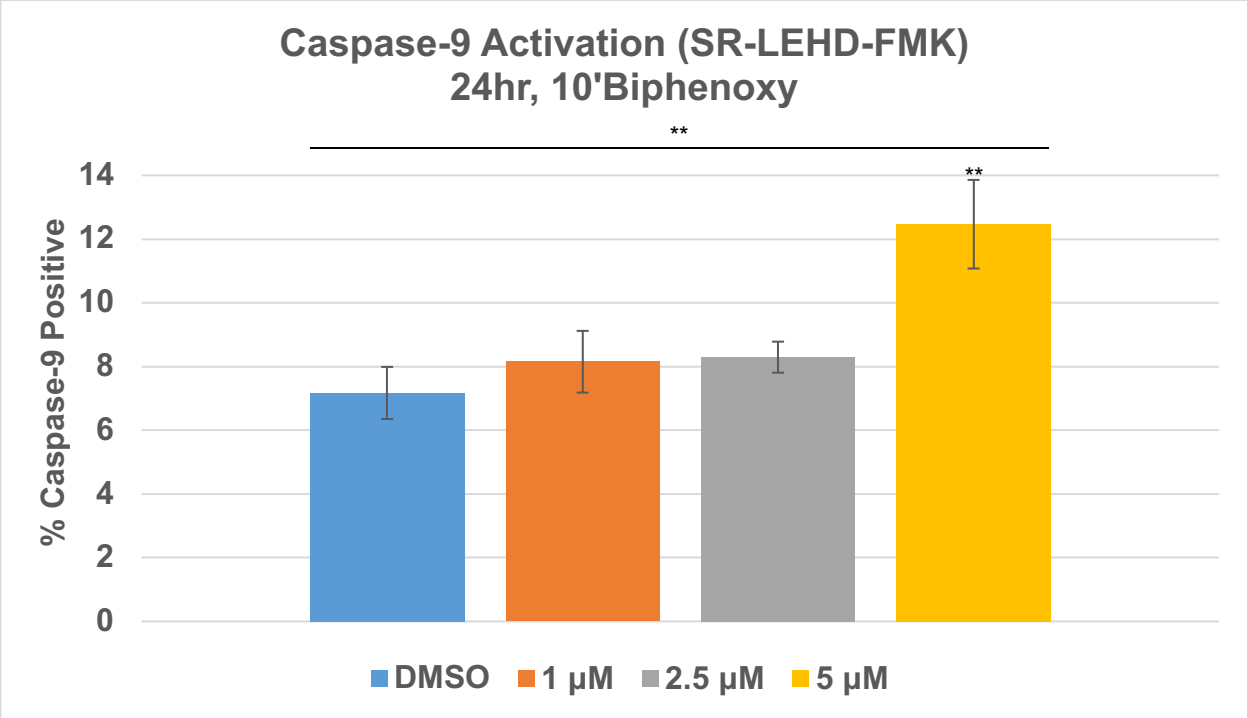

Figure 3.29 Statistical analysis of the caspase-9 flow cytometry experiments Analysis of Caspase-9 activation using SR-LEHD-FMK revealed that 24-hour treatment with 5 µM 10-Biphenoxy AIM causes an increase in Caspase-9 activation in SNB-19 human glioblastoma cells (P = 0.002). ANOVA P = 0.003. Error bars represent standard deviation. Dunnett post-hoc test used for comparisons between treatment and control groups. Symbols represent significance levels (P < 0.05 *, P < 0.01 **, P < 0.001 ***).

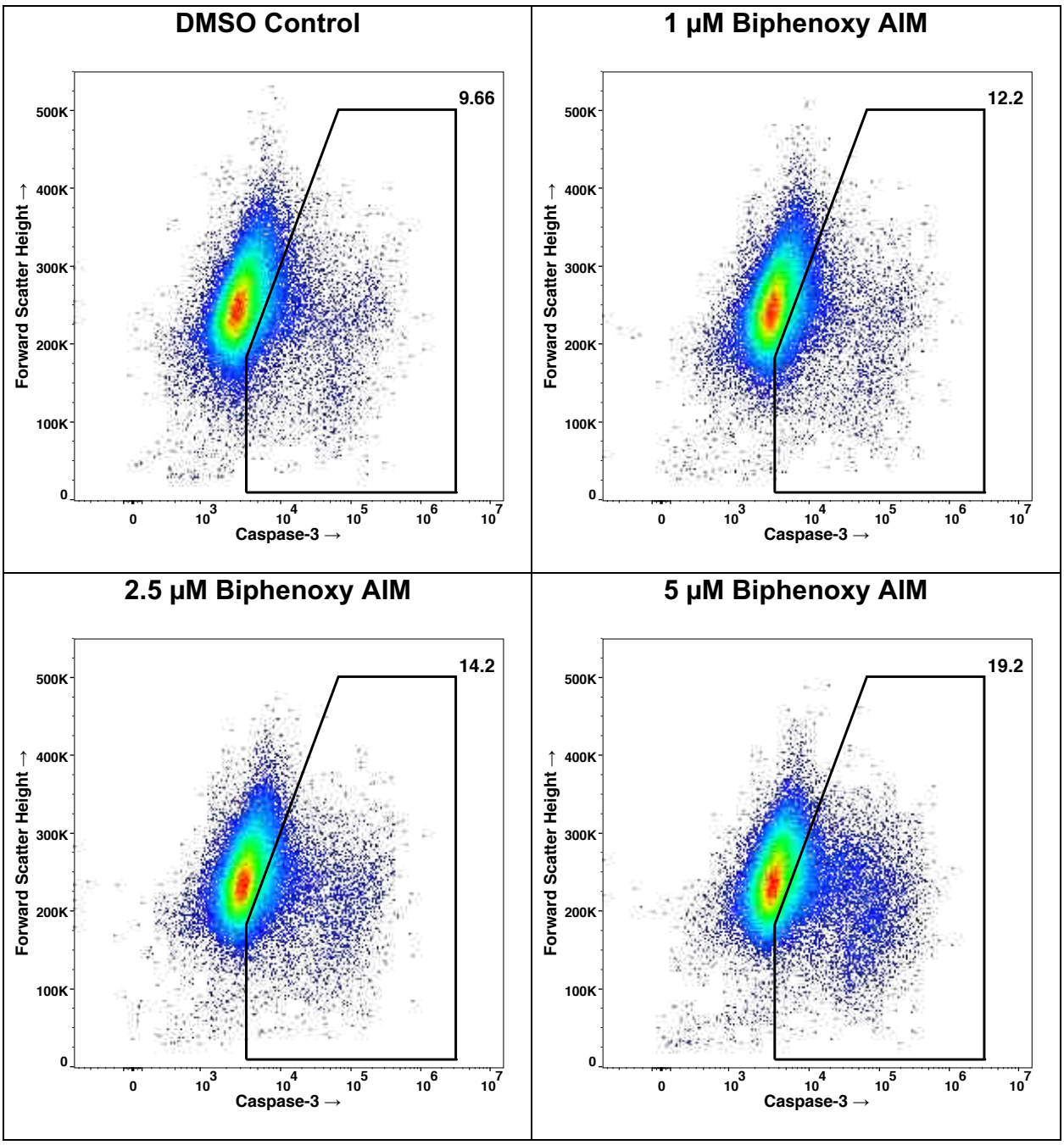

Figure 3.30 Dot-plots of the caspase-3/7 flow cytometry experiments

Representative dot-plots of the flow cytometry experiments with SR-DEVD-FMK to stain for caspase-3/7 activity. Gated region is defined as positive for caspase-3/7 activity.

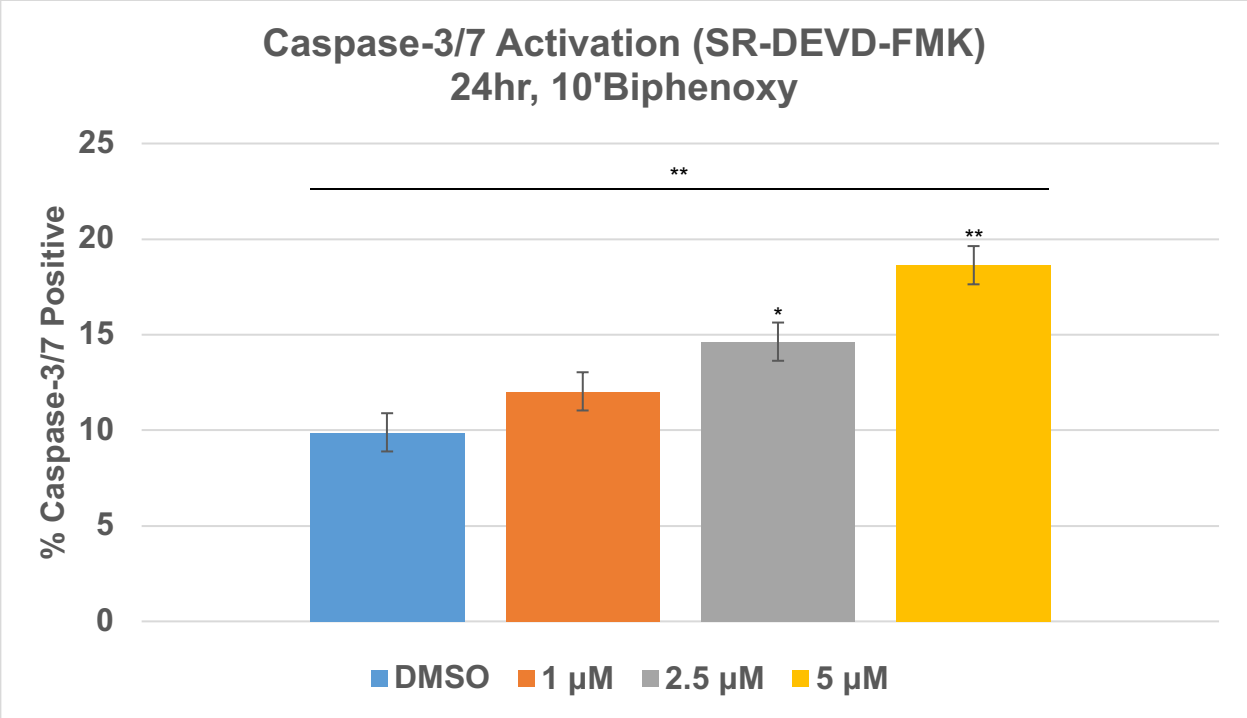

Figure 3.31 Statistical analysis of the caspase-3/7 flow cytometry experiments Analysis of Caspase-3/7 activation using SR-LEHD-FMK showed that 24-hour treatment with 2.5 µM and 5 µM 10-Biphenoxy AIM causes an increase in Caspase-3/7 activation in SNB-19 human glioblastoma cells (2.5 µM treatment P = 0.05, 5 µM treatment P = 0.002). ANOVA P = 0.004. Error bars represent standard deviation. Dunnett post-hoc test used for comparisons between treatment and control groups. Symbols represent significance levels (P < 0.05 *, P < 0.01 **, P < 0.001 ***) (n=3).

Discussion

In this work we elucidated a mitochondrial mechanism of action for the AIMs in tumor cells. We also have provided evidence that suggests this mechanism contributes to their antitumor activity. These data support the hypothesis that the AIMs can inhibit activity of ETC protein complexes and induce loss of the mitochondrial membrane potential ($\Delta\Psi m$).

Our confocal imaging experiments revealed that the auto-fluorescent AIMs display punctate binding in glioblastoma cells, indicating a distinct molecular target. Furthermore, the AIMs did not show a significant amount of fluorescence in the nucleus of SNB-19 cells (**Appendix Figure A.3.2**). This should be an important consideration when considering the AIMs potential interactions with quadruplex DNA in the nucleus, as has been the focus of previous work by our laboratory and collaborators (Gajewski et al. 2009; Han et al. 2009; Mirzaei et al. 2012; Weaver et al. 2015). However, this does not rule out the possibility of AIMs interaction with quadruplexes in nuclear DNA, as quenching of the AIMs fluorescence has been shown previously to occur when binding quadruplex structures (Han et al. 2009). In contrast, the AIMs did appear to colocalize with the MitoTracker™ mitochondria specific fluorescent dye (**Figure 3.6** and **Figure 3.7**). Inspection of the AIMs structure suggested it could accumulate in mitochondria, as this has been seen for other structures with similar lipophilic molecules containing tertiary amines (Smiley et al. 1991; Gorlach, Fichna, and Lewandowska 2015). This led us to determine the cytotoxicity of the AIMs using an LDH cell viability assay not dependent on mitochondrial health for comparison to our previous MTT cell viability experiments that could be affected by mitochondria reductase activity.

The MTT cell viability results indicated the AIMs cause toxicity in tumor cells at low- to sub-micromolar concentrations in human glioblastoma cells (**Figure 3.2** and **Table 3.7**). The LDH results overall showed less toxicity when compared to MTT results for the same cell lines and compounds (**Table 3.7** and **Table 3.8**). This can be interpreted in several ways, as the assays are different measures of cell viability. It was postulated that one possible scenario would be the mitochondrial reductases responsible for reducing the MTT dye were being inhibited by the AIMs. This could produce a lower measured IC_{50} in the MTT experiments relative to LDH; if the enzymes responsible for conversion of MTT to the measurable formazan were inhibited, it would appear less cells were viable in the assay. However, one other possibility was a difference in toxicity due to the four-day incubation period that was utilized in the MTT experiments. In the LDH experiments, the AIMs also displayed higher toxicity in the primary rat astrocytes compared to the rat glioma cell line (**Table 3.8**). This is concerning, as the AIMs are being pursued as potential anticancer therapeutics. However, species differences (rat vs. human) and the specific mutations present in the C6 rat glioma cells may play a role in the toxicity of the AIMs. Taken together, this suggests the AIMs should be tested in healthy human astrocytes and potentially other cancer lineages. To determine if the AIMs were affecting mitochondrial reductase activity as suggested by comparison of the MTT and LDH data, we performed activity experiments in ETC complex proteins isolated from mitochondria and in whole intact mitochondria.

The electron transport chain activity assays contributed several important findings regarding the activity of the AIMs on mitochondria. Primarily, the studies

demonstrate that the AIMs can act as low-micromolar inhibitors of ETC protein complexes in intact mitochondria, and more specifically in isolated Complex II (**Table 3.9**). *This is a significant result as it demonstrates a plausible mitochondrial mechanism of action for the AIMs.* Complex II inhibition has been documented for other antitumor agents as their major mechanism of action (Chen et al. 2007; L.-F. Dong et al. 2008; Ralph et al. 2011). In addition, the inhibition of Complex II was greater for the 10-Biphenoxy AIM than the 10-Phenyl AIM, and this is consistent with their relative induction of apoptosis in SNB-19 cells as demonstrated in the LDH cell viability results. The Complex II + III assay also verifies inhibition in intact mitochondria, but as the assay cannot distinguish between Complex II or Complex III inhibition, it is possible the AIMs have activity at both. However, it is noted that the inhibition in the intact mitochondria is less for both compounds and this would not be expected if a combined inhibitory effect was present. It was also noted that the ratio of inhibition (10-Biphenoxy vs. 10-Phenyl) is also approximately two-fold greater in the Complex II only assay relative to the assay measuring combined Complex II + III activity. Together, these results could indicate that the activity at Complex II is the major inhibition target of the AIMs and this will be an important distinguishment in future studies. To examine the potential mechanism of binding of the AIMs to Complex II, molecular docking studies were performed in collaboration with the Molecular Computational Core Facility (MCCF) at the University of Montana.

Our molecular docking results suggest the AIMs are able to bind the ubiquinone sites of Complex II (**Table 3.10** and **Table 3.11**). These have been reported as binding sites for other Complex II inhibitors in the literature (Miyadera et al. 2003; Sun et al.

2005). The poses generated by the GOLD docking algorithm also are chemically reasonable and the potential molecular interactions observed suggest the AIMs could fit and anchor themselves in the ubiquinone binding pockets (**Figure 3.15** and **Figure 3.17**). Although the molecular docking studies do not prove the mechanism of AIMs interaction with Complex II, the results could serve as an initial binding hypothesis for continued development of AIMs as ubiquinone-site inhibitors. Overall, the molecular docking studies were promising and were in support of our biochemical data.

Our laboratory has previously observed an increase in mitochondrial ROS following AIMs treatment (Kearns 2013). This is consistent with reports in the literature that inhibition of the mitochondrial ETC at various protein complexes can cause generation of ROS as superoxide and hydrogen peroxide (Sun et al. 2005; Chen et al. 2007; L.-F. Dong et al. 2008; Bleier and Dröse 2013). The production of ROS from mitochondrial ETC complexes has also been reported previously to cause damage to mtDNA (Lan-Feng Dong et al. 2007). With this in mind, we performed a time-course study using the AIM measured as the most potent complex II inhibitor to determine the effect of treatment on mtDNA.

The 10-Biphenoxy AIM was also shown to reversibly induce mtDNA damage and reduce mtDNA copy number in glioblastoma cells (**Figure 3.19**, **Figure 3.20**, and **Figure 3.21**). These findings were consistent with results previously observed where hydrogen peroxide treatment caused mtDNA damage and mtDNA copy number reduction, followed by recovery of mtDNA integrity at 24 hours in prostate cancer cells (Chan and Chen 2009). Additionally, hydrogen peroxide treatment has also been shown to lead to loss of $\Delta\Psi m$ in cells (Li et al. 2003). Taken together, our findings and

reports in the literature serve to reinforce our hypothesis that the increase in mitochondrial ROS following treatment with the AIMs is contributing to damage in mitochondria resulting in loss of ΔΨm.

The loss of ΔΨm in glioblastoma cells following treatment with AIMs was demonstrated by our experiments using JC-1 with both a classical and alternative method of analysis. The results suggest that low concentrations of AIMs treatment result in hyperpolarization of the mitochondria (**Figure 3.25** and **Figure 3.27**). This is consistent with our theory of Complex II mediated increase in oxidative stress causing hyperpolarization prior to permeabilization of the mitochondria membrane and the subsequent loss of ΔΨm. Interestingly, it has also been previously observed that the hyperpolarization event occurs at the same time as the excessive ROS generation (Zorov, Juhaszova, and Sollott 2006). Our results also showed a dose-dependent decrease in the number of cells with a normal ΔΨm with increasing doses of the 10-Biphenoxy AIM. These results suggested that the AIMs are disrupting ΔΨm; the loss of ΔΨm is also consistent with previous studies of ETC complex inhibitors effect on mitochondria leading to apoptosis in tumor cells (L.-F. Dong et al. 2008; Byun et al. 2008; Ralph et al. 2011; Wang et al. 2016).

Our results also confirm activation of the mitochondrial-mediated intrinsic pathway of apoptosis, measured as an increase in caspase-9 activation (**Figure 3.29**). Furthermore, caspase-9 activity resulted in a measured increase in activity of executioner caspases 3/7 (**Figure 3.31**). This confirms formation of the apoptosome by activated caspase-9, and initiation of intrinsic apoptosis. Finally, induction of apoptosis in glioblastoma cells without a significant increase in necrosis was confirmed by

Annexin-V and propidium iodide staining (**Figure 3.23**). Overall, our flow cytometry experiments demonstrate that the AIMs are inducing intrinsic apoptosis in glioblastoma cells leading to caspase activation and tumor cell death.

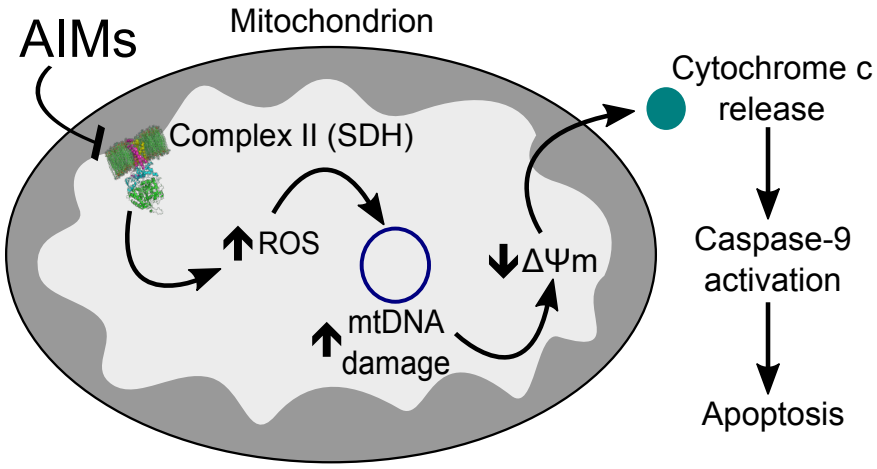

Figure 3.32

Our working hypothesis of the mechanism of intrinsic apoptosis induction by the AIMs through inhibition of ETC protein complexes in mitochondria.

Collectively, these studies have provided strong evidence in support of a novel mitochondrial-associated mechanism of apoptosis, mediated through inhibition of ETC protein complexes, as a contributor to the antitumor activity of the AIMs (**Figure 3.32**). Future studies will investigate the mechanism of Complex II inhibition in depth with a focus on binding kinetics and measure the effect of AIMs on respiration and ATP production in mitochondria. This work will act as the foundation for exploring the possibility of using AIMs designed to target Complex II as potential antitumor agents and guide the continued structure-based drug design of the AIMs.

References

Alexeyev, Mikhail, Inna Shokolenko, Glenn Wilson, and Susan LeDoux. 2013. “The Maintenance of Mitochondrial DNA Integrity—Critical Analysis and Update.” *Cold Spring Harbor Perspectives in Biology* 5 (5): a012641. https://doi.org/10.1101/cshperspect.a012641.

Berridge, Michael V., Patries M. Herst, and An S. Tan. 2005. “Tetrazolium Dyes as Tools in Cell Biology: New Insights into Their Cellular Reduction.” In *Biotechnology Annual Review*, 11:127–52. Elsevier. http://www.sciencedirect.com/science/article/pii/S1387265605110047.

Bleier, Lea, and Stefan Dröse. 2013. “Superoxide Generation by Complex III: From Mechanistic Rationales to Functional Consequences.” *Biochimica et Biophysica Acta (BBA) - Bioenergetics*, Respiratory complex III and related bc complexes, 1827 (11): 1320–31. https://doi.org/10.1016/j.bbabio.2012.12.002.

Byun, Hae-Ok, Hee Young Kim, Jin J. Lim, Yong-Hak Seo, and Gyesoon Yoon. 2008. “Mitochondrial Dysfunction by Complex II Inhibition Delays Overall Cell Cycle Progression via Reactive Oxygen Species Production.” *Journal of Cellular Biochemistry* 104 (5): 1747–59. https://doi.org/10.1002/jcb.21741.

Chan, Sam W., and Junjian Z. Chen. 2009. “Measuring mtDNA Damage Using a Supercoiling-Sensitive qPCR Approach.” In *Mitochondrial DNA*, edited by Jeffrey A. Stuart, 554:183–97. Totowa, NJ: Humana Press. http://link.springer.com/10.1007/978-1-59745-521-3_12.

Chan, Sam W., Simone Chevalier, Armen Aprikian, and Junjian Z. Chen. 2012. “Simultaneous Quantification of Mitochondrial DNA Damage and Copy Number in Circulating Blood: A Sensitive Approach to Systemic Oxidative Stress.” *BioMed Research International* 2013 (December): e157547. https://doi.org/10.1155/2013/157547.

Chen, Yongqiang, Eileen McMillan-Ward, Jiming Kong, Sara J. Israels, and Spencer B. Gibson. 2007. “Mitochondrial Electron-Transport-Chain Inhibitors of Complexes I and II Induce Autophagic Cell Death Mediated by Reactive Oxygen Species.” *Journal of Cell Science* 120 (23): 4155–66. https://doi.org/10.1242/jcs.011163.

Dassault Systèmes BIOVIA, 2018. Discovery Studio, v4.5, San Diego: Dassault Systèmes.

Dong, Lan-Feng, Emma Swettenham, Johanna Eliasson, Xiu-Fang Wang, Mikhal Gold, Yasmine Medunic, Marina Stantic, et al. 2007. “Vitamin E Analogues Inhibit Angiogenesis by Selective Induction of Apoptosis in Proliferating Endothelial Cells: The Role of Oxidative Stress.” *Cancer Research* 67 (24): 11906–13. https://doi.org/10.1158/0008-5472.CAN-07-3034.

Dong, L.-F., P. Low, J. C. Dyason, X.-F. Wang, L. Prochazka, P. K. Witting, R. Freeman, et al. 2008. “α-Tocopheryl Succinate Induces Apoptosis by Targeting Ubiquinone-Binding Sites in Mitochondrial Respiratory Complex II.” *Oncogene* 27 (31): 4324–35. https://doi.org/10.1038/onc.2008.69.

Fedotcheva, N. I., E. G. Litvinova, M. V. Zakharchenko, N. V. Khunderyakova, R. S. Fadeev, V. V. Teplova, T. A. Fedotcheva, N. V. Beloborodova, and M. N. Kondrashova. 2017. “Substrate-Specific Reduction of Tetrazolium Salts by Isolated Mitochondria, Tissues, and Leukocytes.” *Biochemistry (Moscow)* 82 (2): 192–204. https://doi.org/10.1134/S0006297917020110.

Frommolt, Peter, 2010. ic50: Standardized high-throughput evaluation of cell-based compound screens. R package version 1.4.2. https://CRAN.R-project.org/package=ic50

Fulda, Simone, Lorenzo Galluzzi, and Guido Kroemer. 2010. “Targeting Mitochondria for Cancer Therapy.” *Nature Reviews Drug Discovery* 9 (6): 447–64. https://doi.org/10.1038/nrd3137.

Fu, Xudong, Randall M. Chin, Laurent Vergnes, Heejun Hwang, Gang Deng, Yanpeng Xing, Melody Y. Pai, et al. 2015. “2-Hydroxyglutarate Inhibits ATP Synthase and mTOR Signaling.” *Cell Metabolism* 22 (3): 508–15. https://doi.org/10.1016/j.cmet.2015.06.009.
Gajewski, Mariusz P., Howard Beall, Mark Schnieder, Sarah M. Stranahan, Michael D. Mosher, Kevin C. Rider, and Nicholas R. Natale. 2009. “Bis-Anthracenyl Isoxazolyl Amides Have Enhanced Anticancer Activity.” *Bioorganic & Medicinal Chemistry Letters* 19 (15): 4067–69. https://doi.org/10.1016/j.bmcl.2009.06.019.

Giovannini, Claudio, Paola Matarrese, Beatrice Scazzocchio, Massimo Sanchez, Roberta Masella, and Walter Malorni. 2002. “Mitochondria Hyperpolarization Is an Early Event in Oxidized Low-Density Lipoprotein-Induced Apoptosis in Caco-2 Intestinal Cells.” *FEBS Letters* 523 (1): 200–206. https://doi.org/10.1016/S0014-5793(02)02972-1.
Gorlach, Sylwia, Jakub Fichna, and Urszula Lewandowska. 2015. “Polyphenols as Mitochondria-Targeted Anticancer Drugs.” *Cancer Letters* 366 (2): 141–49. https://doi.org/10.1016/j.canlet.2015.07.004.

Han, Xiaochun, Chun Li, Michael D. Mosher, Kevin C. Rider, Peiwen Zhou, Ronald L. Crawford, William Fusco, Andrzej Paszczynski, and Nicholas R. Natale. 2009. “Design, Synthesis and Biological Evaluation of a Novel Class of Anticancer Agents: Anthracenylisoxazole Lexitropsin Conjugates.” *Bioorganic & Medicinal Chemistry* 17 (4): 1671–80. https://doi.org/10.1016/j.bmc.2008.12.056.

Horsefield, Rob, Victoria Yankovskaya, Graham Sexton, William Whittingham, Kazuro Shiomi, Satoshi Ōmura, Bernadette Byrne, Gary Cecchini, and So Iwata. 2006. “Structural and Computational Analysis of the Quinone-Binding Site of Complex II (Succinate-Ubiquinone Oxidoreductase) A MECHANISM OF ELECTRON TRANSFER AND PROTON CONDUCTION DURING UBIQUINONE REDUCTION.” *Journal of Biological Chemistry* 281 (11): 7309–16. https://doi.org/10.1074/jbc.M508173200.

Indo, Hiroko P., Mercy Davidson, Hsiu-Chuan Yen, Shigeaki Suenaga, Kazuo Tomita, Takeshi Nishii, Masahiro Higuchi, Yasutoshi Koga, Toshihiko Ozawa, and Hideyuki J. Majima. 2007. “Evidence of ROS Generation by Mitochondria in Cells with Impaired Electron Transport Chain and Mitochondrial DNA Damage.” *Mitochondrion*, Mitochondria and Life, 7 (1): 106–18. https://doi.org/10.1016/j.mito.2006.11.026.
Jones, Gareth, Peter Willett, Robert C Glen, Andrew R Leach, and Robin Taylor. 1997. “Development and Validation of a Genetic Algorithm for Flexible Docking.” *Journal of Molecular Biology* 267 (3): 727–48. https://doi.org/10.1006/jmbi.1996.0897.

Kearns, Alison King. 2013. “MECHANISMS AND CYTOTOXIC EFFECTS OF NQO1-DIRECTED LAVENDAMYCIN DERIVATIVES AND MITOCHONDRIA-TARGETED ANTHRACENYL ISOXAZOLE AMIDES AS NOVEL ANTITUMOR AGENTS.”
Lai, Kevin, Douglas W. Selinger, Jonathan M. Solomon, Hua Wu, Esther Schmitt, Fabrizio C. Serluca, Daniel Curtis, and John D. Benson. 2013. “Integrated Compound Profiling Screens Identify the Mitochondrial Electron Transport Chain as the Molecular Target of the Natural Products Manassantin, Sesquicillin, and Arctigenin.” *ACS Chemical Biology* 8 (1): 257–67. https://doi.org/10.1021/cb300495e.

Komsta, Lukasz, 2011. outliers: Tests for outliers. R package version 0.14. https://CRAN.R-project.org/package=outliers

Lee, Icksoo, Elisabeth Bender, and Bernhard Kadenbach. 2002. “Control of Mitochondrial Membrane Potential and ROS Formation by Reversible Phosphorylation of Cytochrome c Oxidase.” *Molecular and Cellular Biochemistry* 234 (1): 63–70.
Li, Jian-Ming, Hong Zhou, Qian Cai, and Guang-Xia Xiao. 2003. “Role of Mitochondrial Dysfunction in Hydrogen Peroxide-Induced Apoptosis of Intestinal Epithelial Cells.” *World Journal of Gastroenterology* 9 (3): 562–67. https://doi.org/10.3748/wjg.v9.i3.562.

Liu, Yuanbin, Gary Fiskum, and David Schubert. 2002. “Generation of Reactive Oxygen Species by the Mitochondrial Electron Transport Chain.” *Journal of Neurochemistry* 80 (5): 780–87. https://doi.org/10.1046/j.0022-3042.2002.00744.x.

Mirzaei, Yousef R., Matthew J. Weaver, Scott A. Steiger, Alison K. Kearns, Mariusz P. Gajewski, Kevin C. Rider, Howard D. Beall, and N. R. Natale. 2012. “Improved Synthesis of 3-Aryl Isoxazoles Containing Fused Aromatic Rings.” *Tetrahedron* 68 (50): 10360–64. https://doi.org/10.1016/j.tet.2012.09.084.

Miyadera, Hiroko, Kazuro Shiomi, Hideaki Ui, Yuichi Yamaguchi, Rokuro Masuma, Hiroshi Tomoda, Hideto Miyoshi, Arihiro Osanai, Kiyoshi Kita, and Satoshi Ōmura. 2003. “Atpenins, Potent and Specific Inhibitors of Mitochondrial Complex II (succinate-Ubiquinone Oxidoreductase).” *Proceedings of the National Academy of Sciences* 100 (2): 473–77. https://doi.org/10.1073/pnas.0237315100.

Mosmann, Tim. 1983. “Rapid Colorimetric Assay for Cellular Growth and Survival: Application to Proliferation and Cytotoxicity Assays.” *Journal of Immunological Methods*

65 (1): 55–63. https://doi.org/10.1016/0022-1759(83)90303-4.

Neuzil, Jiri, Lan-Feng Dong, Jakub Rohlena, Jaroslav Truksa, and Stephen J. Ralph. 2013. “Classification of Mitocans, Anti-Cancer Drugs Acting on Mitochondria.” *Mitochondrion*, Mitochondria, Apoptosis and Cancer, 13 (3): 199–208. https://doi.org/10.1016/j.mito.2012.07.112.

Perelman, A, C Wachtel, M Cohen, S Haupt, H Shapiro, and A Tzur. 2012. “JC-1: Alternative Excitation Wavelengths Facilitate Mitochondrial Membrane Potential Cytometry.” *Cell Death & Disease* 3 (11): e430. https://doi.org/10.1038/cddis.2012.171.

Phillips, Nicole R., Marc L. Sprouse, and Rhonda K. Roby. 2014. “Simultaneous Quantification of Mitochondrial DNA Copy Number and Deletion Ratio: A Multiplex Real-Time PCR Assay.” *Scientific Reports* 4 (January). https://doi.org/10.1038/srep03887.

R Core Team, 2014. R: A language and environment for statistical computing. R Foundation for Statistical Computing, Vienna, Austria. http://www.R-project.org/

Rai, Yogesh, Richa Pathak, Neeraj Kumari, Dhananjay Kumar Sah, Sanjay Pandey, Namita Kalra, Ravi Soni, B. S. Dwarakanath, and Anant Narayan Bhatt. 2018. “Mitochondrial Biogenesis and Metabolic Hyperactivation Limits the Application of MTT Assay in the Estimation of Radiation Induced Growth Inhibition.” *Scientific Reports* 8 (1): 1531. https://doi.org/10.1038/s41598-018-19930-w.

Ralph, Stephen J., Rafael Moreno-Sánchez, Jiri Neuzil, and Sara Rodríguez-Enríquez. 2011. “Inhibitors of Succinate: Quinone Reductase/Complex II Regulate Production of Mitochondrial Reactive Oxygen Species and Protect Normal Cells from Ischemic Damage but Induce Specific Cancer Cell Death.” *Pharmaceutical Research* 28 (11): 2695. https://doi.org/10.1007/s11095-011-0566-7.

Ritz, C., Baty, F., Streibig, J. C., Gerhard, D., 2015. Dose-Response Analysis Using R PLOS ONE, 10(12), e0146021.

Schindelin, Johannes, Ignacio Arganda-Carreras, Erwin Frise, Verena Kaynig, Mark Longair, Tobias Pietzsch, Stephan Preibisch, et al. 2012. “Fiji: An Open-Source Platform for Biological-Image Analysis.” *Nature Methods* 9 (7): 676–82. https://doi.org/10.1038/nmeth.2019.

Schindelin, Johannes, Curtis T. Rueden, Mark C. Hiner, and Kevin W. Eliceiri. 2015. “The ImageJ Ecosystem: An Open Platform for Biomedical Image Analysis.” *Molecular Reproduction and Development* 82 (7-8): 518–29. https://doi.org/10.1002/mrd.22489.

Schrodinger. 2015. “The PyMOL Molecular Graphics System, Version 1.8.”
Smiley, S T, M Reers, C Mottola-Hartshorn, M Lin, A Chen, T W Smith, G D Steele, and L B Chen. 1991. “Intracellular Heterogeneity in Mitochondrial Membrane Potentials Revealed by a J-Aggregate-Forming Lipophilic Cation JC-1.” *Proceedings of the*

National Academy of Sciences of the United States of America 88 (9): 3671–75.

Signorell, Andri et al., 2019. DescTools: Tools for descriptive statistics. R package version 0.99.27.

Spiess, Andrej-Nikolai, 2014. qpcR: Modeling and analysis of real-time PCR data. R package version 1.3-8. http://CRAN.R-project.org/package=qpcR

St-Pierre, Julie, Julie A. Buckingham, Stephen J. Roebuck, and Martin D. Brand. 2002. "Topology of Superoxide Production from Different Sites in the Mitochondrial Electron Transport Chain." *Journal of Biological Chemistry* 277 (47): 44784–90. https://doi.org/10.1074/jbc.M207217200.

Sun, Fei, Xia Huo, Yujia Zhai, Aojin Wang, Jianxing Xu, Dan Su, Mark Bartlam, and Zihe Rao. 2005. "Crystal Structure of Mitochondrial Respiratory Membrane Protein Complex II." *Cell* 121 (7): 1043–57. https://doi.org/10.1016/j.cell.2005.05.025.
Thevenaz, Philippe, Urs E. Ruttimann, and Michael Unser. 1998. "A Pyramid Approach to Subpixel Registration Based on Intensity." *IEEE Transactions on Image Processing* 7 (1): 27–41.

Wang, Liang, Xiaojing Zhang, Guozhen Cui, Judy Yuet-Wa Chan, Li Wang, Chuwen Li, Luchen Shan, et al. 2016. "A Novel Agent Exerts Antitumor Activity in Breast Cancer Cells by Targeting Mitochondrial Complex II." *Oncotarget* 7 (22): 32054–64. https://doi.org/10.18632/oncotarget.8410.

Weaver, Matthew J., Alison K. Kearns, Sascha Stump, Chun Li, Mariusz P. Gajewski, Kevin C. Rider, Donald S. Backos, Philip R. Reigan, Howard D. Beall, and Nicholas R. Natale. 2015. "AIMing towards Improved Antitumor Efficacy." *Bioorganic & Medicinal Chemistry Letters* 25 (8): 1765–70. https://doi.org/10.1016/j.bmcl.2015.02.063.

West, A. Phillip, Gerald S. Shadel, and Sankar Ghosh. 2011. "Mitochondria in Innate Immune Responses." *Nature Reviews. Immunology* 11 (6): 389–402. https://doi.org/10.1038/nri2975.

Yakes, F. Michael, and Bennett Van Houten. 1997. "Mitochondrial DNA Damage Is More Extensive and Persists Longer than Nuclear DNA Damage in Human Cells Following Oxidative Stress." *Proceedings of the National Academy of Sciences* 94 (2): 514–19. https://doi.org/10.1073/pnas.94.2.514.

Zorov, Dmitry B., Magdalena Juhaszova, and Steven J. Sollott. 2006. "Mitochondrial ROS-Induced ROS Release: An Update and Review." *Biochimica et Biophysica Acta (BBA) - Bioenergetics*, 14th European Bioenergetics Conference, 1757 (5): 509–17. https://doi.org/10.1016/j.bbabio.2006.04.029.

Appendix

10-Quinoline AIM | 10-Phenyl AIM | 10-Biphenoxy AIM

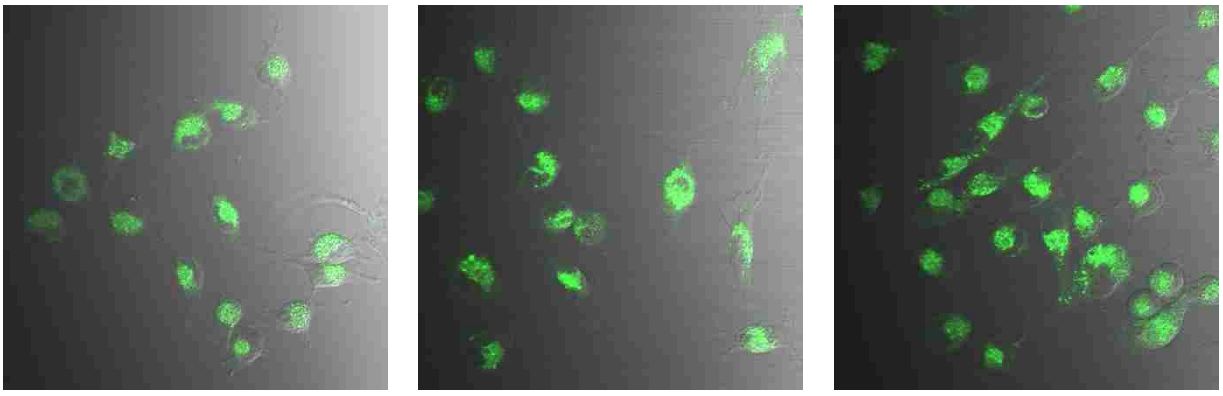

Figure A.3.1

SNB-19 cells treated with 1 μM of the 10-Quinoline AIM (left), 1 μM of the 10-Phenyl AIM (middle), and 1 μM of the 10-Biphenoxy AIM (right).

10-Quinoline AIM | HCS Nuclear Mask | Overlay

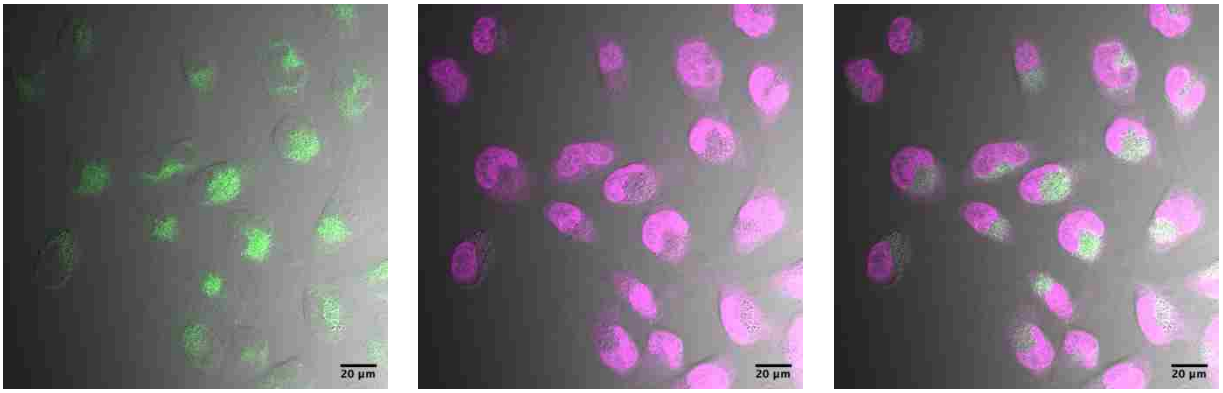

Figure A.3.2

SNB-19 cells treated with 1 μM of the 10-Quinoline AIM (green, left), 1x HCS Nuclear Mask (magenta, middle), and overlay (white, right). Scale bar shown is 20 μM.

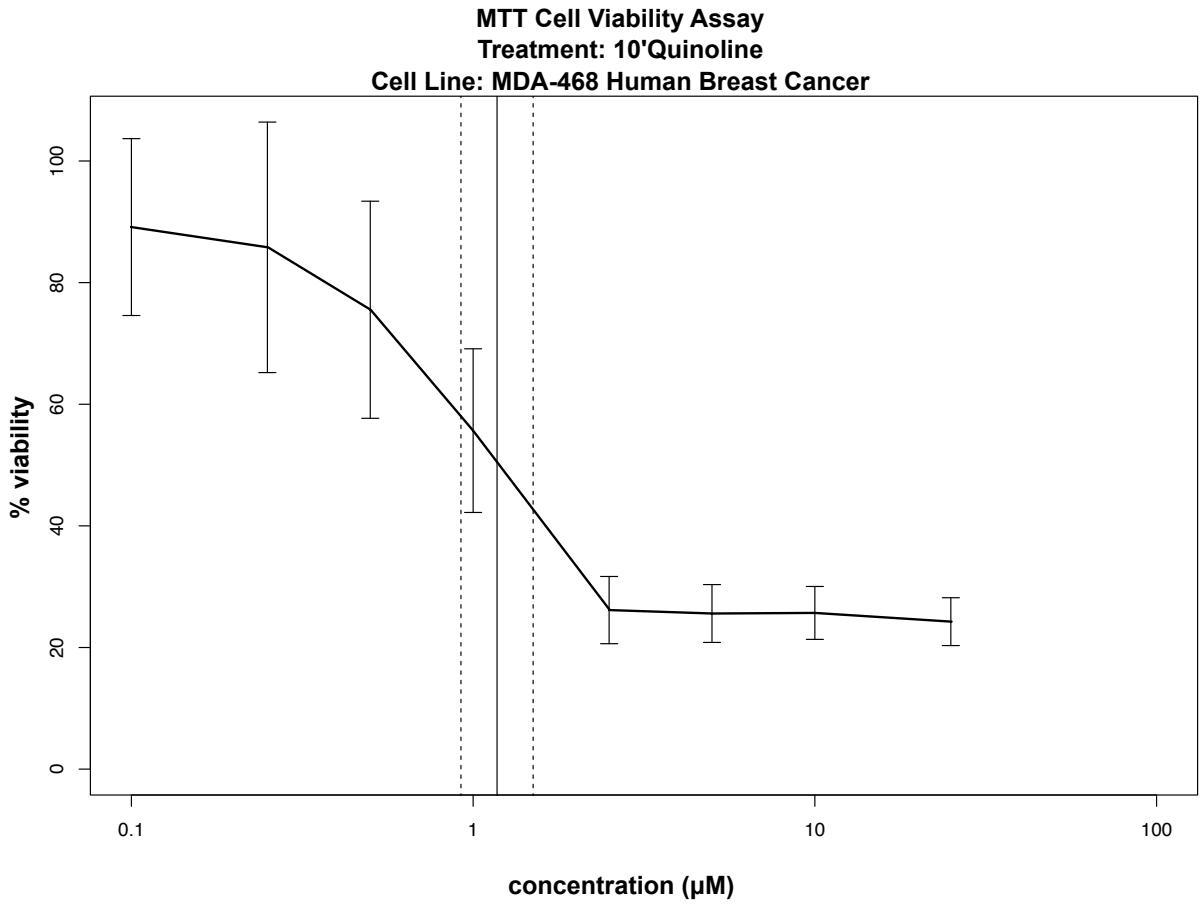

Figure A.3.3

Example of MDA-468 dose-response curve generated using the MTT cell viability assay as described (intermediate range). Error bars represent standard deviations, IC_{50} shown as a vertical black line with dotted lines representing the respective 95% confidence interval.

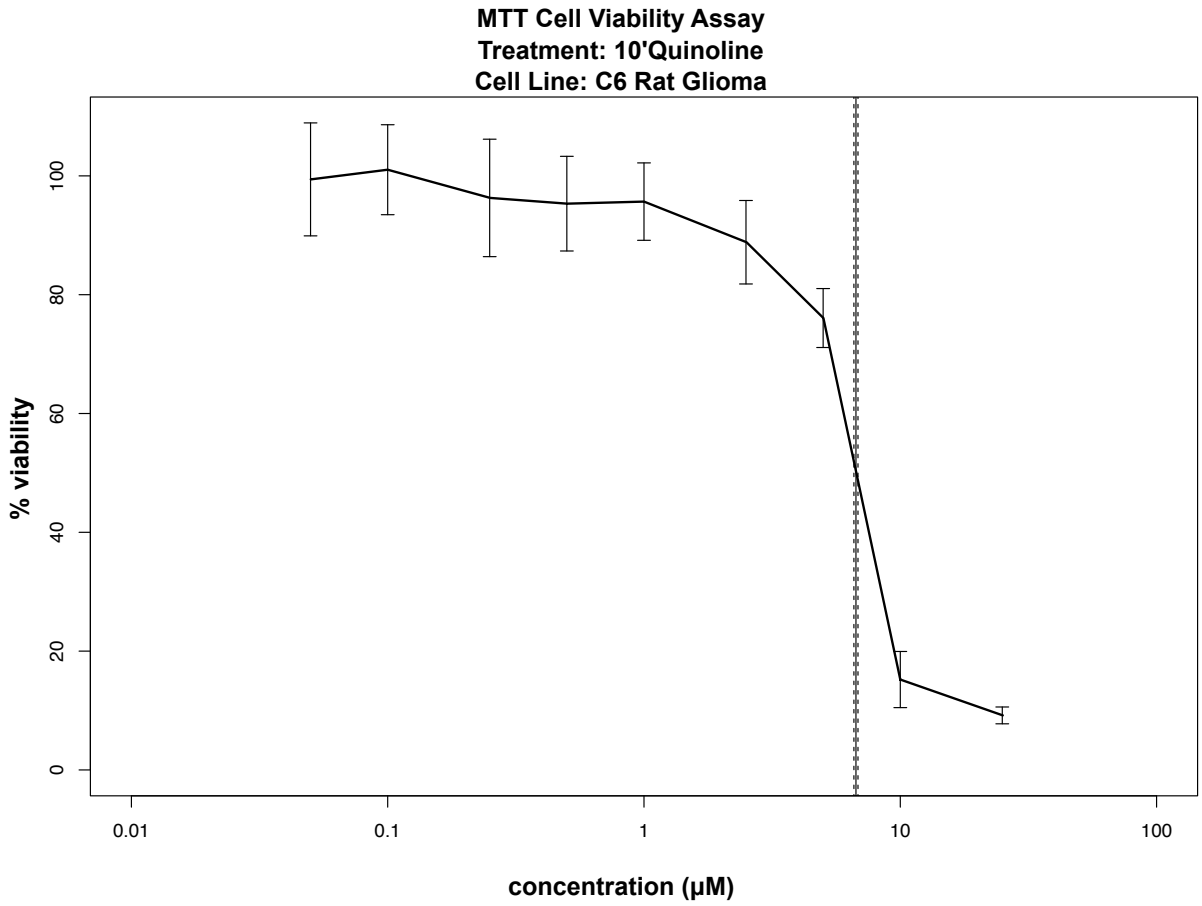

Figure A.3.4

Example of C6 dose-response curve generated using the MTT cell viability assay as described (intermediate range). Error bars represent standard deviations, IC_{50} shown as a vertical black line with dotted lines representing the respective 95% confidence interval.

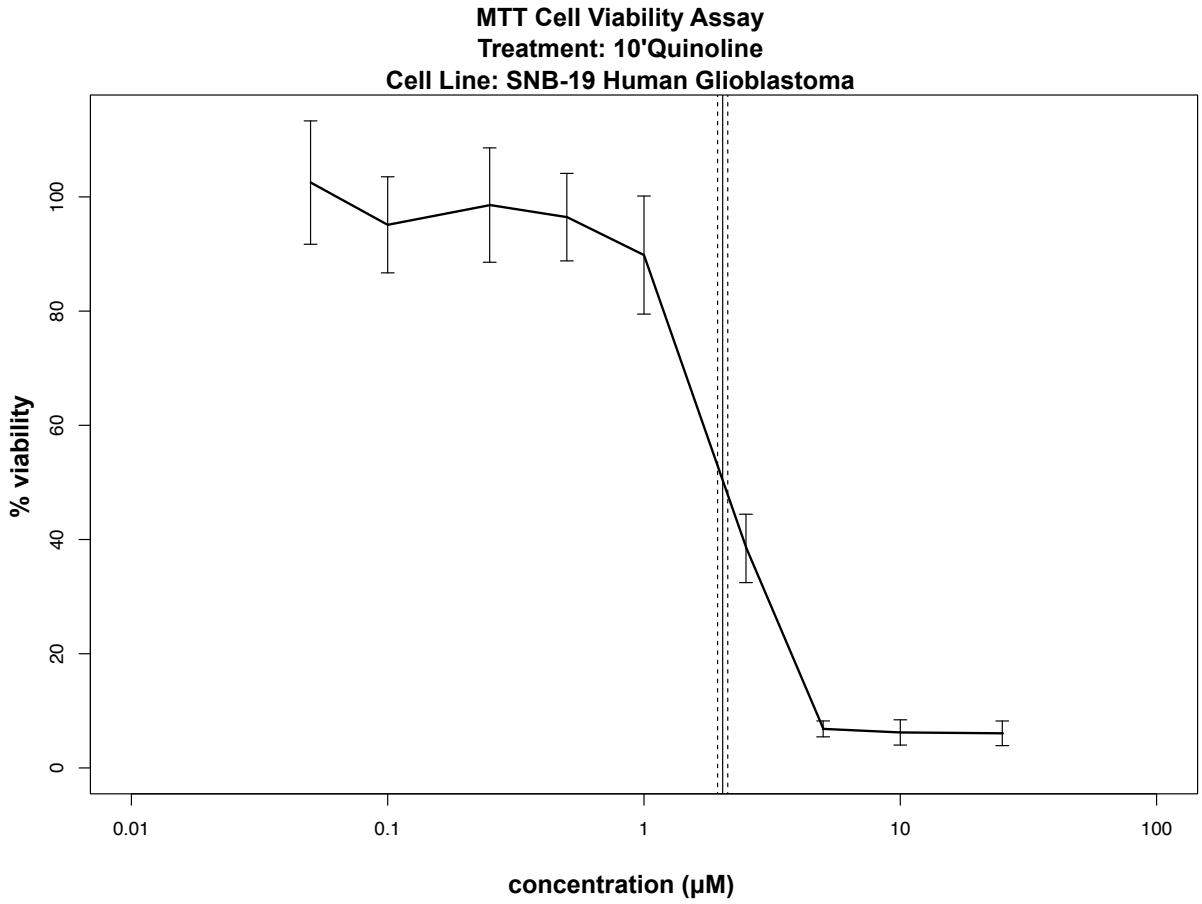

Figure A.3.5

Example of SNB-19 dose-response curve generated using the MTT cell viability assay as described (intermediate range). Error bars represent standard deviations, IC_{50} shown as a vertical black line with dotted lines representing the respective 95% confidence interval.

SNB-19			**MDA-468**		**C6**	
(Human Glioblastoma)			**(Human Breast Cancer)**		**(Rat Glioma)**	
MTT	IC_{50} (μM)	95% CI (±)	IC_{50} (μM)	95% CI (±)	IC_{50} (μM)	95% CI (±)
Chloro	2.41*‡	0.55*				
Phenyl	0.89*§	0.02*	0.82	0.03		
Biphenoxy	0.68	0.04				
O-Pyridyl	>25		6.34†	0.67	>25	
M-Pyridyl	7.76	0.42	1.29†	0.3	>25	
P-Pyridyl	7.08	0.26	3.1†	0.27	16.94	0.5
Quinoline	2.03	0.09	1.17†	0.25	6.71	0.12

*Previously published in BMCL, error for these values is ±Standard Deviation
§Matthew J. Weaver and ‡Alison K. Kearns performed these experiments.
†Michael J. Campbell contributed to these experiments.

Table A.3.1

Summary of MTT Results for 10-substituted AIMs.

SNB-19 **(Human Glioblastoma)**			**C6** **(Rat Glioma)**		**E-18** **(Primary Rat Astrocytes)**	
Compound	IC_{50} (μM)	95% CI (±)	IC_{50} (μM)	95% CI (±)	IC_{50} (μM)	95% CI (±)
10-Phenyl AIM	5.92	0.68	3.76	0.12	2.20	0.16
10-Biphenoxy AIM	4.44	0.16	3.83	0.10	2.09	0.20
10-Quinoline AIM			17.46	0.58	18.32	0.76

Table A.3.2

Summary of LDH Results for 10-substituted AIMs.

Complex I

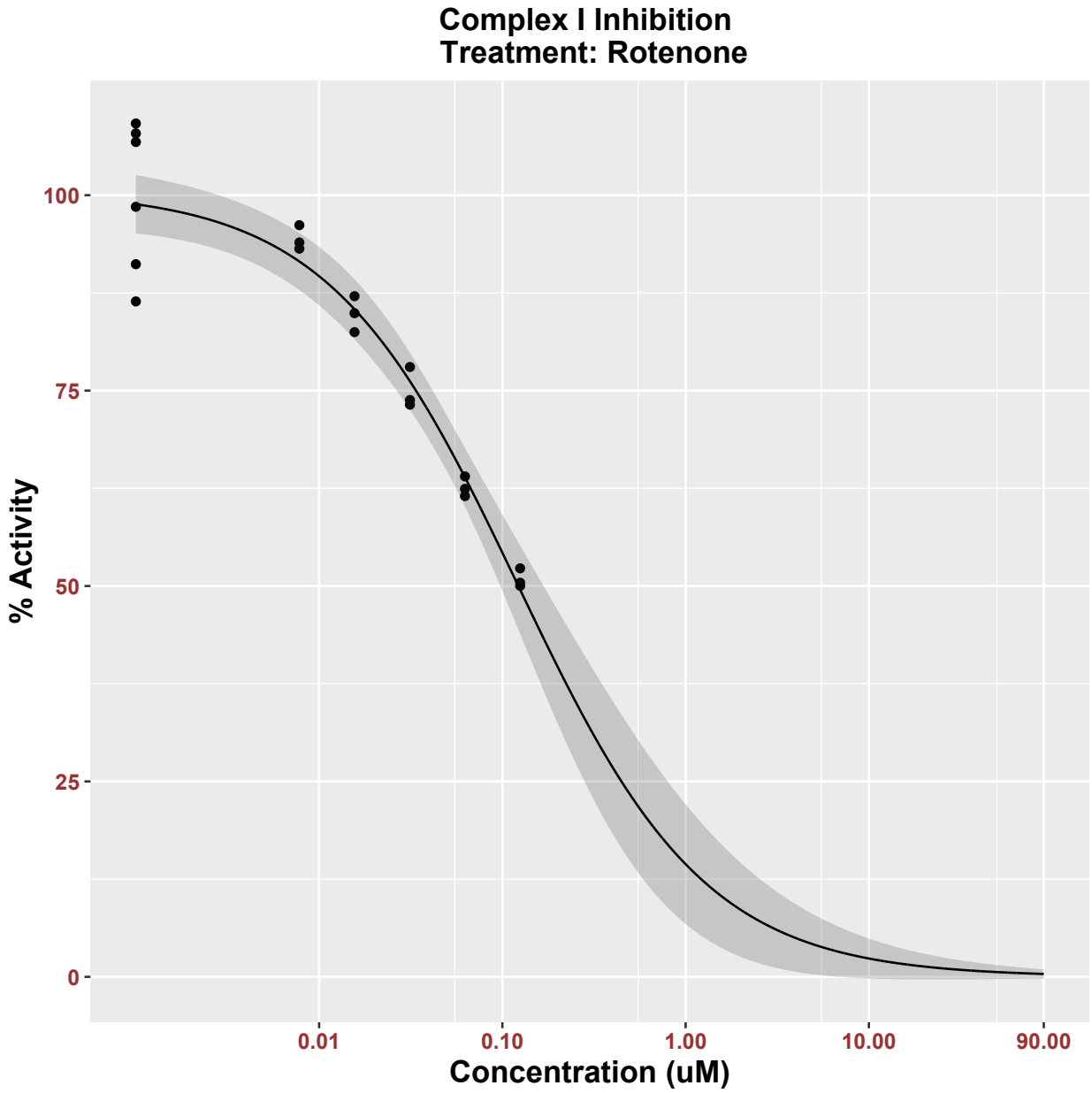

Figure A.3.6

Complex I Inhibition by Rotenone

Points represent individual measurements, curve represents three-parameter logistic fit with shaded area indicating the 95% confidence interval of the fit. (n=3)

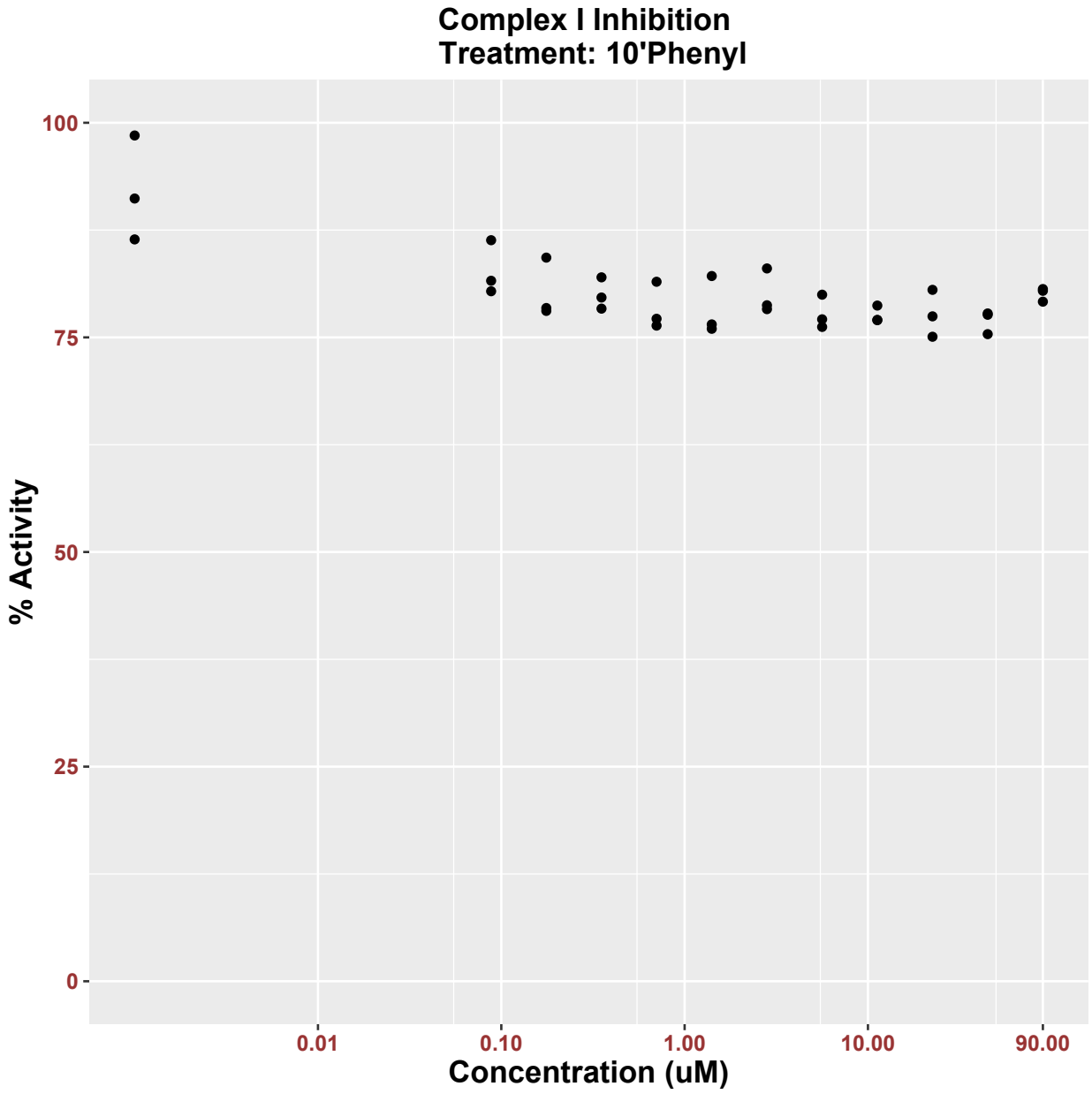

Figure A.3.7

Complex I Inhibition by 10-Phenyl AIM

Points represent individual measurements. (n=3)

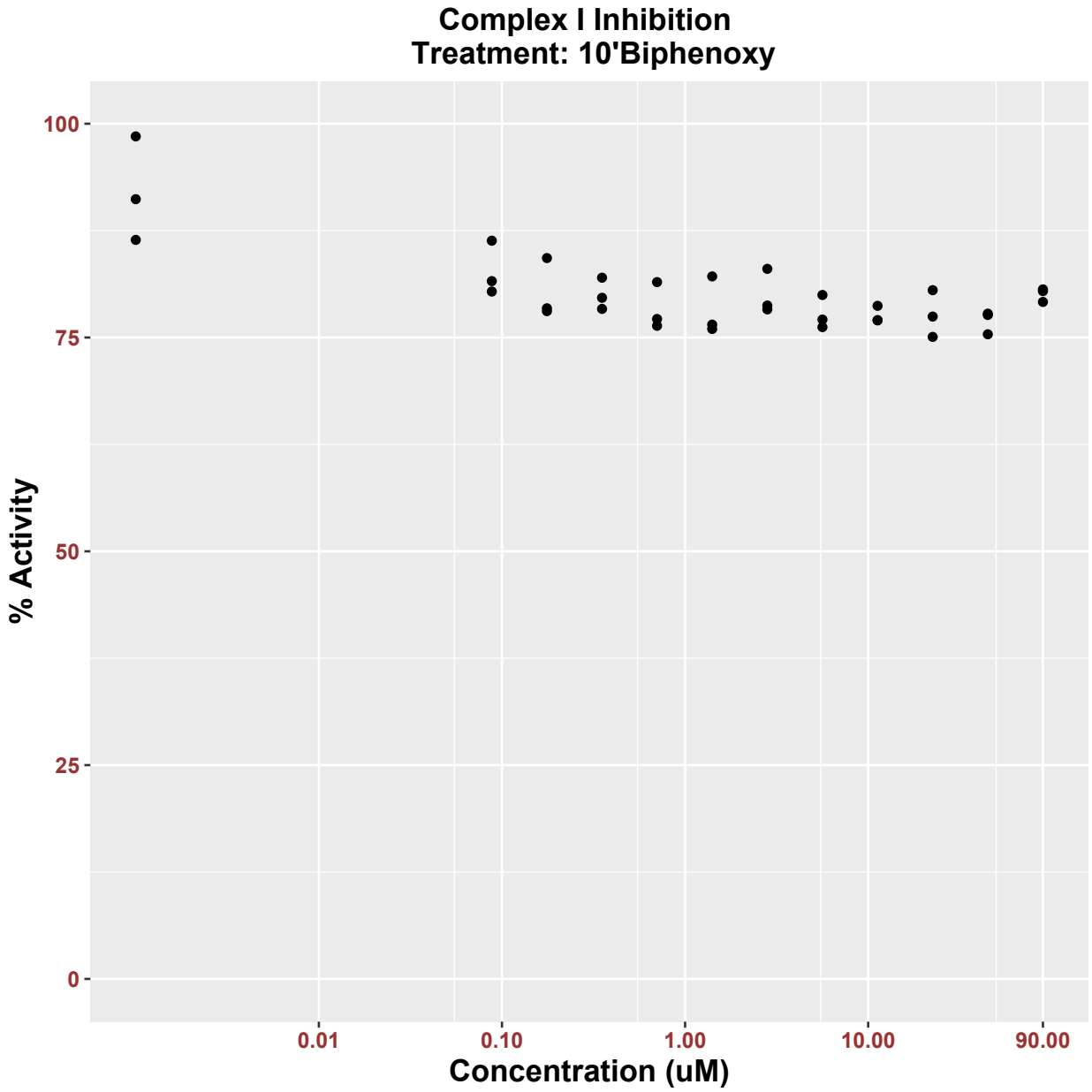

Figure A.3.8

Complex I Inhibition by 10-Biphenoxy AIM

Points represent individual measurements. (n=3)

Complex II + III

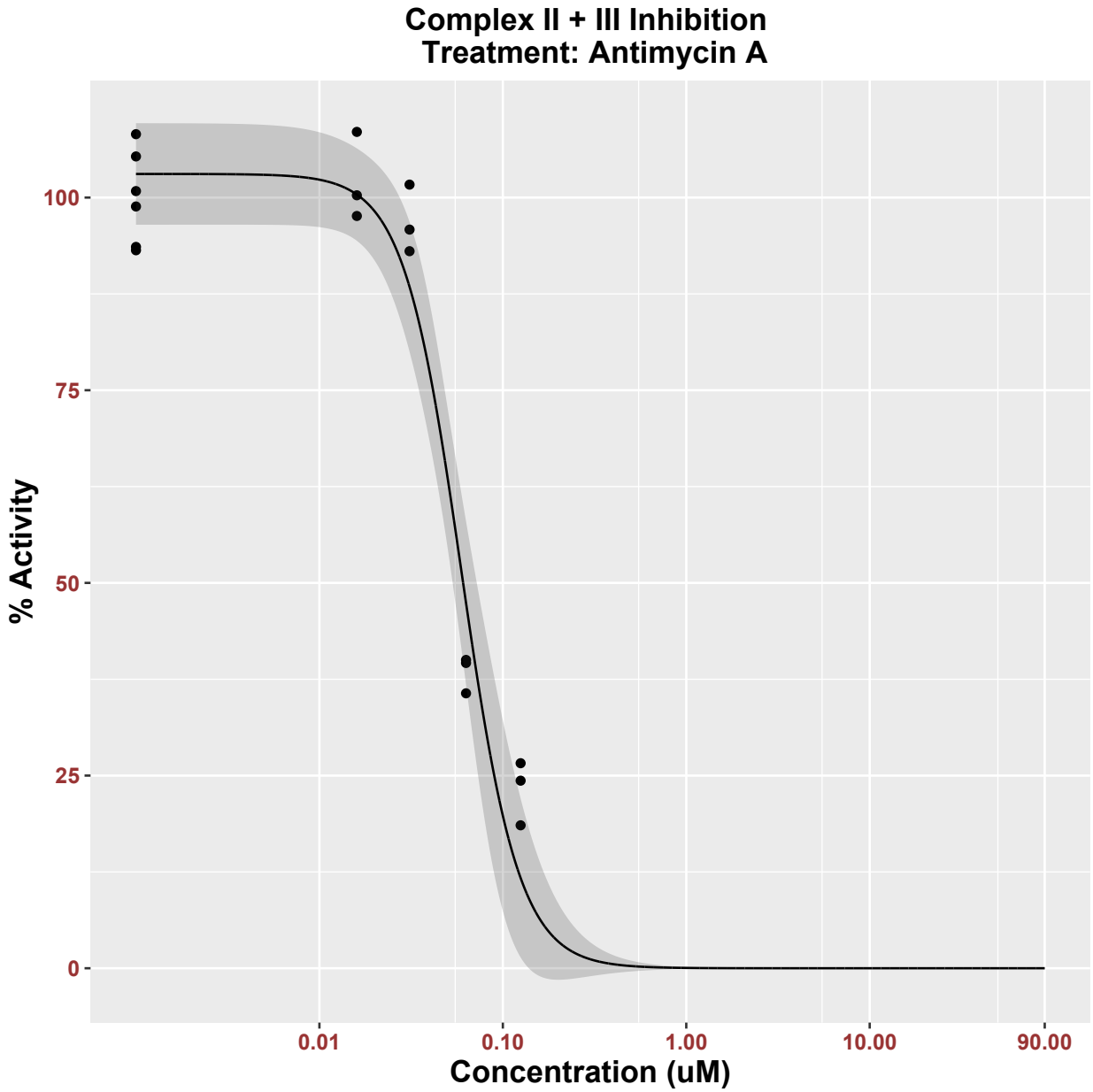

Figure A.3.9

Complex II + III inhibition curve for Antimycin A in intact mitochondria. Points represent individual measurements, curve represents three-parameter logistic fit with shaded area indicating the 95% confidence interval of the fit. (n=3)

Complex IV

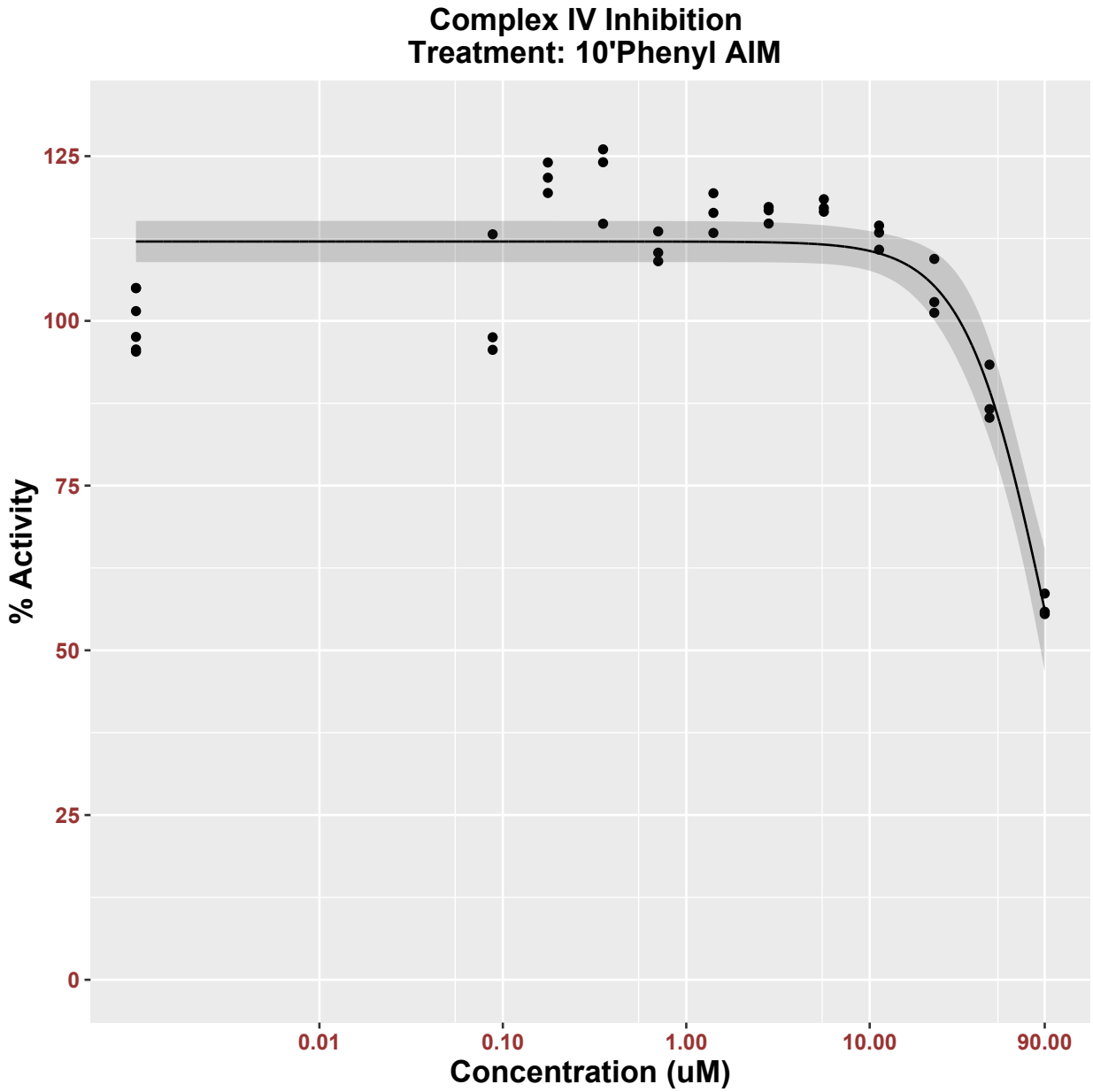

Figure A.3.10

Complex IV Inhibition by 10-Phenyl AIM

Points represent individual measurements, curve represents three-parameter logistic fit with shaded area indicating the 95% confidence interval of the fit. (n=3)

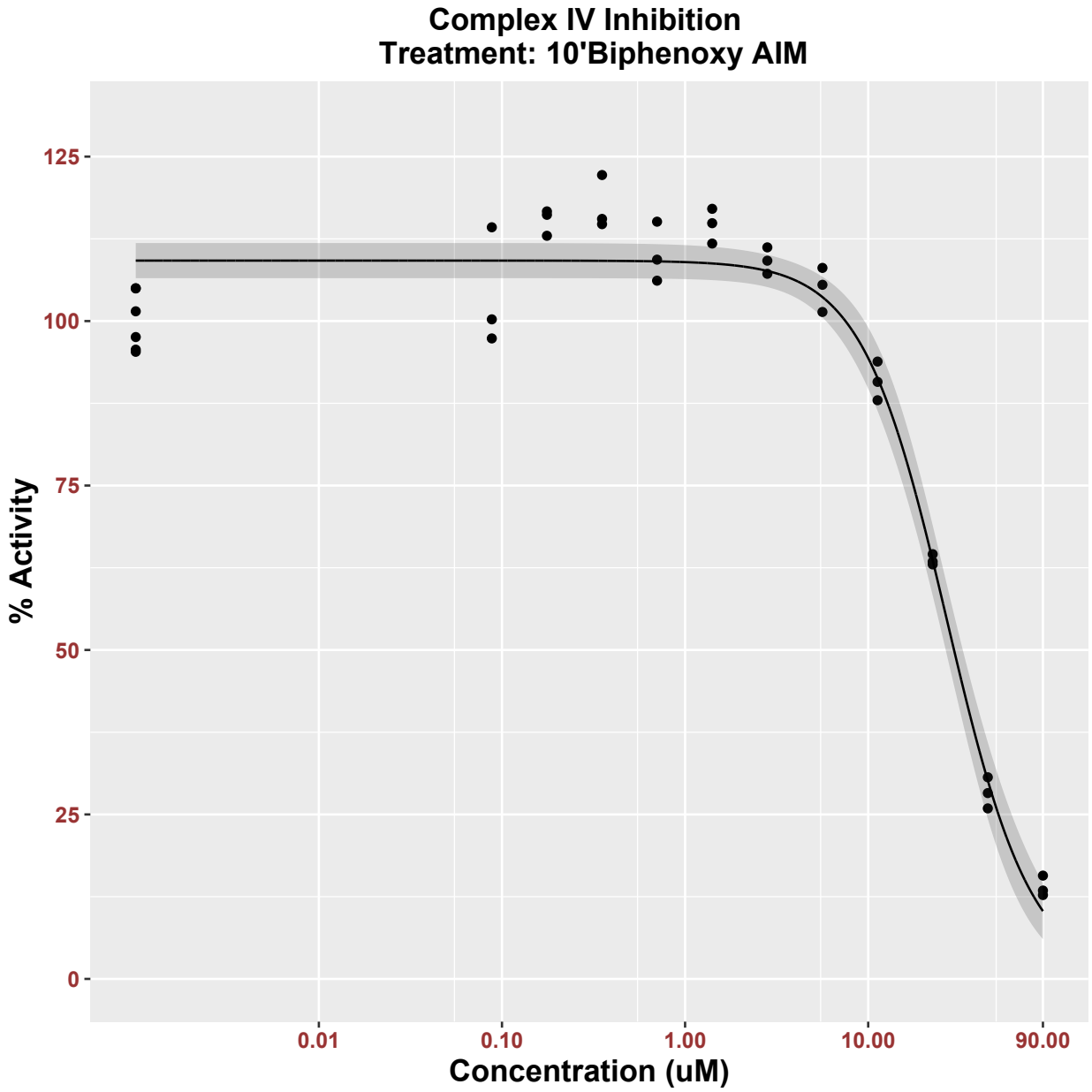

Figure A.3.11

Complex IV Inhibition by 10-Biphenoxy AIM

Points represent individual measurements, curve represents three-parameter logistic fit with shaded area indicating the 95% confidence interval of the fit. (n=3)

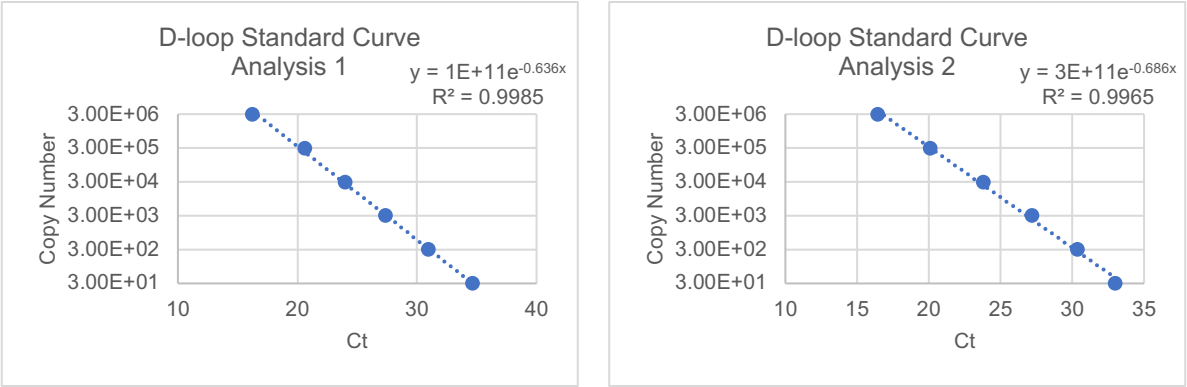

Figure A.3.12

Standards curves for D-loop mtDNA marker. Analysis 1 contained two control samples, three 12-hour samples and three 24-hour samples (native & relaxed). Analysis 2 contained one control sample, three 3-hour samples, and three 6-hour samples (native & relaxed). An exponential fit used to generate the standard curve.

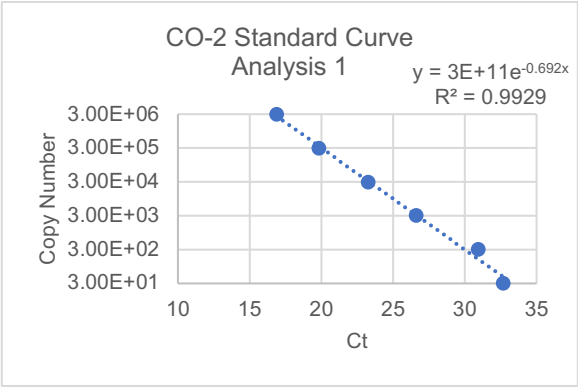

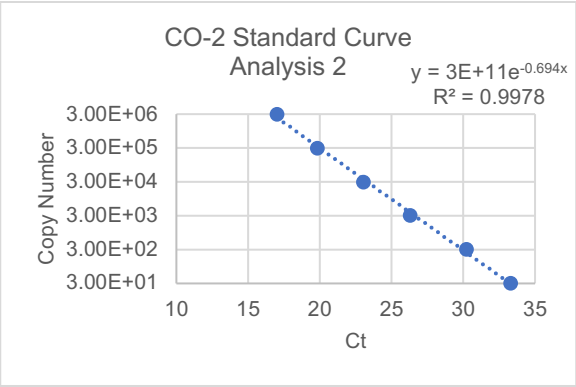

Figure A.3.13

Standards curves for CO-2 mtDNA marker. Analysis 1 contained two control samples, three 12-hour samples and three 24-hour samples (native & relaxed). Analysis 2 contained one control sample, three 3-hour samples, and three 6-hour samples (native & relaxed). An exponential fit used to generate the standard curve.

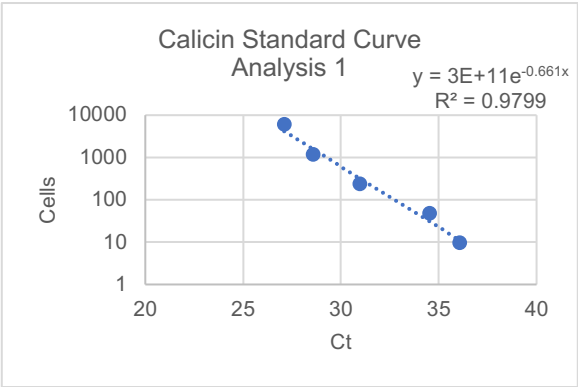

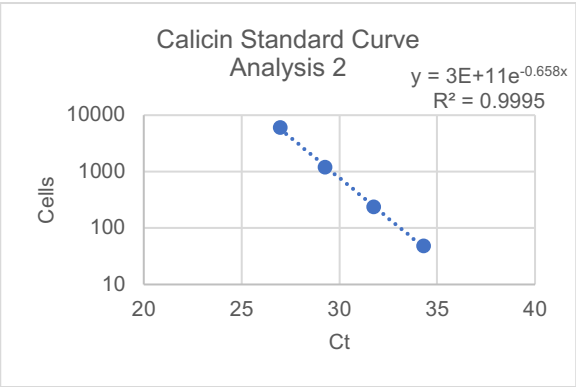

Figure A.3.14

Standards curves for Calicin nuclear DNA marker. Analysis 1 contained two control samples, three 12-hour samples and three 24-hour samples (native & relaxed). Analysis 2 contained one control sample, three 3-hour samples, and three 6-hour samples (native & relaxed). An exponential fit used to generate the standard curve.

mtDNA Damage and Copy Number (10-Phenyl AIM)

Figure A.3.15

Results for 1 μM treatment with 10-Phenyl AIM in D-loop gene of mtDNA (n=2)

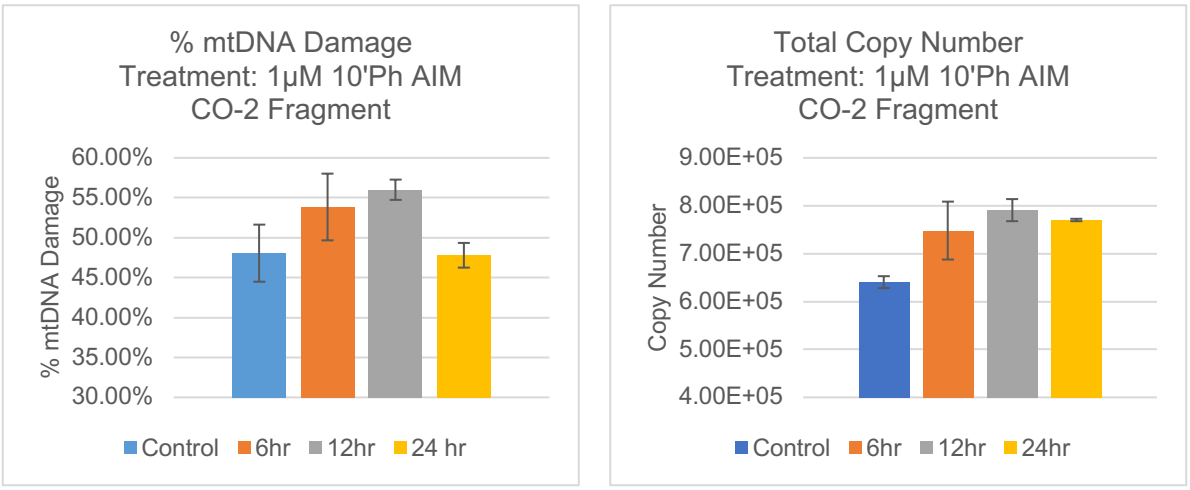

Figure A.3.16

Results for 1 μM treatment with 10-Phenyl AIM in CO-2 gene of mtDNA (n=2)

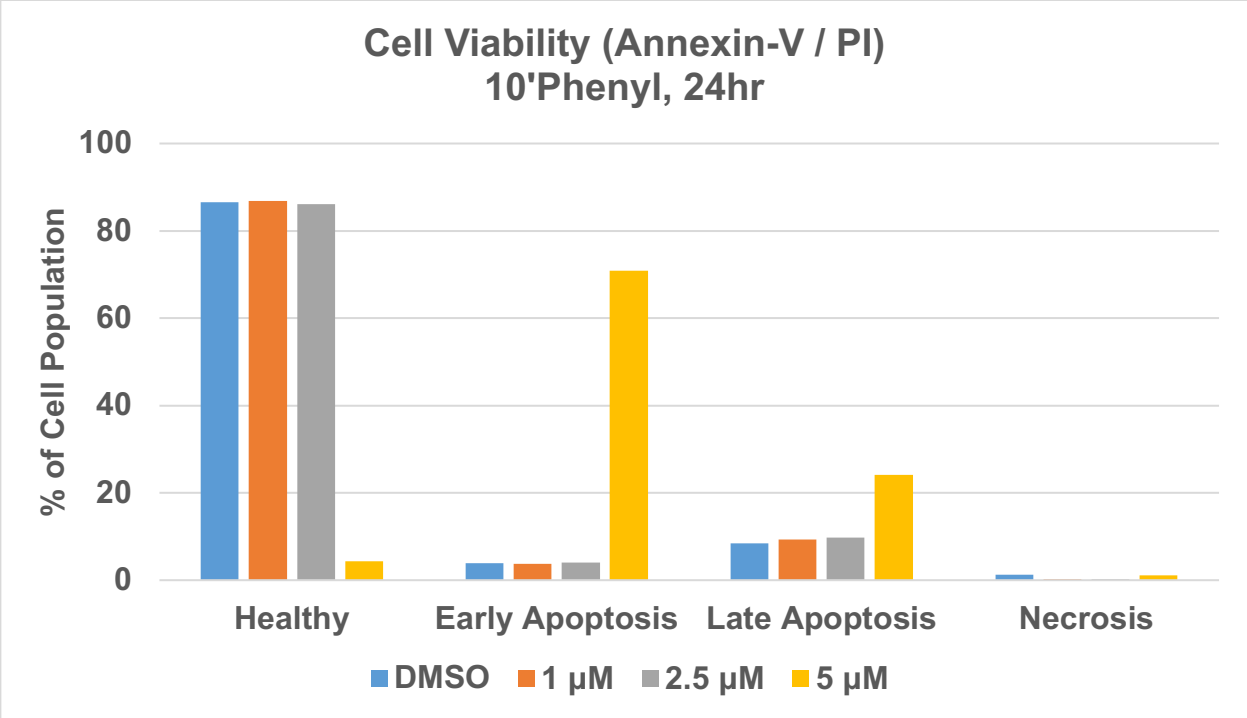

Figure A.3.17

Annexin-V/PI staining of 24-hour treatment with 10-Phenyl AIM at increasing concentrations in SNB-19 human glioblastoma cells. Results of one experiment.

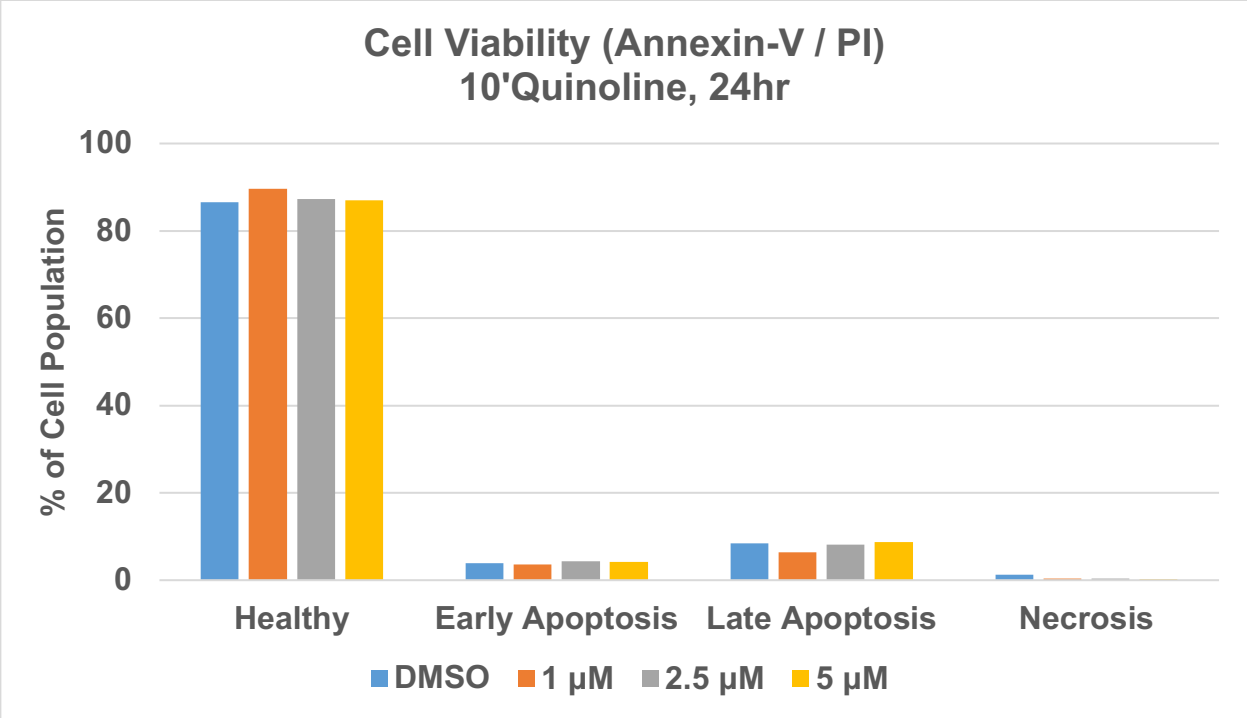

Figure A.3.18

Annexin-V/PI staining of 24-hour treatment with 10-Quinoline AIM at increasing concentrations in SNB-19 human glioblastoma cells. Results of one experiment.

Chapter 4 : Determination of Novel Quinolinediones Antitumor Activity

Sascha Stump[1], Michael J. Campbell[1] and Howard D. Beall[1*]

[1]Center for Environmental Health Sciences, Department of Biomedical and Pharmaceutical Sciences, University of Montana, Missoula, Montana 59812, United States of America

*Corresponding author

E-mail: howard.beall@umontana.edu

Abstract

It has been demonstrated previously that certain forms of cancer overexpress an enzyme known as NAD(P)H:quinone oxidoreductase 1 (NQO1). NQO1 can act to bioactivate antitumor agents through a reductive mechanism. Previous reports have suggested structural analogs of the 5,8-quinolinedione moiety of the naturally occurring compound lavendamycin could serve as substrates for NQO1 and cause apoptosis in tumor cells through bioactivation and redox cycling. In this work, we measure the activity of a novel set of 5,8-quinolinedione analogs in parent breast tumor cells and those overexpressing recombinant NQO1. We also determine the suitability of this set of compounds as substrates for NQO1 using a spectrophotometric assay.

Introduction

NAD(P)H:quinone oxidoreductase 1 (NQO1) is a cytosolic, two-electron reductase that is characterized by its capacity for using either NADH or NADPH as reducing cofactors. NQO1 has been categorized as a detoxification enzyme, and it can protect the cell from a broad range of chemically reactive metabolites (Riley and Workman 1992; Talalay and Dinkova-Kostova 2004). However, NQO1 can also function as an activating enzyme and can reduce quinones and other bioreductive antitumor agents to form reactive metabolites that can damage DNA through alkylation, crosslinking, or generation of reactive oxygen species (Ross et al. 2000).

In previous studies, the NQO1 activity in cancer cells has been positively correlated with the cytotoxicity of quinone antitumor agents (H. D. Beall et al. 1995; Plumb, Gerritsen, and Workman 1994; Robertson et al. 1994). Multiple series of indole-

and quinolinedione agents have been reported to be selectively toxic to cell lines with high NQO1 expression relative to those deficient in NQO1 (Howard D. Beall et al. 1998; Swann et al. 2001; Fryatt et al. 2004). Increased NQO1 expression has also been observed in tumors or cell lines from lung, liver, colon, and breast cancer (Schlager and Powis 1990; Malkinson et al. 1992; Cresteil and Jaiswal 1991).

Lavendamycin is a naturally occurring antibiotic that has been shown to have potent antitumor activity (Doyle et al. 1981) (**Figure 4.1**). However, due to the non-specific cytotoxicity observed with lavendamycin it is not used clinically (Fang et al. 2003). As a result of this, many synthetic analogs of lavendamycin have been developed to improve its solubility and therapeutic index (Hassani et al. 2005, 2008; Cai et al. 2010). It has also been reported that synthetic analogs containing the 5,8-quinolinedione moiety found in lavendamycin can overcome the associated non-specific cytotoxicity and be used as selective antitumor agents in cells overexpressing NQO1 (Cai et al. 2010). Together, these previous findings suggest there is potential for creating lavendamycin-inspired 5,8-quinolinedione analogs with improved efficacy and selectivity for treatment of cancers that overexpress NQO1.

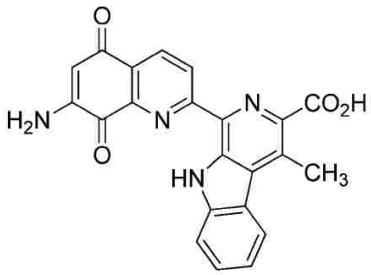

Lavendamycin

Figure 4.1 Structure of Lavendamycin

(Keyari et al. 2013)

In this study we explored the cytotoxic effects of a set of novel 5,8-quinolinediones (**Figure 4.2**; synthesis and characterization by Rob Sammelson's laboratory at Ball State University, Muncie, IN) in two breast tumor cell lines with differing amounts of NQO1 expression to assess the relative cytotoxicity of these compounds by MTT assay. The MDA-468-WT breast tumor cell line was previously shown to have no measurable NQO1 activity. In contrast, the MDA-468-NQ16 cell line, which has been stably transfected with NQO1, was shown to have approximately 1070 nmol/min/mg (total cell protein) NQO1 activity as measured by reduction of dichlorophenolindophenol (DCPIP) (Keyari et al. 2013). In addition, we performed a previously developed quinone reduction assay to determine the suitability of these compounds as substrates for NQO1-dependent reduction and subsequent re-oxidation, as measured by their ability to reduce cytochrome *c* (Keyari et al. 2013).

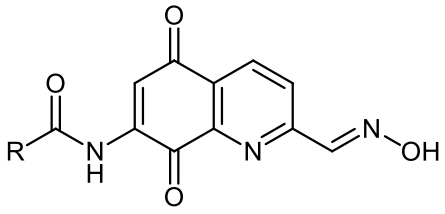

RRS01 R= Methyl Sample 2.1 mg MW= 259.22
RRS02 R= Ethyl Sample 4.7 mg MW= 273.24
RRS03 R= Propyl Sample 6.0 mg MW= 287.27
RRS04 R= Isopropyl Sample 4.4 mg MW= 287.27

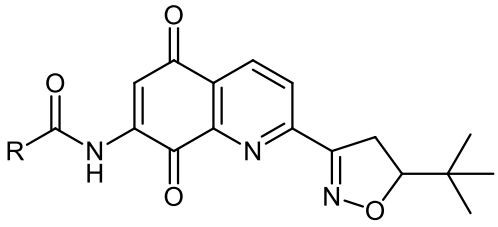

RRS05 R= Methyl Sample 1.6 mg MW= 341.36
RRS06 R= Ethyl Sample 4.2 mg MW= 355.39
RRS07 R= Propyl Sample 4.4 mg MW= 369.41
RRS08 R= Isopropyl Sample 3.3 mg MW= 369.41

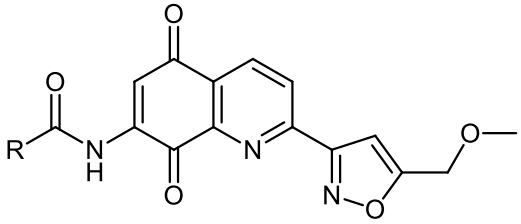

RRS09 R= Methyl Sample 2.6 mg MW= 327.29
RRS10 R= Ethyl Sample 4.4 mg MW= 341.32
RRS11 R= Propyl Sample 2.4 mg MW= 355.34
RRS12 R= Isopropyl Sample 5.0 mg MW= 355.34

Figure 4.2 Novel 5,8-quinolinediones

Methods

Cell Viability Assay

MDA-468-WT or MDA-468-NQ16 cells were grown in RPMI-1640 medium with 10% FBS, L-Glutamine (2 mM) and Penicillin-Streptomycin (1x, 100 µg/mL) added to 80 - 90% confluence under optimal growth conditions (37 C, 5% CO_2, humidified atmosphere). Cells were washed with PBS (2 mL) and then treated with Trypsin EDTA (2 mL) to detach cells from culture flask prior to counting with a Coulter counter. Cells were diluted to 10,000 cells / mL and plated on a 96-well plate with 100 µL per well (1000 cells / well). Cells were grown in optimal growth conditions and allowed to adhere overnight. Treatment solutions were prepared in growth medium at various concentrations using a 5 mM compound stock solution prepared previously in sterile DMSO. Medium was removed from the 96-well plate via aspiration and treatment solutions were added as outlined for the intermediate treatment range (**Table 4.1**). Cells were grown in treatment medium for 24 hours and then treatment medium was removed via aspiration and 100 µL of untreated growth medium was added to each well and cells were allowed to grow for a four-day growth period. Following the growth period, 50 µL of MTT solution (1 mg/mL in growth medium) was added to each well and the 96-well plate was placed on a plate shaker for 5 minutes to mix. The plate was then incubated at growth conditions for 4 hours before removing medium/MTT solution from the wells carefully via aspiration to avoid disturbing the formazan crystals. One hundred µL of DMSO was then added to each well and the plate was placed on a plate shaker for 5 minutes to dissolve the crystals. A SpectraMax 190 plate reader was used to measure

the absorbance of the wells at 562 nm. Three replicate experiments were run per compound.

Table 4.1 96-well Plate Layout MTT Assay (Intermediate Range)

Column:	#1	#2	#3	#4	#5	#6	#7	#8	#9	#10	#11	#12
Treatment:	No Cells	Medium Control	DMSO Control	0.1 µM	0.25 µM	0.5 µM	1 µM	2.5 µM	5 µM	10 µM	25 µM	DMSO Control

Data Analysis

IC_{50} values were calculated using the 'R' statistical computing software and the 'ic50' package (R Core Team, 2014; Frommolt, 2010). This package fits a logistic model to the dose-response data collected using the MTT assay and approximates the concentration of the compound required to inhibit the growth of the cells by 50% versus the DMSO control (IC_{50}).

Quinone Reduction Assay

5,8-quinolinedione reduction was measured using a previously published method (Keyari et al. 2013). The reaction mixture consisted of 70 µM cytochrome *c* combined with either 1 µg (RRS-01 – RRS-08) or 0.25 µg (RRS-09 – RRS-12) of recombinant hNQO1 (gift from David Ross, University of Colorado Denver, Denver, CO) in a solution containing 25 µM of the test compound, 0.7 mg/mL of BSA, 0.1% Tween-20 and 25 mM Tris Buffer at pH 7.4. Immediately prior to reading, 1 mM of NADH from a 20 mM stock was added to create a final volume of 1 mL in a cuvette with a 10 mm pathlength. The solution was inverted to mix and change in absorbance at 550 nm was recorded

immediately using a SpectraMax M4 microplate reader in kinetic mode for 30 seconds. Each reaction was performed in triplicate. Quinone reduction was defined as the rate of cytochrome *c* reduction in μmol/min/mg NQO1.

Results

Cell Viability

Cytotoxicity to the MDA-468 WT and NQ16 cells was determined using the MTT cell viability assay (**Table 4.2**). All of the novel analogs were active against both cell lines at the single digit micromolar level, and several of the 5,8-quinolinedione showed submicromolar activity in the MDA-468 breast tumor cells. The most active compound was the methyloxymethylisoxazole, RRS-10, with an IC_{50} value of 269 nM. Three of the four N-hydroxyimino derivatives showed increased toxicity to the NQO1-transfected variant suggesting a role for this enzyme in selective toxicity. RRS-02 had the highest WT/NQO1 IC_{50} ratio of 1.84, indicating a nearly two-fold greater toxicity to the NQO1-expressing cells. Cytotoxicity was greater going from R = methyl to R = isopropyl for the *N*-hydroxyimino compounds (RRS-01 – RRS-04), the reverse for *t*-butylisoxazoles (RRS-05 – RRS-08), and mixed for the methyoxymethylisoxazoles (RRS-09 – RRS-12).

Table 4.2 Cell viability results for RRS compounds

Cell Viability Results					
Cell Line:	**MDA-468-WT**		**MDA-468-NQ16**		**WT/NQ16**
Compound	*IC_{50} (μM)*	*± 95% CI*	*IC_{50} (μM)*	*± 95% CI*	*IC_{50} Ratio*
RRS-01	3.84	0.05	4.33	0.72	0.89
RRS-02	2.99	0.18	1.62	0.10	1.84
RRS-03	1.43	0.09	1.40	0.08	1.02
RRS-04	1.35	0.12	0.81	0.04	1.67
RRS-05	0.95	0.08	0.80	0.14	1.18
RRS-06	1.13	0.07	1.66	0.07	0.68
RRS-07	1.46	0.08	1.97	0.26	0.74
RRS-08	3.16	0.13	3.68	0.05	0.86
RRS-09	0.83	0.09	1.83	0.24	0.45
RRS-10	0.27	0.02	0.45	0.02	0.60
RRS-11	0.80	0.06	1.19	0.08	0.67
RRS-12	0.73	0.03	0.63	0.04	1.17

Table 4.2

MTT Cell Viability Results for RRS compounds in MDA-468-WT and MDA-NQ16 breast cancer cells. (n=3)

Quinone Reduction

Quinone reduction was monitored using a spectrophotometric assay that measures cytochrome *c* reduction by the NQO1-reduced 5,8-quinolinedione (**Table 4.3**). The methyloxymethylisoxazole compounds (RRS-09 – RRS-12) were by far the best NQO1 substrates, with reduction rates of approximately 100 μmol/min/mg NQO1. NQO1 reduction rates generally decreased with bulk at R as expected (exception was RRS-12). Compound RRS-08 had the greatest bulk at both ends of the molecule and was by far the poorest substrate for NQO1.

Table 4.3 Quinone reduction results for RRS compounds

Quinone Reduction Results		
Compound	Red. Rate (µmol/min/mg)	± SD
RRS-01	25.75	1.72
RRS-02	18.03	0.42
RRS-03	20.13	0.07
RRS-04	12.42	0.11
RRS-05	19.18	0.79
RRS-06	16.31	0.12
RRS-07	13.30	0.22
RRS-08	2.47*	0.09
RRS-09	121.97	3.44
RRS-10	90.90	8.00
RRS-11	88.51	3.47
RRS-12	107.41	3.02

Quinone reduction results for RRS compounds using recombinant hNQO1. (n=3, *n=2)

Discussion

The novel 5,8-quinolinediones have excellent activity against both the NQO1-null and NQO1-expressing MDA-468-WT breast tumor cells, but exhibited mixed results regarding selectivity to NQO1-expressing cells. The most NQO1 selective compounds were RRS-02 and RRS-04, and the most NQO1 protective were RRS-09 and RRS-10. However, many of the other analogs showed better activity in the parent cells, suggesting that NQO1 is protective against those compounds. This has been shown previously for simple 5,8-quinolinediones, whereas those compounds that more closely resemble the lavendamycin structure tend to be more selective to NQO1-expressing cells (Hassani et al. 2005, 2008; Behforouz et al. 2007; Keyari et al. 2013). This result could also be due to involvement of other reductases in the breast cancer cells acting to convert the RRS compounds to bioactive metabolites, as has been suggested previously for other quinone-based compounds (Beall and Winski 2000). This explanation would also align with the observation that although the methyloxymethylisoxazole compounds (RRS-09 – RRS-12) were the most suitable reduction substrates for NQO1 and had the highest antitumor activity, higher NQO1 expression was also protective to the tumor cells for these compounds.

References

Beall, H. D., A. M. Murphy, D. Siegel, R. H. Hargreaves, J. Butler, and D. Ross. 1995. "Nicotinamide Adenine Dinucleotide (phosphate): Quinone Oxidoreductase (DT-Diaphorase) as a Target for Bioreductive Antitumor Quinones: Quinone Cytotoxicity and Selectivity in Human Lung and Breast Cancer Cell Lines." *Molecular Pharmacology* 48 (3): 499–504.

Beall, Howard D., and Shannon L. Winski. 2000. "Mechanisms of Action of Quinone-Containing Alkylating Agents. I: NQO1-Directed Drug Development." *Front Biosci* 5: D639–48.

Beall, Howard D., Shannon Winski, Elizabeth Swann, Anna R. Hudnott, Ann S. Cotterill, Noeleen O'Sullivan, Stephen J. Green, et al. 1998. "Indolequinone Antitumor Agents: Correlation between Quinone Structure, Rate of Metabolism by Recombinant Human NAD(P)H:Quinone Oxidoreductase, and in Vitro Cytotoxicity." *Journal of Medicinal Chemistry* 41 (24): 4755–66. https://doi.org/10.1021/jm980328r.

Behforouz, Mohammad, Wen Cai, Farahnaz Mohammadi, Mark G. Stocksdale, Zhengxiang Gu, Mohammad Ahmadian, Darric E. Baty, et al. 2007. "Synthesis and Evaluation of Antitumor Activity of Novel N-Acyllavendamycin Analogues and Quinoline-5,8-Diones." *Bioorganic & Medicinal Chemistry* 15 (1): 495–510. https://doi.org/10.1016/j.bmc.2006.09.039.

Cai, Wen, Mary Hassani, Rajesh Karki, Ervin D. Walter, Katherine H. Koelsch, Hassan Seradj, Jayana P. Lineswala, et al. 2010. "Synthesis, Metabolism and in Vitro Cytotoxicity Studies on Novel Lavendamycin Antitumor Agents." *Bioorganic & Medicinal Chemistry* 18 (5): 1899–1909. https://doi.org/10.1016/j.bmc.2010.01.037.

Cresteil, Thierry, and Anil K. Jaiswal. 1991. "High Levels of Expression of the NAD(P)H:Quinone Oxidoreductase (NQO1) Gene in Tumor Cells Compared to Normal Cells of the Same Origin." *Biochemical Pharmacology* 42 (5): 1021–27. https://doi.org/10.1016/0006-2952(91)90284-C.

Doyle, Terrence W., David M. Balitz, Robert E. Grulich, Donald E. Nettleton, Steven J. Gould, Chou-hong Tann, and Ann E. Moews. 1981. "Structure Determination of Lavendamycin- a New Antitumor Antibiotic from Streptomyces Lavendulae." *Tetrahedron Letters* 22 (46): 4595–98. https://doi.org/10.1016/S0040-4039(01)82990-7.

Fang, Yanan, Corinne M. Linardic, D. Ashley Richardson, Wen Cai, Mohammad Behforouz, and Robert T. Abraham. 2003. "Characterization of the Cytotoxic Activities of Novel Analogues of the Antitumor Agent, Lavendamycin1." *Molecular Cancer Therapeutics* 2 (6): 517–26.

Fryatt, Tara, Hanna I Pettersson, Walter T Gardipee, Kurtis C Bray, Stephen J Green, Alexandra M. Z Slawin, Howard D Beall, and Christopher J Moody. 2004. "Novel

Quinolinequinone Antitumor Agents: Structure-Metabolism Studies with NAD(P)H:quinone Oxidoreductase (NQO1)." *Bioorganic & Medicinal Chemistry* 12 (7): 1667–87. https://doi.org/10.1016/j.bmc.2004.01.021.

Hassani, Mary, Wen Cai, David C. Holley, Jayana P. Lineswala, Babu R. Maharjan, G. Reza Ebrahimian, Hassan Seradj, et al. 2005. "Novel Lavendamycin Analogues as Antitumor Agents: Synthesis, in Vitro Cytotoxicity, Structure−Metabolism, and Computational Molecular Modeling Studies with NAD(P)H:Quinone Oxidoreductase 1." *Journal of Medicinal Chemistry* 48 (24): 7733–49. https://doi.org/10.1021/jm050758z.

Hassani, Mary, Wen Cai, Katherine H. Koelsch, David C. Holley, Anthony S. Rose, Fatemeh Olang, Jayana P. Lineswala, et al. 2008. "Lavendamycin Antitumor Agents: Structure-Based Design, Synthesis, and NAD(P)H:Quinone Oxidoreductase 1 (NQO1) Model Validation with Molecular Docking and Biological Studies." *Journal of Medicinal Chemistry* 51 (11): 3104–15. https://doi.org/10.1021/jm701066a.

Keyari, Charles M., Alison K. Kearns, Nathan S. Duncan, Emily A. Eickholt, Geoffrey Abbott, Howard D. Beall, and Philippe Diaz. 2013. "Synthesis of New Quinolinequinone Derivatives and Preliminary Exploration of Their Cytotoxic Properties." *Journal of Medicinal Chemistry* 56 (10): 3806–19. https://doi.org/10.1021/jm301689x.

Malkinson, Alvin M., David Siegel, Gerald L. Forrest, Adi F. Gazdar, Herbert K. Oie, Daniel C. Chan, Paul A. Bunn, et al. 1992. "Elevated DT-Diaphorase Activity and Messenger RNA Content in Human Non-Small Cell Lung Carcinoma: Relationship to the Response of Lung Tumor Xenografts to Mitomycin C." *Cancer Research* 52 (17): 4752–57.

Plumb, J. A., M. Gerritsen, and P. Workman. 1994. "DT-Diaphorase Protects Cells from the Hypoxic Cytotoxicity of Indoloquinone EO9." *British Journal of Cancer* 70 (6): 1136–43. https://doi.org/10.1038/bjc.1994.461.

Riley, Robert J., and Paul Workman. 1992. "DT-Diaphorase and Cancer Chemotherapy." *Biochemical Pharmacology* 43 (8): 1657–69. https://doi.org/10.1016/0006-2952(92)90694-E.

Robertson, N., A. Haigh, G. E. Adams, and I. J. Stratford. 1994. "Factors Affecting Sensitivity to EO9 in Rodent and Human Tumour Cells in Vitro: DT-Diaphorase Activity and Hypoxia." *European Journal of Cancer* 30 (7): 1013–19. https://doi.org/10.1016/0959-8049(94)90134-1.

Ross, David, Jadwiga K Kepa, Shannon L Winski, Howard D Beall, Adil Anwar, and David Siegel. 2000. "NAD(P)H:quinone Oxidoreductase 1 (NQO1): Chemoprotection, Bioactivation, Gene Regulation and Genetic Polymorphisms." *Chemico-Biological Interactions* 129 (1): 77–97. https://doi.org/10.1016/S0009-2797(00)00199-X.

Schlager, John J., and Garth Powis. 1990. "Cytosolic NAD(P)H:(Quinone-Acceptor)oxidoreductase in Human Normal and Tumor Tissue: Effects of Cigarette

Smoking and Alcohol." *International Journal of Cancer* 45 (3): 403–9. https://doi.org/10.1002/ijc.2910450304.

Swann, Elizabeth, Paola Barraja, Ann M. Oberlander, Walter T. Gardipee, Anna R. Hudnott, Howard D. Beall, and Christopher J. Moody. 2001. "Indolequinone Antitumor Agents: Correlation between Quinone Structure and Rate of Metabolism by Recombinant Human NAD(P)H:Quinone Oxidoreductase. Part 2." *Journal of Medicinal Chemistry* 44 (20): 3311–19. https://doi.org/10.1021/jm010884c.

Talalay, Paul, and Albena T Dinkova-Kostova. 2004. "Role of Nicotinamide Quinone Oxidoreductase 1 (NQO1) in Protection against Toxicity of Electrophiles and Reactive Oxygen Intermediates." In *Methods in Enzymology*, 382:355–64. Quinones and Quinone Enzymes, Part B. Academic Press. http://www.sciencedirect.com/science/article/pii/S0076687904820196.

Chapter 5 : Conclusions

Sascha Stump[1] and Howard D. Beall[1*]

[1]Center for Environmental Health Sciences, Department of Biomedical and Pharmaceutical Sciences, University of Montana, Missoula, Montana 59812, United States of America

*Corresponding author

E-mail: howard.beall@umontana.edu

Conclusions

Cancer is a disease that will cause a hardship in the life of nearly every person in one way or another, whether it be a personal diagnosis of that of a family or friend. The National Cancer Institute estimates nearly 40% of individuals in the United States will face a cancer diagnosis at some point during their lifetime (Siegel, Miller, and Jemal 2018). Through research, we have made great progress in treating some types of cancer; however, for other forms such as malignant cancers of the brain and central nervous system, the prognosis has remained quite grim (American Cancer Society 2014). The limited success in treatment of certain aggressive forms of cancer such as glioblastoma highlights the need to develop new strategies to create more effective therapies (Y. Wang et al. 2017). This will almost certainly require the examination of new mechanistic targets to allow for creation of more selective and potent antitumor agents. In this work, we detail our significant findings from studies of three distinct molecular targets as they relate to development of novel antitumor agents.

Quadruplex DNA

Targeting quadruplex DNA for treatment of cancer has been the focus of an increasing number of research groups over the past two decades. This has been catalyzed by the discovery of quadruplex-forming DNA sequences in human gene promoter regions and telomeres (Burge et al. 2006; Balasubramanian, Hurley, and Neidle 2011). The realization that stabilizing quadruplex structures with small molecule ligands could affect gene expression and prevent telomere elongation suggests

development of these compounds could lead to creation of promising new anticancer drugs (Neidle 2017).

Structure of the human c-MYC promoter quadruplex

We have reported and characterized the first high-resolution crystal structure of the major quadruplex formed in the human c-MYC promoter region (Stump et al. 2018). The oncogene c-MYC is overexpressed in approximately 70% of all human cancers, and reduction in c-MYC expression has been reported to induce apoptosis in multiple tumor cell types (Siddiqui-Jain et al. 2002; Ou et al. 2007). Stabilization of the quadruplex formed in the c-MYC promoter with small molecules has been demonstrated to inhibit transcription and expression of c-MYC. These previous findings illustrate the significance of the high-resolution crystal structure reported in this work. The core region of the crystal structure is similar to that observed in NMR solution studies, however the flanking regions showed a previously uncharacterized conformation and presented a plausible alternative binding hypothesis (Stump et al. 2018). This crystal structure will aid future and current endeavors to selectively target the c-MYC promoter quadruplex for development of anticancer therapies.

AIMs interact with quadruplex DNA structures

In this work we provided evidence that the AIMs interact with quadruplex DNA structures. Our circular dichroism spectroscopy thermal melting studies demonstrate the AIMs increase the stability of both 3+1 mixed and fully parallel quadruplex topologies formed by human telomeric and c-MYC promoter sequences (Weaver et al.

2015). In contrast, we observed no significant stabilizing effect on an anti-parallel quadruplex formed in the COX I gene of mitochondrial DNA (Huang et al. 2015). This suggests the AIMs chemical structure may discriminate between different quadruplex topologies as it relates to their binding. Discovery of small molecules with selectivity between different quadruplex topologies and loop structures may be necessary to develop better therapeutics; our findings with the AIMs may present an opportunity to design these types of selective ligands (Burge et al. 2006; Neidle 2017). The results with the CSB II DNA:RNA hybrid quadruplex demonstrate the remarkable stability of this structure and suggest it must be resolved by an enzyme such as a helicase in mitochondria to allow for transcription and replication of mitochondrial DNA. Our NMR studies further confirm interaction of the AIMs with c-MYC promoter and telomeric quadruplex DNA sequences through anisotropy induced by the presence of the compounds in solution. The solution NMR results also provide insight about the specific molecular interactions involved in stabilization of the c-MYC promoter and telomeric quadruplexes by the AIMs. These studies together are informing development of the next generation of AIM compounds by the Natale laboratory for targeting quadruplex DNA (Weaver et al. 2015).

Mitochondria

AIMs localize to mitochondria and can inhibit mitochondrial ETC complexes

Our confocal microscopy studies reveal that the AIMs localize to the mitochondria of glioblastoma cells as indicated by their punctate staining and colocalization with a mitochondria specific dye. We have also shown that the AIMs

inhibit activity of the electron transport chain, specifically Complex II, and we provided insights into the potential mechanism of binding. Further, we demonstrated several expected downstream effects of ETC protein complex inhibition. Our results indicate treatment with the AIMs causes rapid damage to mtDNA and a loss in the intact mtDNA copy number in glioblastoma cells. We also measured a loss of mitochondrial membrane potential resulting from treatment with the AIMs. These results suggested that hyperpolarization of the mitochondria occurs at low AIM treatment concentrations, and the literature suggests that this event may precede loss of the mitochondrial membrane potential (Zorov, Juhaszova, and Sollott 2006). Our molecular docking calculations also provide an initial binding hypothesis for AIMs interaction with the ubiquinone sites of Complex II. Together, these studies will inform continued development of the AIMs and could provide the basis for designing AIMs to target the ubiquinone sites of Complex II for treatment of cancer.

AIMs induce the intrinsic pathway of apoptosis in glioblastoma cells

This work shows that treatment with the AIMs in glioblastoma cells causes activation of the mitochondrial-dependent intrinsic pathway of apoptosis. This finding reinforces our hypothesis that destabilization in mitochondria following AIMs treatment is contributing to the induction of apoptosis. In addition, it further demonstrates that the AIMs can overcome the resistance to apoptosis, a known “hallmark of cancer”, and cause tumor cell death. This was verified through measurement of activated caspase-9, an initiator caspase, and the downstream executioner caspases 3 and 7. Further, we show that the AIMs cause an increase in apoptosis without a corresponding increase in

necrosis. This lack of necrosis is favorable for antitumor agents as the necrotic process often damages surrounding healthy tissue.

NAD(P)H Quinone Oxidoreductase 1 (NQO1)

Novel quinolinedione analogs reduce cell viability in breast cancer cells and the effect is not dependent on NQO1 expression or compound suitability as a substrate for NQO1

Our studies in collaboration with the Sammelson laboratory at Ball State University showed that a novel series of quinolinedione analogs had sub-micromolar efficacy against breast cancer cells. We evaluated the series of compounds in both a parent cell line and those transfected to overexpress NQO1. Our results show that the cytotoxicity of the quinolinedione analogs did not depend on NQO1 expression as we initially expected. However, our experiments did demonstrate the suitability of the compounds for reduction by NQO1. Taken together, these results indicate that this series of quinolinedione analogs has significant antitumor activity that is not related to NQO1 expression. This suggests that the activity of these compounds may be due to interactions with other reductases present in the cell and presents an opportunity for continued research.

Future Directions

The findings of this work contributed to the understanding of important targets for anticancer drug development, and the mechanism of action underlying the activity of two classes of novel antitumor compounds. As a result, this has uncovered several new questions and opportunities for future research.

AIMs Interactions with Quadruplex DNA

These studies have provided the basis for developing a more complete understanding of the AIMs interaction with quadruplex DNA. Our crystallization experiments and the knowledge gained regarding the c-MYC promoter quadruplex have already begun to be applied to co-crystallization studies with the AIMs, and success in this endeavor will greatly benefit the continued development of these compounds. The CD spectroscopy experiments demonstrate the feasibility of utilizing this method for the AIMs and could be expanded to other quadruplex-forming DNA sequences to develop a better understanding of the AIMs measured preference for certain quadruplex topologies.

AIMs Activity at the Electron Transport Chain

Our work has shown the capability of the AIMs to inhibit the electron transport chain, specifically Complex II, and proposed an initial binding hypothesis for consideration. However, studies to measure the impact of the AIMs on mitochondrial function in the presence of other ETC inhibitors could provide additional insights regarding their specificity for Complex II and the mechanism of inhibition. Our cell viability studies with primary rat astrocytes highlight the importance of measuring the toxicity of these compounds against healthy human cells in the future. It would also be prudent to screen the AIMs against additional tumor cell lines arising from types of cancer that have been shown to be sensitive to Complex II inhibition such as breast and skin cancer (L. Wang et al. 2016; Guo et al. 2016).

Summary

Collectively, this work has revealed several significant findings that will be important to future endeavors in antitumor drug development. The characterization of the c-MYC promoter quadruplex we report is the first definitive high-resolution crystal structure of this important anticancer target and will provide the basis for design of targeted quadruplex-ligands. Our mechanistic studies with the AIMs demonstrate a plausible mitochondrial mechanism of action through inhibition of the electron transport chain protein complexes, specifically Complex II, and disruption of the mitochondrial membrane potential. This is a novel mechanism that has not been previously shown for these compounds and demonstrates their potential for development as mitochondrial medicines for treatment of cancer. Taken together, the studies presented here advance the field of anticancer therapeutics through elucidation of the molecular structure of an important target, the c-MYC promoter quadruplex, and by laying the foundation for continued development of the AIMs as antitumor agents.

References

American Cancer Society. 2014. “Cancer Facts & Figures.” *Cancer Facts and Figures*.
Balasubramanian, Shankar, Laurence H. Hurley, and Stephen Neidle. 2011. “Targeting G-Quadruplexes in Gene Promoters: A Novel Anticancer Strategy?” *Nature Reviews Drug Discovery* 10 (4): 261–75. https://doi.org/10.1038/nrd3428.

Burge, Sarah, Gary N. Parkinson, Pascale Hazel, Alan K. Todd, and Stephen Neidle. 2006. “Quadruplex DNA: Sequence, Topology and Structure.” *Nucleic Acids Research* 34 (19): 5402–15. https://doi.org/10.1093/nar/gkl655.

Guo, Lili, Alexander A. Shestov, Andrew J. Worth, Kavindra Nath, David S. Nelson, Dennis B. Leeper, Jerry D. Glickson, and Ian A. Blair. 2016. “Inhibition of Mitochondrial Complex II by the Anticancer Agent Lonidamine.” *Journal of Biological Chemistry* 291 (1): 42–57. https://doi.org/10.1074/jbc.M115.697516.

Huang, Wei-Chun, Ting-Yuan Tseng, Ying-Ting Chen, Cheng-Chung Chang, Zi-Fu Wang, Chiung-Lin Wang, Tsu-Ning Hsu, et al. 2015. “Direct Evidence of Mitochondrial G-Quadruplex DNA by Using Fluorescent Anti-Cancer Agents.” *Nucleic Acids Research* 43 (21): 10102–13. https://doi.org/10.1093/nar/gkv1061.

Neidle, Stephen. 2017. “Quadruplex Nucleic Acids as Targets for Anticancer Therapeutics.” *Nature Reviews Chemistry* 1 (5): 0041.

Ou, Tian-Miao, Yu-Jing Lu, Chi Zhang, Zhi-Shu Huang, Xiao-Dong Wang, Jia-Heng Tan, Yuan Chen, et al. 2007. “Stabilization of G-Quadruplex DNA and Down-Regulation of Oncogene c-Myc by Quindoline Derivatives.” *Journal of Medicinal Chemistry* 50 (7): 1465–74. https://doi.org/10.1021/jm0610088.

Siddiqui-Jain, Adam, Cory L. Grand, David J. Bearss, and Laurence H. Hurley. 2002. “Direct Evidence for a G-Quadruplex in a Promoter Region and Its Targeting with a Small Molecule to Repress c-MYC Transcription.” *Proceedings of the National Academy of Sciences* 99 (18): 11593–98. https://doi.org/10.1073/pnas.182256799.

Siegel, Rebecca L., Kimberly D. Miller, and Ahmedin Jemal. 2018. “Cancer Statistics, 2018.” *CA: A Cancer Journal for Clinicians* 68 (1): 7–30. https://doi.org/10.3322/caac.21442.

Stump, Sascha, Tung-Chung Mou, Stephen R. Sprang, Nicholas R. Natale, and Howard D. Beall. 2018. “Crystal Structure of the Major Quadruplex Formed in the Promoter Region of the Human c-MYC Oncogene.” *PLOS ONE* 13 (10): e0205584. https://doi.org/10.1371/journal.pone.0205584.

Wang, Liang, Xiaojing Zhang, Guozhen Cui, Judy Yuet-Wa Chan, Li Wang, Chuwen Li, Luchen Shan, et al. 2016. “A Novel Agent Exerts Antitumor Activity in Breast Cancer Cells by Targeting Mitochondrial Complex II.” *Oncotarget* 7 (22): 32054–64.

https://doi.org/10.18632/oncotarget.8410.

Wang, Yu, Xiangyi Kong, Yi Guo, Renzhi Wang, and Wenbin Ma. 2017. “Continuous Dose-Intense Temozolomide and Cisplatin in Recurrent Glioblastoma Patients.” *Medicine* 96 (10). https://doi.org/10.1097/MD.0000000000006261.

Weaver, Matthew J., Alison K. Kearns, Sascha Stump, Chun Li, Mariusz P. Gajewski, Kevin C. Rider, Donald S. Backos, Philip R. Reigan, Howard D. Beall, and Nicholas R. Natale. 2015. “AIMing towards Improved Antitumor Efficacy.” *Bioorganic & Medicinal Chemistry Letters* 25 (8): 1765–70. https://doi.org/10.1016/j.bmcl.2015.02.063.

Zorov, Dmitry B., Magdalena Juhaszova, and Steven J. Sollott. 2006. “Mitochondrial ROS-Induced ROS Release: An Update and Review.” *Biochimica et Biophysica Acta (BBA) - Bioenergetics*, 14th European Bioenergetics Conference, 1757 (5): 509–17. https://doi.org/10.1016/j.bbabio.2006.04.029.